A MONTE CARLO CODE TO OPTIMIZE THE PRODUCTION OF RADIOACTIVE ION BEAMS BY THE ISOL TECHNIQUE.

Mario Santana Leitner

A DISSERTATION SUBMITTED IN PARTIAL FULFILLMENT OF THE REQUIREMENTS FOR THE DEGREE OF DOCTOR OF PHILOSOPHY IN NUCLEAR ENGINEERING AT THE TECHNICAL UNIVERSITY OF CATALONIA (UPC), PHYSICS AND NUCLEAR ENGINEERING DEPARTMENT (ETSEIB-SEN)

July 2005

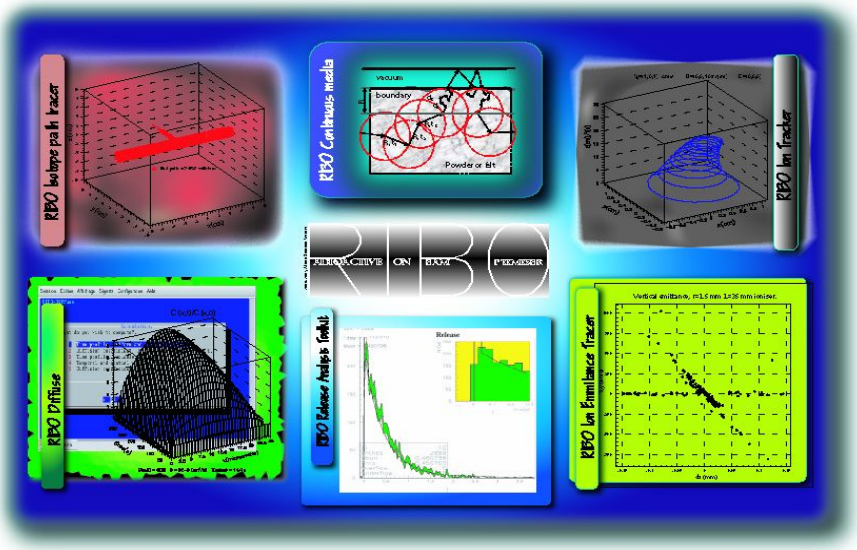

ADVISORS: Dr. Helge Ravn and Prof. Francisco Calviño Tavares

Latest information is posted in the RIBO project homepage at:

http://cern.ch/ribo

Preface

Currently the nuclear chart includes around 3000 nuclides, distributed as β^+, β^- and α-emitters, stable and spontaneously fissioning isotopes. A similar amount of unknown nuclei belongs to the so-called *terra incognita*, the uncertain region contained also within the proton, neutron and (fast) fission driplines and thereby stable against nucleon emission. The exploration of this zone is to be assisted by the use of radioactive ion beams (RIB) and could provide a new understanding of several nuclear properties. Moreover, besides pointing at crucial questions such as the validity of the shell model, the dilute matter and the halo structure, challenging experiments outside nuclear physics are also attended, e.g., explanations of the nucleosythesis processes that may justify why the matter in the universe has evolved to present proportions of elements, and which represents a major challenge to nuclear physics.

These, together with other fascinating research lines in particle physics, solid state physics and medicine, demand utterly exotic and intense ion beams for which a global optimization of all relevant phenomena in beam formation has to be coherently conducted. As a response to this request, a Monte Carlo simulation code has been written, to integrate diffusion and effusion under various

pressure flows and conditions, including the transport through continuous media and enabling diffractive and surface dependent effects, emulating ionization in surface and plasma ion sources and, finally, reproducing the movement of ions under electro-magnetic fields.

Contents

Index

List of Figures

List of Tables

The author would like to thank the myriad persons who were instrumental in helping me to complete this work. Thanks to the people who volunteered their time to read through drafts of this thesis and offer suggestions; Olof Tengblad, Ulli Köster, Oliver Kester, Peter Dendooven and Luigi Tecchio, among others.

Most of all, I would like to express my gratitude to Kari Peräjärvi, who provided an enthusiastic starting impulse and friendly guidance during the definition of the thesis structure. Further thanks go to Antonio Sîber for his valuable contributions in the semiclassical expressions of the collision models.

I appreciate the confidence grated by my thesis advisors, Helge Ravn and Paco Calviño, who let me seek my own way to find and give shape to a theme of my taste, and who, at key moments, provided all their judicious experience and knowledge.

Thanks also to my parents, who supplied the item of greatest worth: opportunity. Thank you for standing by me throughout my educational career.

I wish to express my deepest gratitude to those on the other side of the Ph.D. fence for their patience and support during this long way.

In addition to the colleages at ISOLDE, I need to thank all the people who I met during the research leg of my thesis journey.

Lastly, my PhD would not have been possible without the generous funding of EURISOL, ISOLDE *and, somehow, of the Spanish Ministry of Science and Technology.*

Part I

Development of a Monte Carlo Code to optimize ISOL targets

Chapter 1

Introduction.

ENERGETIC BEAMS of radioactive ions (RIB) are produced at the highest rates in systems where a particle accelerator and a mass selector are directly coupled to a fixed target-ion source irradiated by a beam of light particles. This method, known as Isotope Separator On-Line (ISOL) and proved 50 years ago at the Niels Bohr Institute, produces large amounts of radioisotopes through nuclear reactions in a hot target that favors diffusion and effusion through transfer lines (eventually chemically selective) up to an ion source. Once ionized, the radioisotopes can be accelerated to suitable energies and directed to the experimental stations, where research in nuclear physics, nuclear astrophysics, solid state physics and atomic physics is carried out.

The forefront research programs of the above scientific communities demand highly exotic beams, spurring on the development of new production techniques that are able to comply with those needs.

In this introductory chapter the physics goals that ultimately motivate this thesis are shortly presented, then some basic ideas linked to the system used to achieve these are presented and finally the precise role of this work in the given frame is depicted, setting the steps which follow in the chapters to come.

1.1 CERN and ISOLDE.

CERN is the French acronym for *Conseil Europé en pour la Recherche Nucleaire* (European Council[1] for Nuclear Research), also known as the European Center for Particle Physics Research. Created during the cold war, this international organization located astride the *Département* of Rôhne Alpes (France) and the *Canton* of Genève (Switzerland), a few kilometers west of Geneva, celebrated during 2004 its 50^{th} anniversary. CERN, who counts 21 member states[2] and a large number of non-member states, observers and participating institutes, has become an outstanding example of international cooperation and is a reference laboratory for the research in particle physics. In order to study the nature of matter and of its binding forces, accelerators that act as gigantic microscopes have been built over the years, and a great number of experiments have been developed to focus on specific fields of physics, like ISOLDE where intensive research in nuclear physics, atomic physics and solid state physics is carried out. ISOLDE is an On-Line Isotope Mass Separator facility (fig.1.1) that produces and accelerates a large variety of radioactive ions by irradiating thick targets heated to high temperatures with proton beam bunches[3] taken from the Proton-Synchrotron Booster (PSB). The radioactive nuclides are produced via fission, spallation, or fragmentation reactions in the *target*, then, they are eventually "filtered" in a *transfer line* that connects the target with the so-called *ion source* where they are ionized and further selected. The target and ion source system is therefore a sort of small chemical factory whose ionic output is electromagnetically steered, mass-selected and accelerated to the experimental

An ISOL target is like a chemical ion factory

[1] *Council* is popularly replaced by *Center* or even by *Organization*.

[2] Austria, Belgium, Bulgaria, the Czech Republic, Denmark, Finland, France, Germany, Greece, Hungary, Italy, The Netherlands, Norway, Poland, Portugal, the Slovak Republic, Spain, Sweden, Switzerland and the United Kingdom.

[3] 0.6, 1.0 and 1.4 GeV at about 2 μA

stations. Moreover, since 2003, REX-ISOLDE linear accelerator and charge breeder provide sufficient postacceleration (3.1 MeV/u) to probe nuclear properties through transfer reactions and Coulomb excitation of the exotic species.

Physics at ISOLDE follows different paths. Besides the quest of a deep comprehension of the atomic nucleus (and of the advances in astrophysics and weak-interaction physics) through a systematic study of atomic and nuclear properties of the produced beams, impurity and defect problems in solid-state physics can be explored through pure radioactive implants in semiconductors. Last, but not least, diagnosis and therapy through the use of radioactive isotopes has enabled the integration of life-sciences into the research program of ISOLDE.

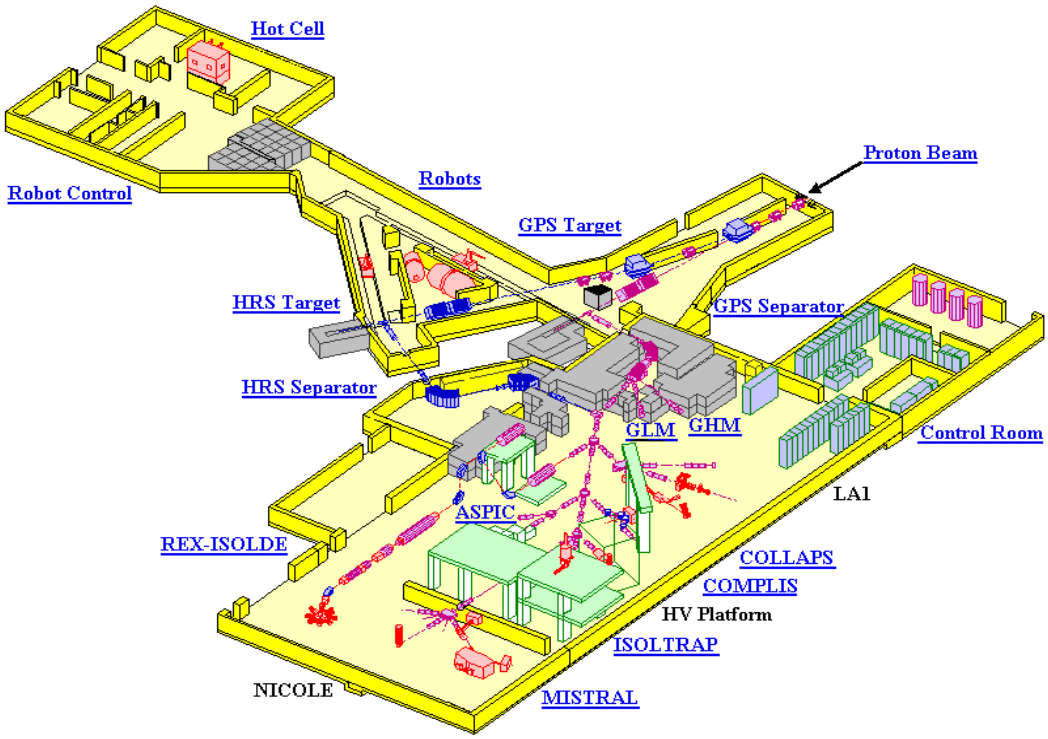

Figure 1.1: A layout of the ISOLDE experimental hall taken from [1].

1.2 Physics motivation and experiments with radioactive ion beams.

The nucleus constitutes a many-body quantal system typically characterized by a few parameters like the number of neutrons and protons (N, Z), the third component of the isospin ($T_z = (N - Z)/2$), the total angular momentum ($J\hbar$), the excitation energy (E), and the nucleon density (ρ). Since the early years of nuclear physics the properties of nuclides have been studied through these numbers and nowadays research has reached the level where extreme values are explored hence demanding exotic[4] probe nuclides with sufficiently high intensities to attain accurate measurements.

1.2.1 Physics cases

A first ISOL-related study theme example in **nuclear physics** is that of the *shell model*, which predicts the so-called shells, nucleon orbits resulting from independent movements under a common interaction potential. This theory apparently fails to explain the first measurements with light exotic nuclides and motivates further experiments with radioisotopes. Some other expected fascinating phenomena, studied for over 30 years in high spin physics, such as *nucleus deformations* (the super or even hyperdeformation), await the experimental confirmation that only highly exotic intense neutron rich beams could provide, by reaching up to spins of 70 $\hbar$. Another client field within nuclear physics concerns the study of very low dense matter; Although it is known that *dilute nuclides* are strongly correlated to fluids, presenting the liquid-gas phase transition and responding to the *nuclear Equation Of State*

A tool to study the shell model, high spins and dilute nuclei

[4] In this jargon this means far from stability.

(EOS), RIBs of a wide energy range are still required to understand the precise influence of the nucleus isospin in the fluids behavior, much as the composition of liquids is needed to understand their own properties. Likewise, low densities may be present in peripheral regions of some isotopes, constituting the *halo*, which is a loosely bound quantum system that attracts considerable interest and which demands intense exotic beams too.

In **nuclear astrophysics**, understanding the nucleosynthesis, that is to say, the sequence of reactions in nuclear explosive events that involves some strongly unstable nuclides and that ultimately leads to the variety of elements present in the universe, is subject to the study of exotic nuclides, produced in RIB facilities. Two outstanding examples are those of the r- and (rp-) processes, where successive captures of neutrons / protons in supernova / binary stars build up neutron / proton rich nuclides that belong to the *terra incognita*, thus of unknown properties (decay probabilities / cross sections) and consequently decaying into daughter elements (heavy elements between Fe and U / light and medium mass elements up to Sn) with not fully known abundances.

Research beyond the *standard model* of electroweak interactions is not exclusively carried out in **high-energy physics** experiments but also through accurate measurements in nuclear β-decay, often done with exotic atoms delivered as intense ionic beams. Some topics in this domain that require this kind of beams are mainly the study of super-allowed β-transitions as a means to test the unitarity of the Cabbibo-Kobayashi-Maskawa (CKM) quark-mixing matrix; the detection of presumed exotic interactions in the nuclear β-decay beyond the traditional vector and axial-vector couplings and the quest of deviations from maximal parity violation or from time-reversal invariance in the strangeness-conserving sector of the Standard Model.

Two additional branches of science that have benefited from RIB are **solid-state physics** and Medicine. The first principally uses the radioactive ions as emitters that are implanted at well-defined depths, and performs experiments with polarized RIBs. **Medical science** benefits from radioactive isotopes both for diagnostic and therapeutic purposes, e.g., radioisotopes extracted from neutron converters in two-stage targets can be implanted (or injected) to combat cancer cells.

1.2.2 Experiments.

Target optimization is starting to enable the successful completion and analysis of a collection of experiments which were out of reach in the past. Below, a sample of a few projected experiments at the moment of the definition of this thesis:

1. Present ISOLDE experiments which require short-lived isotopes of noble gases.

   - IS367: intense beam of ^{6}He to study unbound states in ^{7}He with REX-ISOLDE.
   - IS370: decay spectroscopy of $^{71-75}Kr$ with total absorption spectrometer.
   - IS376: detailed decay spectroscopy of ^{8}He and $^{28-32}Ne$.
   - IS388: precision mass measurements of $^{32-34}Ar$
   - IS394: decay studies of ^{69}Kr
   - I11: intense beam of ^{35}Ar to study the $^{35}Ar(p,\gamma)$ reaction with REX-ISOLDE.
   - P111: ^{35}Ar is first candidate for WITCH experiment.

- P138: decay studies of astrophysical relevant $^{47-49}Ar$.
- IS407: studies with Pb beams in a 5 cm long UC_x target.

2. EURISOL: Ar and Kr are among the NuPECC reference elements whose production methods had been chosen for a detailed comparison.

3. TARGISOL: A vertebral axis of the TARGISOL project is to enable a computer code that can predict the release speed of various elements out of complicated target and ion source geometries from the release data collected in a series of experiments. In order to validate the code it is necessary to measure pure effusion data of several isotopes from various target and ion source geometries.

4. ^{6}He and ^{18}Ne for the βBEAM FACTORY: An efficient extraction of ^{6}He (or alternatively ^{18}Ne) from a large volume target is required.

1.3 Release. Efficiency factors.

The yield of radioactive isotopes may be formulated as the product of the intensity of the primary beam and the efficiency with which this is transformed into an ion beam of a given radioisotope. In particular, in ISOL systems, maximization of the output RIB can be achieved by increasing any of the factors in eq. 1.1:

The final goal is to maximize this equation

$$I\left({}^{A}_{z}X^{+}\right)_{exit} = I\left(Y\right)\cdot\varepsilon_{TOT} = I\left(Y\right)\cdot\left[\varepsilon_{(Y\rightarrow{}^{A}_{z}X)}\cdot\varepsilon_{R}\cdot\varepsilon_{({}^{A}_{z}X\rightarrow{}^{A}_{z}X^{+})}\right] \quad (1.1)$$

Where:

- $I\left({}^{A}_{z}X^{+}\right)_{exit}$ is the final RIB intensity.

- $I\,(Y)$ is the intensity of the primary beam that induces nuclear reactions.
- $\varepsilon_{Y\rightarrow {}^{A}_{z}X}$ is the efficiency to produce isotopes X from the beam Y. It includes all the production cross-sections.
- ε_R is the release efficiency. It expresses the speed of atoms to diffuse from the target, effuse through the system and get ionized before decaying to other species.
- $\varepsilon_{{}^{A}_{z}X\rightarrow {}^{A}_{z}X^{+}}$ is the ionization efficiency (from now on ε_i), describing the ratio of ionized isotopes to the neutral current escaping the ion source.

The task of approaching RIB intensities to the requirements of the physics cases outlined before encompasses the engineering effort to maximize the terms in eq. 1.1. This is a global optimization problem where the rise of one factor tends to lower the others. Thus, the primary beam intensity $(I(Y))$ may be increased by diverting more pulses to the ISOL facility or by upgrading the primary accelerator, but the rise of deposited power could in turn harm the target, melting or sintering it and consequently degrading its release properties (ε_R). Moreover, inside the ion sources ε_R and ε_i tend to be antagonist figures because longer dwell times increase the chances of ionization at the expense of higher decay losses.

As for the mentioned release efficiency, this key factor encompasses several processes involved in the production of radioactive ion beams with the ISOL technique. Once the isotope has been generated in the target bulk, it *diffuses* across solid matter up to a free surface and it then *effuses* through vacuum, following a random walk of collisions with the system walls, eventually *sticking* on them for some time. Finally, after flowing through a (eventually chemically selective temperature controlled) transfer line, the isotope reaches the ion source

Path of an atom in an ISOL *system*

and, in the aimed cases it can be ionized before it finds the outlet orifice, enabling downstream electromagnetic guidance and acceleration. These processes consume a certain amount of time (t) during which radioactive decay may occur, hereby lowering the number of extracted isotopes ($N\,(t)$):

$$N\,(t) \sim exp\left(-\frac{t \cdot ln(2)}{T_{1/2}}\right) \tag{1.2}$$

Where $T_{1/2}$ is the half-life of the isotope.

In view of gaining diffusion rapidity, the target material choice may have to be revised if an alternative projectile-target pair with similar production cross sections shows better diffusion properties. Moreover, the target structure may be redistributed, split in smaller divisions like thinner foils, finer grains.... However, by so proceeding the free effusion flight path is enlarged and the number of collisions to the walls increases. As a consequence, effusion and desorption become slower, specially for isotopes that are chemically affine to the surface walls. Next, effusion to and in the ion source can be improved with new designs of the transfer lines and ion source, but this tends to inhibit the chemical separation and to shorten the confinement in the plasma chamber, ultimately lowering the ionization efficiency.

On top of this complicated scheme, more variables may deserve consideration, such as the variation of the running temperature of the target, or the impact of homomorphic variations of the system dimensions, both addressed at an enhancement of diffusion and effusion. However, this may again have some side effects like the deterioration of the target properties (melting for a serious temperature rise) or the decrease of absolute isotope production due to the shrinkage of the amount of target.

All this justifies the development of a project that can comprehensively cope with all the coupled variables, with the capability to isolate the composing effects and to ease their individual study.

1.4 The Monte Carlo project. RIBO, a Radioactive Ion Beam Optimizer.

The central goal of this work is to provide a reference tool and a set of recommendations and methods to optimize the extraction efficiency of exotic isotopes from target and ion sources systems. The core tool is materialized in a computer program, and more precisely in a Monte Carlo simulation code.

A brief note on **Monte Carlo** codes should be made before continuing. As suggested by their name, Monte Carlo programs make use of random numbers to reconstruct complex stochastic distributions, but they can also be used to approach deterministic problems due to their intrinsic and powerful capability to compute multi-variant integrals. For instance, the area of a given polygon contained in a rectangle can be computed with a simple Monte Carlo program that samples a random point within the rectangle (two uniform numbers r_x and r_y are sampled). The code verifies if the point belongs to the polygon (substituting (r_x, r_y) in the equations of the enclosing curves and checking the resulting sign); the operation is repeated N times. The frequency of successful checks (N_{pos}/N) equals the ratio between the polygon area and that of the enclosing rectangle. This technique may be applied recursively, looped and used in sophisticated ways so as to emulate complex processes.

A MC code is a numerical integration tool

In the frame of this thesis a Monte Carlo radioactive ion beam tracer (RIBO) has been written to simulate the transport of atoms (and ions) at very low energies,

from the target to the beam line, passing through the ion source. In the present point the Monte Carlo project comprehends the following utilities, whose physical foundations will be depicted throughout the thesis, and the use of which will be phrased in the annex sections:

- Main module, `RIBO.mc` (an. B): The main module manages the different programs through an interactive interface. It links the different executables and the external programs.

- Diffusion module, *Diffuse* (ch. 2): It can compute the diffusion time and space profile (*Diffprof*) of atoms in several geometries including the possibility of variable and heterogeneous materials and starting concentrations, and continuous or discrete source or sink terms. It can also be used in an inverse mode (*Diffact*) to extract diffusion properties from fractional activity measurements, or embedded in the Monte Carlo, to sample the release of diffusing particles. This module is assisted by some additional scripts that permit the interactive use of the software (message-boxes), the automatic production of diffusion plots with the Physics Analysis Workstation (PAW) [6] and the smooth convolution of the obtained functions with other time distributions (*DconvE*).

- Effusion tracer (ch. 3): The Monte Carlo program tracks the effusive flow of atoms through rarefied (or slightly pressurized) gases, including functions for temporary adsorption, permanent absorption to the surface walls as well as different interactions with the surface walls, with or without thermalization. Moreover, a hybrid diffusive-effusive transport has been developed for porous media.

- Ionization, *surfION, plION* (ch. 4): *surfION* enables surface ionization and *plION* acts as a FEBIAD ionizer emulator. In both cases databases are available to be consulted and extended as more data are measured and available.

- Ionic tracer, *EMfield* (ch. 4): It computes the path of ions under electric and magnetic fields. This module, used in conjunction with the preceding ones, can also provide information about the beam shape, i.e. emittance.

- Random trajectory emulator, *RATE*: It traces a single particle and stores the trajectory into an array which is called by PAW and 3D-plotted on screen.

- 3D-Geometry Viewer, *3D-RIBO* (an. B): This interface exports the combinatorial geometry for use with a raytracer, POV [7].

- Subsidiary tools, *analyze* (an. B): A marginal set of tools is eventually used for analyzing purposes.

As it happens in other domains, this is an evolving project; upgrades are continuously produced triggered by the proposals from the growing community of its users or by advances in the installed dependencies. Hence, future releases are expected with new features on the menus, more functions and improved interfaces.

1.5 Goals.

The code, and the associated methodology shall then prove their potentiality to optimize and predict yields in real cases such as the key experiments at ISOLDE, EURISOL or the β BEAM FACILITY. A preliminary definition of objectives is:

- To discuss, implement and test the diffusion formulas for basic target constituents.

- To study the impact of typical experimental conditions and uncertainties on the diffusion curves.

- To discuss, implement and validate a general purpose effusion emulator routine, able to determine the conductance of complex systems as well as their transient conduction functions.

- To set the optimization criteria for transport lines; to characterize the delay mechanisms in the target and ion source systems.

- To write a program that inverts the diffusion equation so that diffusion parameters can be extracted from activation measurements and thereby be used as input to simulations.

- To create an extended effusion subroutine that can simulate the diffusion of atoms through continuous media.

- To provide an extension of the effusion routines for non-molecular flow regimes, so that effusion paths can be computed even for cases where interactions between particles start to become frequent.

- To establish a method to measure the diffusion coefficient, average sticking time and porosity of powder and fiber targets. To determine these parameters for a collection of relevant atom-target combinations.

- To model ionization processes and to implement them.

- To describe ionic trajectories in presence of electro-magnetic fields and to couple the ion transportation functions with the main code through ionization and recombination.
- To present applications of the software to relevant physics projects.
- To provide first order beam intensity estimations and preliminary designs for EURISOL.
- To provide enough instructions, documentation and auxiliary tools for other users to use the programs. To lay out the way for future upgrades.

The first part of the thesis is devoted to the implementation of the models that shall best emulate the release steps: diffusion, effusion (including continuous media, sticking and pressure effects) and ionization. The second part applies the resulting program to the analysis of the mainly used and forecast target filling morphologies; parallel and rolled thin foils, powder and fibers.

Chapter 2

Diffusion.

Diffusion [8]...

- *"The spread of cultural elements from one area or group of people to others by contact."*
- *"The process whereby particles of liquids, gases, or solids intermingle as the result of their spontaneous movement caused by thermal agitation and in dissolved substances move from a region of higher to one of lower concentration"*
- *"Reflection of light by a rough reflecting surface. Transmission of light through a translucent material"*
- *"The softening of sharp outlines in a photographic image."*

★

DIFFUSION IS OFTEN THE DOMINANT delaying mechanism in the extraction of atoms from targets. A careful analysis of this process is therefore justified. In this chapter the main relevant diffusion formulas, together

with the assumed hypothesis will be presented and numerical analysis will cast some light on various systems. A section will be dedicated to the experimental techniques that are employed to infer the diffusion parameters and to the software that has been developed to ease the subsequent analysis. Finally, the sampling techniques used in the Monte Carlo code are presented and considerations are made for time dependent effects like shock waves and the grain growth.

To start the chapter, a brief revision of the mathematical basis of diffusion is made with emphasis on the principles and formulas that will be adopted for the rest of this text.

2.1 Diffusion in solids. Fundamental equations.

One of the governing delay processes in the escape path of isotopes through ISOL systems is the diffusion within solids (in-grain diffusion). This classical problem is extensively treated in the literature [9, 10]. The dissertation to arrive at some practical formulas begins by writing the boundary condition and the second law of Fick [11]:

$$\left.\begin{array}{c} D \cdot \left(\frac{\partial C(\vec{r},t)}{\partial \hat{n}}\right) = k \cdot C_s \\ \frac{\partial C(\vec{r},t)}{\partial t} = D \cdot \nabla^2 C\left(\vec{r},t\right) \end{array}\right\} \tag{2.1}$$

where:

- Space and time are represented by $\vec{r}$ and t, respectively.
- D is the diffusion coefficient. It is well known that D depends on the temperature but normally not on the concentration. The

temperature dependence is conveniently described by the Arrhenius relation:

$$D = D_0 \cdot e^{-Q/RT} \tag{2.2}$$

Where Q is the activation energy for diffusion, R the universal gas constant, T the absolute temperature. D_0 corresponds to the maximum diffusion coefficient, for infinite temperatures. D is usually under-bounded by D_{self} (self diffusion), which in turn may be determined with the LeClaire [12] empirical relationship:

$$Q_{self}\,[cal/mol] = 38 \cdot T_m\,[K] \tag{2.3}$$

T_m being the absolute melting temperature.

- C is the volumetric density of atoms ($\frac{number\ of\ atoms}{volume}$).
- C_s is the superficial density of atoms.
- k is a proportionality constant.
- The atoms are assumed to flow in the direction of the normal of the surface, $\hat{\mathbf{n}}$[1].

Experimental studies on irradiated targets (section 2.4, page 24) indicate that the sojourn time on the free surface of a solid can be neglected with respect to the diffusion time invested by the atom to reach that point (the surface concentration is very low; $C_s = 0$). Moreover, the diffusion coefficient is supposedly

[1]This notation already restricts us to those geometries where the normal direction inside the solid can be unambiguously defined, the most representative examples being slabs, cylinders and spheres.

homogeneous and constant, $D \neq D(\vec{r}, t)$, and, for thin targets, the diffusing matter is assumed to be homogeneously distributed at the beginning of the diffusion cycle, which should be considerably shorter than the duty cycle[2].

$$\begin{cases} C(x,0) = C(0); & 0 < x < a \\ C(x,t) = 0; & x \leq 0 \cup x > a \end{cases} \tag{2.4}$$

The resulting solution [13] for the diffusion flux (f), considering isotropy in D, was assembled in a compact expression by Fujioka [14]:

$$f(\hat{t}) = \frac{2n}{\pi^2} \sum_{m=1}^{\infty} \frac{e^{-N_m \cdot \hat{t}}}{N_m} \tag{2.5}$$

is valid for foils/slabs (n = 1), fibers/cylinders (n = 2) and particles/spheres (n = 3),

$$N_m = \begin{cases} (m-1)^2; n = 1 \\ (j_{0,m}/\pi^2); n = 2 \\ m^2; n = 3 \end{cases} \tag{2.6}$$

Where $\hat{t}$ is a non-dimensional parameter corresponding to the ratio of the elapsed time to the diffusion time constant, $\hat{t} = t/\tau_D; \tau_D = \frac{1}{\eta} = \frac{a^2}{\pi^2 D}$, $2a$ being the thickness of the slab or the diameter of the cylinders or spheres (d). $j_{0,m}$ represents the m^{th} positive root of the Bessel function of order zero.

[2] Periodicity of the beam pulses

2.2 Inter grain diffusion. Effusion or Diffusion?

Diffusion and Effusion are very close concepts

The extraction of atoms from powder or fiber targets involves two regimes of diffusion. At first the atom diffuses from the interior of a particle or fiber to its surface. This is the so-called *in-grain diffusion* and can be approached by the classical expressions (2.1). In the following step the exiting atom moves through the grain/fiber structure/felt, until it reaches the powder/mesh boundary. In this *a priori* effusive-like process the geometry is rather obscure, its knowledge being limited to a few average parameters. Whence, this flow is called *inter-grain diffusion*[3] and the corresponding average parameters can be thought to be embedded in some kind of inter-grain diffusion coefficient. Those concepts, of

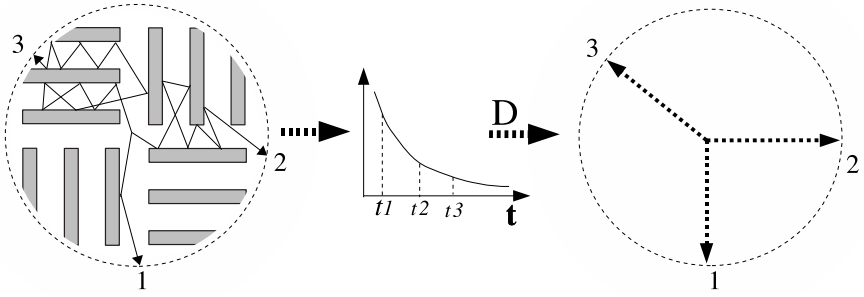

Figure 2.1: To increase computing speed, diffusion formulas may be applied for macroscopic cases, if preliminary effusion simulations provide acceptable bulk diffusion coefficients.

microscopic nature, may be extended to macro-structures like that of a foil target, where a continuous zone of target-spacers is bounded by an (imaginary) wrapping surface. Pursuing the analogy, a bulk diffusion coefficient could be assigned to these structures upon dedicated simulation or experiments (see fig.2.1). Those coefficients could then be used in the classical formulas (2.1) to describe the migration of atoms from cylindrical, spherical or parallel faced

[3] It is also known as *bulk diffusion* or as *volume diffusion*.

blocks (2.5). The resulting diffusion profile should then be convoluted to the effusion curve of the remaining system (transfer lines, ion source). Some advantages of the diffusive approach to macro-structures:

- A huge amount of CPU time is saved when an effusion process (simulated) is replaced by diffusion (analytical).
- Immediate (re)computation after basic resizing of the bulk boundaries[4].
- Careful data taking of the average parameters provides also information of the target inner structure.

And some drawbacks are:

- In foil targets, space is anisotropic and, thus, diffusion coefficients are no longer scalar [15]. The classical formulas then require a tensorial treatment. Moreover, if foil spacing/thickness is not constant, the diffusion tensor will be position dependent.
- The target zone may not necessarily be spherical, cylindrical nor plane. Then a solution has to be worked out numerically from Fick's laws.
- Plain convolution assembles consecutive, non-reversible processes. However, atoms are backscattered inside the target structure chaining a succession of in-grain diffusion and pure effusion phases. Thus, the global release curve has to be corrected with the proper re-diffusion coefficients.

Diffusion is a somehow larger concept than Effusion (ch. 3), but in this context its name is often reserved to those microscopic, blurry circumstances where averaging is required. If the inner geometry of the solids can be written into

[4]However, a significant change of the external geometry will imply new (maybe lengthy) effusion simulations for the transport in the vacuum.

equations, then the transport flow simulations may be carried out and the term *Effusion* is used. In this thesis, the effusion approach is used for inter-grain / inter-fiber / inter-slab diffusion. Chapter 3 focuses on these items [16].

2.3 Space-Time dependent phenomena.

Classical solutions overlook various distorting factors that appear with variable intensity during ISOL runs. Their absolute value or their time modulation are seldom known with good precision. In the following subsections some of these effects will be depicted and in 2.5 solutions will be proposed for their prediction and evaluation.

2.3.1 DC effects.

Rising the operational temperature produces an increase in the extraction efficiency. This enhancement is limited to the maximum bearable temperature in the system components, typically the minimum melting temperature, $\min\{T_m^i\}$ or the temperature at which the vapor pressure becomes excessive.

Target endurance and performance are antagonists

Attaining a constant (DC) temperature close to the highest achievable temperature maximizes the starting isotope beam current, but such a severe use of the target will accelerate its deterioration and, therefore, the efficiency will drop very rapidly. The time integral of the release efficiency (ε_R) casts a figure of merit that ought to be the aim of the optimization schemes for a total elapsed time T_M.

$$\int_{t=0}^{t_M} \varepsilon_R(t) \cdot dt \tag{2.7}$$

Individual fibers, grains or foils in a target may at some point be in contact with neighboring components. This might be so from the very beginning or it can also happen due to the slight dilatations and to the softening that is produced as a direct consequence of high running temperatures. In strongly heated targets, diffusion is favored and the contact points between grains, fibers or foils offer a bridge for atoms to diffuse from one part of the target to its contiguous one. This process, known as *sintering*, welds the contact points and leaves internal joints. Sintering is manifested as *grain growth* in powders and as slab coalescence in foiled targets. The characteristic diffusion thickness, "2a" rises accordingly and so does the diffusion time constant.

2.3.2 AC time effects. Shock wave.

The primary beam deposits a great quantity of energy even in thin targets. That heat is translated into a transient temperature rise, which can amount to some 100-200 degrees centigrade during about 600 milliseconds. For DC beams the beam heat contribution is constant.

2.3.3 Space dependent temperature.

The existence of temperature gradients implies, as can be seen from the Arrhenius relation (eq.2.2), subsequent gradients of D. The prediction of those may be carried out numerically, though most often the knowledge of the temperature distribution is merely limited to the hypothesis of inhomogeneity, with no precision on the spatial variation. The diffusion curve is then obtained as a linear combination of a fast diffusing component (hot spots) and a slower component. The result is extremely sensitive to the relative weights of each part [17].

2.3.4 Target damage.

The impact of strong temperature variations is only known to a phenomenological degree and sometimes not at all. In some cases an autopsy of the target is done[5] to reveal if sintering or other effects have taken place. If such effects were accurately quantified, it would still not be trivial to simulate the deformed shapes that are observed and even less to introduce a time-dependent deformation from the original shape to the final one.

Attention has to be paid to the incidences in the on-line data that are taken as benchmark for code validation purposes. The experiment logbook should be checked for the temperature evolution of the target, the intensity of the primary beam as well as any power failure. The release curve measured at the end of the experiment is often slower than expected due to the sintering that takes place in the target, where effusion, and specially diffusion are negatively influenced. If that were the case, the simulations should be tested with a somewhat bigger diffusion thickness parameter. Other important parameters should be revised too, e.g., ionization efficiency, temperature of line and target.

2.4 Experimental Techniques.

One of the experimental techniques used to determine the diffusion parameters is the fractional activity print. The diffusion law of Fick (2.1) accepts source and/or sink terms. Such is the case of an on-line irradiated target where the concentration of radioactive atoms is constantly fed by the nuclear reactions (*source*) while their instability produces decay losses (*sink*). The corresponding differential equation for an isotope of half-life $T_{1/2}$ produced by a flux of primary

[5]This is not always easy; among radiological issues some materials like Ta become brittle and break into pieces when cutting apart the target container.

particles of intensity I and generation cross section σ in a target of density ϱ is [18]:

$$\frac{\partial C}{\partial t} = D\frac{\partial^2 C}{\partial x^2} - \frac{C}{T_{1/2}} + \sigma\rho I \tag{2.8}$$

The density flow out of a slab of thickness a being:

$$\frac{dC}{dt} = \frac{2\sigma I}{a} C_0 \cdot \left(D \cdot T_{1/2}\right) \cdot \tanh\left[\frac{a}{2\sqrt{D \cdot T_{1/2}}}\right] \tag{2.9}$$

2.5 Computer software related to diffusion.

Fick's diffusion laws usually lead to explicit but unclosed (infinite sum) formulas that express the amount of atoms released as a function of time. Such formulas exist for the rate of release (f) and for its time-integrated figure (F), the last being directly related to the fraction (A) of atoms remaining in a given sample $(A = 1 - F)$.

Diffusion formulas depend on time (t), geometric shape [14], diffusion coefficient (temperature dependency comes in here) and thickness ($d = 2 \cdot a$), where the two last variables are merged in a single parameter, η:

$$\eta = D\frac{\pi^2}{a^2} = {\tau_D}^{-1} \tag{2.10}$$

τ_D is the diffusion time constant.

2.5.1 `Diffuse`.

`Diffuse.sh` is a (UNIX-Linux) interactive bash shell skin script module that calls a core program written in FORTRAN (diffuse.f), which can perform a

variety of calculations derived from Fick's Laws[6]. In its most basic and frequent use, `Diffuse` evaluates the expressions of Fujioka [14] (described in 2.1) for a given time constant and geometry type (foil, fiber or sphere) at different times, thus yielding the diffusion time-profile. This is useful when the conditions for the corresponding equations (2.5, 2.6) are reasonably fulfilled, that is: if the diffusing atoms are generated homogeneously throughout the geometry, if the diffusion coefficient is also homogeneous, isotropic and constant ($D \neq f(\vec{r}, \hat{\phi}, t)$) and with the proviso that there are no sink or source terms (see eq. 2.4). However, in presence of thick[7] targets non-uniformly irradiated, for AC beams or temperature cycling systems, or for any other circumstance eventually described in section 2.3 and violating the previous assets, Fick's equations have to be used in their most fundamental form. `Diffuse` includes a one dimensional finite-difference, finite-elements implementation of Fick's *first* equation:

$$\vec{J} = -D \cdot \left(\frac{\partial C}{\partial \hat{n}} \right) \tag{2.11}$$

Where $\vec{J}$ represents the current of isotopes ($\frac{i}{cm^2 \cdot s}$) and C the volumetric concentration of those (i/cm^3).

In the 1-dimensional case, the slab, of cross section S and half width A is divided in m foils of thickness a, and time is discretized in steps Δt[8]. The total amount of isotopes in each foil slice is $I(n,t) = S \cdot a \cdot C(n,t)$ where n is a pointer

[6] Usage details can be found in the annex B.10.

[7] "Thick" here is relative to the beam radiation stopping range.

[8] Time intervals are not necessarily constant, the program adjusts the time-binning so that stability of the method is guaranteed.

comprised between 1 and m. Thus, the *differential equation* can be written as an *equation in differences*:

$$\Delta I(t+\Delta t(t),n) = J_{net}(t,n)\cdot S\cdot \Delta t(t) \quad (2.12)$$

$$= -(D(t,x)/a)\cdot \Delta t(t)\cdot \left(\frac{C(n+1,t)-C(n-1,t)}{a}\right) \quad (2.13)$$

Above, J_{net} represents the net flow from a given slide to the two neighboring elements.

The space-time discrete implementation of diffusion does not only allow plotting x-t concentration charts, but also, it is written in such a way that variable and inhomogeneous diffusion coefficients and concentrations (sink terms, decay, pulsed sources, ...) can be introduced, so that the effects described in 2.3 can be simulated. But, before proceeding to visualize some of those phenomena, the `Diffuse` routine will be validated against the theoretical formulas of Fujioka.

`Diffuse` deals with variable and inhomogeneous factors

2.5.2 Validation of diffusion.

The finite method sketched above is validated in the region where there are mathematical expressions describing the fractional diffusive release of atoms from foils. *A priori*, validation should be successful because both Fujioka's expression and `Diffuse` are based on Fick's equations. However, errors of stability and of implementation are not to be discarded and, therefore, benchmarking the code at each step is important to gain confidence in results. Honoring this spirit, the numeric routine of `Diffuse` was run in the range of diffusion time constants $\tau_D = 0.025 - 25\ s$, and then the analytic option was run for the same values. The time profile was recorded in the interval $t = 0.1 - 10\ s$.

$4 \cdot \tau_D$	t (s)	0.1	0.2	0.5	1.0	2.0	5.0
0.1	Ref.	29.82	10.97	0.5461	$3.68{\cdot}10^{-3}$	$< 10^{-6}$	$< 10^{-6}$
	Num.	29.83	10.97	0.5464	$3.68{\cdot}10^{-3}$	$< 10^{-6}$	$< 10^{-6}$
1.0	Ref.	77.28	67.87	49.26	29.82	10.97	0.5462
	Num.	77.30	67.89	49.27	29.82	10.97	0.5464
10.0	Ref.	92.82	89.84	83.94	77.28	67.87	49.26
	Num.	92.86	89.87	83.96	77.30	67.89	49.27
100.0	Ref.	97.73	96.79	94.92	92.82	89.84	83.94
	Num.	97.93	96.92	95.00	92.87	89.88	83.96

Table 2.1: Remaining fraction ($\%$) in slabs of diffusion time constant τ_D as function of time, analytic and numeric values. The initial concentration is flat and the diffusion coefficient is homogeneous and constant.

Table 2.1 shows that errors in the remaining fraction typically stay under 0.01 $\%$ and under 0.2 $\%$ in the worst case (towards ratios $\hat{t} = t/\tau_D < 0.01$). Some remarks about this method:

- The methodology could be extended to two-dimensional and three-dimensional geometries without crossing any conceptual frontier.
- Time steps are adjusted at each step so that the maximum relative variation of concentration stays well below 10 $\%$.
- The bounding cells see nil concentration at the free side, at a distance a/2 (concentration in the air immediately touching the bounding cells is already taken as zero).

2.5.3 Analysis of diffusion under space dependent factors.

A gradient in the starting concentration or in the diffusion coefficient entails particular diffusing profiles. The first factor may appear when atoms are implanted/generated with/through an irradiating beam whose range is well defined and is shorter than the slab width. Gradients in the diffusing coefficients

are typical of non-uniformly heated targets. Moreover, if the slab has a gradient of density or composition, the two effects are simultaneously expected.

Effect of the starting concentration profile.

The successful validation of the numeric routines of `Diffuse` allows plotting confidently the remaining fraction as a function of time and space. The study case will be that of Kr diffusing in a 25 μm thick Nb foil, where the diffusion coefficient at 2200 K is about $9 \cdot 10^{-9}\ cm^2/s$ [19]. If the generation is instant and homogeneous through the depth of the foil, then the concentration of stable Kr isotopes in the foil shall evolve with time as shown in fig.2.2. As expected, the distribution is symmetric and it can be remarked how the central part takes longer to sense the "perturbation" induced at the faces. Now, let us inspect a scenario where Kr is generated by irradiating the Nb foil with a low energy beam such that the range of projectiles is shorter than the thickness of the foil. In particular, the source routine in `Diffuse` is modified so that the initial concentration distribution is:

$$C(y,0) = 1 \cdot exp\left(-\frac{y \cdot 10}{A}\right) \cdot \left(1 - exp\left(-\frac{y}{a}\right)\right) \tag{2.14}$$

With $y = 1 - x$, x being the depth coordinate in the foil. The resulting evolution is represented in fig.2.3. It is remarkable how the gradient of concentration (this can be identified as a driving force in Fick's laws) and also the asymmetry induce a faster diffusion (the peak of concentration is now closer to a free surface than in the symmetric case, which already intuitively ought to boost the diffusion), as represented in the comparative graph 2.4.

Inhomogeneous production enhances diffusion

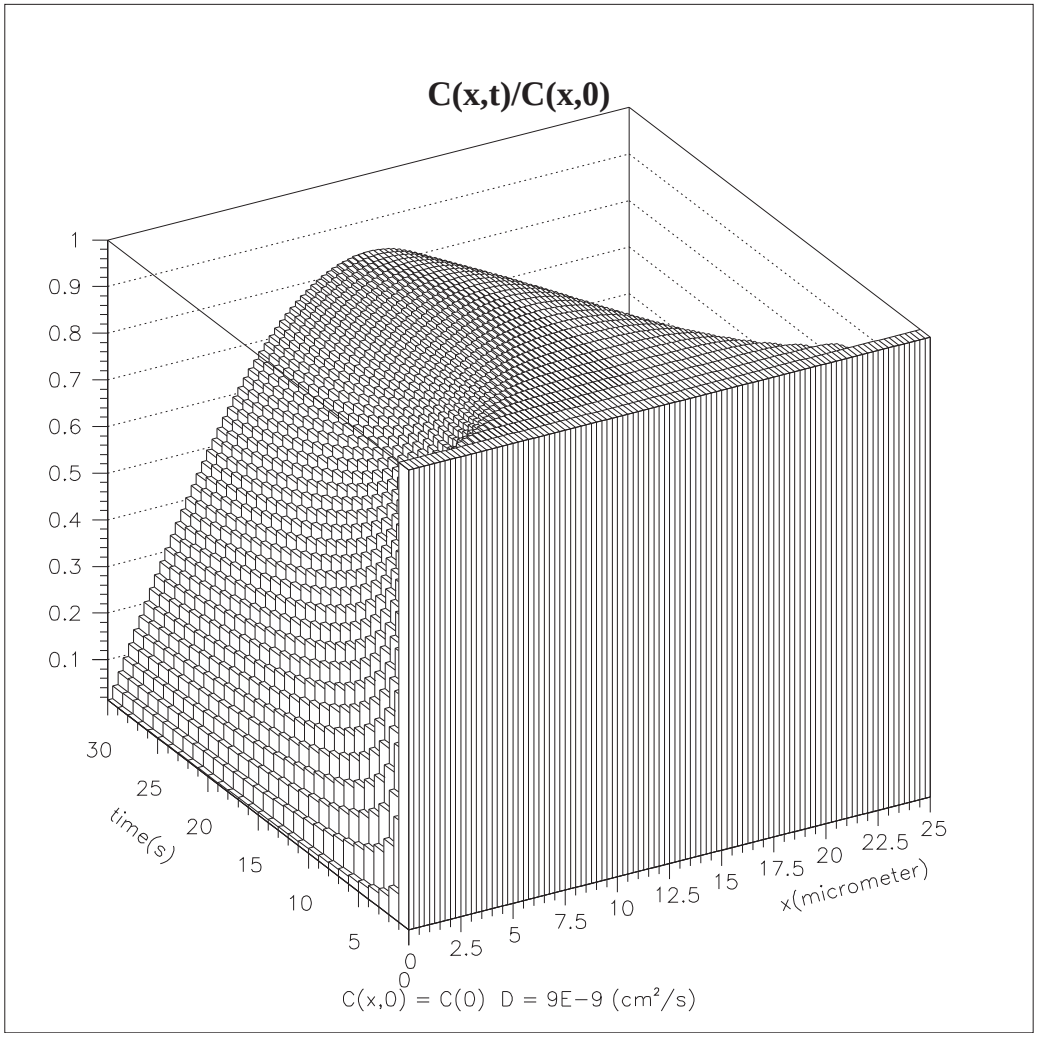

Figure 2.2: Fractional concentration (concentration(t)/concentration(t=0)) as a function of x and t for stable Kr in a 25 μm Nb foil. Starting generation is homogeneous.

Effect of the diffusion coefficient profile.

Fick's first equation (2.11) needs to be rewritten to include space gradients of the diffusion coefficient:

$$\vec{J} = -D \cdot \left(\frac{\partial C}{\partial \hat{n}}\right) - C \cdot \left(\frac{\partial D}{\partial \hat{n}}\right) \tag{2.15}$$

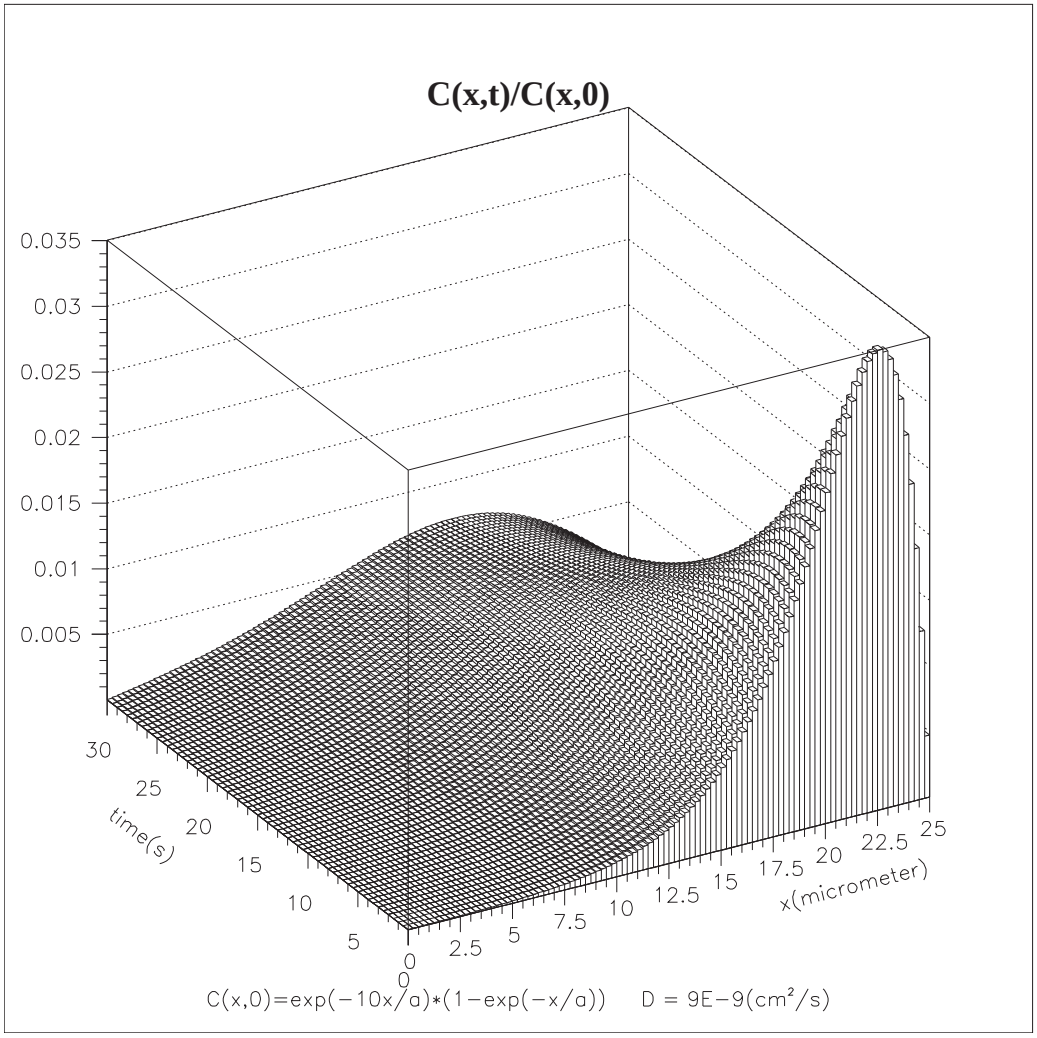

Figure 2.3: Fractional concentration of stable Kr in a 25 μm Nb foil as a function of x and t. Starting generation is heterogeneous and asymmetric.

The concept of *thin* foils intrinsically implies a flat distribution of D, but, for thicker slabs, temperature gradients are likely and thereby gradients in D[9]. A test case has been run with `Diffuse`, which accepts profiles of D that can even change with time. The example differs from the basic homogeneous case described in 2.5.3 only in the fact that D changes linearly through the slab,

[9]If the temperature impact is severe, then the metallic structure of the slab may change permanently, affecting the Diffusion coefficient.

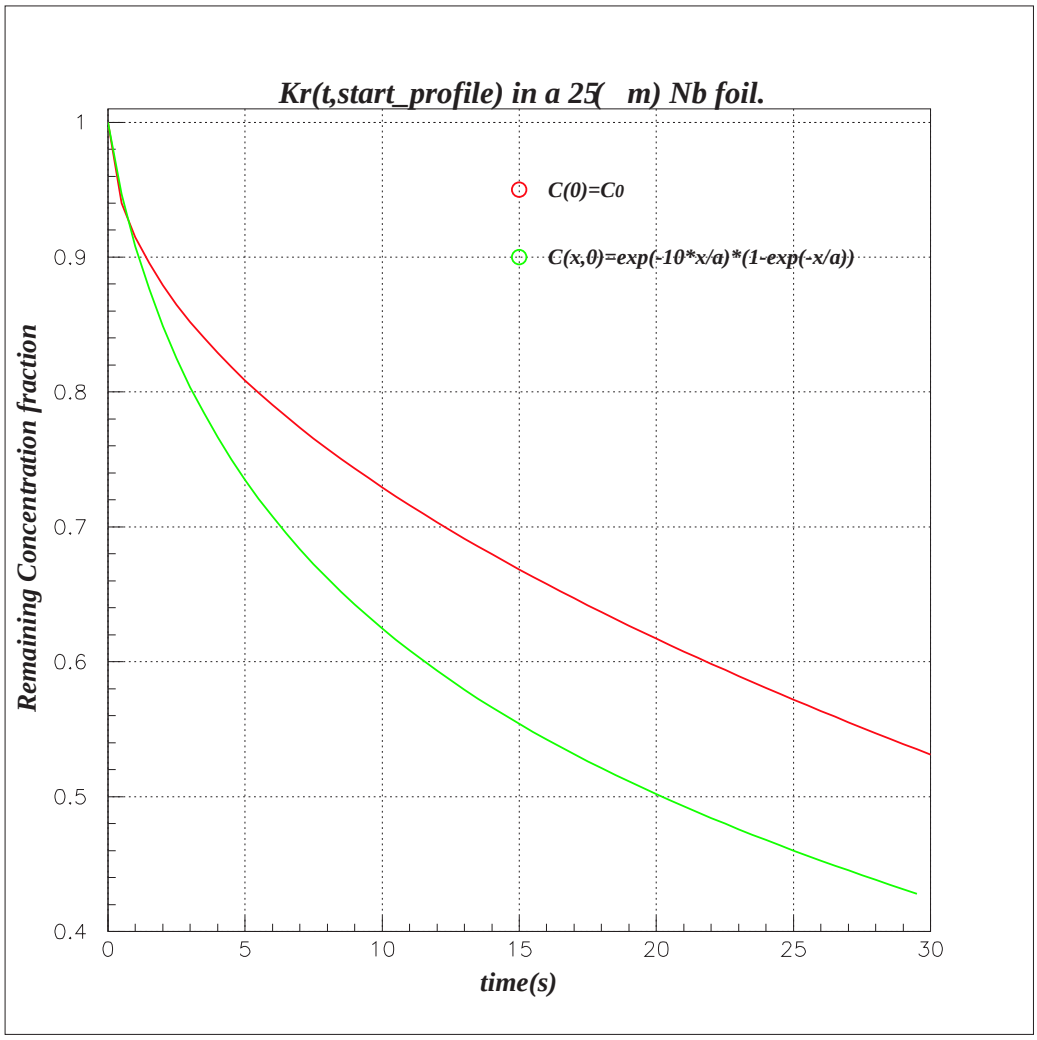

Figure 2.4: Relative remaining concentration of stable Kr diffusing from a 25 μm Nb foil. Study cases: homogeneous and heterogeneous starting concentration.

varying from $2 \cdot D_0$ to 0 from one face to the other. The average diffusion coefficient is still $D_0 = 9 \cdot 10^{-9}\ \frac{cm^2}{s}$. Fig.2.5 suggests how atoms tend to migrate towards the face where the diffusion coefficient is higher.

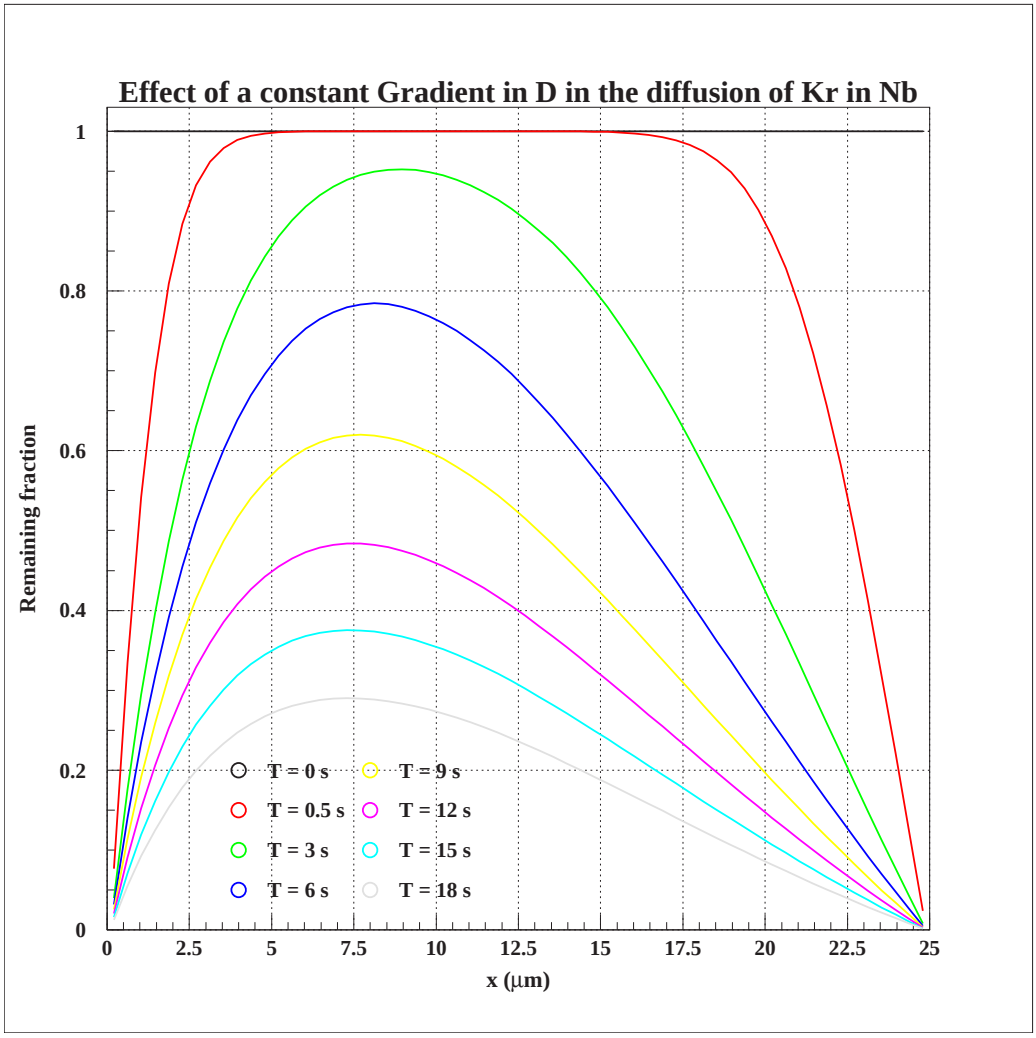

Figure 2.5: Fractional concentration (concentration(t)/concentration(t=0)) as a function of x and t for stable Kr in a 25 μm Nb foil. Starting generation is homogeneous but the Diffusion coefficients changes linearly from $2 \cdot D_0$ to 0.

Correlation between the diffusion coefficient and the concentration.

A general simplifying assumption for diffusion calculations is that the diffusion coefficient is almost independent of the concentration, although this is not always necessarily fully valid. This barrier to the accuracy of results faints away with `Diffuse`, provided that the space function of variation is known. This is so because the method of finite elements and finite differences allows not only

setting up a profile of C ($C(x)$) and D ($D(x,t)$), but also to set up dependencies of the sort $D(C(x,t),x,t)$.

2.5.4 Analysis of diffusion under time dependent factors.

The variation of experimental conditions as a function of time may bias diffusion measurements or even fake them completely. This section illustrates how `Diffuse` can aid to identify and isolate the impact of these factors as long as (at least) educated guesses of their magnitude can be made. From the variety of time dependent phenomena, the thermal spikes and the pulse structure will be studied in combination with the radioactive decay. The grain growth usually takes place in a much slower scale than the diffusion process, so it is not further analyzed although the procedure would be exactly the same. In the first place, the diffusion curve in presence of radioactive decay shall be analyzed.

Effect of a the radioactive decay in the diffusion curve.

The radioactive decay for a given time lapse Δt and half-life τ acts as a sink term that reduces the concentration in each slice of a the slab by the same factor r:

$$r_{\Delta t} = exp\left(-\frac{\Delta t \cdot ln\,(2)}{\tau}\right) \tag{2.16}$$

The concentration for every foil bin i at Δt is:

$$C\,(i,\Delta t,r) = C\,(i,\Delta t,1)\cdot r \tag{2.17}$$

Now, in the next time step, the diffusion law will empty and fill the bins according to Fick's first law (eq.2.15), but since all concentrations are r times

lower, the gradients too are r times lower, and the step variation of concentration due to diffusion in presence of the decay law (r) is:

$$\Delta C\left(\Delta t, r\right) = \Delta C\left(\Delta t, 1\right) \cdot r \tag{2.18}$$

Thus, applying the decay factor again, $\forall i$ the concentration at i after $2\Delta t$ will be obtained as:

$$\begin{aligned} C\left(i, 2\Delta t, r\right) &= \left(C\left(i, \Delta t\right) \cdot r + \Delta C\left(\Delta t, r\right)\right) \cdot r \\ &= \left(C\left(i, \Delta t\right) \cdot r + \Delta C\left(\Delta t, 1\right) \cdot r\right) \cdot r \\ &= C\left(i, 2\Delta t, 1\right) \cdot r^2 \\ &= C\left(i, 2\Delta t, 1\right) \cdot exp\left(-\frac{2 \cdot \Delta t \cdot ln\left(2\right)}{\tau}\right) \end{aligned} \tag{2.19}$$

Whence, the exponential decay factor may be taken out as common factor, and the diffusion law under radioactive decay can be expressed as:

$$\Delta C\left(x, t, \tau\right) = \Delta C\left(x, t, \infty\right) \cdot exp\left(-\frac{t \cdot ln\left(2\right)}{\tau}\right) \tag{2.20}$$

This property is crucial for a simple management of diffusion formulas with radioactive ion beams, and it will be used from this point on.

Decay can't always be decoupled from diffusion

Two exceptions have to be highlighted. In eq. 2.19, the factor r can be taken out because it affects equally the two terms inside the parenthesis. However, if a third term appeared then it may break this property. This happens in these cases:

- D depends on x. In this case (described in 2.5.4) an additional "diffusion force" appears as a consequence of the gradient in the diffusion parameter. This term is not scaled with the factor r. In these cases `diffuse` should be used for a correct calculation of diffusion.

- Time sources like pulses do also break this property. This case is studied in next section.

Finally, it should be remarked that all these principles are equally valid for geometries other than the slabs, e.g. spheres or cylinders.

Effect of a temperature spike. Shock wave.

Following the principles laid in 2.3.2, `Diffuse` can be used to speculate about the effect of a fast rise of temperature, mainly linked to the heat deposited by the primary beam. The example taken above will be kept: Kr diffusing from a 25 μm thick Nb foil at 2273 K. The temperature rise will be assumed to be of about 100 degrees and it will last 1 second. In order to see what is the corresponding impact in the diffusion coefficient, we can get hold of the Arrhenius equation (eq. 2.2) and, in absence of more precise data, assume that Kr diffuses as Nb in Nb, so that the self activation energy of Nb can be used (see eq. 2.3). This means that the diffusion coefficient is about 7.5 times higher than the working temperature value; $D_{shock} = 7 \cdot 10^{-8}\ \frac{cm^2}{s}$. Although real cases may involve greater temporal improvements of the diffusion coefficient, fig.2.6 indicates that the release fraction is relatively robust to such changes.

Diffusion release with pulsed generation of atoms.

At ISOLDE the beam is pulsed, the typical super-cycle period being 14.4 s[10]. If the diffusing radioisotopes are very short-lived (as compared to the pulse period) then the pulsing nature does practically not affect the diffusion curve. Otherwise, convolution operations have to be carried out or, alternatively, `Diffuse` can be run by activating a pulsed source:

[10] A super-cycle is composed of several beam bunches separated by 1.2 s

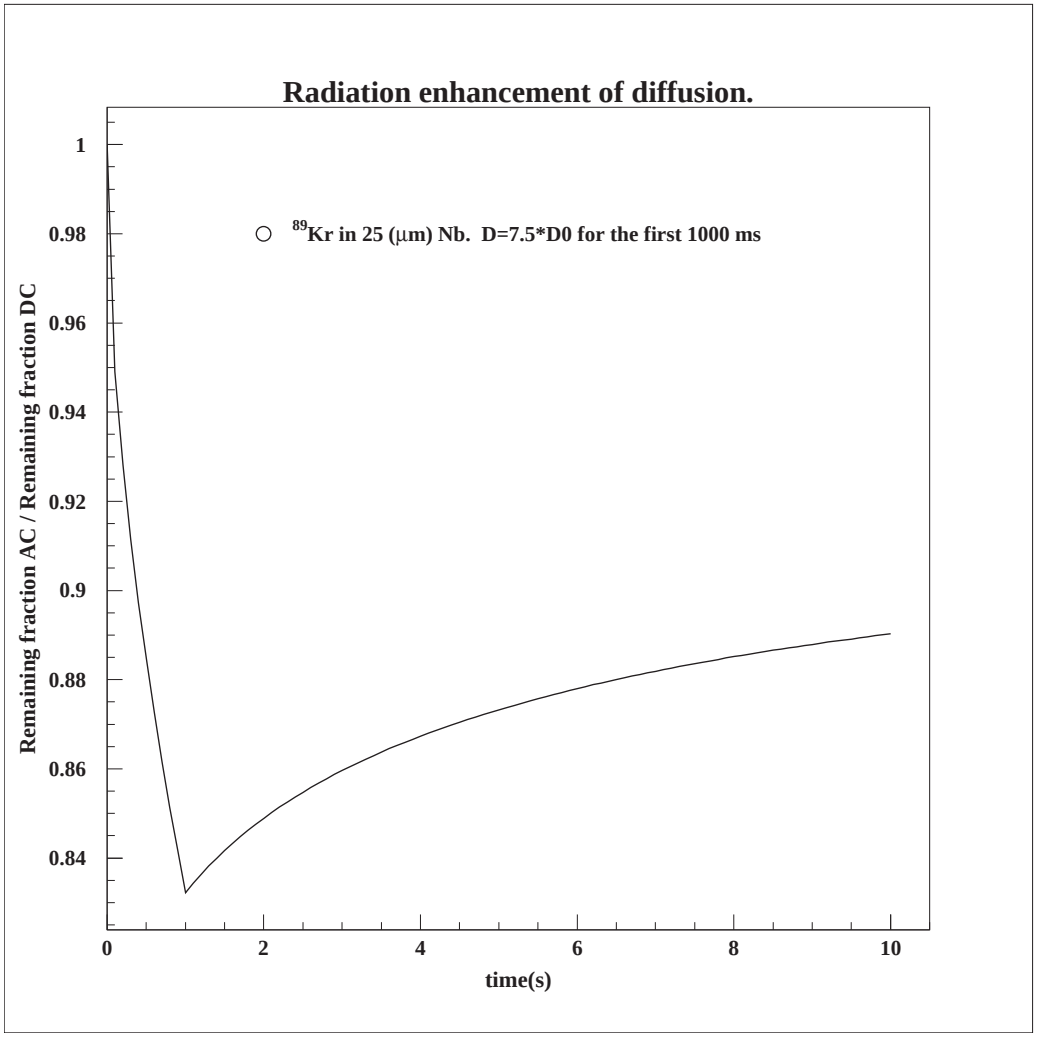

Figure 2.6: Fractional concentration (concentration(t)/starting concentration) ratio for a D enhancement factor 7.5 lasting 1 s and for the constant D for stable Kr in a 25 μm Nb foil. Starting generation constant.

```
      SUBROUTINE timeN(N,i,m,t,dt,a)
        real*8 N(m,2),t,dt,tao,pulse,a,x
        integer*4 i,m
* decay law
        tao=0.097                                                    11
*         tao=27.0
*         N(i,1)=N(i,1)*exp(-log(2.0)*dt/tao)
* pulsing source
        x=(a/m)*i
```

```
      pulse=0.5                                                          12
      IF (mod(t,pulse).lt.1.0001*dt.and.t.gt.pulse) THEN
        N(i,1)=N(i,1)+functC(x,a)*1
      END IF
    END
```

For a stable isotope of relatively high diffusion time constant (as compared to the pulse period), the concentration in the foil would stack up at each pulse until the gradient of concentration with respect to the outer air would be high enough to compensate the income with outflow via diffusion. In broader terms, a dynamical equilibrium is reached around a central value that depends on the half-life, diffusion parameter and pulse period. Fig 2.7, computed with `Diffuse`, corroborates this fact for several Kr isotopes diffusing in a 25 μm Nb foil. Fig.2.8 shows the evolution of the profile with the stacked pulses for the reference study case.

2.5.5 Inversion of the diffusion function. *Diffact.*

Diffact is a the diffusion inversion function utility included in `Diffuse`. This FORTRAN application computes the function $F^{-1}(\eta, t)$ to express η (defined in section 2.1) as a function of the fractional activity and of the measurement time, $\eta(1 - F, t)$. This operation, which involves inverting terms from 'infinite' sums had initially been designed as an optimized iterative binary search method. However, the program was revised to do a direct search, much faster, simpler and precise, described below:

1. The input data are a release fraction F_r and the corresponding time t_r. The sought value is the diffusion parameter η_r. Thus, we have $F(\eta_r, t_r) = F_r$.

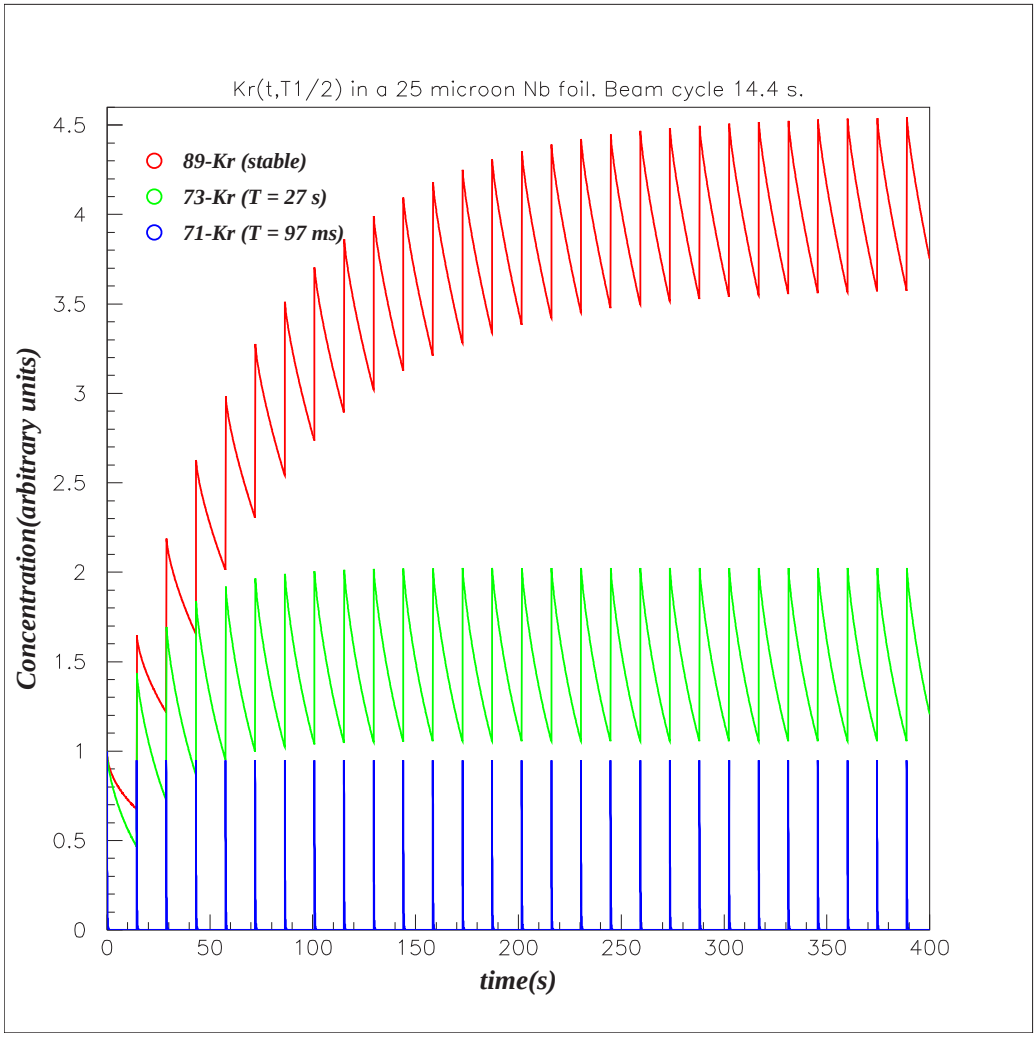

Figure 2.7: Concentration of ^{89}Kr, ^{73}Kr and ^{71}Kr in 25 μm Nb foils irradiated with a pulsing beam of period 14.4 s

2. The program takes a starting value for η_s and a time step Δt and it computes the release fraction for every time step, $F(\eta_s, \Delta t)$, $F(\eta_s, 2 \cdot \Delta t)$, ... until the obtained value is just under F_r: $F(\eta_s, k \cdot \Delta t)$, $t = k \cdot \Delta t$.

3. Now in virtue of the non-dimensionality of the power in the exponentials:

$$\eta_s \cdot t = \eta_r \cdot t_r \Rightarrow \eta_r = \eta_s \cdot \frac{t}{t_r} \tag{2.21}$$

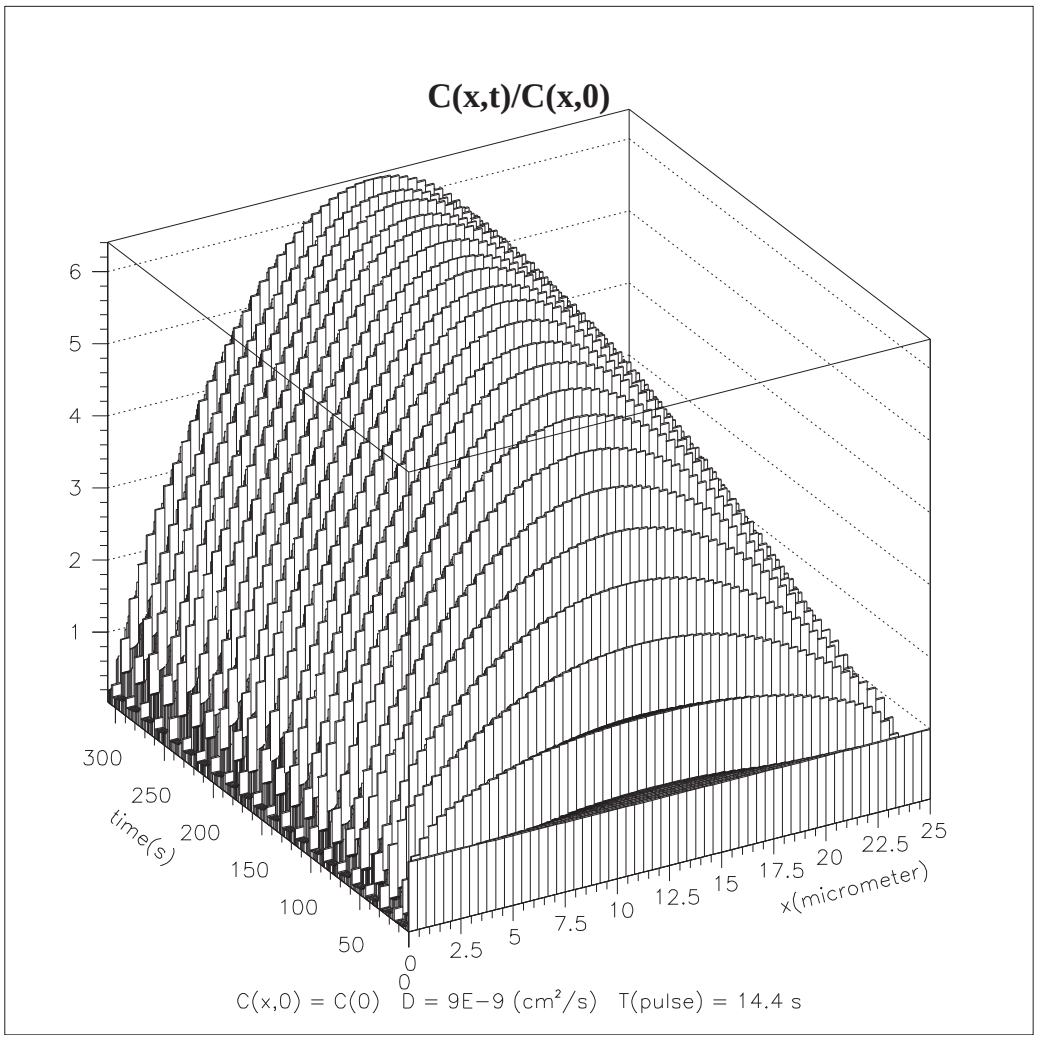

Figure 2.8: Evolution of the ^{89}Kr profile in a 25 μm Nb foil irradiated with a pulsing beam of period 14.4 s

4. Taking into account the finiteness of the method, it is more appropriate to set:

$$\eta_r = \eta_s \cdot \frac{t - 0.5 \cdot \Delta t}{t_r} \tag{2.22}$$

5. The relative error e_r can be readily estimated as:

$$e_r = \frac{\Delta t}{t - 0.5 \cdot \Delta t} \tag{2.23}$$

Diffact may be used at ISOLDE to extract the diffusion coefficient of samples irradiated by the "RABBIT" technique. Note that this routine can be applied also to the cases described above, with variable and heterogeneous profiles of C and η.

2.5.6 Sampling diffusion times in the MC.

Sampling diffusion from the analytical laws is a natural way to proceed in a MC code [17]. The present MC release code does also include this alternative although other methods are used as well. In the following paragraphs the sampling method is described and alternatives are discussed further down.

The MC code integrates two subroutines for diffusion. The first of them, *Diffusion*, integrates `Diffuse` to create a one-dimensional mesh that expresses the integral probability of release as a function of the diffusion time, t_d. The mesh, resulting from the application of Fick's laws, is composed of 5000 equidistant points in the interval $0 \leq t_d \leq t_{\max}$, where t_{max} is internally pre-calculated for optimum representation of the diffusion curve.

This subroutine belongs to the initialization sequence, which means that it is only calculated once[13]. An array with the (integral) diffusion probability function is stored in memory for future consultation.

The second subroutine is called *Difftime*. This function samples a diffusion time from the diffusion integral array generated with *Diffusion* by use of the inverse transform method. In annex A.2 details are provided about the binary search method that inverts the function $t_d(P)$. Sampling *diffusion times* is a natural idea in MC simulation codes because it allows passing from an analytical law to single, stochastic events. Thus, an individual diffusion time can be generated,

[13]It will therefore only add a fixed time to the simulation size and will not increase the time per history.

then an effusion time will be computed and so forth, so that the particle can be tracked from beginning till end, emulating, *simulating* a real history. This procedure is schemed in fig.2.9.

This integral treatment is neat and handy, it has the **advantage** of casting the wished law (in our case the overall[14] delay time distribution $P(t_p)$) by only having to *sample* diffusion, to *simulate* effusion times and to *sort* the sum of the two into a histogram. The main **disadvantage** of this method is that it introduces an (unnecessary) statistical spread into a deterministic physics law. The process of sampling inevitably implies an associated variance; extra histories will therefore be required to dim the statistical blur. If the analytic diffusion distribution[15] could be used straight ahead to compute $P(t_d)$, then simulation sizes could be cut down significantly. This alternative method is described below.

Sampled times are easy to integrate in a MC but they are not fully precise

2.5.7 Convoluting diffusion with effusion. *DconvE*.

(This program is integrally printed in annex A.2). An alternative way to obtain the intrinsic delay time distribution $P(t_p)$ sketched in fig.2.10 is based on the following identity:

$$p_p(t_p) = \int_0^{t_p} (p_e(t) \cdot p_d(t_p - t)) \cdot dt \tag{2.24}$$

A discrete diffusion profile $p_d(t_d)$ can be produced straight from Fick's laws (eq. 2.1) as it is done in *Diffusion*. The corresponding effusion discrete distribution is obtained by simulating N points and sorting them into a histogram. For practical reasons, the same bin size is taken in the histograms of the two distributions.

[14] diffusion + effusion + ionization.
[15] No variance.

DconvE is a macro for VISUAL BASIC compatible spreadsheets, which, in the first place computes the diffusion distribution and then it convolutes it numerically with a given simulated effusion distribution. This process has the great **advantage** of suppressing the statistical spread in the diffusion distribution and thereafter in the final function. Thus for a given precision, convoluting requests a shorter simulation time than diffusion sampling. This is particularly important for those simulations that request a longer CPU time per history.

The **drawbacks** are the following:

- "Adding" **distributions** that correspond to consecutive effects implies *convoluting*, whereas "adding" **events** of consecutive effects requires plain *sums*. Convoluting is certainly less intuitive and more complex than summing.

- The method removes statistical errors linked to sampling diffusion, but it may add systematic ones if the delicate numerical issues involved convoluting discrete distributions are not carefully controlled.

- The tail of the intrinsic release curve for a given cutoff time is not easily deduced when this method is used. This renders more difficult the computation of release fractions.

2.6 Conclusions.

- The diffusion time constant (τ_D) evaluates the speed of diffusion for a given atom-target pair. It is directly proportional to the diffusion coefficient and inversely proportional to the square of the characteristic thickness of the sample.

- A temperature rise increases the diffusion coefficient (Arrhenius law dependence) but it may also damage the target, catalyzing the growth of the grains, coalescing and sintering target elements and thereby multiplying the characteristic thickness. Therefore, increasing the temperature may not entail a net gain in terms of release speed.

- The diffusion of isotopes from the target bulk is adequately described by Fick's law (2^{nd}). Analytical, explicit though infinite solutions exist for the main cases: foils, particles and fibers. These formulas assume a homogeneous starting concentration and a constant temperature.

- If the starting concentration and/or diffusion coefficient are not homogeneous or if there are time-dependent terms, then Fick's first law can be used to compute the diffusion release of atoms.

- The radioactive decay law can be decoupled from the diffusion release law in most cases. A major exception appears in targets where the diffusion parameter is not homogeneous.

- At ISOLDE the primary beam is pulsing with a typical period of 14.4 s. The diffusion release under such time structure is practically identical to that of a single pulse, so that the pulsing structure can be ignored. Moreover, the effect of the shock wave is relatively moderate.

  The analysis and optimization of targets will be assisted with applications that perform the following tasks:

  1. Invert the diffusion function (**Diffuse**>**Diffact**): This is used to infer the diffusion time constant of a diffuser-matrix pair from experimental measurements (fractional activity print).

2. Plot the diffusion time function (`Diffuse`): The output of **Diffact** may be taken as input to `Diffuse`. Like *Diffact*, `Diffuse` can account for space and time dependent profiles, sink and source terms and correlation between the diffusion coefficient and the concentration. This program yields the diffusion release function and the diffusion release profile as a function of t.

3. Convolute diffusion with another time function (**DconvE**): It generates a diffusion profile (like the previous function), and it convolutes it to another time function (typically effusion data). The global release curve is obtained.

4. Sample diffusion times from the diffusion time function (**Diffusion**): This is useful for simulation purposes because it allows obtaining total release times for individual particles by simple addition to simulated effusion times.

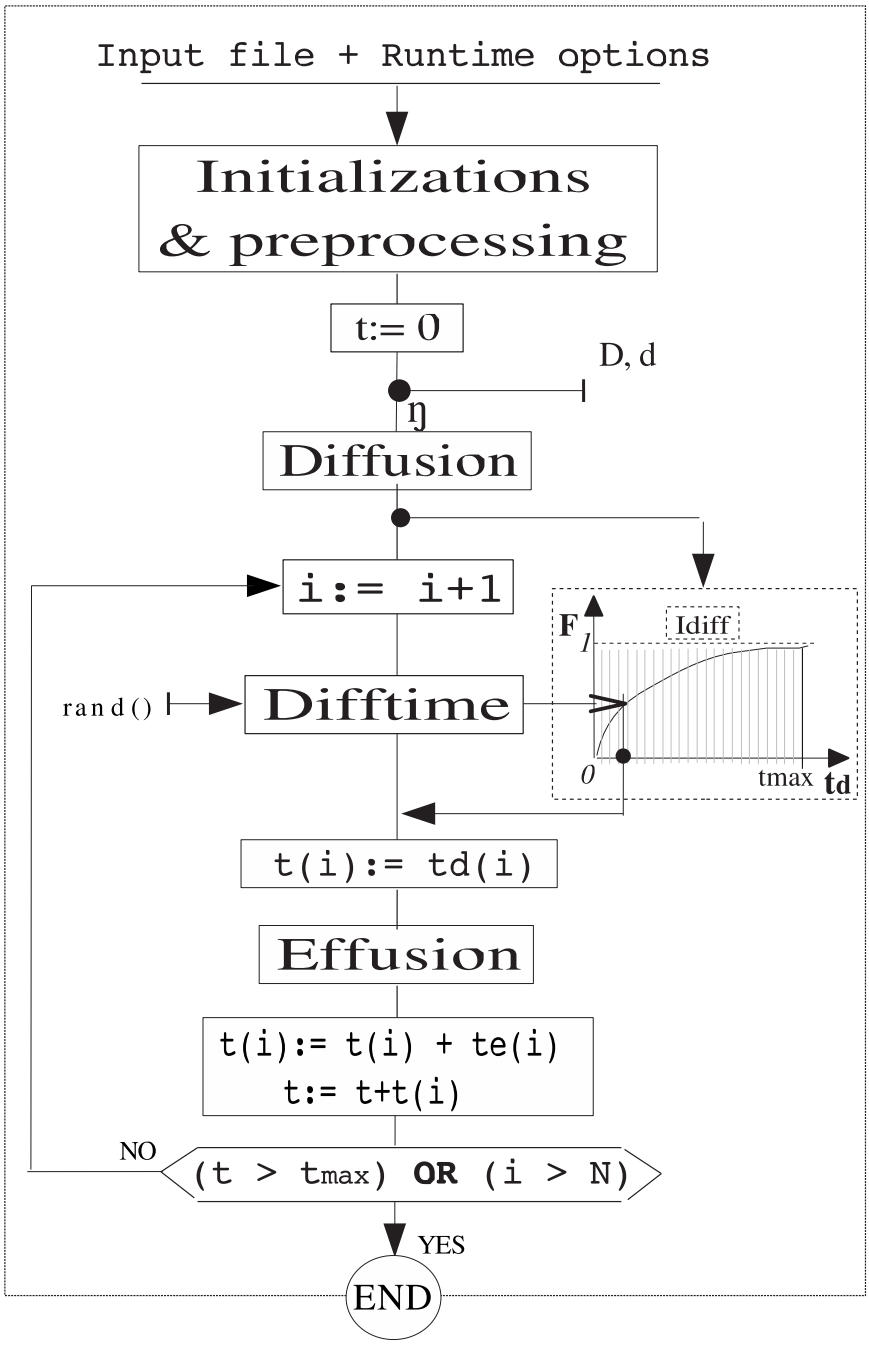

Figure 2.9: Scheme to obtain diffusion+effusion **events** from the Monte Carlo code exclusively. *Diffusion* generates and stores in a buffer the integral diffusion release profile. Then the code samples diffusion times from this distribution and adds individual effusion (+ionization, . . .) times.

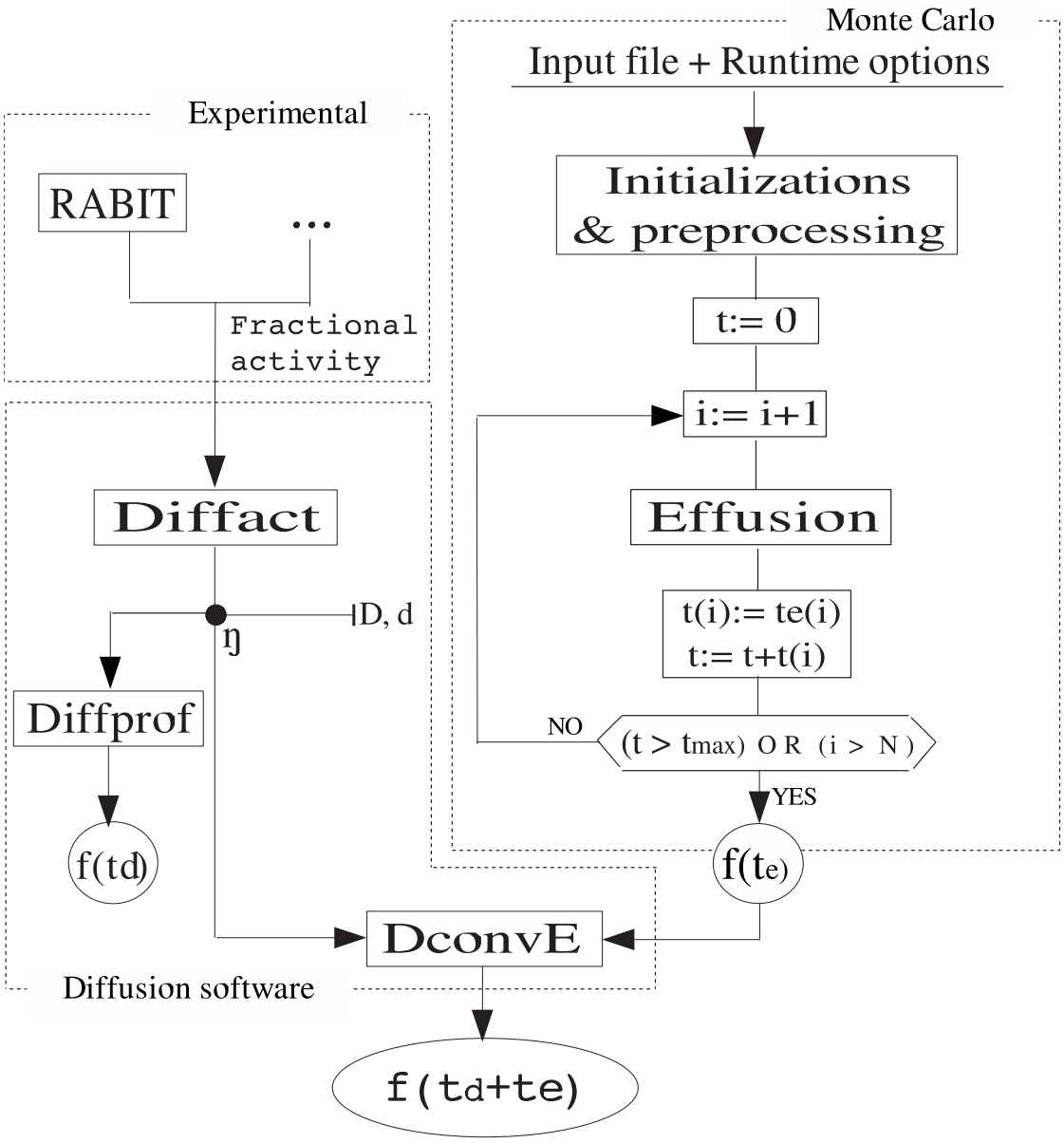

Figure 2.10: Scheme to obtain diffusion+effusion **distributions** by simulating effusion times with the *Monte Carlo* code and convoluting those (*DconvE*) to the analytical diffusion functions. The diffusion parameter may be obtained from experimental data through *Diffact*. The diffusion profile can be plotted separately with *Diffprof*.

Chapter 3

Effusion.

Effusion [8]...

- *"Unrestrained expression of words or feelings."*
- *"The escape of a fluid from anatomical vessels by rupture or exudation."*
- *"a: The flow of a gas through an aperture whose diameter is small as compared with the distance between the molecules of the gas; b: the fluid that escapes."*
- *"A pouring or flowing out, or the fluid that does so."*

★

THIS CHAPTER STUDIES THE EFFUSION PROCESS; the models that best describe it and how to implement them in a simulation program. The kinetic-theory analytical approach will be introduced as well as its limitations and some first order corrections. Moreover, combined analytical and simulated calculations will be presented as a powerful tool to solve the most time consuming problems. Extension of the effusion concept to non-molecular flows and the link to diffusion are the subject of the last point of the chapter.

3.1 Effusion. Basic concepts.

Effusion is the process that describes the somehow erratic path that gas atoms follow when they move freely within a vacuum bounded (walls) system. Although this concept could be extended to any regime, it usually refers to molecular flow, where, in absence of a pressure gradient, atoms don't tend to move with a privileged direction of motion. Thus, trajectories will be straight lines between two consecutive collisions with the system walls.

The velocity after each collision (speed and direction) follows a statistical distribution that can be approached with different models. At present, none of them is entirely satisfactory, remaining theoretical investigations limited to the scarce knowledge of the structure of the surface layers of solids and of their interaction potentials with the impacting molecules[1].

Whatever the model for individual collisions, the stochastic character of the reflected atom velocity distribution best suits the Monte Carlo approach (confronted to other paths like analytical or numerical integro-differential methods), outstanding for its simplicity and clarity. The MC method, founded in the simulation of random functions in order to calculate their distribution characteristics, has historically shown a slow convergence, but, in present times, computational power is already at the level to provide statistically significant results in short times (in cases where CPU exigencies are too demanding, a wise combination of MC and analytic methods can prove very efficient).

[1] More difficulties arise from the requirement to describe the surface finish and cleanliness, or, even more, their eventual time evolution.

3.1.1 Collision modes.

When an atom hits a surface various things can occur. The atom's potential may interact with those of the substrate, it could dwell on the surface for a brief instant of time; eventually it may slide over and finally it can either be re-emitted or it may condense or stick to the surface, creating a monolayer [20].

The principal reflection probability laws that are derived from these phenomena are elastic scattering[2] and inelastic Lambertian reflection. Other laws mixing, composing or circumstantially tending to either of the two are presented further in 3.2 (page 55).

Elastic reflection.

Elastic reflections [22] are often referred as mirror-like collisions. In the elastic collision assumption the tangential component of velocity is conserved whereas the perpendicular one is inverted. In the inversion process the atom transfers the vertical kinetic energy to the crystal and this returns it back to the atom. Hence, the kinetic **energy is conserved** and the outgoing angle depends on the ingoing one.

Elastic collisions can take place provided that the projectile does not chemically interact with the surface atoms. As stated in the introduction, macroscopic elastic collisions[3] can only be observed when the surface is micro polished. Additionally, it will be shown later that such type of collisions are favored for a very light projectile and a very hot surface.

The MC `RIBO` code offers the user the chance to force collisions to be elastic. Annex A.3.1 shows the implementation of such function in `RIBO`. It should be

[2] Snell-Fresnel law of reflection [21].
[3] To what concerns the direction.

underlined that this practice is only recommended in one of the following situations:

1. Computing an upper limit for the release speed of atoms.
2. Simulating the transport of light in non-refractive systems.
3. Simulating the effusion of very light inert atoms in micro-polished, ideally clean and very hot vacuum systems.

Diffuse reflection.

Diffuse reflection is often described by the cosine law [23]. In that case the probability distribution of the emission angle scales proportionally to its cosine to the normal of the surface[4] (see fig.3.2.D).

Section 3.2.2 is entirely devoted to ideal diffuse reflection, often baptized Lambertian or Lorentzian reflection.

3.1.2 Surface topology. Roughness and waviness.

The surface finish (roughness) alters the geometric local axis system, thus the emerging angle in the global axis and the surface interaction potentials (cleanliness). In a macro scale, polished surfaces tend to show a typical rough structure of peaks and valleys, usually resulting from the basic surface forming process, which results in features of high frequency. In mechanical terms, "*roughness* refers to a set of closely spaced irregularities caused by the cutting tool motion and surface non uniformity, while the term *waviness* is reserved to the widely spaced irregularities caused by vibration and chatter of the machine

[4]The cosine law should be understood to apply to the solid angle normalized probability distribution.

set-up" [24]. There are as many conventions on the set of parameters to describe the surface finish as domains of application (illumination science, mechanical studies, solid state) and existing industrial gages. Intuitively, to a first degree, the texture can be described through the first and second momenta (average and spread operators) of the hills heights and spacing (vertical and longitudinal dimensions).

The roughness will certainly affect reflection of waves, as the outgoing angle with respect to the surface plane will depend on the local orientation of the surface. This will be true if the wavelength is much smaller than the roughness descriptors, and can be checked by using the *De Broglie* relationship for matter (eq.3.1). An important parameter is the so-called *apparent roughness*, which is the local projection of the vertical shift on the incident direction. This parameter is used to explain why surfaces look smooth from grazing angles while their roughness is plainly revealed for orthogonal beams.

A good measure would be the ratio $\frac{\lambda_{De\ Broglie}}{apparent\ roughness}$

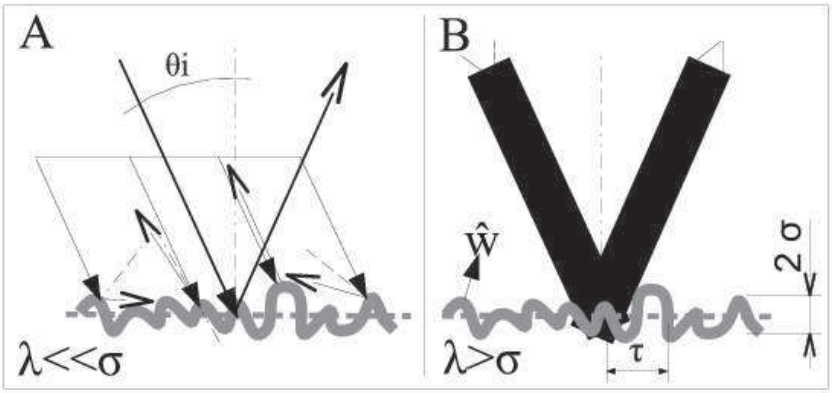

Figure 3.1: The apparent roughness of a surface depends on the wave length of the impacting atom and on its incidence angle.

In illumination studies, the roughness is measured in *radiometers* down to the $\mathring{A}$ scale by recording the radiance for different orientations of a measuring head of a pencil beam impinging with different angles to a sample. In mechanics, a

profilometer scans a stylus across a surface and the vertical movements caused by the surface irregularities are registered and analyzed to cast the statistical figures, with a precision similar to that of the scattering equipment [25]. Those metronomic numbers normally gather the statistics (maximum, average, dispersion) under three categories: height of the peaks, spacing between them and height to distance correlations (slopes) in the dimpled surface [26].

3.1.3 Transport of light. BRDF.

When diffraction and refraction are negligible, the transport of light constitutes a good reference for the study of atom to surface interactions, and, in particular for the analysis of the effects of the surface finish. This is so because of the nature of light, which does not chemically interact with the surfaces. Then, in a microscopic scale, light reflects specularly[5], but macroscopically, where the roughness of the surface is accounted for, reflection can range from specular to specularly diffuse and even to ideally diffuse (Lambertian). Then, the final direction after a bounce is expressed as the convolution of the fundamental reflection law with the surface orientation probability distribution: *reflection law* $\otimes$ *surface orientation*.

The local orientation is a key factor

This is the base point for illumination science and computer realistic image synthesis, where the final goal is to obtain the *General Bidirectional Reflectance probability distribution (BRDF)*. The BRDF, a function that in principle includes the incident and reflected directions (2 x 2 variables), can be obtained experimentally by hemispheric reflection measurements [27, 28], or indirectly through the use of sophisticated surface roughness gages. The second method

[5]Mirror-like reflections, where the angle of incidence equals the angle of reflection.

yields also the typical roughness descriptors Ra, RMS[6] down to 10 nm (mentioned above in 3.1.2).

To export the illumination results to the vacuum science, atoms should also be able to 'see' the roughness. Getting hold of the quantum wave description of matter, the *De Broglie* wave length (λ) of an atom of mass m at a temperature T is:

$$\lambda = \frac{h}{p} \tag{3.1}$$

With h the Plank constant and p the impulse. Typically, mass and temperature ranges between 1-200 amu and 298-2500 K, respectively, so that wave lengths normally vary between 0.5-20 nm. Such waves, far from absorbing surface irregularities, singularise them. Hence the prior discussion is extensible to atomic transport in vacuum systems. In fact, even for noble gases, the sensitivity of the atoms to the irregularities goes beyond the precision of the micro roughness gages, which means that the BRDF cannot be obtained with those instruments. The hemispheric reflectance methods could only be employed with very costly equipment, able to create pencil beams of the sought atoms to impinge with a sample wall surface, in conjunction with sophisticated detection equipment. This cannot be easily brought to practice since it should be repeated over for every atom-surface combination. But luckily, coming back to the first argument, experience from vacuum systems shows that Lambertian reflection (see 3.2.2) is very often the best way to proceed. This discussion, which plays a central role in the frame of the atomic transport and thus of the thesis, yields the following conclusions:

vacuum systems mostly show Lambertian collisions

[6] Ra is the *roughness average* and corresponds to the absolute area over or under the reference line in the evaluation length; RMS is the *root mean square* of this concept.

- What is sought is the general bidirectional reflectance, BRDF, the function that expresses the reflected direction in terms of the incident direction.
- The reflection of atoms, regardless of their inert or interacting nature, usually has a strong diffuse component ($\rightarrow$ incident independent).
- The diffuse component is built up by chemical interactions, but those are dominated by the stochastic microscopic orientation of the surface at each given point as compared to the planar orientation in the macroscopic scale.
- There is no easy practical way to measure picoroughness nor to directly measure the BRDF for atom-surface collisions.
- For ultra-polished surfaces special theories have to be contemplated. For the rest of the cases the Lambertian reflection will be assumed.

Main collision options are sketched below.

3.2 Collision Models.

3.2.1 Maxwell model.

The Maxwell model, a comprehensive though complex framework of collisions that embraces both elastic and diffuse reflections, was developed around arguments belonging to the kinetic theory [29, 30], classical mechanics and chemical-surface postulates. The probability distribution function of reflection with a direction ($\hat{\vartheta}$) and energy E ($P_{Maxwell}$) results from a linear combination of the elastic ($P_{Elastic}$) and diffuse ($P_{Diffuse}$) terms:

$$P_{Maxwell}(\hat{\vartheta}, E) = (1 - f) \cdot P_{Elastic}(\hat{\vartheta}, E) + f \cdot P_{Diffuse}(\hat{\vartheta}, E) \tag{3.2}$$

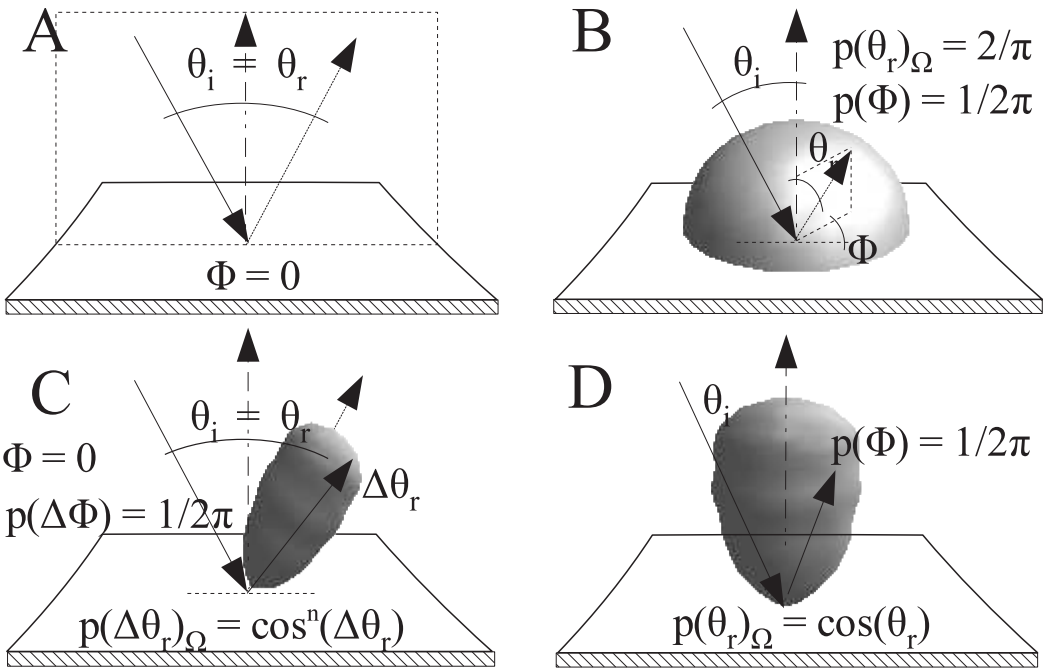

Figure 3.2: Reflection can be **A)** specular (Snell), **B)** diffuse isotropic, **C)** specular diffuse (Phong) or **D)** specular cosine-law like diffuse.

where the weighting factor, f is a so-called *accommodation coefficient*, which quantifies the degree to which the impacting atom accommodates to the surface before reemission, or, in other words, the amount of thermalization (energy exchange) and lost memory of the impinging direction.

Among other considerations, two qualitative principles that help in the determination of f are:

- In accordance with the laws of classic mechanics, the energy exchanged in the collision between two particles is maximum when their masses are equal.

- Experimentally it is observed how, the larger the angle of incidence, the more nearly the tangential momentum of the reflected molecules is conserved. The theoretical justification is that for very oblique impacts a strong shielding from one surface molecule to the one behind takes place. Moreover, the apparent roughness is minimized for grazing collisions.

These and other premises are incorporated in a semi classical model that accounts for crystal vibrations, described in section 3.2.4 (page 61).

3.2.2 Lorentz-Lambert model.

Either by the presence of roughness in its own or also by the additional effect of atomic absorption in the surface, atoms tend to follow the ideal diffuse reflection (Lambertian)[7], known as cosine law:

"The intensity of light reflected from a surface is proportional to the cosine of the angle between the vector L to the light source and the normal vector N perpendicular to the surface" [31].

Note that the amount of atoms is independent of the azimuthal angle and of the incident direction. Therefore, the BRDF depends only on one space variable (polar angle of exit). Its simplest expression, once normalized to the solid angle honors its name:

$$p(\theta)_\Omega \propto \cos(\theta) \tag{3.3}$$

[7] Lorentz formally assumes molecular roughness deletes any memory of the projectiles so that f equals unity.

This means that a detector placed at an angle θ from the normal to the surface at the impact point will measure the reflected atoms with a probability proportional to $\cos(\theta)$.

For sampling purposes it is useful to express the cosine law in polar unnormalized space. This is achieved by introducing the solid angle factor,

$$d\Omega\left(\theta\right) = 2\pi r^2 \sin\left(\theta\right) \cdot d\theta \tag{3.4}$$

Whence,

$$p(\theta) \propto 2 \cdot \cos(\theta) \cdot \sin(\theta) = \sin(2\theta) \tag{3.5}$$

Where the constants have been conveniently absorbed to simplify the final formula. The *inverse transform method* is then used to sample the polar angle from the statistical law (*r* is a uniform random number).

$$r = \frac{\int_0^\theta \sin(2\theta) \cdot d\theta}{\int_0^{\pi/2} \sin(2\theta) \cdot d\theta} \Rightarrow \theta = \cos^{-1}\left(\frac{r'}{2}\right) \tag{3.6}$$

Concerning the **energy transfer**, Lambertian diffusion [32] is often associated to thermalization; the speed of the outgoing atom is sampled from the Maxwell-Boltzmann distribution. A few remarks should be made at this point:

1. For noble gases, macroscopic diffuse reflection is presumably only due to the roughness of the surfaces, micro-reflections being specular. In those cases energy should be conserved. However, after the typically high number of collisions it is expected that the atoms will have slowly thermalized even for quasi elastic collisions.

2. The MC code prompts the user to specify whether speeds ought to be sampled from the Maxwell Boltzmann law or if, alternatively, the average speed should be directly taken all the time. The first option (more time consuming) is only recommended for cases where the number of collisions is very low[8]. The implementation of these features in the `RIBO` code is detailed in Annex A.3.

Unless otherwise specified, this will be the default collision law used from now on.

3.2.3 Phong, Torrence-Sparrow and Blinn models.

The Phong, Torrence-Sparrow and Blinn models, strongly linked to the surface finish state, are usually used in the illumination circles. They result from the composition of the Fresnel law defining a central angle of emission ($\hat{\phi}_s$), a modified cosine law, which is applied around that central angle and, eventually, additional surface considerations. Although some trends may be extrapolated from light to atomic transport, it should be minded that light and atoms interact differently with the surfaces, the latter 'feeling' the potentials of the wall atoms.

Phong model.

The goal of Phong model [33] is to reproduce the imperfect specular reflectors, shiny but not entirely polished, so that effects are visible on more than one pixel[9].

Fig.3.2.C (page 56) schematically represents this model, of weak physical meaning but, surprisingly, quite performing in certain domains. Atoms are scattered inside a cone (α) centered around the Snell direction of reflection angle.

[8] In these situations the flight times of equal trajectories could have a visible spread that would, in turn, widen the release function.

[9] This model is currently used in computer imaging techniques.

The probability to be scattered with a deviation angle α is proportional to the l^{th} power of the cosine of α [10]. For mirror like surfaces, *l* is high and the pure Snell law is readily recovered. As an example, the reflection of visible light ($\lambda \sim 550\ nm$) on aluminum is well directed: $l = 200$. This value should be much lower for an atom hitting a surface at 2000 K ($\lambda \in [0.1 - 100]\ nm$).

Note that for l = 1 the cosine law is *not* obtained because the central direction of reflection does not correspond to the surface gradient (it follows the Snell law). Additionally, vectors penetrating the surface can be obtained by sampling Phong's law, so further corrections are needed.

Despite the mentioned drawbacks, due to its simplicity, the law has been implemented as a latent option in `RIBO`. This function should find its major use in the domain of illumination, e.g., fiber optics design, should the code ever be used for those disciplines.

Annex A.3.4 shows the details of the implementation of this law into the program.

Torrance-Sparrow and Blinn model.

The simplicity of Phong is sacrificed in Torrance-Sparrow and Blinn model to provide a scientific link between the surface roughness and the reflection law. The surface is simulated as a collection of mirror-like micro facets with randomized orientations in each of which Fresnel (Snell) law takes place. In

[10] The polar angle that completes the definition of the reflection around $\hat{\phi}_s$ is sampled uniformly. This makes it possible to sample directions that indeed penetrate the surface, which demands re-sampling.

Torrance-Sparrow [34] the distribution function (D_T) of the directions (α) of the micro facets on the surface is:

$$D_T = e^{-(c\cdot\alpha)^2} \tag{3.7}$$

The reflected distribution function includes the orientation distribution, the law of reflection (Fresnel) and the *Geometric Attenuation Factor* (G), which accounts for the self-shadowing [35] of incident and/or reflected beams[11]. Formulas of the last factor have been retrieved from optics theory and use the refraction index as key parameter.

Blinn model [36] frameworks the micro facets as ellipsoids of revolution whose eccentricity (ε) grows (from 0 to 1) as specularity is lost. The probability distribution (D_B) for the orientation (α) of the surface in this model is:

$$D_B = \left(\frac{\varepsilon^2}{1 + (\varepsilon^2 - 1) \cdot \cos^2(\alpha)} \right)^2 \tag{3.8}$$

More sophisticated physical optic descriptions have appeared since, in the attempt to correctly predict the diffuse, directionally diffuse and specular components of the reflected light [37, 38]. Users are invited to customize the collision routines to accommodate these models for dedicated applications.

3.2.4 Inelastic semi classical model.

The inelastic atom-surface scattering framework in the semi classical regime fuses the forced oscillator model with the impulse approximation and the Debye spectrum model for surface phonons. A simplified version of the semi classical model [39, 40], focused on inert atoms, has been adapted for this work [41], and

[11] e.g. an emerging grazing beam collides with the neighboring micro facet.

constitutes another intermediate (sometimes diffractive, some others diffuse reflective) treatment of atom-surface collisions.

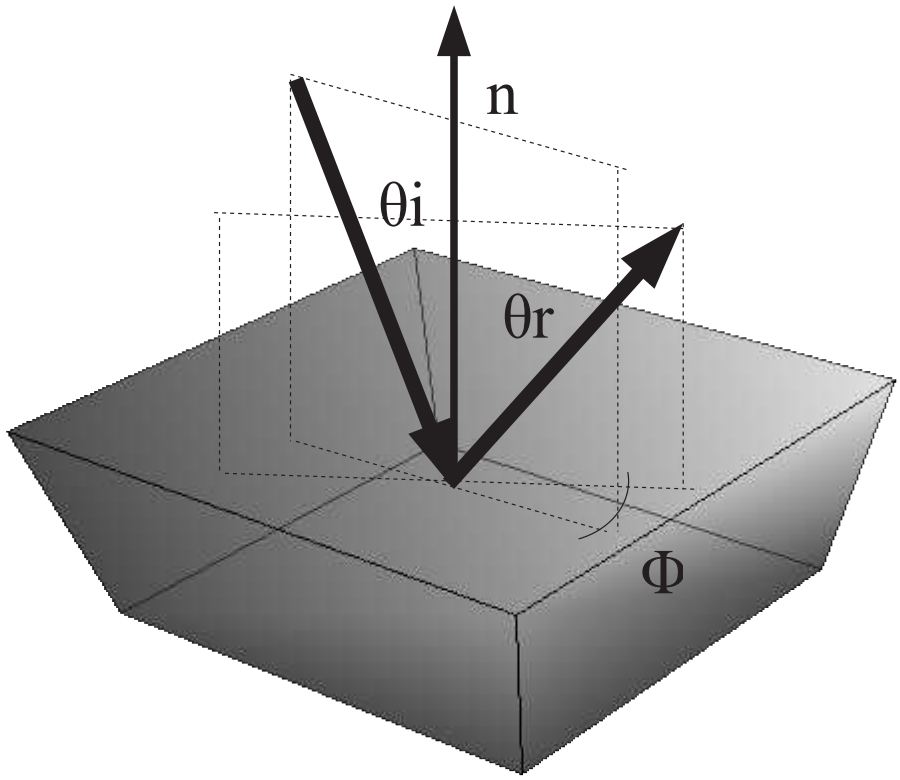

Figure 3.3: In the semi classical model the velocity of the reflected particle fluctuates around the plane defined by the incident velocity and the surface gradient.

The spectrum of inert atoms in the semi classical regime has no azimuthal or polar symmetry (fig.3.3) and can be formulated as:

$$N\left(\hbar\Delta K_x, \hbar\Delta K_y, \Delta E\right) = \Gamma \cdot e^{-\frac{(\hbar\cdot\Delta K_x)^2}{2\cdot\sigma^2(\hbar\cdot\Delta K_x)}} \cdot e^{-\frac{(\hbar\cdot\Delta K_y)^2}{2\cdot\sigma^2(\hbar\cdot\Delta K_y)}} \cdot e^{-\frac{(\Delta E-\mu)^2}{2\sigma^2(\Delta E)}} \tag{3.9}$$

where the scattering amplitude Γ acts as a normalization constant, irrelevant to the sampling process:

$$\Gamma = 2 \cdot \pi^{3/2} \cdot \sigma\left(\hbar \cdot \Delta K_x\right) \cdot \sigma\left(\hbar \cdot \Delta K_y\right) \cdot \sigma\left(\Delta E\right) \tag{3.10}$$

Element	He	Ne	Ar	Kr
D$[meV]$	8	20	50	90

Table 3.1: Average projectile impact depth on a Cu (1 1 1) substrate

ΔK_x, ΔK_y are the x, y components of the tangential wave-vector ΔK (parallel to the surface xy-plane), ΔE is the energy transferred to the surface (perpendicular component). μ and σ describe the first and the second (statistical) moments. In particular, μ refers to the *mean* energy transfer. According to Baule's [42] formula, and neglecting substrate temperature effects:

$$\mu = 4 \cdot E_z \cdot \frac{\lambda}{(1+\lambda)^2} = 4 \cdot E_z \cdot \left\{\lambda - 2 \cdot \lambda^2 + \ldots\right\} \tag{3.11}$$

E_z corresponds to the orthogonal kinetic energy (z-axis):

$$E_Z = (m/2) \cdot (\vec{v} \cdot \hat{n})^2 \tag{3.12}$$

Some remarks should be made at this point.

- The Beeby correction consists in replacing E_z by $E_z + D$, where D is the average depth of the projectile impact into the surface interaction potential. D roughly scales proportionally to the projectile mass[12]. Beeby values for a Cu (1 1 1) surface are tabulated in 3.1.

- Formula 3.11 has been expanded in powers of λ, a parameter describing the ratio of mass between the projectile and the surface atom ($\lambda = A_{proj}/A_{eff.subst}$). It should be noted that the projectile interacts with the

[12]This property, observed from the available data is used in `RIBO`.

potential of several neighboring surface atoms, meaning that the effective mass of the substrate is:

$$A_{eff.subst} = n \cdot A_{substrate} \tag{3.13}$$

Where n is taken as $n = 3$.

- In certain cases $\lambda << 1$, then, from the linear term of the power series:

$$\mu = 4 \cdot E_z \cdot \lambda \tag{3.14}$$

- Baule's formula is invariant to kinematics inversion ($A_{projectile} \rightleftharpoons A_{substrate}$) (n=1):

$$\mu(\lambda) = \mu\left(\frac{1}{\lambda}\right) \tag{3.15}$$

  The symmetry concerns only the mean energy transfer. An interchange of substrate and projectile would be noticed in the spread of ΔE and in the probability distribution of the reflected direction.

- A corollary from the previous property is that the energy transfer is limited to: $\lambda = 1/\lambda = 1$.

The Gaussian function for the shift of transferred energy ($\sigma(\Delta E)$), is obtained from:

$$\sigma(\Delta E) = \sqrt{\eta \cdot k_B \cdot (3 \cdot T_D + 8 \cdot T)} \tag{3.16}$$

Here T and T_D represent the natural and the so-called Debye temperatures of the surface. Main Debye bulk temperatures are shown in table A.2 (page 24 of the

annexes) (typically surface Debye temperatures scale as $T_D(bulk) \cdot 2^{-1/2}$) and can be deduced from the calorific capacities [43, 5].

As for the second moments, $\sigma(*)$, they are computed in the following way for the wave-vectors:

$$\sigma\left(\hbar \cdot \Delta K_x\right) = \sigma\left(\hbar \cdot \Delta K_y\right) = \sigma\left(\Delta E\right)/C \tag{3.17}$$

The constant C has units of speed and includes the information of the crystal; the lattice constant, *a*, and its Debye energy, E_D ($E_D = k_B \cdot T_D$):

$$\frac{1}{\lambda} \cdot C = E_D \cdot \frac{2 \cdot \pi \cdot \hbar}{1.6 \cdot a} \tag{3.18}$$

The basis has just been established for the calculation of the dispersion of the variables (ΔE), and ($\Delta K_{x,y}$). Three fixed values can then be sampled from the Gaussian laws: ΔE^c, $\Delta K^c_{x,y}$ and, finally, the kinetic parameters after the collision (total kinetic energy and parallel momenta) correspond to the solution of the system:

$$\begin{cases} K^c_{x,y} = K_{x,y} + \Delta K^c_{x,y} \\ E^c = E + \Delta E^c \end{cases} \tag{3.19}$$

with the constraints:

$$\begin{cases} K^C_i \in \mathbf{R} \\ E \geq 0 \end{cases} \tag{3.20}$$

The second degree 3-eq system is readily decoupled and the solution is checked against the constraints.

$$E^2 = E_x^2 + E_y^2 + E_z^2 = \frac{\hbar^2}{2 \cdot m} \cdot \left(K_x^2 + K_y^2 + K_z^2\right) \tag{3.21}$$

Since $\Delta_{x,y}$ and ΔE are found independently, it may happen, for example, that while E decreases, $K_{x,y}$ increase too much, and then only an imaginary K_z fulfills eq. 3.21. When this occurs, the vertical speed is nil, $K_z = 0$; the atom actually slides over the surface with its tangent velocity determined by $K_{x,y}$, and the defect of energy is provided by the bound to the surface potential. The second condition is violated simply when $E - \Delta E < 0$, which happens with a probability that can be calculated with the tabulated tails of the gaussian function. In practical terms, when any of the two fails, the atom will be assumed to stick to the surface for a brief instant of time until the next crystal vibration takes place. Then it will be re-emitted with a speed following the cosine law. Annex A.3.3 details the implementation of these functions into the code.

The semi-classical model tends to the specular model for light **noble** atoms, i.e. He, impinging tangentially onto crystals of low lattice parameter and high Debye temperature. In fact, it is sufficient if $\lambda \to 0$, then:

$$\mu \to 0 \Rightarrow \Delta E \to 0 \Rightarrow \Delta K_{x,y} \to 0 \Rightarrow \begin{cases} E^c \to E \\ K_{x,y}^c \to K \end{cases} \tag{3.22}$$

Surprisingly, the model (eq. 3.15) forecasts quasi-elastic collisions also for very heavy noble gases (e.g. Rn). In the opposite extreme, non-noble gases stick to the surface and, therefore, they are attributed the Maxwell-Lambert model. An intermediate behavior, combining purely Lambertian collisions with specular and

hybrid ones, is analytically observed, with different proportions, in the remaining noble gases (Ne, Ar, Kr, Xe).

To conclude, the semi classical model proves as an elegant theory to conciliate the apparently opposed *elastic collisions* hypothesis with the *cosine law lemma*, all cemented with the sticky character and the ratio of masses projectile/surface. However, data are still missing and the effect of roughness is not yet clear. Moreover, compared to the Maxwell-Lambert model, more operations are needed to compute the ejection velocity after each collision. These drawbacks advise a default use of the commonly accepted *cosine model*, knowing that results will be on the safe side (pessimistic) and with the chance on execution to opt for the semi classical model.

it includes most physical surface effects, except for the roughness

3.2.5 Diffraction.

The study of specular reflection of atoms on surfaces must be regarded as a problem of diffraction of matter waves whose *De Broglie* wave length widely surpasses the roughness dimensions. This idea has already been used to justify the Lorentz law, but diffraction can also appear as a specialized form of specular reflection for patterned textures of the right periodicity. It should be stressed that diffraction is more likely for light projectiles (this is reproduced by the Semi-classical model, 3.2.4). Verified examples of this phenomenon are the diffraction of H, H_2 and He on NaCl and LiF, while heavier projectiles like Ne, Ar or CO_2 hardly experience this effect.

For these and for other cases, the user of the Monte Carlo code can decide to simulate collisions as purely diffractive by choosing the option S (see Annex B.4).

3.2.6 Comparative analysis of effusion under the different collision models.

The stochastic character of the azimuthal angle in the cosine law, where collisions can 'send particles back' makes this model presumably slower than that of specular collisions, at least for straight systems. As for the semi-classic model, it should stand in between the two, closer to the slowness of the Lambertian model but slightly faster due to those collisions where adsorption or sliding do not take place.

Fig.3.4 compares the effusion of He under the three models in a 20 cm long Ta cylinder of diameter of 2 cm, at 2000 K. The temperature and the gas have been chosen to maximize the difference between Lambertian and semi-classical effusion. The starting distribution is randomized. It can be seen how specular effusion is faster than semi-classical effusion, which, in turn, is quicker than Lambertian effusion. In general terms (other than He at high temperatures) Lambertian effusion and semi-classical effusion are quite similar and remain on a safe-side for yield estimation purposes. A fourth curve (continuous line) compares the release curve in the cosine-law assumption when the energy is sampled from the Maxwell-Boltzmann law after each collision (option 'N' in the code) and when the average value of the distribution is taken all over (option 'Y' in the code). Again, this example favors the impact of this effect, because here the number of collisions is quite moderate and the theorem of the central limit is far from being fulfilled.

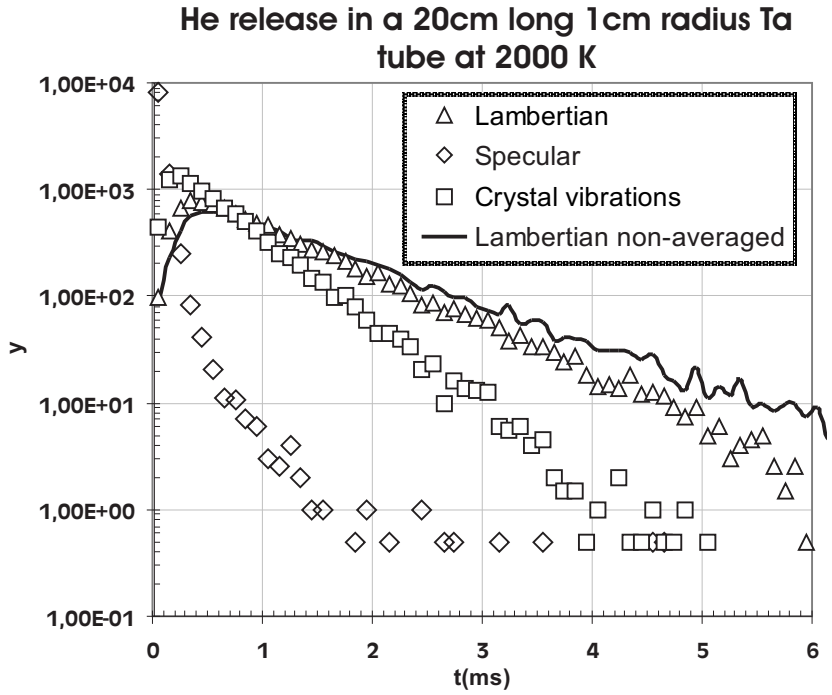

Figure 3.4: Effusive release of He in a 20 cm long Ta tube of $r = 1$ cm at 2000 K for ($\diamond$) specular reflection, ($\square$) semi-classical reflection, ($\triangle$) cosine-law collisions in average mode and for individually sampled energies ($-$).

3.2.7 Conclusions.

Much has been discussed on whether the elastic or the Lambert-inelastic collision models should be applied. Some MC codes simulating effusion in tubular geometries [44, 45] follow the intuitive criterion of adopting Lambertian reflection for all elements except for the non-sticky ones (noble gases), where there is virtually no time to allow interactions between the surface and the element[13].

However, experience in the field of vacuum design dictates an extended use of the cosine law. This indication is backed up by the conclusions of light reflection

[13]The previous kinematical history would be forgotten if the atom stuck to the surface for an appreciable lapse of time, emission being exclusively governed by the crystal vibrations.

studies, where the roughness of the surface can justify in its own the diffuse character of reflections[14].

3.3 Interaction between atoms. Chemical interactions. Effect of pressure.

3.3.1 Chemical interactions, Atom-surface effects.

When a molecule hits a surface, various events are possible depending on the chemical interactions between the projectile and the substrate. Most likely the molecule will stick for some time and then be re-emitted but it can also be reflected immediately or condense on the surface. This last effect is exploited in ISOL transfer lines acting as chemical selectors to condense impurities. The most important statistically determinate constants of interaction between the molecules and the wall atoms are [4]:

- The *reflection coefficient,* which expresses the probability that an atom impinging on a surface is re-emitted after a lapse of the order of the crystal vibration period.

- The *sticking coefficient* refers to the probability of prolonged[15] retention of a gas molecule on a surface. This is used as the differential characteristic of an elementary adsorption event.

[14] This is so for low wavelengths/roughness ratios, even in absence of refractions, meaning that the concept should be extensible to atomic collisions regardless of the chemical interactions.

[15] In terms of oscillation periods.

- The *stimulated gas desorption coefficient* is a figure that tells the number of desorbed gas particles as a consequence of the impact of a particle (ion, atom, molecule, lepton or hadron) in the surface.

- The *condensation coefficient* is similar to the sticking coefficient with some nuances on the nature of retention.

In fact, the nature of the interaction of a given molecule with the surface depends on the primary chemical valence forces, which, in turn, vary in presence of extraneous molecules stuck on the surface. This justifies preliminary heating to promote purification. In order to determine whether the surface might present monolayers of impurities, the surface coverage (γ_i) can be estimated as [23]:

$$\gamma_i = N_i \cdot \tau_a \cdot \sigma \tag{3.23}$$

If the conditions above are favorable to condense the species i in great amounts (due to high chemical adsorption σ, long sticking time τ_a[16] or high bombarding flux N_i), the new impacting molecules will interact with the formed monolayer and the adsorption times (self-interaction) will change.

The `RIBO` Monte Carlo code yields the number of atom-surface impacts, and it can be forced to specify the coordinates of those, which renders it a powerful tool to determine the surface coverage in different areas of the vacuum system. Additionally, the MC program includes two simplified parameters, derived from the previous concepts.

- The *absorption coefficient* expresses the probability that an atom impinging on a surface condenses on it (indefinitely). The MC code accepts different absorption coefficients for each surface of the system; the output file

[16] The adsorption time τ_a depends on the energy of the incident particles.

includes a report with the number of aborptions in each surface and the global absorption efficiency.

- The (average) *sticking time* corresponds to the mean period of retention of an atom in a surface. This value, combined with the number of collisions (simulated) allows the computation of integrated adsorption times for each extracted atom ($number\ of\ collisions\times\ <\ sticking\ time\ per\ collision\ >$). The sticking times in fact correspond to the average values of the Frenkel equation [46]:

$$t_s = t_0 \cdot e^{-E_d/kT} \tag{3.24}$$

  - t_s is the sticking time at the absolute temperature T.
  - t_0 is the sticking time at infinite temperature $T = \infty$
  - E_d interaction energy.
  - k Boltzmann constant.

  The interaction energy of the adsorbed atom on the surface E_d coincides with the partial molar adsorption enthalpy ΔH_a when the activation energy is negligible and the surface coverage low. The enthalpy of adsorption ΔH_a and the characteristic time t_0 depend exclusively on the temperature and the chemistry of both elements, but precise measurements of those are hindered by the presence of impurities, which explains the huge scatter of experimental values between authors. One of them, Eichler, developed a semi-empirical model for different adsorbates on metallic surfaces [47], from which indicative tables have been computed [48].

RIBO does not sample sticking times from the probability distribution laws; it takes directly the average sticking time ($< t_s >$), the purpose being a faster computation of each history. This does by far not enlarge the statistical uncertainty of extraction times because each history (*i*) involves several thousands to various millions of collisions meaning that the theorem of the central limit is strictly verified[17] (the variance resulting from assuming $< t_s >$ and not $t_s(i)$ tends to $|\langle t_s \rangle - t_s\,(i)| \cdot N^{-1/2}$ for N collisions).

3.3.2 Interaction between particles in vacuum.

It has just been seen how gas atoms may interact with monolayers made of atoms that previously condensed *on the system walls*. This thesis is framed in the assumption that the flow of radioactive atoms is molecular, that is to say, no interactions between gas atoms take place *in the vacuum* so that the vacuum merits its name. This is certainly so for most cases, but it may happen that gases other than the rare species are liberated in high amounts. Then atoms can bounce once or more with residual gas between two consecutive wall collisions.

Probability of atom-atom collisions as a function of pressure

The mean free path is related to the likeliness of atom-atom collisions through the kinetic theory of gases. A simple hard-sphere collision model estimates the collision cross section as $\sqrt{2} \cdot \pi \cdot d_0^2$, where d_0 is the atom diameter ($[\mathring{A}]$) and the

[17] Slight deviations may occur in those special cases where a tiny component (therefore receiving few impacts per particle) has a radically different adsorption enthalpy.

$\sqrt{2}$ prefactor takes into account the fact that the target atom is not at rest. Thus, the mean free path is readily written as:

$$\lambda = \frac{1}{n \cdot d_0^2 \cdot \pi\sqrt{2}} = \frac{k \cdot T}{P \cdot d_0^2 \cdot \pi\sqrt{2}} \tag{3.25}$$

Where:

- T is the absolute temperature.
- k is the Boltzmann constant.
- P is the pressure.

The probability distribution function for the distance (S) between collision phenomena of this type has the shape of a decay exponential where the scale constant is λ:

$$p\,(S) = \frac{1}{\lambda} \cdot \exp\left(-\frac{S}{\lambda}\right) \tag{3.26}$$

The chance that an atom-atom collision take place in a flight distance *S* is:

$$P(S) = 1 - \exp\left(-\frac{S}{\lambda}\right) \tag{3.27}$$

The average free flight distance between consecutive collisions (also written as FP in other sections of this work), can be estimated from Clausius [49, 50] formula[18]:

$$FP = \frac{4 \cdot V_{void}}{A} \tag{3.28}$$

[18]This formula is strictly correct for diffusive scattering within a sphere and it provides an order of magnitude for other geometries.

V_{void} represents the free volume and A the area of the enclosing walls. In typical working conditions flight distances range from 1 μm to about 50 cm at the most.

As FP/$\lambda \rightarrow 0$ the chance of atom-atom collisions becomes negligible and the `RIBO` code can be used in the molecular mode[19].

Deviation of trajectory upon collisions to residual gas atoms

In the following calculations **1** refers to the effusing atom and **2** to the residual gas atom; u correspond to velocities in the general fix frame $\{x, y, z\}$ while v is used for velocities expressed in a Cartesian frame oriented with the initial speed of the colliding atom $\{a, b, c\}$. Speeds before collision are labeled as i; and as f after the impact.

The initial speed of the tracked atom of mass m_1 in the frame whose first component is parallel to its velocity is, by definition:

$$\left.\begin{array}{c} v_a^{1i} = u = +\sqrt{u_x^2 + u_y^2 + u_z^2} \\ v_b^{1i} = 0 \end{array}\right\} \tag{3.29}$$

As for the residual atoms (**2**), of mass m_2, they have speeds distributed according to the Maxwell-Boltzmann law (MB subscript) and isotropic directions. Nonetheless, in the polar system, when sampling isotropic velocities, solid angle correction needs to be applied to preserve normalization, thus, the incidence angle between the velocities of the colliding atoms (θ) in the laboratory frame has the distribution function:

$$p\left(\theta\right) = \sin\left(\theta\right) \tag{3.30}$$

[19] Even if a few elastic collisions took place during the errand path of the atom, this would hardly impact on the release probability distribution.

Sampling θ from 3.30 ($\theta = \arccos(rand())$) the target atom velocities are obtained:

$$\left\{ \begin{array}{l} v_a^{2i} = -v_{MB} \cdot \cos(\theta) \\ v_b^{2i} = -v_{MB} \cdot \sin(\theta) \end{array} \right\} \tag{3.31}$$

Now the angle between the velocity vectors can be computed in the center of mass frame system:

If elastic collisions are assumed the total energy and momentum is conserved, then:

$$\kappa = \tan\left[\arctan\left(\frac{v_{MB} \cdot \sin(\theta)}{u + v_{MB} \cdot \cos(\theta)}\right) + \theta\right] \tag{3.32}$$

Hence:

$$\Delta v_a^{2fi} = v_a^{2f} - v_a^{2i} = 2\frac{v_a^{2i} - v_a^{2i} + \kappa \cdot (v_b^{2i} - v_b^{2i})}{(1+\kappa^2) \cdot \left(1 + \frac{m_2}{m_1}\right)} \tag{3.33}$$

and:

$$\left. \begin{array}{l} v_a^{f1} = v_a^{1i} - \frac{m_2}{m_1}\Delta v_a^{2fi} \\ v_b^{1f} = v_b^{1i} - \kappa\frac{m_2}{m_1}\Delta v_a^{2fi} \end{array} \right\} \tag{3.34}$$

The reference system is oriented along the velocity of the tracked atom.

$$\hat{n}_a = \frac{\vec{u}^i}{u^i} \quad \hat{n}_b = \frac{\vec{u}^i{}_y - \vec{u}^i{}_x}{\sqrt{\vec{u}_x^{i2} + \vec{u}_y^{i2}}} \quad \hat{n}_c = \frac{-\vec{u}^i{}_x - \vec{u}^i{}_y - 2\vec{u}^i{}_z}{\sqrt{\vec{u}_x^{i2} + \vec{u}_y^{i2} + 4\vec{u}^{i2}_z}} \tag{3.35}$$

Expressing these equations into matricial or tensorial form:

$$\bar{N} = \begin{bmatrix} n_{ax} & n_{ay} & n_{az} \\ n_{bx} & n_{by} & n_{bz} \\ n_{cx} & n_{cy} & n_{cz} \end{bmatrix} = n_{ij} \tag{3.36}$$

The exiting velocity of the projectile can in fact have any orientation around the axis defined by the initial velocity. Therefore, a uniform random number is sampled to select the polar angle φ:

$$\varphi = 2\pi \cdot rand\,() \tag{3.37}$$

The according transformation of coordinates is applied through the rotation matrix around the vector $\bar{a}$ with an angle φ:

$$\bar{\Gamma} = \begin{bmatrix} 1 & 0 & 0 \\ 0 & \cos\varphi & -\sin\varphi \\ 0 & \sin\varphi & \cos\varphi \end{bmatrix} = R_{1\varphi} \tag{3.38}$$

With the two prior transformations, the velocities after the impact can be expressed in the coordinate axis x, y, z through:

$$\bar{\Gamma} \cdot \bar{N} \cdot \bar{u} = \bar{v} \Rightarrow \bar{u} = \bar{N}^T \cdot \bar{\Gamma}^T \cdot \bar{v} \tag{3.39}$$

Whence, in dyadic notation:

$$\left.\begin{array}{c} u_i = n_{im} \cdot \Gamma_{mn} \cdot v_n^f \\ i \in \{x, y, z\} \end{array}\right\} \tag{3.40}$$

3.4 Vacuum technology formalism. An analytical approach to effusion.

Under molecular flow conditions the throughput of gas (Q) scales proportionally to the pressure drop (ΔP) through a constant (C) which depends only on the geometry of the conducting element [51].

$$Q = \frac{\Delta P}{Z} = C \cdot \Delta P \tag{3.41}$$

The deduction of this parameter, called *conductance*, or of its inverse, *impedance* is explained in detail in annex A.1. It should be noted that the cosine law of collisions is assumed (through Clausius [49]) as well as the kinetic gas theory (to link velocities and pressures) and the Maxwell-Boltzmann distribution. The expression reached for a single generic element is:

$$C = \frac{4}{3} \cdot \frac{\bar{v}}{\int_0^L \frac{O}{A^2} \cdot dl} \tag{3.42}$$

Where $\bar{v}$ is the mean velocity of the particle distribution, O the perimeter of the conduction; A and L being its area and length, respectively.

The big advantage of the vacuum formalism is that Q, P and Z act as I, V and R, in electric circuitry theory and, thereby, the algebra of Kirchhoff can be analogously applied to compute complex vacuum systems with elementary elements (whose conductance is determined by eq. 3.42) associated in parallel and/or series.

$$\left.\begin{aligned} \frac{1}{C_{series}} &= \sum_i \frac{1}{C_i} \\ C_{parallel} &= \sum_i C_i \end{aligned}\right\} \tag{3.43}$$

It should be outlined, however, that the law holds if elements are set strictly in series, with their axis superimposed at the joints. Otherwise, in presence of "elbows", the input velocity distribution to the ulterior elements is conditioned by those sharp swerves and the corresponding conductance is not consistent with that derived from the kinetic theory. This is a *first limitation* of this method, unable to compute accurately the global conductance of such structures. In turn, brusque changes of cross section (e.g. collinear tubes of different diameter) don't fake the results provided that the conductances of the transitions (orifices) are included in the calculations[20] in eq. 3.42. The previous arguments break the symmetry of the vacuum ohmic laws to an inversion of the flux direction. Thus, conductances are not fully commutative; their order affects the overall transmission.

Conductances do not fully commute

Now it remains to reveal the link between the conductance formalism and the searched release curves. The way is straightforward when a second equation is found to relate P and Q:

$$Q = \frac{d}{dt}\left(P \cdot V\right) \tag{3.44}$$

Substituting 3.44 into 3.41 yields:

$$C = \frac{V}{P} \cdot \frac{dP}{dt} \Rightarrow P\left(t\right) = P\left(t_0\right) \cdot e^{-\frac{C}{V} \cdot \left(t - t_0\right)} \tag{3.45}$$

In fact, what is searched for is the shape of the release of the gas as a function of time, $Q(t)$. Using again 3.44:

$$Q\left(t\right) \propto e^{-\frac{C}{V} \cdot t} \tag{3.46}$$

[20] Make $l \mapsto 0$

the finite speed of the propagation introduces an 'annoying' term

This is a decaying exponential function (thus the maximum is at $t = 0$). The throughput has that shape only at the entrance of the resistance, but not at the exit (where the release is measured). This is so because the gas perturbation needs some time to propagate from one extreme to the other. In other words, the vacuum kinetic theory method cannot predict the transient mode that builds up a release peak. In some occasions this peak is very close to zero and the theory is fully valid. Inversely, the conductance of a system can be extracted from the effusion release curve obtained by whichever method, e.g., Monte Carlo. Otherwise, the release curve must be some sort of combination of functions, defining a peak rise and its corresponding decay. Typically this means that a fast exponential (saturation) function corrects the plain decay exponential:

$$E_2\left(t\right)_u \propto \left(1 - e^{-f(C)\cdot t}\right) \cdot e^{-\frac{C}{V}\cdot t} \tag{3.47}$$

where the *rise time* should depend on the conductance: $f(C)$. A third exponential, describing a slower decay component is often introduced to fit release curves [52]. Its presence can be justified by the delays produced in the diffusion process. Then:

$$R\left(t\right) = C\left(1 - \exp\left(-\frac{t}{\tau_r}\right)\right) \cdot \left[\alpha \cdot \exp\left(-\frac{t}{\tau_f}\right) + (1-\alpha) \cdot \exp\left(-\frac{t}{\tau_s}\right)\right] \tag{3.48}$$

The symbols used above are:

- C is a normalizing constant.
- τ_r, τ_r and τ_r are the rise, fast and slow fall time constants.
- α is a weighting-shaping constant.

Now, considering that diffusion in fact involves a series of exponentials, those series should be reflected in the final expression of release. Works of [53] provide analytical descriptions of release with enough parameters to obtain good fits of results and then pursue subsequent predictions for altered configurations. This all approach is theoretically neat, but not too practical as is, the errors involved in fitting several exponential functions eventually being excessive. At this point a link between the conductance and a more easy to measure magnitude is needed. The following section studies the solution to this question.

3.5 Validation of effusion.

Dushman [54] observed that the conductance of cylindrical tubes (C) may be expressed in terms of the conductance of their inlet tubes (C_{or}) through a proportionality constant k':

$$C = k' \cdot C_{or} \tag{3.49}$$

with (same symbols as in 3.42):

$$C_{or} = \frac{1}{4} \cdot \bar{v} \cdot A \tag{3.50}$$

Moreover, under the assumption that the molecular flux density distribution is uniform at the inlet opening over the whole cross section, the constant k' turns out to be **Clausing coefficient** [55] (P_0), that is, the probability that an atom entering the section exits by the other end, or, in other words, the ratio between the flux of atoms traversing a given section (F_{out}) and the total ingoing current (F_{in}). It is often implicitly understood that atoms are diffusively scattered on the

system walls, which are macroscopically smooth, that the gas is rarefied, Maxwellian and that there is no mechanism of loss like absorption (F_{abs}), ionization (F_{ion}) or decay (F_{decay}). However, the concept can be extended to those cases, the flux balance being:

$$F_{in} = F_{out} - F_{reflect} - F_{ion} - F_{abs} - F_{decay} \tag{3.51}$$

RIBO has a conductance estimator

For the simplest geometry of a tube or radius r and length L, with no loss factors (just the three first terms of eq. 3.51), there exist several analytical models and numerical calculations [55, 56, 57, 58], which can be used to benchmark the effusive transport in the simulation code. The RIBO program contains a 'conductance calculator' mode, where the user has to specify the entry and exit sections of the element to be analyzed. The main section is preceded by a slim prechamber where atoms are generated following the cosine law before heading at the probe section[21]. The program terminates tracking of the atoms when they cross the first section twice (meaning that they have been reflected back to the origin) or when they traverse the end section, in which case a counter N_i is increased. At the end of the simulation the Clausing number is obtained as $P_0 = \frac{N_i}{N}$ where N is the total number of simulated atoms. The absolute error $(1 \cdot \sigma)$ is $\Delta P_0 = \sqrt{\frac{P_0 - {P_0}^2}{N}}$.

Simulations were carried out for tubes of aspect ratio (L/r) 0.1, 0.2, 0.5, 1.0, 2.0, 5.0 and 10.0. This set was then repeated for situations where the walls had an absorption coefficient (c_{abs}) of 0.25, 0.50, 0.75 and 1.00. In total 35 simulations with $1 \cdot 10^5$ histories each, which took no more than 15 minutes in a 2.8 GHz,

[21] The Clausing values of literature specify that the probe channel connects two large vessels filled with Maxwellian gas. Obviously, the shape of those reservoirs will determine the velocity spectra at the entry of the section and this will ultimately affect the Clausing coefficient. Results for an isotropic starting distribution differ from reference values by about 3-5 $\%$.

256 Mb laptop running LINUX kernel 2.66 - 1.435.2.3. In absence of absorption, results are compared with the calculations of Clausing [55]. The accordance of simulations and analytical calculations is well within 1 $\%$, that is, in the region of stochastic (Monte Carlo) and numerical errors (formulas), which permits to mount further steps of complication with confidence.

When the walls become absorbent, a fraction of the flow condenses in the walls and P_0 shrinks accordingly. The extreme case of 100 $\%$ absorbing surfaces (a kind of black body) is particularly interesting because P_0 then represent the **viewing factors** between the injection and extraction sections[22]. These values can be evaluated analytically in a few basic cases and numerically in some other situations; for complicated geometries `RIBO` may be a useful tool to extract viewing factors for dosimetry or heat radiation problems. The numerical calculation used to benchmark the MC code for black body-like systems[23] made two n-grids for the base and the top of the cylinder and computed $\frac{1}{n^2}\sum_{i,j}^{n,n} r^{-2}$, the result was normalized to the semi-sphere 2π.

Again, comparison of simulated and numerical values, shown in table 3.2 is reassuring. As for the intermediate values of c_{abs}, results show a smooth behavior between the two validated extreme situations.

Running in the specular mode immediately yields Clausing coefficients identical to 1, for whichever aspect ratio, as expected[24].

In [4] Clausing coefficients are plotted for geometries derived from the tubular case, combining sections of different diameters, with bends, orifices, etc. Among them, one case is selected for an additional test of the code's virtue to emulate effusive transport under diffuse collisions. The geometry is like the one used

[22] In this case, an isotropic distribution must be forced at the source.

[23] This case is not that rare, it happens effectively when the mean sticking time of an isotope on a given surface is much longer than its half-life.

[24] In a tube the drift component of the flow is conserved for specular collisions.

L/r	0.1	0.2	0.5	1.0	2.0	10.0
c_{abs} = 0.0						
Ref. [4]	0.9524	0.9092	0.8013	0.6719	0.5142	0.1909
Ref. [55]	0.9524	0.9092	0.8013	0.6719	0.5136	0.1973
MC sim.	0.9524(7)	0.9102(9)	0.8028(12)	0.6723(15)	0.5137(16)	0.1916(10)
c_{abs} = 1.0						
Numeric	0.78(15)	0.658(5)	0.4225(8)	0.2327(2)	0.09382(3)	4.9E-3
MC sim.	0.7847(13)	0.6561(15)	0.4203(16)	0.2313(13)	0.0937(9)	0.0049(2)

Table 3.2: Clausing conductance coefficients for a tube of aspect ratio L/r, diffuse reflection without absorption and with full absorption. Reference values 1 and 2, numeric calculation and Monte Carlo simulation.

before, but with an inner tube that reduces the pumping speed. Fig.3.5 sketches the geometry and the free parameters and table 3.3 shows the simulated and the reference values. Once more, the accordance is better than 1 $\%$. Finally, an extra

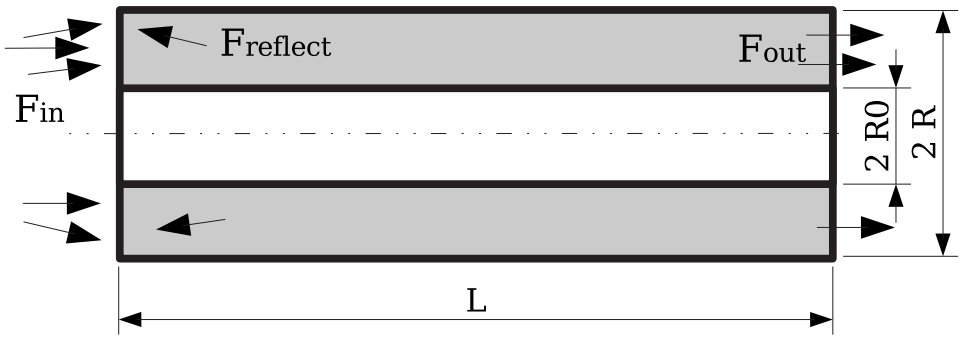

Figure 3.5: Scheme of the computation of Clausing coefficient with an ingoing flow (F_{in}) and outgoing (F_{out}). Generation follows the cosine law.

test of effusion transport can be done almost instantaneously by using Clausius equation (eq.3.52, page 91) to compare the theoretical average flight distance between two consecutive collisions in a sphere with simulated values. Simulations are carried out for spheres of radius 1, 2, 5 cm releasing gas through an orifice on the sphere surface with a radius of 0.01 cm. The average simulated flight distances for $5 \cdot 500$ histories are found to be 1.3350(4), 2.6674(6) and

R_0/R	L/R	1	2	5	10
0.25	Ref.	0.60	0.457	0.271	0.173
	sim.	0.614(2)	0.455(2)	0.267(1)	0.163(1)
0.50	Ref.	0.52	0.376	0.19	0.13
	sim.	0.530(2)	0.375(2)	0.209(1)	0.121(1)
0.75	Ref.	0.40	0.268	0.138	$<$0.085
	sim.	0.385(2)	0.256(1)	0.130(1)	0.0724(8)

Table 3.3: Clausing conductance coefficients for a tube of aspect ratio L/R, with an inner tube of radius R_0. A rarefied gas flows between the two tubes suffering diffuse reflections. Reference values are taken from [4]. Each case simulated $1{\cdot}10^5$ particles.

6.6664(8) cm, while the theoretical values amount to 1.3333, 2.6667 and 6.6667 cm.[25]

3.6 Effusion in continuous media.

In section 2.2 (page 20) a diffusive approach to transport in highly packed artificial structures (like parallel foiled targets) was suggested. The thin line between effusion and diffusion is again crossed with an effusive treatment of inter-grain diffusion. This technique, thoroughly described below was applied to the release curves of ISOLDE UC_x targets in order to extract the unknown diffusion and effusion parameters. Several parameter-dependent effusion curves are convoluted with the η-diffusion from spheres/fibers, where η was already defined in 2.10 (page 25).

[25] If such a test were carried out by forcing isotropic dispersion then the average distance between points of the sphere would be measured. This again suggests that geometric calculations (e.g. viewing factors, integrals...) can be performed with the `RIBO` program.

3.6.1 Powder and fiber targets.

Up to this point the RIBO MC code dealt only with geometrically well-defined targets (e.g. periodical foiled structures), where "real" individual random trajectories could be tracked. Nonetheless, many isotopes are optimally produced in refractory oxides or carbides..., which usually come as powder or as a fibered felt. The next phase in the design of the code is to incorporate the capability to simulate continuous media by taking a statistical approach of effusion (we can't know where each individual grain of powder/fiber is).

Statistical approach to effusion

For the sake of simplicity and for coherence with the syntax of the whole MC code, two parameters were selected as geometry descriptors: average grain size and track length, that is, the average free flight path (FP) between two consecutive collisions of an effusing atom inside the powder (or fiber). The first parameter concerns mainly in-grain diffusion and is discussed later. Yet, a third parameter is needed to fit the *average sticking time* of an atom to the walls (t_s). The time and angular distributions to exit a macro sphere are initially obtained to enable subsequent macro-steps (= radius of the sphere probe) that will speed up calculations quite considerably. Outside the powder (or fiber) domain, effusion takes place as usual. Bulk re-diffusion appears naturally in the method.

3.6.2 Methodology.

a. Parameterization: As just stated, the transport of atoms is parameterized with: [1)] the average flight path (FP) of an effusing atom between two consecutive collisions inside the powder, [2)] the powder/fiber size (d) and the diffusion coefficient, which are merged in the diffusion parameter ($\eta = D \cdot \frac{\pi^2}{d^2}$), and [3)] the average sticking time on the surfaces (t_s). When the isotope is

born inside the target, first it diffuses out of the grain/fiber and then it will follow a random walk in the intergrain/interfiber space. Such path is made up of free flights (whose distance averages FP) between consecutive collisions, which are in turn supposedly governed by the cosine law applied on a surface assumed to be randomly oriented in a 2π sphere. Additionally, each collision may involve an average adsorption-desorption time, t_s[26].

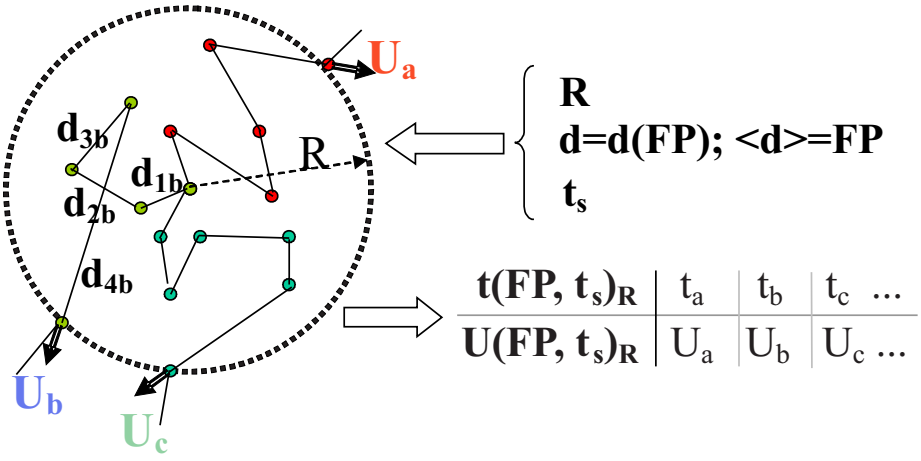

Figure 3.6: Macro-step tracking in continuous media: 10000 Random walks from a sphere are built up by cosine-law collisions on randomly oriented objects at an average distance of FP. Each collision consumes an additional (sticking) time t_s. The exit times and angles are stored in a 2-D histogram for future sampling.

b. Variance reduction: Trajectories of atoms inside the powder may involve several millions of collisions, entailing lengthy simulations. In principle any macro portion of powder (e.g. a sphere of radius $R \gg FP$) is isotropic (if it is away from the phase boundaries), then atoms could be assumed to jump over with according macro-flights (δr = R) with the proviso that the movement inside this macro portion has been previously studied. If this could be done, atoms would move in bigger steps (R $\gg$ FP) and calculations would be abridged.

[26]Not to be mixed up with the slow time constant of the triple exponential fit.

The prior study to enable this variance reduction method consists in obtaining the escape-time-angle probability distribution functions. Atoms are initially tracked inside a huge number of powder spheres (as schemed in fig.3.6) where collisions to randomly oriented obstacles[27] take place after each FP and modify the ongoing atom with the cosine law probability distribution. The escaping time and angle (relative to initial velocity) from each macro-sphere are stored in a 2-D histogram from which delays and directions are sampled by applying the rejection method after performing bilinear interpolation.

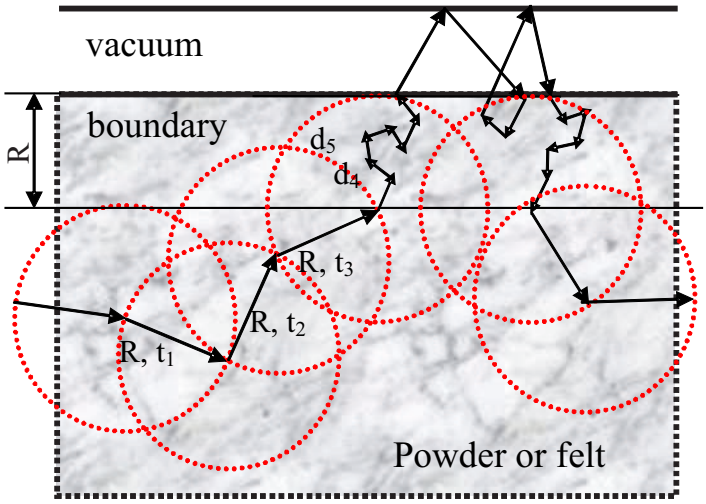

Figure 3.7: Accelerated and "real" path of the atoms deep inside a powder, in the vacuum and in the boundary area. Re-diffusion appears naturally in this model.

c. Boundary effects: Some remarks need to be made about the behavior of the atoms close to the powder free surface. Firstly, the macro-step reduction method shall not be used at distances lower than FP because the spheres would be truncated and the azimuthal isotropy would no longer hold. Secondly, re-diffusion into the powder, which arises naturally in this method,

[27] Sampled within the 2π erad, thus from tangential to full-frontal collisions.

usually means that the atoms penetrate a few Flight Paths into the powder until they are expelled by an “unlucky collision”.

If the powder is looser, meaning that the flight path is bigger, atoms effuse faster out of the powder, but when they re-diffuse in, the penetration depth is bigger and they are trapped for a longer time. Bearing in mind this effect, it cannot be fully discarded that an effusion curve corresponding to a packed powder could indeed be faster than one obtained from a target with loose structure.

d. Re-diffusion: In many a forum the question arises on whether re-diffusion takes place and how to quantify it. The MC code has no parameter-governed clause to control diffusion towards the target bulk. Such check is not needed because the MC effusion algorithm includes re-diffusion intrinsically. In fact, all atoms that bombard the target bulk interface re-diffuse in the target, at least to some extent. Some will just collide once and be expelled back to the vacuum, others will linger for some time close to the bounding interface and some others will deepen into the powder/felt. In fact, what happens is analogue to the case of foiled targets, where atoms can effuse back from the free volumes to the spacings between foils. In-grain re-diffusion is neglected in `RIBO`.

e. Fitting of parameters: This methodology should be applied to as well-documented experimental release data as available (e.g. release of ^{90}Kr from ISOLDE UC targets).

1. For a given sticking time, t_s, three trial FP, FP_1, FP_2, FP_3 are simulated.

2. Effusion for any intermediate flight path FP can be obtained by quadratical interpolation between the three effusion curves: E_{FP} = cint(E_1, E_2, E_3)

3. The effusion function E_{FP,t_s} is then convoluted with the diffusion profile, D_η, which corresponds to diffusion in spheres or fibers whose diffusion parameter (see section 2.5, page 25) is $\eta \Rightarrow E_{FP,t_s} \otimes D_\eta = R_{FP,t_s,\eta}$.

4. The process is repeated over until the point when the simulated release curve matches the experimental release, $R_{FP,t_s,\eta} \approx R_{exp}$. The quality of the result is judged mainly by the ability to reproduce the tail and the peak of the experimental release curve.

f. Visual fitting: The apparently cumbersome iterative optimization procedure just depicted can be accelerated by using some semi-empirical rules, which have been distilled from the use of the code in the cases presented in the coming chapters. Those (rules) are:

- Diffusion coefficient. It controls the position of the release peak and the slope of the release tail. A small diffusion coefficient will delay the release peak and will lower the (negative) slope of the release tail.

- Flight path: It governs the relative height of the release peak. Shorter flight paths, which refer to tighter structures, decrease the importance of the release peak. In looser targets, a bigger portion of the atoms have a good chance to leave the target material quickly and thus, to fly to the ion source populating the release peak. However, this effect is rather moderate: The *total* flight path in a loose target is only slightly

smaller than in denser materials. This is so due to the erratic character of the inter-grain diffusion; the atom makes larger expeditions in search of the open surface; $\Rightarrow$ each quest has a higher chance to find the free surface at the cost of a larger journey. Finally these opposed factors are mildly inclined to lower the flight path. This result is general in average terms as long as the path is strongly erratic. In the present thesis this path has some patterns (the cosine law is more focused than the isotropic reflection), which means that the favorable effect is even lower. Thus, for noble gases, the FP has little influence on the delay time. Moreover, noble gases often show poor diffusion properties so that the FP effect becomes negligible. This circumstance utterly hardens the fit of FP in noble gases[28]. For sticky elements, the FP has a great influence because the number of collisions is strongly proportional to the inverse of FP.

A good way to relate FP and porosity is through Clausius equation (eq.3.52):

$$FP = \frac{4V}{S} \tag{3.52}$$

It can then be concluded that FP influences the in-target dwell time mainly through the sticking time.

g. Some shortcuts to parameter fitting: The previous steps have shown a way to infer release parameters for many isotopes and target combinations. The method has been sketched for the highest complication level, where neither the geometry (FP) nor the diffusion or desorption parameters are known. Luckily, some relevant real cases offer advantageous shortcuts. This is

[28]This is most annoying because t_s is already known (= 0) so it would have been simpler to use noble-gas data as tool to find FP.

so for noble gases, where the sticking time is known ($t_s \rightarrow 0$) as well as for analytical geometries (the method is obviously valid in those simpler circumstances) for which no FP needs to be found, or for atom-matrix combinations where the diffusion constant is already measured. Landolt-Börnstein [59] provides an extensive database of diffusion coefficients.

h. Yield predictions: New diffusion and desorption data constitute a valuable source of information. Other applications are imaginable, but release parameters are here precisely used to infer the extracted fraction from future target setups. The new targets are sketched and described in an input file for the MC code. Simulations are run for FP, t_s and results are convoluted with D_η.

h. Remarks: The previous recipe attempts to solve systems with three unknowns, FP, t_s and η. It would be naive to expect that release from a complex target could be dictated by a compatible determined system. Real systems are just not like that. Sometimes no triplet (FP, t_s, η) is capable of overlapping the simulated and the experimental curves: in some cases two variables are confused in one, in other situations, or for some value ranges, some parameters seem to have little or no effect on the release curve. Help may be obtained by using the analytical model [53] to check results.

i. Results: Results of fits for various ISOLDE matrices are shown in A.7 (on page 23 at the annex sections.).

3.7 Conclusions.

- Specular reflection can only occur in the absence of marked condensation on the surface. If surface forces are not weak diffuse reflection will take place regardless of the surface finish. This point singularizes atomic transport with respect to light reflections, where, in turn, refraction can take place.

- Another necessary condition for specular reflection is that the matter wave length exceeds the apparent roughness. This justifies specular (diffractive) reflections at grazing angles and/or low energies.

- Mirror-like reflections speed up effusion,specially for straight geometries; improving the surface finish rises the extraction efficiency when atom and surface present no chemical affinity.

- When adsorption and/or roughness effects are relevant the cosine-law and thermalization hypothesis are adopted. These imply that atoms forget the incident velocity (direction and modulus), that emission favors normal (close to zero) angles and that the velocity follows the Maxwell-Boltzmann distribution, at the temperature of the substrate. According to comparison to measured and numerical values (Clausing conductances) the `RIBO` MC code can accurately reproduce the effusion under cosine-law reflections.

- The semi-classical model takes into account the crystalline structure of the walls. This model, implemented in the program, is a bit more complicated than the other two and usually tends to the cosine-law model.

- Other models exist, some are used in illumination science and could be imported for atomic transport under particular conditions.

- The interaction of atoms with residual gas has been introduced in the simulation code through statistical mechanics (to determine the free mean path) and with the hard-sphere model of collisions.

- Effusion in continuous media where knowledge of the exact geometry is limited to statistical parameters has been introduced in the code in a special module that uses three average parameters (flight path, diffusion parameter and sticking time). Variance reduction techniques based on the concept of macro paths are used.

- Besides the main goal of plotting and understanding release curves, the code can serve as tool to obtain the impedance of vacuum elements, or to infer the release parameters.

Chapter 4

Ionization and ionic transport.

Ionization [60, 61]...

- *"A process in which an atom or molecule loses or gains electrons, acquiring an electric charge or changing an existing charge."*
- *"1. The formation of or separation into ions by heat, electrical discharge, radiation, or chemical reaction. 2. The state of being ionized."*

★

ATOMS NEED TO BE IONIZED so that they can be accelerated and guided with electromagnetic fields. After diffusion and effusion, this is the third step covered by the `RIBO` Monte Carlo code. A fourth step, describing the motion of ions under electro-magnetic fields completes the picture provided by `RIBO` for the extraction efficiency of radioactive ion beams. This chapter frameworks the ionization process that takes place in some ion source types and describes the subsequent ionic transport or recombination. This shall open a way for future improvements of the ion sources.

4.1 Ion sources.

Atoms that have been released from the target or catcher surface ought to be rapidly transported to the ion source to be converted into singly or multiply charged ions, which will allow further electromagnetic guidance and acceleration. Despite the fact that the widespread use of heavy-ion beams in the accelerator context and in industry stimulates the development of an ample choice of ion-source types, most of them cannot cope with the so-called *performance criteria* [62] of the exotic feed material supplied by ISOL type facilities.

The central goal of this thesis is to optimize the efficiency of production of exotic beams. Up to now, most of the speech has been expressed in terms of a single factor in the overall efficiency: the release speed. This is a key term for rare atoms since it will determine the decay losses, but other contributions should not be overlooked as they may become critical too. Therefore, the quest of the layouts that will maximize the output of isotopes shall not be restricted to geometric considerations in target and transfer lines, but it should also assimilate the ionization efficiency.

Before loading a processor with simulation jobs, the performance criteria should be considered:

Ionization Efficiency ε_i: It is defined as the ratio of ions extracted from the source to the number of atoms fed into the source in absence of decay losses. By default, the ionization efficiency refers to singly charged ions. Although variable factors like the chemical affinity of the atoms may hinder the accurate determination of the ionization efficiency, measurements are mostly

precise for gases, which can be fed in continuously (and with a known composition of the support gas mixture), but they remain poorer for the rest of species.

Selectivity: Isotope mass separation can be complemented by previous chemical separation in the ion source. However, the *selectivity*, that is, the ability of a given source to lower the background contamination will generally affect negatively its *universality*, as these properties are generally antagonist. Besides, some ion sources have their ionization efficiency quenched by impurities, meaning that chemical selection should be preferably carried out in a transfer line between target and ion source. Nonetheless, the introduction of a transfer line will delay the effusive conduction[1].

Speed: It plays, as emphasized throughout the thesis, a key role for short-lived isotopes. Starting recommendations for a faster extraction are:

- Construction materials should have low chemical affinity with the atoms to be ionized in order to reduce desorption times.
- For high partial vapor pressures of the target material, high pumping speed out of the ion source exit is desirable.
- For surface ionizers the intrinsic delay time, in general terms, ought to be shortened. This can be achieved by reducing the ion source dimensions while increasing the outlet orifice and the wall temperatures. If the reduction is homomorphic, then the number of collisions will be conserved and so the ionization efficiency. Otherwise, it should be checked whether losses in the ionization efficiency overcompensate

[1]The demand of chemical selection often opposes the optimization of the ionization and of the release efficiency.

the gain in the decay loss factor. It should be remarked that for those ion sources where ionization takes place in the ion source *volume* (e.g. FEBIAD ion sources), a reduction of the intrinsic delay time may go parallel to a reduction of the ionization efficiency; an optimum configuration should be iteratively searched by use of the MC release code.

Emittance: The *emittance* and the *beam shape* express the angular divergence and distribution of ions in the beam. These parameters will be crucial for the transport efficiency up to the experiments. Thus, a high yield might be obtained at the expense of lower transport efficiency. This is just the case of FEBIAD ion sources, where it has been proved that ionization efficiency is inversely proportional to mass resolving power [63]. The present state of the art of the `RIBO` project includes ion transport and a first-stage emittance predictor. This concept is further explained in 4.8.

Energy spread: As for the dispersion in the direction of velocities (emittance) a beam with major spread in energies (that is, in speeds) is neither suitable for mass separation nor for some experiments, e.g., collinear laser spectroscopy has its resolution limited by the Doppler effect broadening that arises from the energy spread of the ion beam [64] (FEBIAD), [65, 66] (surface ion sources).

The general scheme of work recommended to deal with extraction and ionic production is:

1. In view of the chemical and atomic considerations, of the performance criteria, and of prior experience, an/several ion source(s) is/are chosen.

2. The geometry in the `RIBO` input file should be written so that the ion source module can be easily decoupled from the rest of the geometry.

3. The MC program can then be run for that particular ion source.[2]

4. Then, the ion source module can be replaced by a second candidate ion source and analogue new simulations should be carried out, and so on. Usually there will be a single candidate ion source.

4.2 Surface ion sources.

"Surface ionization takes place when an atom or molecule is ionized when it interacts with a solid surface. Ionization only occurs when the work function of the surface, the temperature of the surface, and the ionization energy of the atom or molecule have an appropriate relationship" [67].

4.2.1 Surface ionization.

Positive surface ion sources reach high efficiencies $(\sim 80\ \%)$ for elements whose ionization potential is low $(\leq 5eV)$, and they usually show a high selectivity since neighboring elements tend to have quite higher ionization potentials. Good ionizers withstand high temperatures; they have low vapor pressures and high work functions.

The MC `RIBO` code follows each particle in its erratic path of collisions to the walls of the system. For surface ionizers a function that describes the probability

[2] Some ion sources should be previously tuned or defined.

of ionization after each collision is needed. This function is straightforwardly the degree of ionization α[3], defined as [48, 68]:

$$\alpha_s = \frac{[X^+]}{[X^-]} = \frac{g_+}{g_0} \cdot \exp\left(\frac{\Phi - W_i}{kT}\right) \tag{4.1}$$

for positive surface ionization, and as:

$$\alpha_s = \frac{[X^-]}{[X^+]} = \frac{g_-}{g_0} \cdot \exp\left(\frac{A_E - \Phi}{kT}\right) \tag{4.2}$$

for negative surface ionization.

Where $g_\pm$, g_0 represent the statistical weights of the ionic states and of the atomic ground state (defined as $2 \cdot J + 1$ with J the quantic total angular momentum number). W_i and A_E correspond to the *ionization potential* and to the *electron affinity*, respectively. The surface has a *work function* ϕ and temperature T.

The `RIBO` MC package includes a database [48], *sion.dat*, with the parameters Z, Wi, Ae, g_0, g_+, g_- of the projectile (the effusing atom). The database starts with two comment lines and is followed by 101 lines that contain the mentioned parameters for an equivalent number of atoms. Editing and particularly enlarging this table is encouraged and will not alter the behavior of the program; the only restriction is to leave a zero at the last row as end mark. Analogously the substrate characteristics are stored in *workf.dat*, a table with two heading lines that precede a set of rows corresponding to SigmaZ for each compound, its work function and the *type of compound*. Zero stands for an element, 1 for a boride, 2 for a carbide, 3 for an oxide... More elements and categories can be introduced provided that a zero (0) is left as the end row.

The user may edit the database

[3]The exact function for the surface ionization probability is $\frac{\alpha_s}{1+\alpha_s}$, which tends to α_s since $\alpha_s \to 0$

The program *surfION* (see annex A.5) reads over the atom and surface databases and prompts the user to select an atom and a substrate. If a missing element were chosen or if the user explicitly wished to define a new element (by setting z=0) then the code would ask for the input electron properties and the statistical weights. Once the parameters defined, the surface temperature is set and *surfION* yields the degree of positive and/or negative surface ionization.

4.2.2 Electro-magnetic fields in surface ionisers.

A complete simulation of a surface ionizer should include the transport of ions under the electromagnetic fields. According to their origin, these fields can be classified as:

1. *Radial plasma field*: The ioniser is heated at about 2500 K, which enhances the release of electrons from the walls by thermal emission. In the interior of the cavity, the thermoions and the surface ionized atoms, effusing much more slowly than the electrons (square root mass factor) compensate the density of electrons, creating a neutral plasma inside a potential well of characteristic height U_p and radial thickness λ_{Debye}.

   Laser ionized species are born in the neutral zone. They feel the repulsion of the negative charge zone and thereby have lower chances to hit the walls and to recombine. Surface ionized species, however, are generated with the potential of the walls, which means that they have enough energy to reach the opposite wall and re-neutralize.

   Whatever the type of ionization, the trajectory of the ions is deflected, enlarging the axial path.

The height of the barrier U_p for a Ta substrate at temperature T = 2500 K corresponds to [48]:

$$U_p\ [V] = kT \cdot ln \frac{A^* T^2}{\frac{I_{total}}{S}\sqrt{\frac{M}{2\pi m_e}}} \simeq 2.26 + 0.43 \cdot ln\,(r[mm]) \qquad (4.3)$$

where

- U_p is the characteristic barrier.
- kT is the Maxwell-Boltzmann energy.
- A^* is the Richardson constant, $A^*(Ta) \simeq 120\ A\ cm^{-2}\ K^{-2}$.
- T is the absolute temperature of the substrate.
- I_{total} is the total feed temperature, $I_{total} \simeq 100\ nA$.
- S is the area of the extraction orifice, hence $S = \pi \cdot r^2$.
- M is the average mass, often dominated by medium nuclei, $M \simeq 100$.
- m_e is the mass of the electron.

2. *Extraction field*: Preliminary numerical calculations performed with SIMION [69] cast an extraction field that reaches a depth in the ioniser of the order of the diameter of the tube.

3. *Drift field due to electric heating:* A current of about $700\ A$ circulates through the ioniser tube, the resistivity of which is about $50\ \mu\Omega\ cm^{-1}$. The corresponding electric field, about $0.35\ V/m$, will be neglected due to its feeble intensity.

4. *Magnetic field:* According to the Biot-Savart law, the current through the target oven must induce a magnetic field in the ioniser. The magnetic field

lines will go around the target oven and will be vertical in the axis of the ioniser. This will give a certain transverse kick to the ions, pushing them to the walls and thus favoring recombination.

4.3 FEBIAD ion sources. Plasma ionization.

In a FEBIAD[4] ion source electrons emitted from a hot cathode are accelerated and focused through a grid at a certain potential and then they describe spiral trajectories in an ion chamber due to an axial magnetic field. The neutral atoms, which bounce randomly in the ion cell, will eventually interact with the electron stream and lose some electrons. Once the ions are formed, they will be extracted, accelerated and mass selected.

Fig.4.1 sketches the standard ISOLDE plasma ion source. This setup and some derived variations are further used for several calculations, with different fillings in the target oven (represented with a circular cross section).

4.3.1 Electron beam ionization.

The rate of reactions between two moving species is well studied in plasma and fusion theory:

$$R \cdot d\vec{x} = \int f_a f_e \sigma\left(\vec{v}_r\right) \cdot d\vec{v}_a d\vec{v}_e \tag{4.4}$$

Where $f_a \cdot d\vec{v}_a$, and $f_e \cdot d\vec{v}_e$ are the corresponding densities of atoms and electrons with speed comprised between $\vec{v}_a$, $\vec{v}_a + d\vec{v}_a$ and $\vec{v}_e$, $\vec{v}_e + d\vec{v}_e$,

[4]Forced Electron Beam Induced Arc Discharge [70].

respectively and $\sigma(\vec{v}_r)$ is the cross section for the reaction (ionization) between the two particles at the relative speed $\vec{v}_r$.

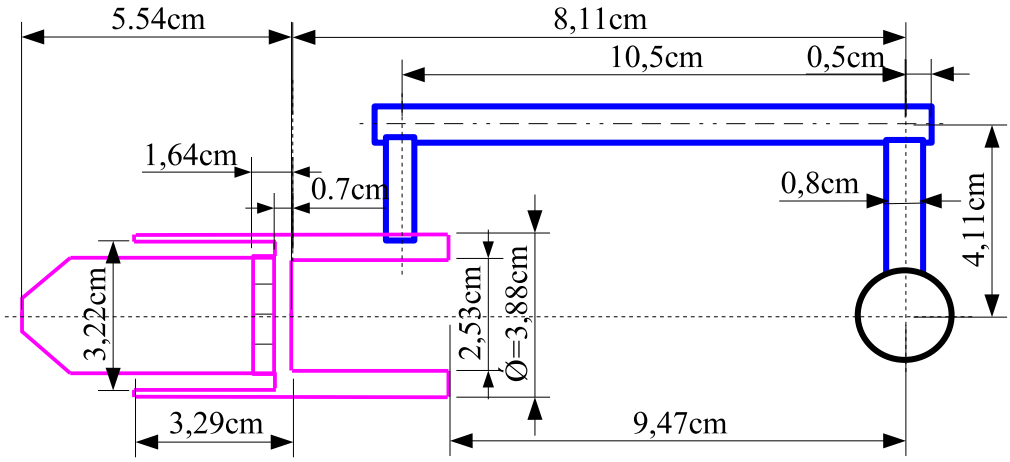

Figure 4.1: ISOLDE standard FEBIAD MK7 ion source and transfer line.

In order to deal with eq. 4.4 the following steps and assumptions are taken:

1. The speed of the electrons, although not fully known (the effective acceleration potential may vary between 50-100 V, and there exist other fields), is certainly much higher than that of the atoms (500-3000 m/s) so that the relative velocity is equalized to that of the electrons. Thus:

$$\vec{v}_r = \vec{v}_e - \vec{v}_a \cong \vec{v}_e \tag{4.5}$$

2. In addition, the *electron speed* is fixed at a single value even though it might show a certain spread[5].

$$R \cdot d\vec{x} = n_e \cdot n_a \cdot \sigma(\vec{v}_e) \cdot \vec{v}_e \cdot d\vec{x} \tag{4.6}$$

here n_e and n_a represent the densities of electrons and atoms.

[5]The plasma produces electromagnetic forces that modify the initial velocity of the electrons.

3. The ionization cross section can be read from several formulas, like the one provided by Lotz [71, 72]:

$$\sigma_i \approx A_i \cdot \frac{\ln\left(\frac{E_e}{E_i}\right)}{E_i \cdot E_e} \tag{4.7}$$

For a noble gas $A = 4 \cdot 10^{-13}\ cm^2\ eV^2$. E_i and E_e are the energies (eV) of the ion and of the electron, respectively[6]. `RIBO` includes a program, *plIon.f* that computes the n^{th} ionization cross section of a given element or compound for a certain electron beam energy. The electron beam plasma ionization cross section database used by *plION.f* is stored in *plION.dat*. This file contains cross sections [73] for single and multiple ionization for noble gases as well as for small molecules, hydrocarbons, oxygenates, silicon compounds, etc. and can be enlarged if the format is respected. Annex A.4 includes a printout with the elements of the database.

higher charge states could be simulated

4. The *density of electrons* may be expressed as the flux divided by the speed $n_e = \Phi / v_e$. The density of the atoms can be written as $n_a = dN_a/dV$ (N_a is the number of atoms in dV), whence:

$$R \cdot d\vec{x} = \Phi \cdot \sigma\left(\vec{v_e}\right) \cdot dN_a \tag{4.8}$$

5. Now, if this equation is applied to a single atom $(dN_a \equiv 1)$, then, the number of ions generated in the time interval *dt* should be interpreted as the *differential probability for ionization* (dp_I) in *dt*:

$$dp_I = \Phi_e \cdot \sigma\left(\vec{v_e}\right) \cdot dt \tag{4.9}$$

[6]The Lotz constant is $4.5 \cdot 10^{-14}\ cm^2\ eV^2$, then, taking into account the complete shell of the noble gas, with 8 electrons, the value $A = 4 \cdot 10^{-13}\ cm^2\ eV^2$ is recovered.

6. The *probability of survival* $p_s = (1-p_I)$ for a flight time of an atom between two wall collisions is:

$$\begin{aligned} p_s(t_r) &= (1 - \Phi_e \cdot \sigma(\vec{v}_e) \cdot dt_r)^N \\ N &= \tfrac{tr}{t_I} \rightarrow \infty \end{aligned} \tag{4.10}$$

where tr is the flight time between two consecutive collisions and t_I the mean time between two ionizations.

7. Evaluating the limit on this expression, the survival probability adopts the simple form:

$$p_s = exp(-\sigma(v_r) \cdot \Phi_e \cdot t_r) \tag{4.11}$$

and the ionization probability is:

$$p_I = 1 - exp(-\sigma(v_r) \cdot \Phi_e \cdot t_r) \tag{4.12}$$

8. In the MC code, *ionization times* are sampled by the inverse transform method:

$$t_I = -\tau_I \cdot \ln(r) \tag{4.13}$$

Where r is a uniform random number and:

$$\tau_I = (\sigma \cdot \Phi)^{-1} \tag{4.14}$$

is the *ionization time constant* of the system.

9. Finally, the MC code compares the ionization time with the flight time between two collisions, t_r. If $t_I \leq t_r$ then the particle is ionized, otherwise the atom bounces. In the next free flight, an ulterior check will be performed and so forth until the atom is ionized or exits the ion source.

10. If the atom leaves the ion source through the exit hole in neutral state then the ionization efficiency lowers. The ionization efficiency is computed by making the ratio of neutral to ionized currents.

4.3.2 Electromagnetic processes.

The $^{(1)}$deceleration of the electron beam in the ion plasma, the $^{(2)}$helicity effect on their trajectories produced by a solenoidal magnetic field, and the $^{(3)}$efficiency of extraction of the ions from the plasma constitute three key processes related to charged particle dynamics under electromagnetic fields. These fields can be computed with powerful numerical codes like MAFIA [74] or SIMION [69]. Once established a clear picture of the plasma and of the external fields, the `RIBO` code may be run with the `EMfield` module.

The present work could be pursued in that direction, as it was done for surface ionisers (4.2) although that should only make sense if the other effects of the same order of importance were also covered, for which a detailed study should be carried out. This is out of the scope of the present work. Instead, a different, simplifying approach is taken for this problem.

The second of the above mentioned effects enlarges the path of the electron through the plasma and it is optimized experimentally every time by tuning the magnetic field. As for the first and third effects, they arise from the interaction between charged particles, whose description requires knowing simultaneously the position of all of them. It should be recalled that the MC technique shoots

particle after particle and it records the results after collecting enough statistics. The order between particles is irrelevant ⇒ interactive effects cannot be included but through an average constant term[7]. The three effects have been reduced to two parameters, which have been fitted through an array of calculations with experimental results as reference data. The first parameter is the effective electron intensity through the plasma, determined by the cathode grid transparency and by the path enhancement due to the solenoid field. The second parameter is the average electron energy through the plasma. The effect of the extraction efficiency is somehow distributed between the two parameters. If N is size (number of histories) of a simulation, N_i the number of ions, then the ionization efficiency is steadily $\varepsilon_i = 100 \cdot N_i/N\ [\%]$.

The electron flux in ISOLDE MK7 FEBIAD ion sources was set to $4.6 \cdot 10^{16} \frac{e}{cm^2 s}$, corresponding to a current in the anode of about 18 mA. Table 4.1 summarizes simulations for this flux and for E_e = 40 and 100 eV.

E$[eV]$	**He**	**Ne**	**Ar**	**Kr**	**Xe**
100	0.115(25%)	0.43(9%)	2(14%)	4.44(9%)	7.64(9%)
40	0.24(13%)	0.16(15.4%)	2.73(9%)	4.27(9%)	7.22(9%)
experimental	0.14	0.36	2	4.3	11

Table 4.1: Experimental and simulated FEBIAD ionization efficiencies at 40 and 100 eV effective electron energies at $4.6 \cdot 10^{16} \frac{e}{s \cdot cm^2}$

4.4 Laser ion sources.

Laser ionization occurs when atoms under photonic bombardment of the right wavelength are progressively promoted to excited states until they reach a

[7]This methodology is widely used in physics, e.g., multi-electron atoms in Atomic Physics. In that case, though, the complexity that is averted has to do with solving the Schroedinger equation for many bodies.

continuum, unbound state. This method, highly selective but traditionally restricted to a few schemes[8], has not yet been included in the MC code although its implementation could be envisaged were the ionization schemes and the laser characteristics (including fluctuations) properly described and available in auxiliary data files.

The conceptual implementation (similar to that of electron bombardment ionization) shall start by defining the characteristic ionization half-life:

$$\tau_{12} = \frac{1}{\Phi \cdot \sigma_{12}(\lambda)} \tag{4.15}$$

Φ being the photon flux of wavelength λ and $\sigma_{12}(\lambda)$ the absorption cross section for atoms in the ground state. The remaining steps are analogous to those described for equation 4.14 (page 106) in section 4.3. For the same token, procedures that are more complicated could be mounted to match multi-photon excitation schemes (as shown in graph 4.2). For instance, for a two stage ionization process, upon first excitation the atom would be accordingly labeled ($I = 0 \rightarrow I := I + 1$). Then, comparing flight times with de-excitation and second-excitation characteristic periods, it would be decided if the atom returned to the original state (thus losing the excited label, $I := I - 1 \rightarrow I = 0$), if it stayed in the first exited state or if would be promoted to the final ionic state ($I := I + 1 \rightarrow I = I_f$). For the time being, a random number calibrated with the experimental laser efficiency can be used to decide whether an atom is ionized or not, and an average ionization location in the ionizer can be fitted to reproduce the experimental release curve. This is much simpler but it provides less information about the effects associated to a given laser beam.

[8]Nowadays many elements have been laser ionized.

4.5 ECR ion sources.

In an Electron Cyclotron Resonance Ion source (ECRIS) a solenoidal (axial) and a radial magnetic field define a minimum-B-structure, that is, a sort or ellipsoidal confinement region in the plasma where the magnetic field is lower. Electrons on the surface of the plasma, match their gyration cyclotron frequency to that of the injected microwaves and thus enter into a resonant mode. The energetic electrons eventually cross the plasma producing consequent ionizations and, eventually, they escape the magnetic trap and drag out ions to the extraction (the electric charge of the plasma tends to remain neutral). ECR ion sources are reliable, highly efficient and produce intense multi-charged beams of almost any element.

Simulation of all those processes (multi ionization also appears in 4.4) is complex and deals with some unknown or imprecise parameters (plasma shape, etc.). However, the whole process can be grossly fitted with a virtual elliptical cell (no real walls, therefore no bounces) where electrons produce ionizations with an unknown, yet tunable macroscopic ionization cross section, Σ_i[9].

4.6 Ionic transport.

In molecular flow, the interaction of atoms is negligible because the chance of atom-atom collisions is very low. Nevertheless, after ionization, Coulombian repulsive forces keep the atoms apart, modifying, deflecting their trajectories. Moreover, the ions see the external electromagnetic guidance fields (extraction, acceleration, focusing...). These effects may alter the predictions for the ionization efficiency: for instance, due to space charge effects, surface ionized

[9]The ionization probability is proportional to the traveled path in the plasma, Σ_i being the proportionality constant (it includes the effect of spinning), $dP_i = \Sigma \cdot dx$

ions may collide again with the walls and get neutralized; electron beams see different potential in plasma ion sources, depending on the sheath effects... A remarkable phenomenon related with the former effects is the *enhancement of ionization efficiency due to cavity effect*: the relatively high working temperatures of the ion sources induce thermal ionization, that is, electron emission. The (negative) space charge induced by the electron cloud helps to keep the (negative) ions away from the walls therefore lowering the number of re-neutralizations.

Computation of ion extraction shall not only help to understand the ionization conditions, but also it will assist in the prediction and optimization of the beam emittance and the arrangement of optical elements needed for an efficient transport of the beam.

Initially the `RIBO` release code assumed that, once ionized, particles were immediately extracted without major issues. This alone was specially misleading for surface ionisers, where the chance of recombinations is very high. For an integrated tracking of atoms from the radioactive target down to the experiment the coordinates and speeds of the ions should have been stored at the moment of ionization, and from the resulting files appropriate distribution functions could be created as input conditions for ion transport specific software[10].

However, a recent upgrade in the `RIBO` code has enabled the transport of ions under electromagnetic fields. This feature saves coupling issues, and allows quick swapping between the curved motion of ions and the straight trajectories of neutral particles appeared in recombination with the surface walls.

Details of the implementation of this regime and a few checks of the overall behavior are provided in the next subsections.

[10]Some of these programs [75], based on finite differences, are able to solve the Laplace, Poisson and Vlasov equations, to integrate the trajectories of ions in 3D Magnetic fields, including plasma boundaries, multiple charge distributions, etc.

4.6.1 Electromagnetic equation for point-like charges.

The motion of a *discrete* charge q moving with velocity $\vec{v}$ in a *constant*[11] electro-magnetic field $\{\vec{E}, \vec{B}\}$ can be expressed as:

$$\frac{d\vec{p}(t)}{dt} = q \cdot \left(\vec{E} + \vec{v} \times \vec{B}\right) \tag{4.16}$$

Above, $\vec{p}$ is the linear momentum, $p = \gamma m \vec{v}$ with m the rest mass. For ions at moderate temperatures (T = 2500 K fully belongs to this regime) *relativistic corrections are negligible* so that the factor γ is set as $\gamma = 1$.

If, in addition, radiation damping through cyclotron emission [76] is not taken into account[12], then 4.16 can be rewritten as:

$$\frac{d\vec{v}(t)}{dt} = \frac{q}{m} \cdot \left(\vec{E} + \vec{v} \times \vec{B}\right) = \frac{q}{m} \cdot \left(\vec{E} + [B]\,\vec{v}\right) \tag{4.17}$$

Where the effect of the magnetic induction $\{B_x, B_y, B_z\}$ in the velocity is expressed through the matrix $[B]$:

$$[B] = \begin{bmatrix} 0 & -B_z & B_y \\ B_z & 0 & -B_x \\ -B_y & B_x & 0 \end{bmatrix} = n_{ij} \tag{4.18}$$

[11] If the fields change with time other terms appear: $\vec{\nabla} \times \vec{E} = \frac{d\vec{B}}{dt}$

[12] This effect, which scales to the third power of the inverse mass, could be important for electrons, but it is deemed unimportant in ions, much heavier particles.

Let us now assume that $\bar{B}$ and $\vec{E}$ are constant in a given environment r_ε of the present coordinates x, y, z. Then, 4.17 corresponds to a second order linear differential equation system:

$$\frac{d\vec{v}(t)}{dt} + [P]\,\vec{v} = \vec{Q} \tag{4.19}$$

with:

- $[P] = \frac{q}{m}\,[B]$
- $\vec{Q} = \frac{q}{m}\vec{E}$

Eq. 4.19 is solvable, the solution for the boundary conditions $\vec{v}(t=0) = \bar{v}_0$ being:

$$\frac{d\vec{v}(t)}{dt} = exp\left(-\int_0^t [P]\cdot d\tau\right)\cdot\int_0^t exp\left(\int_0^\tau [P]\cdot d\tau'\right)\vec{Q}\cdot d\tau + exp\left(\int_0^t [P]\cdot d\tau\right)\cdot\vec{v}_0 \tag{4.20}$$

The terms of 4.20 may be computed but the general expression is slightly cumbersome and thereby not optimal for fast computation. Instead, matricial exponential functions can be developed with Taylor polynomial series ($[I]_3$ is the identity matrix):

$$exp\left(-\int_0^t v\cdot d\tau\right) = [I]_3 - [P]\cdot t + \frac{1}{2}\cdot[P]^2\cdot t^2 + ... \tag{4.21}$$

Now, coming again to the homogeneity of $\vec{B}$ and $\vec{E}$ within a radius r_ε around the present coordinates x, y, z, for time intervals compatible with this asset

($|\bar{v}|\cdot\delta t \leq r_\varepsilon$), the differential equation 4.20 can be discretized. This, combined with the development in power series casts:

$$\vec{v}(\kappa) = \vec{v}_0 + \left(\vec{E} + [B]\,\vec{v}_0\right)\cdot\kappa + \frac{1}{2}\cdot[B]\cdot\left(3\vec{E} + [B]\,\vec{v}_0\right)\cdot\kappa^2 + \frac{1}{6}\cdot[B]^2\left(7\vec{E} + [B]\,\vec{v}_0\right)\cdot\kappa^3 + \ldots \tag{4.22}$$

where $\kappa = \frac{q\cdot\delta t}{m}$

Whence, for a starting position $\vec{r}(t=0) = \vec{r}_0 = \{x, y, z\}$ in the time step number n, the starting position at $n+1$ will be:

$$\vec{r}(\kappa) = \vec{r}_0 + \vec{v}_0 \cdot \delta t + \frac{1}{2}\cdot\left(\vec{E} + [B]\,\vec{v}_0\right)\cdot\kappa\cdot\delta t + \ldots \tag{4.23}$$

Equations 4.22 and 4.23 provide the solution for a discretized track of a particle, where, in each step n, the MC code consults $\vec{B}\{x, y, z\}_n$ and $\vec{E}\{x, y, z\}_n$ and from $\{\vec{v}, \vec{x}\}_n$ it computes $\{\vec{v}, \vec{x}\}_{n+1}$. This method will be more or less precise, more or less stable, and less or more quick depending on the time step δt_n.

4.6.2 Time-step for the emulation of the electromagnetic drift.

The ratio of the norms of any two consecutive terms in the series 4.22 is of the order of $B\cdot\kappa$. Since B is given by the problem, for large values of $kappa$ many terms of the series will be required for a precise path, meaning that the code will do less steps but each step will consume more CPU time. The opposite token is also true, if κ is small enough, a few terms will be enough to describe a correct trajectory, but the overall number of steps will be high and thus the total CPU time. The optimum solution is CPU, problem and OS-platform dependent. The `RIBO` code allows defining a threshold tol_1 that acts in the following way:

$$\kappa = \frac{tol_1}{B} \Rightarrow \delta t = 3.76 \cdot 10^4 \cdot \frac{tol_1 \cdot A}{B} \tag{4.24}$$

A is the massic number and $q = |e^{-1}|$. A tolerance of $tol_1 = 0.05 - 0.01$ has proved a correct behavior, but other values are not excluded.

If the magnetic or electric field show strong gradients, then, as underlined in the previous subsection, the time steps have to be moderate enough so that the space dependence can be accommodated to the trajectory. From the time step obtained above, the MC code computes the coordinates r_{n+1} and then it checks whether the relative variation of $\vec{B}$ is acceptably small or not:

$$\frac{|\vec{B}(\vec{r}_{n+1}) - \vec{B}(\vec{r}_n)|}{0.5 \cdot |\vec{B}(\vec{r}_{n+1}) + \vec{B}(\vec{r}_n)|} < tol_2 \tag{4.25}$$

If the test is not passed, the time step is adjusted proportionally to the surpass ratio. The same principle is applied for the electric field.

Finally, the code needs to verify if the resulting space-step is “considerably smaller” than the typical dimensions of the geometry (in order to see the walls ’on time’, etc.).

$$|\vec{v}| \cdot \delta t < tol_3 \tag{4.26}$$

To start with, equal values for tol_1, tol_2, tol_3, may be taken, but for specially conflictive cases, the user can customize them.

4.6.3 Recombination.

If the trajectory of the ion intercepts a wall then it will collect an electron from the surface and become neutral[13]. After recombination, the atom will again move in straight lines, unaltered by the electromagnetic fields up to next ionization.

4.7 Neutral and ionized currents.

Simulations can be carried out to obtain the extraction profile of atoms (neutral current) or ions. Even when ionization is considered, if the ionization efficiency is low, it may be useful to merge the neutral and charged currents into the release curve as a means to preserve statistics. Doing so does rarely introduce visible systematic errors in the release function because the two currents have very similar time distributions. This can be done in two different ways:

- If a particle hits the outlet orifice the particle counter is increased $N := N + 1$ and the ionization counter is kept $Ni := Ni$. If, in turn, the particle is ionized $N := N + 1$ and $Ni := Ni + 1$. Nevertheless, in both cases the extraction times are used to plot the release curve[14]. The ionization efficiency will obviously be $\varepsilon_i = Ni/N$.

- An equivalent way to proceed is to impose ionization as necessary end condition i.e. neutral atoms hitting the escape orifice will actually be reflected. Each forced collision will increase a virtual history counter $(Nv := Nv+1)$. At the end, the number of ionized particles will be precisely the number of stories $Ni = N$ and the ionization efficiency will be obtained as $\eta_i = Ni/Nv = N/Nv$,

[13] Unless surface ionization to a higher charge state took place

[14] The exact solution would only consider the extraction times from the ionized particles.

The RIBO code output includes a mark on exiting particles so that escape times can be classified according to the ionic state of the atom. In this way, the shapes of the neutral and ionized currents can be compared, and it can be decided whether they can be merged or not. In addition, it is possible to see what the effect is of the ionization on the release speed.

4.8 Beam transport efficiency.

The optimization of the radioactive ion beam ought to be contemplated with a global perspective, including the efficiencies of all the loss processes that take place between the production and the delivery to the experiments. One of these phases is the beam transport from the ion source to the experimental area, generally assumed as the accelerator operator duty. However, target and ion source developments cannot disregard the beam shape of the produced beam since that may diminish the transport efficiency. The link between targetry and accelerator physics can be identified in the beam *emittance* concept.

The emittance is a figure that measures the $velocity \times momentum$ phase space volume, which expresses the spread of the beam spot. In the transverse plane (i.e. transverse to the direction $\hat{z}$), if the two perpendicular directions u_i (i.e. $\hat{x}$, $\hat{y}$) are decoupled, then the emittance in each of these directions, ϵ_i is [77]:

$$\epsilon_i = \frac{1}{\pi} \cdot \int di \cdot di\prime \tag{4.27}$$

With $di\prime$ the angle formed by the projection of the speed in the perpendicular direction u_i and the extraction axis, and di the distance from the i-axis position and the axis.

The `RIBO` MC code contains a function (*emittance*) that computes the average emittance in two planes transverse to the extraction vector and the emittance maps. The next chapter makes use of this concept to investigate the consequences of changes of the geometry of the surface ioniser (consult graph 5.1.1, and table 5.4).

4.9 Conclusions.

- The ionization efficiency is one of the factors of the final yield of isotopes, often more critical than decay losses.

- The optimization of the ionization efficiency is constrained by the performance criteria; selectivity and ion source endurance. Moreover, since atoms are ionized during their free flights or at the collisions to the walls, ionization is strongly coupled to effusion: Ionization abridges effusion paths and effusion bounds the chances of ionization. The two processes are therefore integrated into the same simulation code.

- The present state of the implementation of ionization is:

    1. Electron impact ionization in FEBIAD chambers is included in the MC code, which uses a database (**plion.dat**) containing cross-sections. After tuning a single parameter that contains the uncertainties of the fields inside the plasma, simulated ionization efficiencies match typical experimental values.

    2. Surface ionization allows a smooth integration in the code, which consults two databases (**sion.dat** and **workf.dat**). Simulated ionization efficiencies agree with measurements values.

3. Laser ionization has been sketched and could be implemented relatively easily.

4. Electric and magnetic fields can be defined. Ions will be accelerated accordingly and shall as well recombine upon eventual collisions with the walls.

5. The average emittances and the emittance ellipses in the transverse plane can be obtained through `RIBO>emittance`.

- The extraction and the ionization processes often imply collective effects between the charges. Due to its sequential nature, the MC code cannot account for the interactions between the simulated particles unless they are computed as an external average distorting effect.

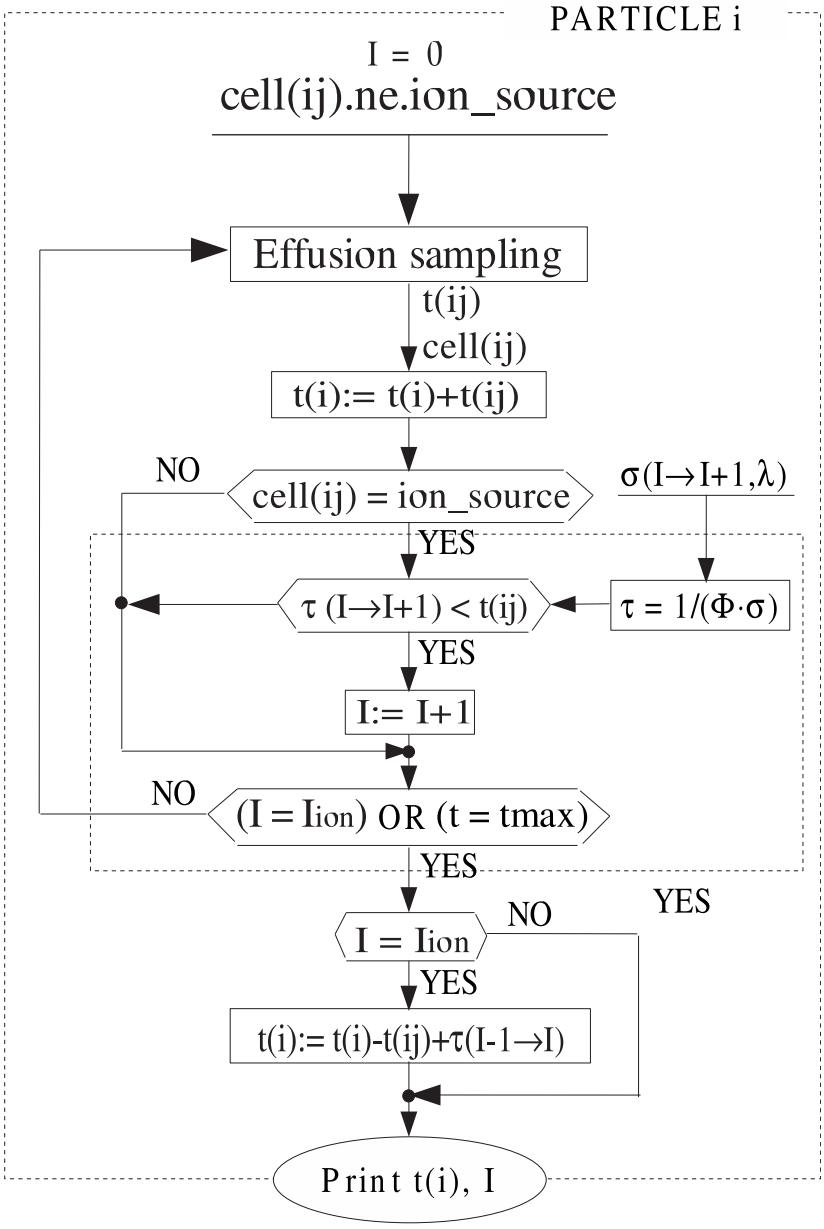

Figure 4.2: Schematic project to introduce multi-step single laser ionization into the Monte Carlo code.

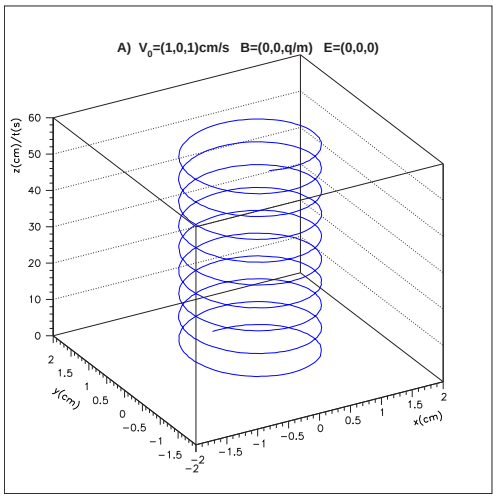

(a) B_z, $E = 0$.

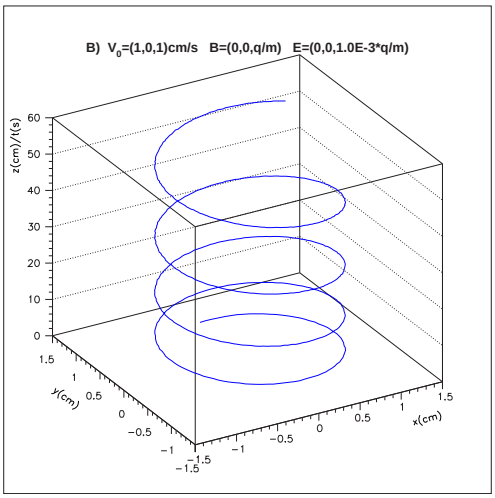

(b) B_z, E_z.

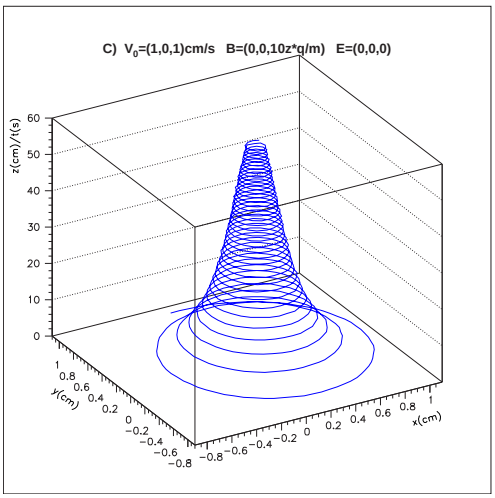

(c) $B_z(z)$, $E = 0$.

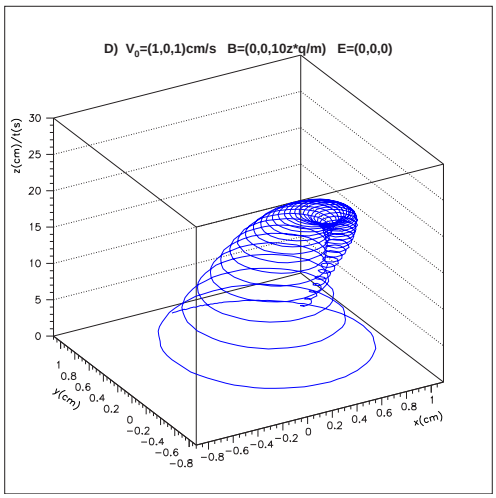

(d) $B_z(z)$, E_x.

Figure 4.3: Calculated trajectories of an ion submitted to constant electric and magnetic fields.

Part II

Applications to outstanding physics cases

Chapter 5

Release of Li and Be. Planar foiled targets.

As anticipated in ch.1 (eq.1.1), the intensity of a given radioactive beam ($I\left({}^{A}_{z}X^{+}\right)$) can be expressed as the product of the intensity of a primary beam of flux Φ (protons, neutrons, heavy ions...) and the corresponding efficiencies of generation (cross section of production), extraction (rapidity to diffuse and effuse before disappearance by decay, explained in ch. 2 and 3) and ionization (ch. 4).

The previous chapters - and the thesis in general - are devoted to the maximization of $I\left({}^{A}_{z}X^{+}\right)$ through the optimization of the extraction efficiency (ch. 2, ch. 3) and of the ionization efficiency (ch. 4 and the present chapter). An alternative way to raise the final beam intensity would be to proportionally increase the primary beam intensity. In fact, diffusion could then be even enhanced by the higher radiation rate thereby introducing an amplification factor (breaking proportionality) on the final yield. However, this promising path implies high power depositions and therefore it could eventually compromise the

structural strength of the target, softening, sintering or deforming it, and thus possibly reducing the extraction efficiency.

This chapter collects and operates on some of the information of the Radioactive Ion Beam Test (RIST) project [78, 79]. The RIST project intended to develop a high power ISOL target in an effort to conciliate high heat dissipation (focused on heat radiation at high temperatures) with acceptable extraction properties. The solution, still far from the MW of the neutron sources, was designed to evacuate 25-30 kW of heat while keeping fast diffusion and effusion in thin (25 μm) Ta foiled and hollowed discs set in a tube. The potential of Ta foil structures has also been tested in the low power region, with extreme extraction efficient layouts, in the so-called RIST-ISOLDE targets.

high power: RIST

low power: RIST-ISOLDE

Moreover, considerations are made about how to minimize the decay losses without a dramatic drop of the ionization efficiency, while keeping a decent beam emittance.[1]

5.1 Li beams from RIST-ISOLDE and RIST.

Dedicated measurements of the above mentioned factors as well as of the ionization efficiencies should, in conjunction with the use of `RIBO`, shine some light on the phenomena that hinder the extraction efficiency.

The probe target, known as *"Ta129"*[2] [80] (fig.5.1), is made of 200 15-cm-long 1-cm-high parallel dimpled stripes of Ta with a thickness of 2 μm. The temperatures in the target and ionizer are kept at 2410 K and 2500 K. The proton beam impinges directly onto the target with a Gaussian spread of 0.7 cm. ^{11}Li

[1] In practice, the extraction and the emittance are globally optimized by adjusting the pressure of the support gas.

[2] Also called RIST-ISOLDE target.

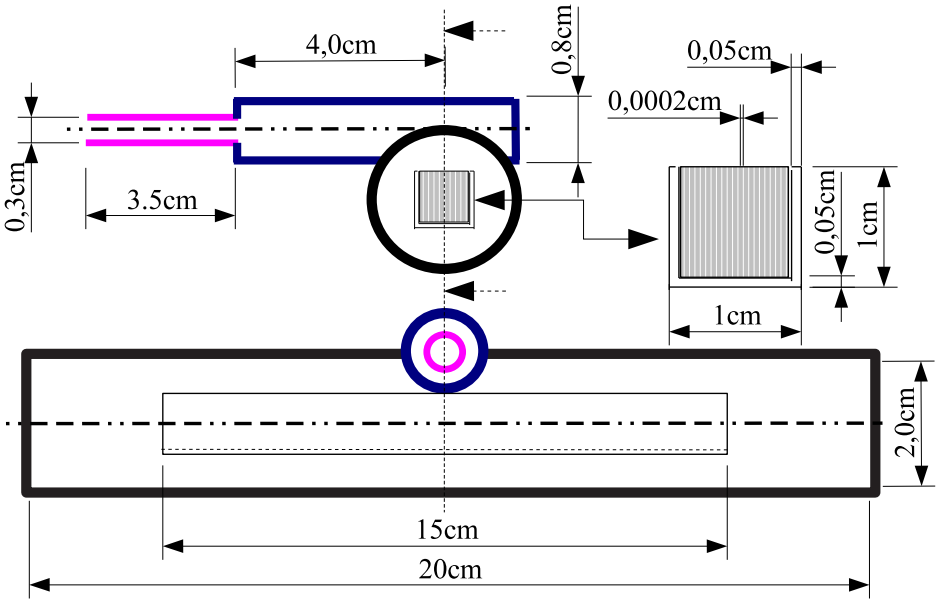

Figure 5.1: Schematic layout of a RIST-ISOLDE prototype target.

ions, of utter interest as halo nuclei [81, 82], are produced by surface ionization on the final W cylinder. Surface ionization is activated interactively at runtime by selecting the option *ionsou=3*. Then, by executing the routine *surfION* the degree of ionization is obtained:

```
'.-------------------------------------------------'
'|                                                 |'
'|   SSSS  U   U  RRR   FFFF  II   OOOO   N   N   |'
'|  S      U   U  R  R  F     II  OO  OO  NN  N   |'
'|   SSS   U   U  RRRP  FFF   II  O    O  N N N   |'
'|      S  UU UU  R R   F     II  OO  OO  N  NN   |'
'|  SSSS    UUU   R  R  F     II   OOOO   N   N   |'
'|-------------------------------------------------|'
''

Nmax1, Nmax2= 102 27
atom:
element (Z)? (0 if you want to define parameters)
```

```
  3
substrate:
element (Z)? (0 if you want to define parameters)
  74
0:element; 1:Boride; 2:Carbide; 3:Oxide;4:CeCompounds
  0
gplus,gzero,gminus,Wf,Wi,Ae
1.  2.  1.  4.54  5.39  0.62
T?[K]
  2500
positive surface ionization
alphaS=  0.00966894758
negative surface ionization
alphaS=  6.25593804E-09
betaS=  0.00957635431
```

betaS is the highest value between the negative and the positive ionization probabilities. In this example, $Pion$ is $9.5 \cdot 10^{-3}$ and the simulation is run with the geometry described above (5.1).

This section presents the methodology and particularities of the coupled study of effusion loss processes, ionization efficiency and beam shaping. Absolute extraction values depend on accurate measurements of the desorption enthalpies, plasma and extraction fields, among others. Dedicated measurements of those factors as well as of the ionization efficiencies should, in conjunction with the use of `RIBO`, throw some light on the phenomena that hinder the extraction efficiency. As for the release function, the sticking time has to be determined and then the resulting effusion distribution needs to be convoluted to the diffusion function. The sticking time of Li in Ta is estimated by the Eichler systematics (see 3.3.1, page 70) to be $t_s = 10^{-9}s$. The diffusion coefficient can in turn be

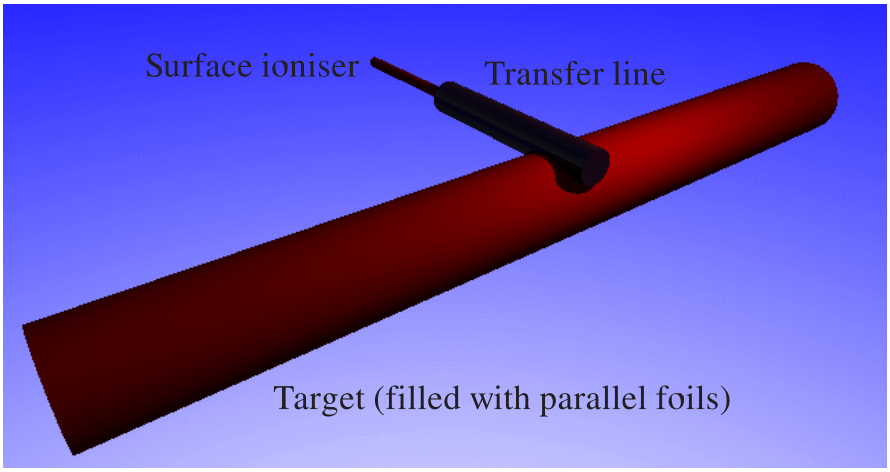

Figure 5.2: Ray trace image of the "Ta-129" target, generated with `3D-RIBO` and Povray.

fitted through the analytical model [53], leading to D(^{8}Li, Ta, 2423 K) $\in$ (0.9-2)$\cdot 10^{-8}\frac{cm^2}{s}$.

The release fraction associated to the experimental data is obtained by weighting the experimental 3-exponential[3] fitted curve [52] (t_r = 10, t_f = 160, t_s = 6300 ms, α = 1) with a given decay exponential fraction corresponding to the radioactive decay law:

$$\varepsilon_R = \lim_{\tau\to\infty} \frac{\int_0^\tau (3-exp-function)\cdot \exp(-t\cdot \ln(2)/T_{1/2})\cdot dt}{\int_0^\tau (3-exp-function)\cdot dt} \tag{5.1}$$

The release fraction of the simulated data is computed with the program *analyze*, which reads the effusion profiles (number of collisions and flight times) and gets the release fraction for any given (η, t_s, A) triplet. Since this method departs from all the individual components of the delay function (unlike the experimental

[3] A function that contains an exponential factor for the fast rise and a linear combination of a fast and a slow decaying exponential, as was shown in eq. 3.48

curve where effusion, sticking and diffusion are already convoluted), it can additionally include the mass correction on the effusion profile[4].

To conclude the definition of the preliminary scenario, it should be noted that the pulsed nature of the ISOL proton beam is indicted to induce a thermal shock wave in the target with considerable impact on the diffusion process and thus on the release function.

5.1.1 Optimization of the ionizer shape.

The following sections will provide some hints about the trends that shall lead to an optimum target and ion source ensemble for the RIST-ISOLDE targets. Then, the RIST target will be presented as an alternative to high power beams. Atoms may lose electrons in the collisions with the ioniser walls. The ionized atoms will then move affected by the plasma and, eventually, by the extraction fields[5]. Most of the times, they will collide with the walls and recombine. In further collisions, the atoms will be ionized once again, and so forth. Eventually, in the successful cases, they will exit the tube as ions, with a certain angle with respect to the axis and at a given distance from it. These last values, assembled in a single parameter for each plane (horizontal and vertical), called emittance (more information in 4.8 and 4.1 on pages 117 and 96), describe the divergence of the beam, which is a measure of its quality and, therefore, of the future source-to-experiment transport efficiency. In general terms, a low aperture of the ioniser improves the emittance.

In addition to the emittance, the decay losses and the ionization efficiency are too determined by the diameter and the length of the ioniser. When ionizers are long

[4] It corrects the (pure, no sticking) effusion component as $\sqrt{M}$.

[5] A more detailed description of these fields in surface ionisers was carried out in 4.2.1

and narrow (low aspect ratio), the effusing atoms see a tiny conductance; the release is then slowed down and the corresponding extraction efficiency is low for the most short-lived isotopes. As counterpart, to what concerns ionization, low aspect-ratio ionisers may be more efficient. In such structures, since the average view factor of the extraction orifice is poor, the fact that an atom exits the tube in ionized state depends strongly on the last fraction of the ioniser, which is precisely where the extraction potential is stronger.

The presence of these antagonist effects gives room to the optimization of the ioniser shape. Moreover, the decay loss factor implies that results will be isotope dependent. In order to study all these phenomena, a set of simulations has been run for diameters and a lengths of the W ionizer of 2.33, **3.5** and 4.66 mm, and 2.0, **3.0** and 4.0 cm, respectively, and for different Li isotopes.

Before going to the highest level of complexity, it may be interesting to study the ideal case of an infinitely strong extraction field all over the ioniser. The optimum geometry in this scenario will serve as an upper-bound for the extraction efficiency.

Optimization of the ionization with ideal extraction.

In FEBIAD ion sources, the ionization efficiency increases monotonously with the *impedance*[6]; longer effusion dwell times imply higher chances to have particles ionized so the optimum ionizer shape is the one which best negotiates the compromise between effusion losses and ionization gains. In the case of surface ionisers with ideal strong fields covering the whole surface ioniser, what should be maximized is the number of collisions to the surfaces and not necessarily the effusion times. In fact, considering the ionizer as an independent

[6]Defined as the inverse of the vacuum transport conductance. Definitions are formalized in sec 3.4, (page 78).

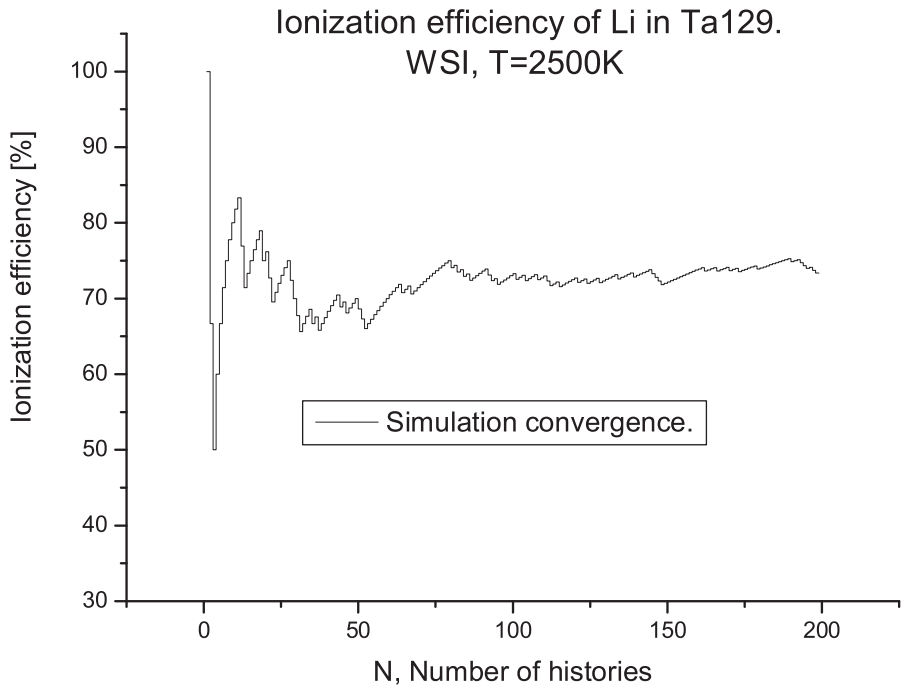

Figure 5.3: Convergence of the simulated ionization efficiency.

entity, decay losses could be lowered at no ionization efficiency cost with a simple scale reduction of the source dimensions, of index $\lambda < 1$. However, if the ensemble target+ion source were considered, no immediate conclusion about the benefits of an ion source scale reduction strategy could be reached. This would be so because the conductance from target to ionizer would be reduced as λ^2 (shrinkage of the connecting orifice), meaning that the improvement in the ionization efficiency might indeed entail some global extraction losses (due to a poorer effusion). The principles set, the way is now open for optimization by use of the tools provided by `RIBO`. Let us now try to seek the best diameter and length for an hypothetic ISOLDE surface ionizer at infinite overall extraction

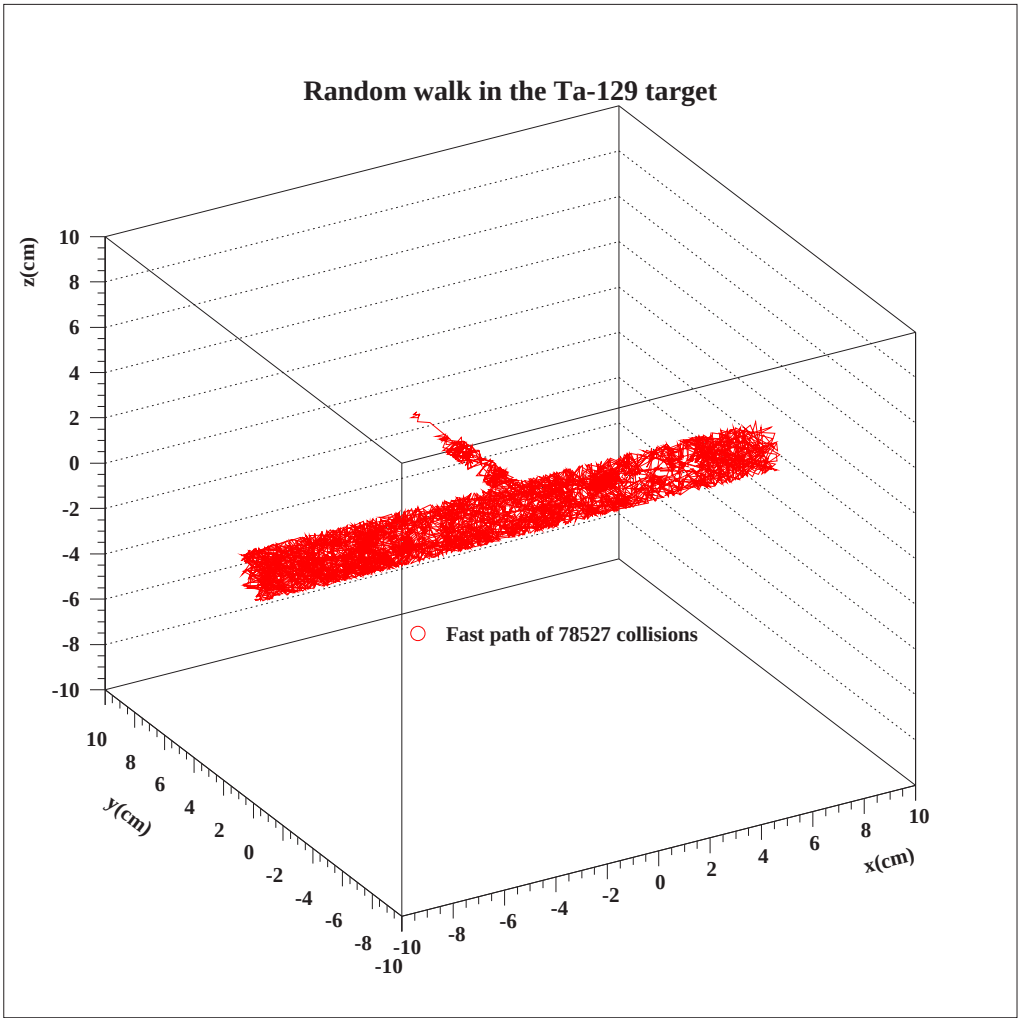

Figure 5.4: Trace of a trajectory inside the RIST-ISOLDE target. The atom escaped as neutral after 78527 collisions. The script *RATE* was used for this purpose.

field. With two design variables, if we take four test values for each of them[7], then the array of results grows up to 16 cells (simulations). In order to keep the global computing time moderate, the ionization efficiency for the reference case (length = 3.5 cm, diameter = 3 mm) is plotted as a function of the number of simulations (`RIBO` has a print mode for average figure analysis) and it is seen how even 300 particles could be sufficient to attain the ionization efficiency

[7]Simulations without ion transport are faster so a bigger mesh can be taken.

within 2 % (fig.5.3). Finally, simulations are run for 4000 particles each. Results for the ionization efficiency are shown in table 5.1. Those numbers are then multiplied by the corresponding extraction efficiencies obtained by running the MC `RIBO` code with surface ionization, effusion and adsorption/desorption for an empty target (the same target oven, transfer line and ionizer but without the thin slabs, in order to speed up simulations). The final values are tabulated for several Li isotopes in table 5.2. For long-lived isotopes, the dominant term is the

$\varepsilon_i(L[cm], r[mm])\,\%$	$r_1 = 1.0$	$r_2 = 1.5$	$r_3 = 2.0$	$r_4 = 2.5$
$L_1 = 2.5$	90.85	76.78	62.23	50.13
$L_2 = 3.5$	91.43	**76.10**	61.08	50.13
$L_3 = 4.5$	91.50	76.63	61.60	50.10
$L_4 = 5.5$	90.75	76.40	60.70	49.30

Table 5.1: Upper Li ionization efficiency $\varepsilon_i[\%]$ for different r[mm]/L[cm] W ionizer configurations at an infinite extraction field (reference case is **bold**).

ionization efficiency (ε_i), implicating that the optimal configuration will have a low aspect ratio (r/L), which enhances ionization at the expense of effusion. For short-lived species, release is mainly dictated by the effusion speed[8] so that looser structures are needed (high aspect ratio of the ioniser). For intermediate cases, the maximum yield is reached as a compromise between effusion and ionization. These tendencies are confirmed in table 5.2, which provides hints for the less intuitive intermediate cases. Thus, ^{6}Li and ^{8}Li production could be increased around 30-40 $\%$ with a smaller ioniser tube radius while ^{9}Li looks optimally produced with the present ioniser shape and ^{11}Li beams shall increase by 10 $\%$ with slightly longer and less tight tubes. Now, moving to more realistic fields, let us see what is the importance of recombination and whether the electric fields can compensate for re-neutralization losses.

[8] As well as by diffusion, but this is a constant term in this analysis.

	r_{1-4}	1.0	1.5	2.0	2.5	r_{1-4}	1.0	1.5	2.0	2.5
$L_1 = 2.5$		1.41	1.02	0.67	0.44		1.32	1.02	0.69	0.45
$L_2 = 3.5$	^{6}Li	1.43	**74.5**	0.65	0.44	^{8}Li	1.34	**63.8**	0.66	0.45
$L_3 = 4.5$	7500	1.43	1.01	0.66	0.44	840	1.34	1.01	0.67	0.45
$L_3 = 5.5$		1.41	1.01	0.64	0.42		1.32	1.01	0.65	0.44
	r_{1-4}	1.0	1.5	2.0	2.5	r_{1-4}	1.0	1.5	2.0	2.5
$L_1 = 2.5$		1.09	1.01	0.75	0.51		0.70	1.06	1.13	0.99
$L_2 = 3.5$	^{9}Li	1.12	**41.1**	0.71	0.51	^{11}Li	0.74	**2.18**	0.97	0.98
$L_3 = 4.5$	178	1.10	1.02	0.73	0.51	8.5	0.71	1.04	1.06	1.01
$L_3 = 5.5$		1.08	1.01	0.71	0.50		0.69	1.04	1.05	0.98

Table 5.2: Relative yield Y(r[mm]/L[cm])/Y(1.5/3.5) of Li isotopes including decay and ionization factors. The cell Y(3.5/3) of each box expresses the absolute extraction efficiency $\varepsilon_R \cdot \varepsilon_i[\%]$ for the standard ionizer shape, D/L=0.3/3.5 and sticking time $t_s = 2 \cdot 10^{-9} s$. These values correspond to immediate extraction without recombination.

Optimization of the ionization under realistic fields.

Coming again to the statements of the beginning of this section, the extraction, ionization and emittance were computed for several aspect ratios with a plasma sheath potential (focusing field) and an extraction field (axial accelerating field) like the ones introduced in section 4.2.1 on page 99. Results are shown in table 5.3. As for the first component, equation 4.3 includes the cavity size dependency[9], and the second field is scaled so that the depth-to-radius ratio is always constant.

Upon ionizations, particles are tracked following the curved trajectories induced by the deflection, they recombine when they collide with the surface, and, if they exit the tube in ionic state, their position and velocity divergence for each perpendicular plane (to the extraction axis) are stored in the *emit.map* file. The ionization efficiency, the charge state and the extraction time are printed, as usual, in the output file. Comparison between table 5.1 and 5.3 illustrates how deeply the ionization efficiency is hindered by recombination. This fact justifies

[9]The potential barrier grows as $log\,(R_{cavity})$.

$\varepsilon_i(L[cm], r[mm])\,\%$	$r_1 = 1.0$	$r_2 = 1.5$	$r_4 = 2.0$
$L_1 = 2.33$	5.0($\pm$8.1%)	4.3($\pm$5.3%)	4.5($\pm$10.3%)
$L_2 = 3.5$	4.3($\pm$5.3%)	**5.0($\pm$7.9%)**	1.95($\pm$11.2%)
$L_3 = 5.25$	0.375($\pm$25.8%)	0.575($\pm$14.7%)	0.638($\pm$13.9%)

Table 5.3: Li ionization efficiency $\varepsilon_i[\%]$ ($\pm$relative error %) for different r[mm]/L[cm] W ionizer configurations at typical extraction and plasma fields (reference case is **bold**).

the presence of the extraction potential. In fact, a simulation of the ionization efficiency without an extraction field casts a result of 2.1 ± 0.2 %, which means that the 30 kV extraction system multiplies by a factor 2.5 the beam intensity.

The cylindrical symmetry of the geometry of the ioniser and of its fields is presumed from the sketch of fig.5.1 and it is veryfied in the optics, as shown in fig.5.1.1. Moreover, the emittance ellipse maps at the outlet of two surface ionizers of different aspect ratio indicates the gain of beam quality associated to more closed cavities. To support this statement, table 5.4 displays the average[10] emittances ($[mm\ mrad]$) as a function of the ioniser shape. Finally, the decay

$\varepsilon_i(L[cm], r[mm])\,\%$	$r_1 = 1.0$	$r_2 = 1.5$	$r_4 = 2.0$
$L_1 = 2.33$	-0.71	-0.80	-2E-3
$L_2 = 3.5$	-0.82	**-0.70**	1.1E-3
$L_3 = 5.25$	8E-4	-3.3E-3	-3.6E-3

Table 5.4: Average emittances ($[mm\ mrad]$) of Li at the extraction of surface ionisers under typical electric fields (reference case is **bold**). Note that a focused beam has a negative emittance of high absolute value

losses were computed applying the decay law for each isotope to the computed time profiles, and the efficiencies thereby obtained were multiplied by the ionization efficiencies. Results of the global efficiency ($extraction \times ionization$) are displayed in table 5.5. If, for a given accelerator optic, the beam transport efficiency could be expressed as a function of the

[10] Averaged over N particles and on the two transverse planes.

values of emittance tabulated above, then, a global figure of merit including decay, ionization and beam shaping could be established.

	r_{1-3}	1.0	1.5	2.0	r_{1-3}	1.0	1.5	2.0
$L_1 = 2.33$		0.8	0.84	0.07		0.84	0.65	0.08
$L_2 = 3.5$	^{6}Li	1.94	**5.0**	0.11	^{8}Li	1.56	**4.3**	0.12
$L_3 = 5.25$	7500	0.84	0.38	0.12	840	0.58	0.37	0.13
	r_{1-3}	1.0	1.5	2.0	r_{1-3}	1.0	1.5	2.0
$L_1 = 2.33$		0.63	1.04	0.11		0.44	1.28	0.2
$L_2 = 3.5$	^{9}Li	1.04	**2.7**	0.15	^{11}Li	0.8	**0.25**	0.23
$L_3 = 5.25$	178	0.34	0.34	0.15	8.5	0.22	0.29	0.19

Table 5.5: Relative yield Y(r[mm]/L[cm])/Y(1.5/3.5) of Li isotopes including decay and ionization factors. The cell Y(3.5/3) of each box expresses the absolute extraction efficiency $\varepsilon_R \cdot \varepsilon_i[\%]$ for the standard ionizer shape, D/L=0.3/3.5 and sticking time $t_s = 2 \cdot 10^{-9} s$. These values include recombination and ionic transport under plasma and extraction electric fields.

5.1.2 Optimization of the target shape.

With the limitation imposed by some more or less rigid constraints[11], many geometric parameters are left to the maximization procedure. However, some of them are more versatile than others. As an example, three simulations were carried out with slabs of 2, 10 and 20 μm. The spacing between slabs was adjusted so that the total amount of target would be conserved. This presents multiple advantages:

1. Results need no normalization before comparison.

2. Importance of diffusion, sticking and effusion is quickly unveiled.

3. Hot spots induced by the shock wave effect might lead to sintering of foils. If foils coalesce, the average foil thickness increases but the total amount of

[11]The weight is limited for portability of the hot target with a robot system, the size is limited by the vacuum hosting dimensions.

target remains constant. In other words, if all parameters (diffusion, sticking, temperatures...) were well known, then the coalescence degree could be detected and fitted by comparison of the experimental release curve to the three simulated curves.

The other dimensions and the remaining conditions are kept the same. The convolution procedure is analog to the one used before.

Pure effusion is independent of the number of foils

If the pure effusion curves (no sticking) for the three cases are plotted, then the corresponding graphs appear superimposed (almost no remarkable difference between the three). This fact, rather surprising at the beginning, is corroborated by the average flight path, which only decreases slightly in thicker foils: 197.4, 194.7 and 191.7 m for 2, 10 and 20 μm.

Let us intuitively prove this statement; within certain limits the average distance between collisions scales to the average spacing between foils, therefore to the number of foils. In order to remove the number-of-foils dependency in the average flight path the average number of collisions must be inversely proportional to the number of foils. Simulations show that this is indeed so: 470000, 106900 and 61500 collisions for the 2, 10 and 20 μm foils.

For Li the sticking time per collision can be estimated from the Eichler-Miedema empirical model to be of the order of 2 ns, meaning that the average adsorption-desorption delay times are 0.94, 0.21 and 0.12 ms. These values have no impact on the release curve at the time scale of the other two delay mechanisms, pure effusion and diffusion. Then, as effusion is identical for the three cases, only diffusion matters (desorption is negligible here) and thus the optimal configuration is the one with the highest number of thinnest foils. Moreover, it is straightforward to compute the intrinsic release curve for any configuration; it just requires convoluting a thickness dependent analytical

Li release	A	6	8	9	11
d[μm]	$\eta \downarrow T_{1/2}[s] \rightarrow$	7.5	0.84	0.178	8.5E-3
20	0.054	59.03	23.51	7.00	0.07
10	0.217	78.28	43.35	17.20	0.28
2.0	5.43	97.87	83.80	54.02	2.86
2.0	experimental	98	83	53	2.4
1.5	9.65	98.51	87.53	59.52	3.74
1.0	21.7	98.98	90.75	65.94	5.16
0.5	86.9	99.27	93.03	72.39	7.62

Table 5.6: Experimental and simulated (fitted) released fractions of several Li isotopes in foils of various thicknesses for the RIST-ISOLDE target. η represents the reduced diffusion parameter and $T_{1/2}$ the mean half-life, both in seconds.

function of diffusion with the effusion curve, 'frozen' for all simulations. This is particularly suitable, it means that the fractional release curve can be computed with the analysis program described before; by a mere change of the diffusion parameter the same run is repeated over for several groups of isotopes with a common diffusion parameter (η) for each group. Results are shown in table 5.6 and the corresponding graph (5.6).

If the effusion curve were strictly constant (for the same total amount of target material, regardless of the distribution), the optimum release would happen for an infinite number of foils of thickness $\rightarrow$ 0 (fastest diffusion time constant). Nevertheless, optimization is constrained by the excessive local heating due to the proton beam deposited energy and the thickness-dependent life endurance. Autopsies performed on target *Ta129* seem to confirm that about 30 % of the 200 2-μm foils had coalesced after proton irradiation. This means that for a given beam and target material it may not pay off the costly ultra thin structure because the foils are due to sinter after a few proton pulses, thereby delaying diffusion and effusion (closed cavities are originated).

Similar simulations could be carried out to improve other design parameters like the length of the foils or its relative position (distance and angle) with respect to the outlet orifice. A breakthrough idea was studied in the RIST target, to which the following section is dedicated.

5.1.3 The RIST target.

The RIST target was conceived as an adaptation of the thin Ta foils concept (just discussed) to accept powerful primary beams. In this case, the 2 μm foils are shaped as hollow discs separated by equally broad spacers[12]. Simulations with this 5000 cell geometry remain lengthy for the present CPU-program conditions (further optimization and parallelization would help), but a one week simulation[13] produced already reasonable results, displayed in fig. 5.9.

5.2 Be beams from RIST-ISOLDE and RIST.

Like Li, Be was produced with the *Ta129* target, although ionization was carried out with a laser ion source. This function (laser ionization) has not yet been fully included in the Monte Carlo program, so effusion had to be scaled from the simulations done for Li. Nevertheless, conclusions differ greatly from those of Li because the release parameters are quite different. D(Be, Ta, 2413 K) is about 1.4· 10^{-7} cm^2/s (E_a = 234 KJ/mol, $log(D_0) = -1.78$ [83]) and t_s is reported to be about 10 μs. This means that diffusion happens much faster than it did with Li, but effusion is considerably slower due to sticking, which is 10000 bigger than in Li. Therefore, the diffusion-controlled character is lost.

An integral simulation of Be would require laser ionization

[12] A thicker version exists with a 25 μm periodic structure.
[13] In a 2.4 GHz machine on a cluster running with Red Hat Linux 7.3.

5.3 Conclusions.

- Simulation arrays permit to rapidly speculate about the incidence of having a foil thickness other than the one used.

- The release of Li is diffusion controlled. The thinner the foils, the better, but sintering limits the minimum foil thickness. Experiment times could be shortened by using 1 μm foils, but the integrated amount of beam would probably not be bigger.

- The impact of the surface ionizer shape has been discussed in terms of ionization efficiency. For long-lived isotopes, ionization is the critical process and therefore the number of collisions is maximized. In those cases, a reduction in the diameter of the ioniser may be the best choice. For short-lived species opposite changes are recommended. Preliminary optimum shapes have been found, but the accuracy of the results pends upon the calculation of the ion extraction efficiency as a function of the studied variables.

- Despite neglecting laser ionization by taking the effusion curves of Li (mass scaled), the obtained release data for Be isotopes match the experimental values very accurately.

- Calculations for RIST targets challenge the computational power. However, reasonable results have been produced.

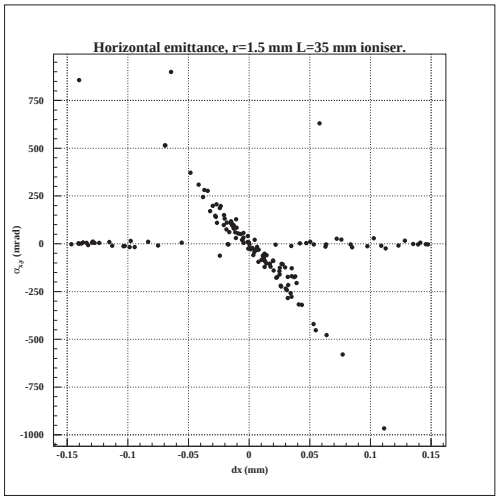

(a) $\epsilon_x m$, $r = 1.5\ mm$

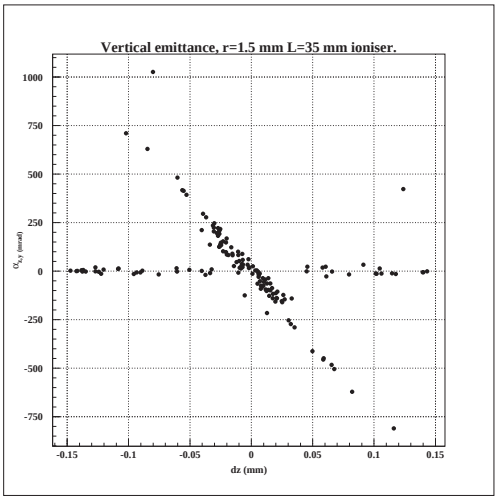

(b) $\epsilon_z m$, $r = 1.5\ mm$

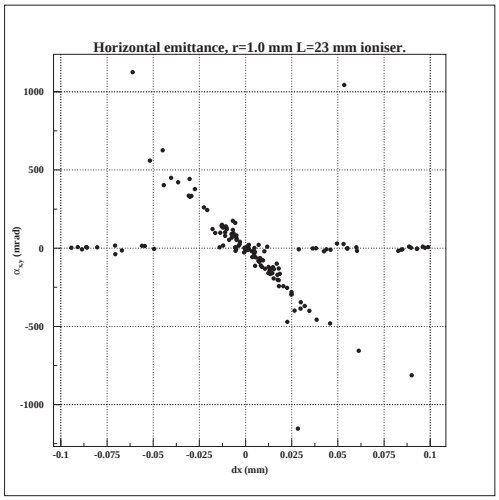

(c) $\epsilon_z m$, $r = 1.0\ mm$

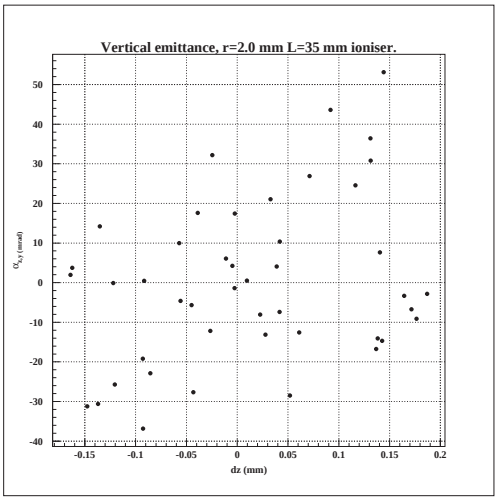

(d) $\epsilon_z m$, $r = 2.0\ mm$

Figure 5.5: Simulated Li emittances ($\epsilon_{x,z} m$) at the exit of a 3.5 mm long surface ioniser of radius r.

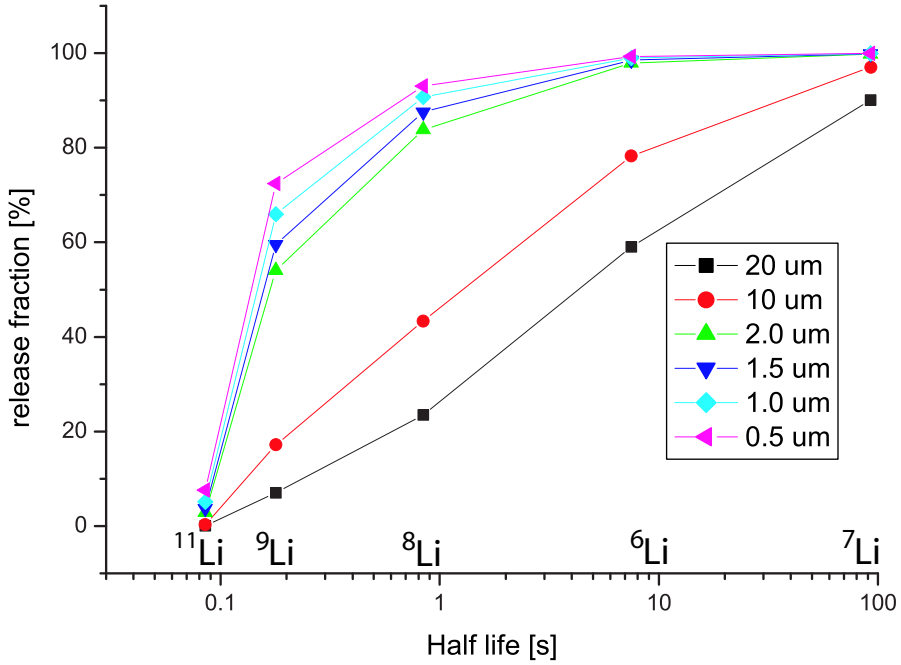

Figure 5.6: Simulated Li release fractions as a function of half-life and foil thickness.

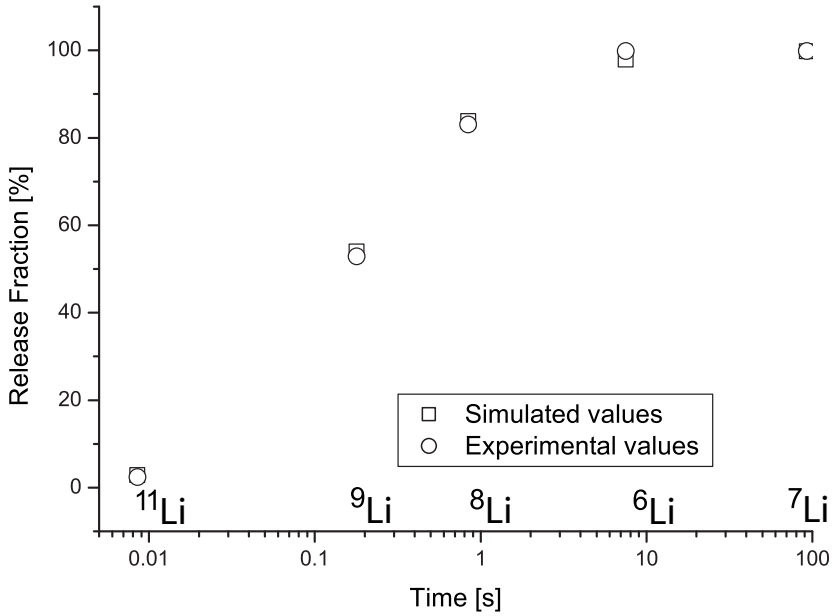

Figure 5.7: Simulated and experimental release fractions for several Li isotopes.

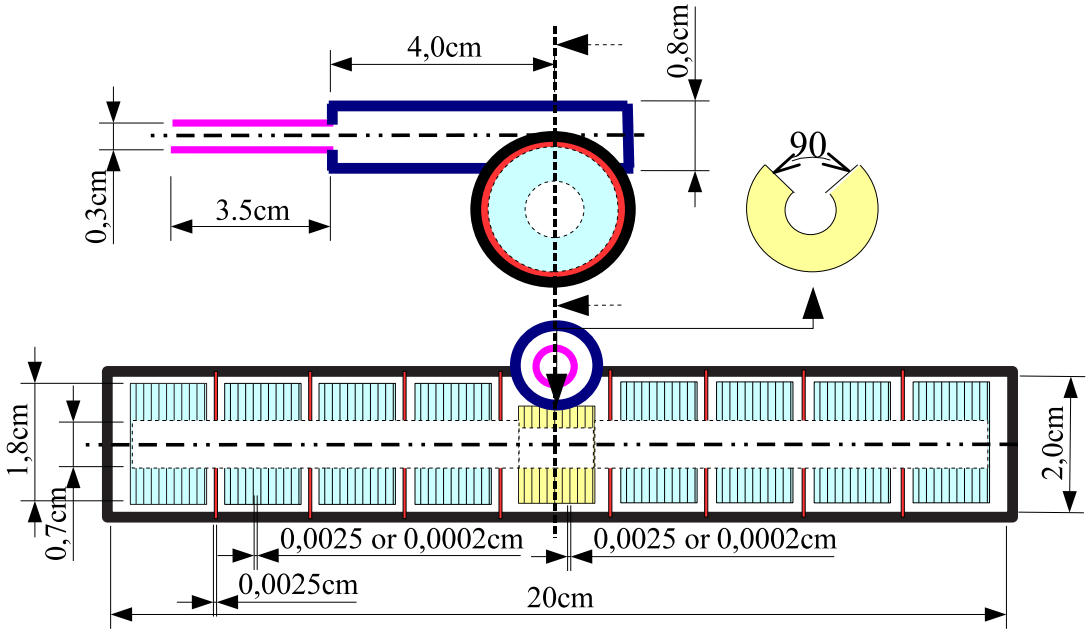

Figure 5.8: Schematic layout of the RIST targets.

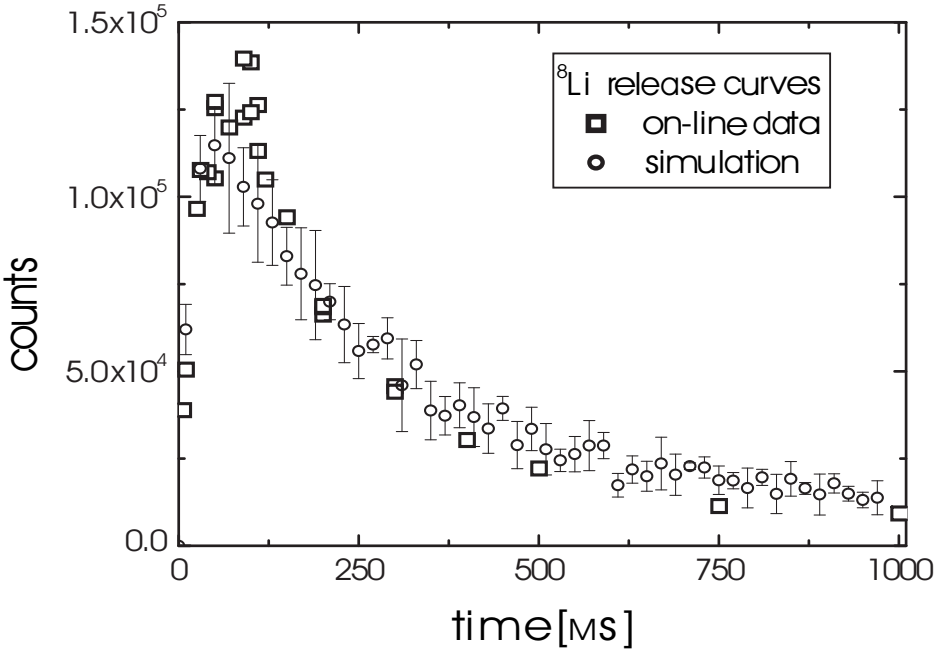

Figure 5.9: Experimental and simulated intrinsic release of ^{8}Li from the RIST target.

Chapter 6

Kr yields in rp-process studies. Rolled foiled targets.

THE PRODUCTION OF NEUTRON-DEFICIENT Krypton isotopes having astrophysical importance has been repeatedly studied at the ISOLDE PSB facility at CERN. The non-observation of ^{69}Kr is a challenging motivation for the yield optimization. To investigate several effects on yield, the Monte Carlo code has been extensively applied leading to proposals of modifications in the target and to scan the potential of other structures like powders or felts [84].

6.1 Physics Motivation.

The neutron-deficient krypton isotopes are important for studying the astrophysical rapid proton capture process (rp-process), which is a nucleosynthesis process occurring at high stellar temperatures and hydrogen densities, for example in accreting neutron stars [85]. The rp-process proceeds as a sequence of rapid proton capture reactions and β^+ decays through neutron-deficient nuclei. The region near neutron-deficient krypton isotopes is

specially interesting due to two waiting point nuclei ^{68}Se and ^{72}Kr. At these points the rp-process is inhibited because of the long beta decay half-lives of the waiting point nuclei and the proton-unbound nature of proton capture daughter nuclei, ^{69}Br and ^{73}Rb [86, 87]. The situation changes, if the daughter nucleus lives long enough to capture another proton. Then the rp-process is able to go on via 2p-capture and the effective lifetime of the waiting point can be remarkably reduced.

The proton capture Q-value for ^{68}Se is important for modeling the rp-process. It can be inversely determined by measuring the decay energy of the ground state proton decay of ^{69}Br. Since ^{69}Br is proton-unbound by at least 450 keV [86], it must be produced via beta decay from ^{69}Kr. In addition to protons from ^{69}Br ground state decay, beta-delayed protons with an energy of about 4 MeV and a half-life of the order of 30 ms are expected from the decay of ^{69}Kr [88].

The beta decay of ^{69}Kr was studied at ISOLDE PSB facility at CERN [89]. Krypton isotopes were produced in spallation reactions in a dedicated Nb foil target irradiated by a 1.4 GeV proton beam. The target was filled with 10 rolls each of them made by turning over 100 times a 25 μm thick dimpled Nb strip. These elements were evenly spaced by 3 mm long spacers. The central cavity was made of a set of parallel thin foils directed towards the outlet hole. A plasma ion source with a water-cooled transfer line was used for ionization and the ions were mass-separated by the HRS separator[1].

A set-up consisting of two silicon detectors forming a ΔE-E -telescope was used to observe beta-delayed protons from the ^{69}Kr beta decay. Data on ^{69}Kr were collected for about 20 hours. Neither beta-delayed protons from ^{69}Kr nor protons from ^{69}Br ground state decay were found [84], which gives an upper limit of

[1] High Resolution Separation [90].

4.9×10^{-5} at/μ C for the ^{69}Kr yield. During the experiment, data on ^{71}Kr and ^{73}Kr were also collected. Beta-delayed protons from ^{71}Kr and ^{73}Kr were observed with yields of 4.7 at/μ C and 0.8×10^{4} at/μ C, respectively. The yields were consistent with the results from previous experiments on neutron-deficient krypton isotopes at ISOLDE (e.g. ref. [91, 92]).

6.2 Studies of Release properties of ISOLDE targets.

A survey of the release of Kr and other isotopes from various target materials was carried out. These measurements are complementary to the use of the MC `RIBO` code, specially when the diffusion coefficient, the sticking time or the target porosity are unknown. In those circumstances, the combined action of experiments and simulations can give consistency to the first and benchmark the last.

Merging multiple on-line and off-line experimental results, it was observed that Kr is released from all examined materials, i.e., from $SrZrO_3$, Y_2O_3, Zr, ZrO_2, Nb and Mo (fig.6.1). From preliminary results, it can already be anticipated that, for example, the release of Kr is faster from Y_20_3 felt than from ZrO_2 felt or that the release of Kr is at least as fast from a Zr foil as from a Nb foil. A more extensive and complete study is presented in [93]. The yields of Kr nuclei from SrO and ZrO_2 targets were determined on-line, using the monitoring tape-station set-up. Both targets were connected to an ISOLDE type FEBIAD ion source using a water-cooled transfer line (MK7) [94]. The ionization efficiency of Kr was about 3 % in each case. The proton beam energy was 1.0 GeV. Further details are given in Table 6.1. Similarly, on-line measurements have been

Zr foils release as fast as Nb foils

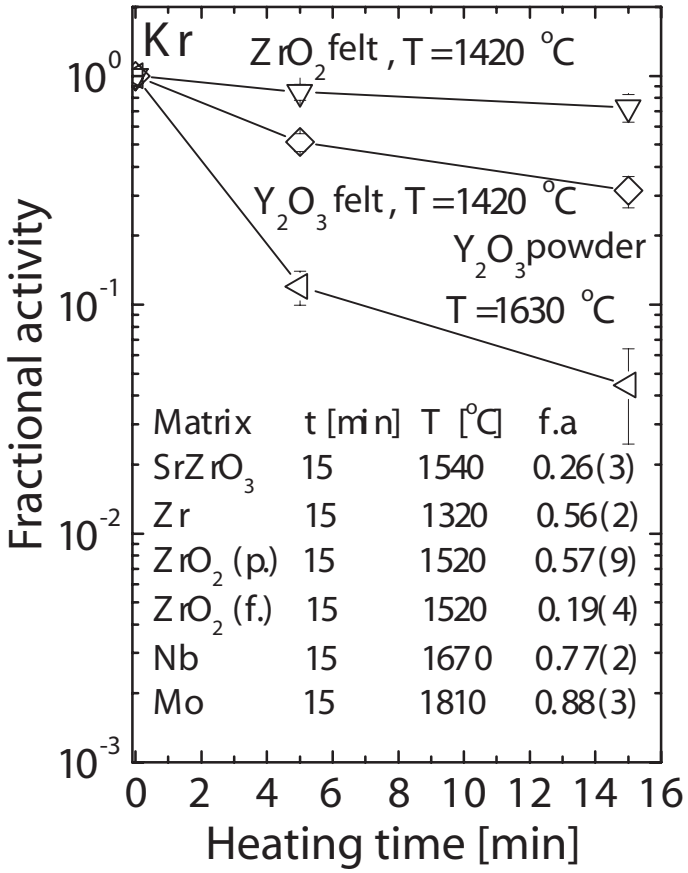

Figure 6.1: The diffusion of Kr from several targets is evaluated through fractional activity tests.

performed for several geometric configurations of Nb rolled targets. The Yields of Kr from SrO and ZrO_2 felt targets are presented in fig.6.2. The abnormal low ^{73}Kr yield from a SrO target is probably due to fluctuations in the measurement. fig.6.2 together with table 6.1 proves that the Nb foil target (foil thickness 25 μm) [91] is still a competitive choice for the production of short-lived and n-deficient Kr isotopes like ^{69}Kr. Thus, although R& D is under way for fiber targets (chapter 8), the last two on-line experiments were done with Nb foil targets.

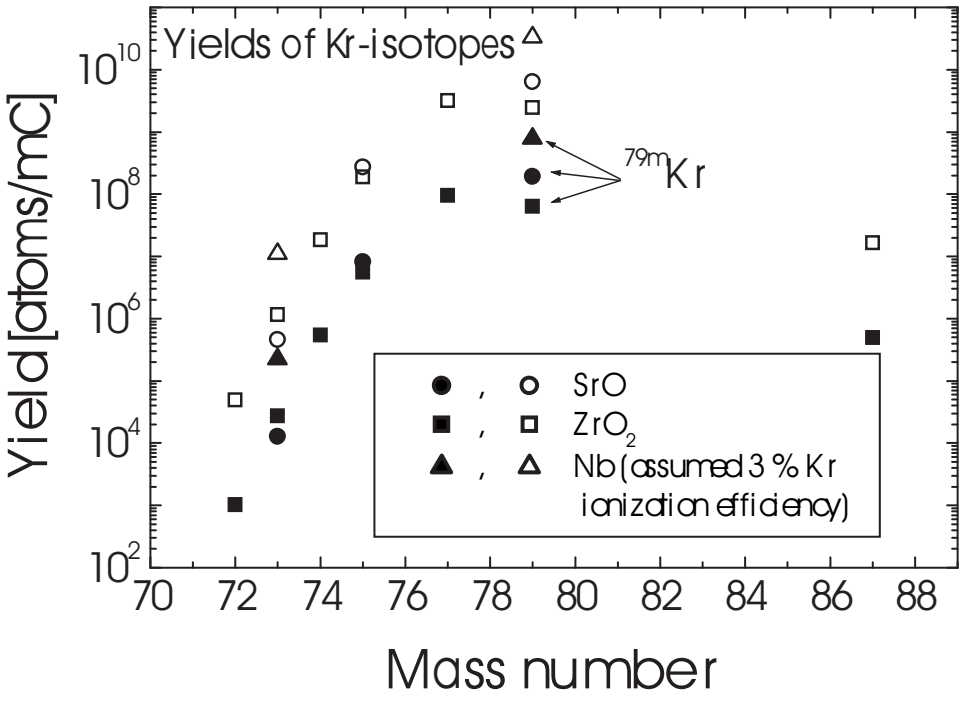

Figure 6.2: Yields (●,■,▲) and in-target production yields (○,□,△) of Kr nuclei from SrO, ZrO_2 and Nb targets.

Target			Line	On-line	Release			
Material	$g \cdot cm^{-2}$	T(K)	T(K)	eff [%]	α	$t_r[ms]$	$t_f[ms]$	$t_s[s]$
SrO	18	1733	2353	3	0.78	67	397	3.89
ZrO_2	8	2123	2293	3	0.71	90	938	12.7
Nb	42	2173	2173	9	0.82	75	829	23.1

Table 6.1: Overview of target-MK7 features, operation conditions and release characteristics of Kr. $t_r[ms]$ is the fast rise, $t_f[ms]$ and $t_s[s]$ are the fast and the slow fall, the latter group being balanced through α, as shown in eq.3.48

6.3 Nb rolled target. Effusion simulations.

Although the geometry of rolled targets may, at first sight, look rather complex, basic simplifications render the problem more manageable, e.g., the n-turned rolled foils are written as n concentric hollow cylinders. The resulting sketch, shown in fig.6.3, was used, together with the description of the transfer

(selecting) line and the ion source of fig.4.1 (page 104), as input for the first chronological effusion simulation carried out by RIBO.

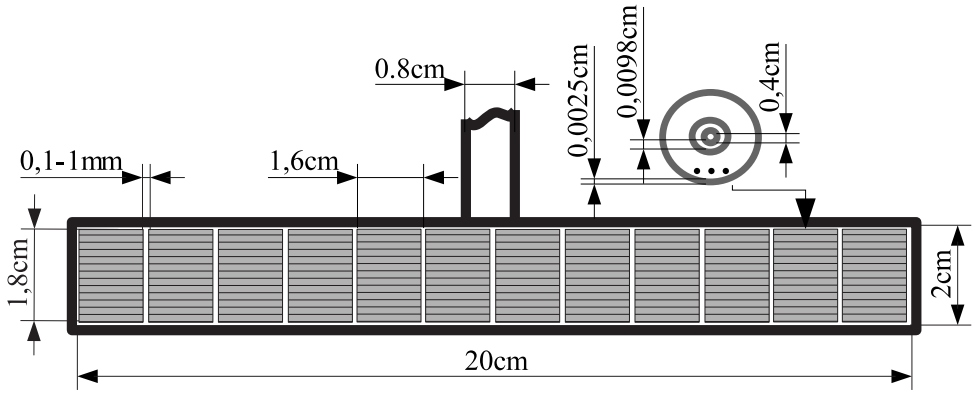

Figure 6.3: Schematic description of an ISOLDE Nb roll target.

6.3.1 Experimental effusion profile in Nb targets.

When the experimental data were analyzed in the frame of the experiment, the diffusion process had not yet been included in the RIBO package. Moreover, it was considered an instructive exercise to study the effusion curves as independent entities. The process for obtaining the experimental effusion curve from the intrinsic release data required some manipulation.

At ISOLDE, 1 GeV or 1.4 GeV protons are delivered in 2.4 μs-long pulses grouped in supercycles of 14.4 or 16.8 s. For a given proton pulse the release profile is a result of applying the radioactive decay ($d(t)$) to the convolution of the effusion ($h(t)$) and the diffusion processes ($f(t)$)[2]; the contribution of the preceding proton pulses (period t_{SC}) to the amount of isotopes at a given time (t) is already corrected for in the intrinsic release curve computed by fitting the experimental release data. The same token applies to the radioactive decay. It

[2]This function is described in 2.5, 2.6 with a the halfwidth of the foils, 12.5 μm.

then remains to extract the effusion profile from the combined expression *diffusion* $\otimes$ *effusion* (eq. 6.1).

$$\left.\begin{array}{c} N\left(t,t_{SC}\right)=\left\{d\cdot\left(f\otimes h\right)\right\}\circ\left(t\right)+\left\{d\cdot\left(f\otimes h\right)\right\}\circ\left(t_{SC}+t\right) \\ d\left(t\right)=\exp\left(\ln 2\cdot\frac{t}{t_{1/2}}\right) \\ f\left(t\right)=\frac{2}{\pi^2}\sum\limits_{m=0}^{\infty}\frac{\exp\left(\left(m-1\right)^2\cdot\left(\pi/a\right)^2D\cdot t\right)}{\left(m-1\right)^2} \\ \left\{h\otimes f\right\}\circ\left(k\Delta t\right)=\sum\limits_{i=0}^{k}f\left(\left(k-i\right)\Delta t\right)\cdot f\left(i\Delta t\right)\cdot\Delta t \end{array}\right\} \quad (6.1)$$

Diffusion was assumed to follow the law 2.5, in the case of slabs ($m=1$, eq. 6.1,3rd) with a diffusion coefficient $9\cdot\ 10^{-9}\ \frac{cm^2}{s}$ taken from [19]. Deconvolution was achieved by inverting the expression 6.1 numerically. The result is plotted with a solid line in fig.6.4.

6.3.2 Effusion simulations.

In order to optimize the yield of short-lived neutron-deficient krypton isotopes, the Monte Carlo code was used to study the delay time in the transfer of atoms from the target to the ion source as a function of target geometry and material. Zero sticking time on surfaces was assumed. The starting distribution of effusing particles was derived from the radial structure of the impinging proton pulse. In the simulations 12 Nb foil rolls (length of 1.5 cm each) were placed in a Ta target container (length 19.5 cm) in two different configurations, one for 1.0 mm inter-roll spacing, and the other for 0.1 mm. With 1 mm regular roll spacing we have 2 mm gap at both ends for the target container while with 0.1 mm spacing we have 7 mm end gaps. Normally rolls are dropped into the target container, with little possible control over the final configuration. In fact, even if the rolled strips where initially placed at known positions, their corresponding coordinates

after, e.g., target transportation, would be undetermined because there is no physical constraint inside the target container to prevent displacements. For each

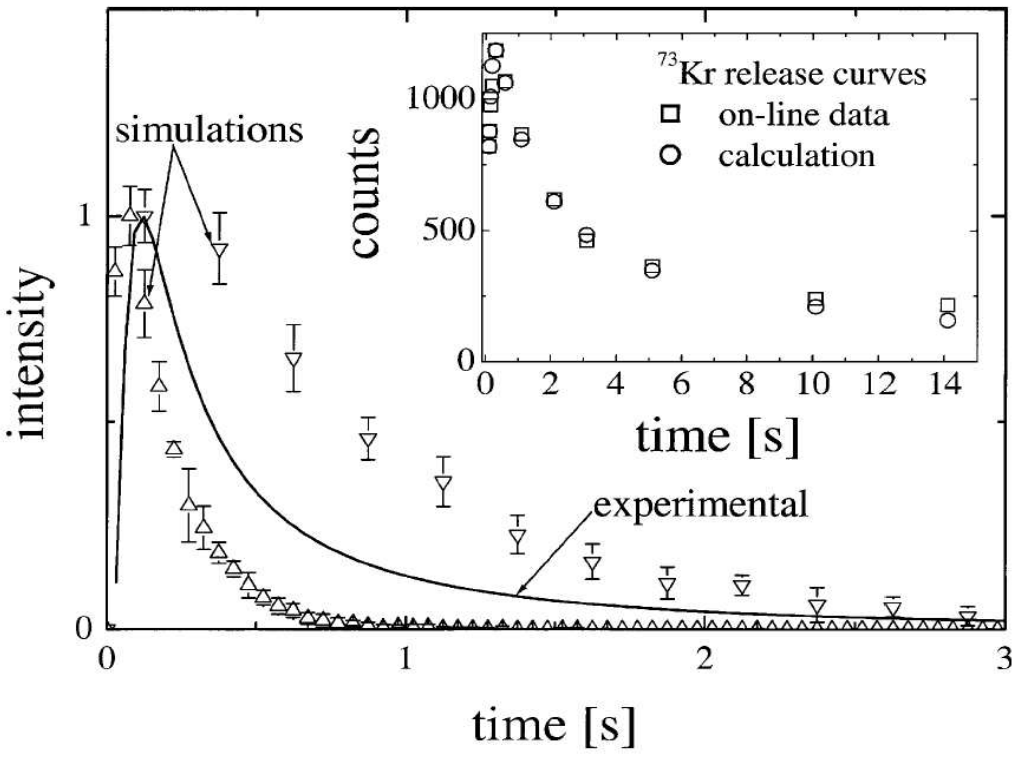

Figure 6.4: Experimental (−) and simulated (△ for 1 mm and ▽ for 0.1 mm spacing) Kr effusion (big graph) and release (small graph) curves from a standard Nb rolled ISOLDE target.

geometry, about ten thousand particles were computed. Fig.6.4 represents the outcome of these simulations; up triangles correspond to 1 mm roll spacing and down triangles to 0.1 mm (note that all curves in fig.6.4 are normalized to the same maximum amplitude instead of equal area). These results indicate that the distance between rolls is an important tuning parameter of the ISOLDE roll foil targets. The shape of the experimental curve should be approached by simply adjusting the spacing between the target roll units.

The distance between rolls is decisive

6.3.3 Target scaling rules.

Simulations performed to extract some scaling rules show that the 1 mm spacing option leads clearly to a faster release. Nevertheless it could be argued whether this should be necessarily a general premise. Fig.6.5 (page 158) is intended to guide discussions in this sense. Let us start by assuming an even distribution of rolls inside a cylindrical oven with the exit hole placed in the central position fig.6.5.1. If an extra volume of space where added at either (or both) end(s), fig.6.5.2, it would certainly act as a sink because the particles that fell there would have a lower probability to escape than in the starting distribution[3]. Another possible setup could be made by evenly approaching the rolls, fig.6.5.3. That is the case for the 0.1 mm distribution as compared to the 1.0 mm inter-roll distribution. The later configuration lowers the radial mobility of isotopes in the jump from one roll to its neighbor. In particular, this reduces the solid angle of escape from the central cavity to the exit orifice. As most isotopes leave the target this way (a small fraction comes from the side channel), the spacing defines a factor that modulates the escape time, thus the release probability. In view of these facts, it can be stated without much doubt that *lowering the regular space between rolls has multiple negative effects*. This is why the 1.0 mm setup improves the release shown by the 0.1 mm setup.

Endcap spaces degrade the effusion

Shifting the symmetric regular distribution to a non-centered position (6.5, 5^{th} figure) creates an extra end volume that might be thought to be compensated by the corresponding decrease in the opposite end. Anyhow, the overall conductance will be penalized by a very poor exit factor (tiny viewing angle of the outlet hole). Discarding the latter modifications, one more question (fig.6.5.4) is what should be the optimum length of the evenly spaced rolls. This is a tougher point

[3]The ratio (S/V), proportional to conductivity, decreases.

to be discussed from geometric principles. In fact, it implies a change in the total target mass, with a consequent, but not obligatory proportional, change of the initial isotopes; and a most likely variation of the conductance, thus of the extraction efficiency. Whether the overall effect is positive or not cannot be answered in general terms, as it will depend on the half-life of each isotope. Naturally, for stable or long-lived isotopes a greater filling will higher the yields. At the end of the present chapter and in chapter 7, guidelines are given for the isotope dependent target mass selection.

One could still think of other cases, e.g., would it be positive to enlarge or shorten the target container while keeping the same filling, i.e., modifying the distance between rolls? and, equivalently, what would happen if the radial dimension of the container were modified? Moreover, for non noble gases, the number of collisions comes into the game too. Soon very many variables appear. Here not all cases have been examined, just the first ones, for standard 20 cm long 2 cm diameter ISOLDE containers. The goal of `RIBO` in this context is precisely to serve as tool for a technical research network to investigate all lines of improvement.

6.4 Nb hybrid target. Global simulations.

Following the experience and knowledge acquired in the prior experiment it was concluded that an even distribution of rolls over the cylinder length should be guaranteed. Moreover, close to the experiment date it was suggested to test the effect of a ”fast component” based on the parallel thin foil configuration used for RIST like targets (5.1, page 124).

The target build-up and the whole experiment where closely followed. Results where analyzed and compared to simulations. Improvement in the predictive character of the RIBO code is noted, although some question marks remain open.

6.4.1 Design and build up of the hybrid target.

The major goal of the experiment was to measure events corresponding to the highly exotic ^{69}Kr. It was therefore justified to sacrifice target mass for the sake of efficiency. A way to do that was to suppress some rolls to higher the pumping speed. Still, needing to conserve the 20 cm long container, it was suggested to include a central group of parallel 2 μm slabs, aligned facing the outlet hole. The outcome is an hybrid between the rolled and the parallel type of targets. It was also decided to intercalate spacers to guarantee a regular placement of the rolls and slabs inside the target container. Fig.6.6 illustrates the schematic setup, while fig.6.7 shows a real view of the target components.

6.4.2 MC simulations.

In this stage the MC code already included tools to visualize the convergence of simulations in real time. Thus, the simulation size was determined by observation of the oscillations of the average numbers cast by RIBO in a test execution. The stabilization of those occurred at about 5000 histories for this target, half of what had been required for the Nb rolled target. The simulation was executed slightly longer to allow a tighter convergence of the time-binned effusion data.

6.4.3 Effusion and diffusion.

The MC simulation of the effusion behavior gives the flight time-share between the target (inside the Ta container), the transfer line and the ion source. Most of the effusion time was spent in the target ($\sim$56 %), but also a significant fraction of time was used in the ion source ($\sim$30.5 %) and in the transfer line ($\sim$13.5 %). The average number of collisions was 1.7×10^6, the majority of which took place in the target, where flight paths between two collisions are very short. From this partial result, it could already be concluded that if the temperature in the transfer line were 2300 K instead of 300 K, total effusion could be 8.5 % faster.

At the moment of this (second) experiment, diffusion had already been vastly included in calculations. In this case, the diffusion profile for an infinite slab was firstly plotted from its analytical infinite expression and then convoluted with a histogrammed effusion distribution, obtained in turn by simulation[4].

6.4.4 The release behavior.

The global release curve was obtained by convoluting and binning the diffusion and the effusion functions. Simulations now become more realistic than in ref. [95], where the spacing between rolls had not been forced to a fixed and known value. However, the release peak prediction is now slightly pessimistic. This suggests that the proposed shock wave effect might indeed take place; the beam impact would then rise the temperature by about 100 K during some tens of milliseconds and diffusion would be accordingly enhanced during that period[5].

[4] Alternatively, diffusion may be sampled and added to effusion for every history. Despite being simpler and more intuitive, this approach might magnify the statistical spread (sampling procedure).

[5] It should again be pointed out that the transient profile cannot be obtained by varying T over time in the formulas 2.5. A numeric solution must be worked out.

Source\Isotope	^{73}Kr	^{72}Kr	^{71}Kr	^{69}Kr
Experimental fit	50.5	41.6	0.9	0.18
Simulation (via sampling)	71.4	63.2	0.6	0.05
Simulation (via convolution fitting)	69.8	61.0	0.5	0.07
2 μm rolls	97.5	96.2	5.7	0.7

Table 6.2: Extraction efficiency $[\%]$ from 25 μm Nb rolls of various Kr isotopes at 2250 K. Differences between columns are due to the decay factor.

The *release fractions* were evaluated for the experimental curve and for the simulated one. The latter calculation was carried out in two different ways (via sampling and via convolution-fitting). Calculations for hypothetic 2 μm thick rolls were additionally computed by applying *analyze*, an analytical package that complements `RIBO` core MC code. The results are shown in table 6.2. The discrepancy between experiment and simulation cannot be attributed to the errors in the analysis phase. The diffusion process is again found as the main responsible of the deficiencies in the simulations, although the prediction of effusion might be also improved by taking into account a micrometric detailed input file.

6.5 Target optimization.

Atoms diffuse about 150 times faster out of 2 μm thick foils than from 25 μm rolled strips. This effect was manifested in the release peak, which increased over 10 % as a result of the contribution of the thin foils, which represent 0.7 % of the total target mass. Nevertheless, a sometimes slower effusion and, for all, the loss of the target mass, limits this promising exploit. Crude extrapolations indicate that substituting rolls by parallel foils would at best duplicate the extraction of ^{71}Kr and ^{69}Kr while the production of $^{73-72}$Kr could be undermined by a factor 6.

The fraction of short-lived noble gas atoms extracted from a powder or felt target is considerably higher than the one obtained from the regular foiled version. However, achieving this would require that the departing material could be fibered or set into a refractory powder that is able to stand the severe target conditions without sintering or melting. Powder targets like UC_x fulfill these heat-standing criteria but their cross sections for the production of neutron-deficient Kr isotopes are too moderate. These targets ought to be globally optimized, the amount of generated isotopes and their corresponding extraction efficiencies simulated in one go. For this purpose, `RIBO` was extended with a module that simulates the transport of atoms in powder and fiber targets, where geometry can be described in terms of a few average parameters. This regime, together with the MCNPX production simulations, is extensively tested and applied for the prediction of yield of neutron rich isotopes in [96], chapter 7.

As an alternative to a change of material, simple target length scaling can be considered too. Simulations proved that all the rolls contribute similarly to the release. This is so because in such a poorly conductive geometry the erratic path followed by the effusing atoms is very long, which renders the initial position as mostly irrelevant. Thus, if extra rolls were added at the extremes, they would be almost as efficient as the inner ones but the average effusion paths of all atoms (regardless of the birth position) would all be longer[6] and the effusion efficiencies would go down accordingly. Therefore supplementary target mass will only be worthwhile when the half-life can allow the extra release time without major decay losses.

The size of a target made by a continuous filling may be straightforwardly optimized by changing a single parameter[7] on the input file and re-simulating

[6] because the target container would have to be larger in order to host the extra rolls.
[7] like the position of the end cups of the containing target cylinder.

over. Once the trends revealed, extrapolation to targets with discrete filling is, at most, a matter of deciding between two neighboring configurations. Following this lemma, the release optimization study of Kr in UC_x matrix carried out in [96] chapter 7 can be adapted to rolled foils targets. For long-lived isotopes, gains would almost scale to the target length whereas for ^{69}Kr the optimum length should be found at about 15 cm. This tendency is more accentuated for sticky elements. Note that, in this kind of studies, effects like beam opening and scattering demand some consideration as well.

6.6 Conclusions.

- The release of exotic neutron-deficient Kr isotopes from foiled targets seems rather limited, diffusion being the main concern.
- Geometric arrangements may at best double the production, meaning that the quest for ^{69}Kr should be directed at the research and test of refractory powders with high generation cross section for this isotope. The first candidate could be Y_2O_3 [95]. Chapter 7 investigates the potential use of refractory powders for the production of neutron rich isotopes.
- Distributing rolls evenly over the whole length of the target container should enhance the release speed.
- The presence of end wells (rolls compressed close to the transfer line) decreases the release efficiency.
- The right target length should be found by combining a production code (MCNPX [97], FLUKA [98, 99]...) and the release simulation code, `RIBO`.

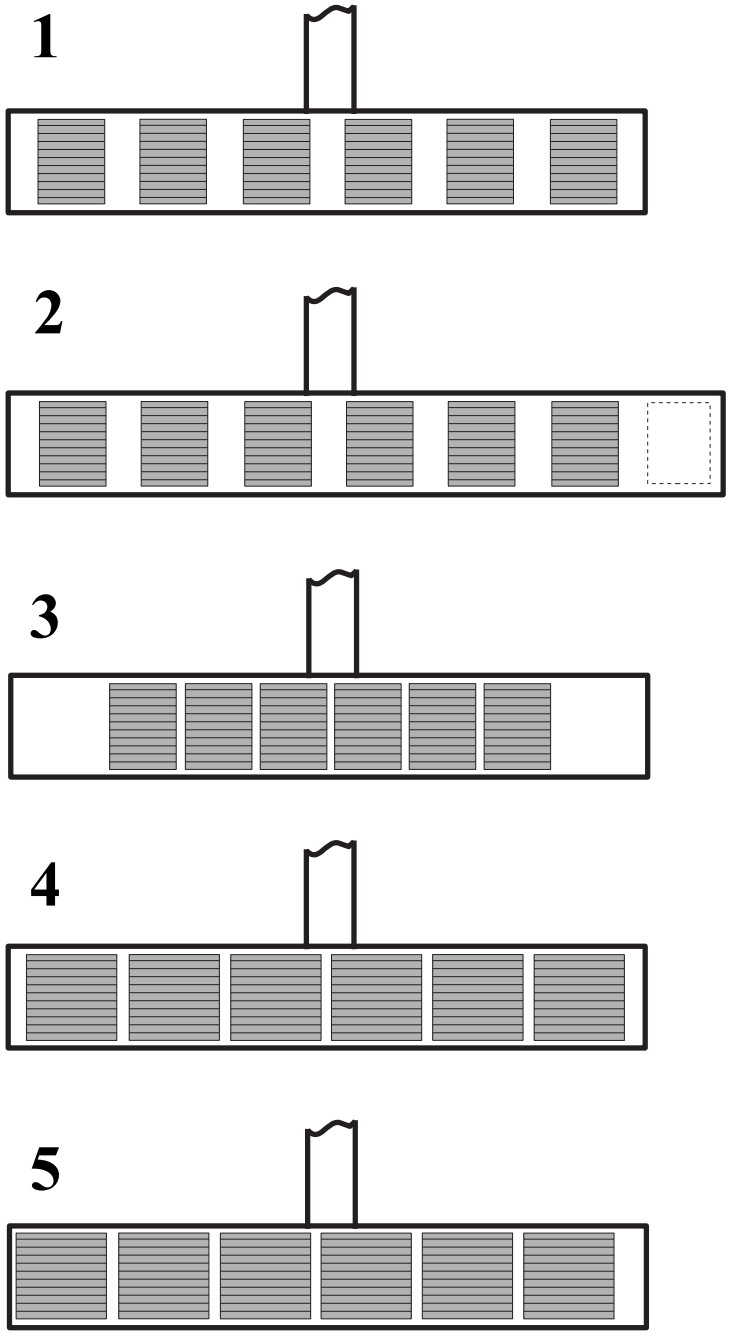

Figure 6.5: Basic filling vectors of a tubular target with Target elements.

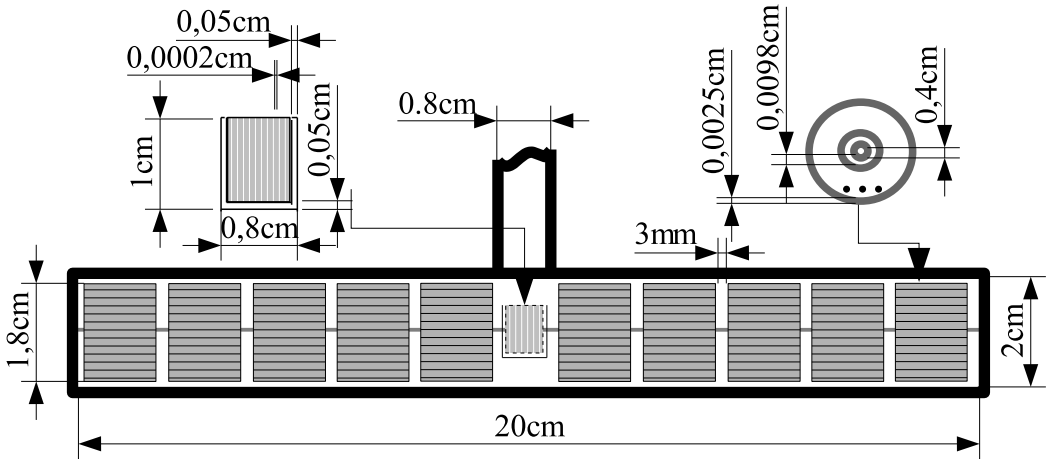

Figure 6.6: Schematic layout of the simulated Nb rolled/foiled “hybrid” target.

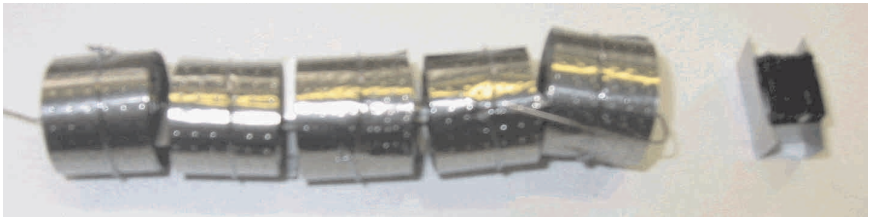

Figure 6.7: “Hybrid target”. A group of 5 Nb rolled foils separated by spacers and the fast diffusing group of thin parallel foils.

Chapter 7

Predictions and optimization of EURISOL beams.

7.1 Introduction: EURISOL. Projected targets.

7.1.1 EURISOL.

What is it.

THE EURISOL PROJECT [100], sustained by the European Commission and conducted by ten major European Nuclear Physics laboratories, aims at a preliminary design of a powerful ISOL RIB facility, which should fulfill many of the physics question-marks outlined in 1.2.1 (page 5).

State of the art.

“Recent years have seen a successful development of accelerators producing intense particle beams. This development has not yet been followed by similar investments in the development of the high-power targets needed to make

efficient use of the available driver beam power, for producing secondary radioactive ion beams (RIBs) of intensities which may be several orders of magnitude greater that those at presently operating facilities.
This identifies the target and ion-source (TIS) assembly (and the associated techniques) as one of the most crucial elements for a future EURISOL facility and it is essential to raise the status to the same level as that of other key accelerator techniques. This new field of accelerator technology that produces and accelerates radioactive ion beams using the ISOL method (i.e. the 'isotope separation on-line' method) is presently characterized by the relatively small number of active specialists who are at the moment fully occupied by the needs of the facilities now in operation. There is also a lack of commonly-agreed calculation codes and techniques" [96], pag.C-7.

Goals.

EURISOL has limited its task initially to the key elements defined by NuPECC[1], meaning that the preliminary design will be optimized for: Be, Ar, Ni, Ga, Kr, Sn and Fr. These are optimally produced in one of the following scenarios:

1. The proton rich nuclei of all the elements are best produced in spallation reactions induced by a 100 mA proton beam directly on an optimized target.

2. The neutron rich isotopes of Be and Ar are best produced in fragmentation of a heavy target by the 100 mA proton beam directly on an optimized target.

3. The fission products Ni, Ga, Kr and Sn are maximized in a large fissioning target surrounding a compact, high power spallation neutron source.

[1]Nuclear Physics European Collaboration Committee.

"The calculations are based on the experimental parameters discussed below. . . (...). In the performed intensity predictions, it has been assumed that needed modifications to the target geometries due to the higher proton beam intensities can be done without losing the observed fast release. This aim can be accomplished by integrating the release Monte Carlo code as an essential part of the future high power target design. Similar gains could be expected on the more than 600 isotopic beams listed in the ISOLDE database [101]." [96].

Elements and optimal targets.

The NuPECC elements are not all optimally produced by the same type of target. Many of them will show the highest yields for a concentric "megatarget", made of an extruded ring of refractory fissile material, which hosts a converter rod in its axis. Intense beams of some light elements are in turn produced in other target configurations, like those discussed in chapter 5 or chapter 6. In this chapter, after a brief summary of the future target scenario, a thorough analysis on fissile targets will be carried out and, finally, all results will be compiled in a single family of tables.

7.1.2 RIST targets.

These targets, analyzed in chapter 5, are made of thin Ta foils disposed in annular discs or straight strips. They are attributed the highest yields for the most exotic Be-isotopes, belonging to NuPECC aims.

7.1.3 The two-stage target.

The acceptance of the production potential offered by 1 GeV protons at 4 mA is subjected to the advent of new target technologies that shall enable to drain the corresponding 4 MW of deposited power. A dedicated primary 'converter' target, separately cooled and acting as secondary source could serve as sink for the incident charged beam power (e.g. protons, electrons). The secondary flux of neutral particles (e.g. neutrons, photons) would then irradiate a thick ISOL target inducing fission reactions. As compared to charged beams, the secondary neutral radiation would drastically reduce the heat deposition, thus lowering the possibility of destruction by overheating and by the effects of thermal shock waves, specially for pulsed beams [102].

Primary beams.

The primary beam does not necessarily need to be protonic; other alternatives have been considered in the last years:

- *Deuteron beams* of intermediate energy (ideally around 80 MeV) impinging onto low Z converters have proved a powerful means of producing intense neutron-rich nuclear beams from UC_x targets using a hot plasma source or a surface ionizer [103, 104]. Related works were undertaken by IPN Orsay in the frame of PARRNe [105, 106] and involved experiments at CRC (Louvain-la-Neuve), K.V.I. (Groningen) and ISOLDE, among other collaborations.

- An *a priori* inexpensive setup is that of an *electron beam* impinging on a metallic converter (W, Au, Ta...) or directly into the target. The bremsstrahlung radiation that is produced interacts with the fissile target

generating the sought isotopes directly by photofission or indirectly through fission reactions induced by photoneutrons [107]. PARRNe pursued its survey on primary beams with the study of photofission in UC_x targets, including irradiations with 50 MeV electrons with the LEP pre injector (LPI) at CERN [106]. Extrapolation from the obtained results lead to conclude that a 50 MeV electron beam of 10 A would intensify the yield of nuclear beams by two orders of magnitude as compared to yields obtained at PARRNe-2 with a 26 MeV deuteron beam of 1 μA.

- At ISOLDE *proton beams* may be converted in Ta or W rods to neutron beams that in turn generate fission products in the target. The conversion mechanisms are sufficiently understood and simulation codes are available for predictions, e.g., MARS [108]. The use of spallation neutrons is attractive for the generation of neutron-rich isotopes in actinide targets, where the production ratio towards their proton-rich isobars is higher than the one obtained with direct protons; hence isobaric contamination is reduced by a factor 7 to 50. In addition, even in pulsed mode, spallation neutrons do not produce damaging thermal shock waves in the targets.

Primary target. Converter.

The design of a primary target to use as converter in conjunction with a MW proton beam is a key issue for EURISOL type facilities. At ISOLDE measured and simulated yields have been compared for fission targets irradiated by a neutron flux produced by proton interaction in thick rods of high Z (tungsten and tantalum) [108]. R&D in other projects like SPES [109] and the SPIRAL-II [110] certify that the use of solid converters is feasible under 100 kW incident beam power.

However, problems arise when using solid targets that have to convert beams of a few MW. It has been envisaged to use liquid metal jet targets for those occasions. Tests have been performed for liquid lithium at the IFMIF project [111] (40 MeV deuteron $\sim$ MW) and for RIA [112] (^{238}U beam, 400 kW). The converter for 1 GeV proton beam should be a high Z element in order to optimize the size and neutron yield. The working scenario chosen for the MW GeV proton beam is that of a liquid high Z metallic windowless free surface Hg jet, optimized for size and yield of neutrons.

The concentric target.

A natural idea to increase the solid angle subtended between converter and target is to decrease the distance between the two or, better, to surround the converter by target material. Ideally the converter would be fully enclosed by the target (solid angle of 4π erad), but apertures have to be allowed to intake the proton beam and to extract the heat from the converter, which means that the solid angle must be lowered. A classical project of this type consists of an annular target with an axial cylindric converter [112]. This is indeed the configuration that will be used as starting point for EURISOL yield predictions in what from now on will be referred as *megatarget*. This target was conceived in order to substantially increase the amount of generated isotopes (thickness factor) while capturing a bigger portion of the spallated neutrons (concentric). The starting target radial thickness was taken as 50 *mm* (instead of 10, at ISOLDE); the inner radius 12.5 *mm*, the outer 63.5 *mm*, with 1 *mm* radial space between oven and target material. Longitudinally, the *megatarget* would double the standard ISOLDE measures, thus 400 *mm* with 1 *mm* space at the extremes and a 8 *mm* central void,

strategically placed to increase the pumping speed towards the extraction orifices, also at mid length.

Adaptation of the target oven to the FEBIAD and surface ion sources was negotiated so that the new transfer lines would not introduce major changes with respect to the former ones. By so proceeding, chemical separation remains warranted and, at the same time, gain factors may be exclusively attributed to the improvements in the target shape.

FEBIAD-MK7 version.

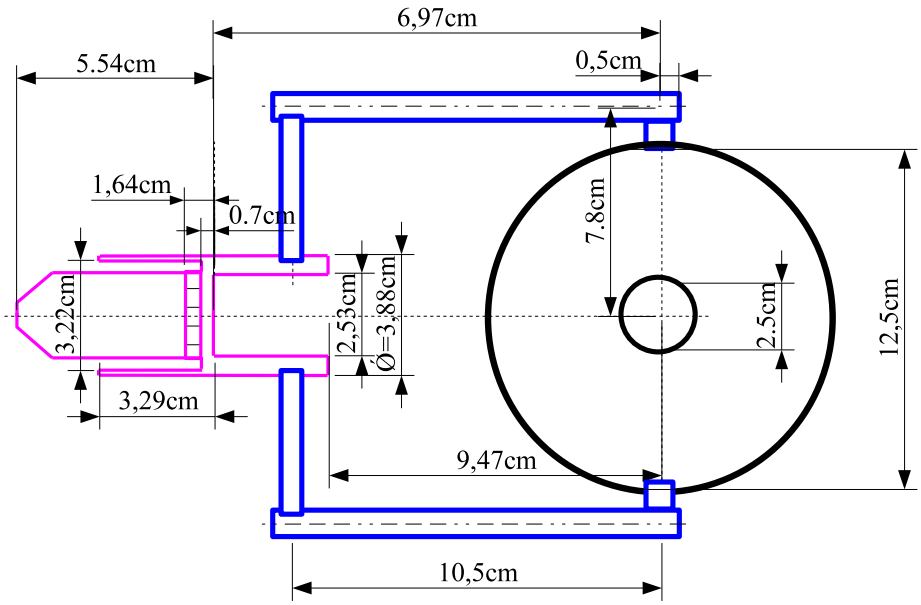

Figure 7.1: FEBIAD MK7 adaptation (two lines) to a 12.5 cm diameter target.

The comparison of fig.7.1 to fig.4.1 (page 104) illustrates the scale gain of target material and the subsequent need of line reshaping. After computing grossly the conductances of each straight section and applying the vacuum association rules, it was found that the new line had a time constant 40 % lower ($\frac{1}{1.6}$) than that of

the standard ISOLDE target. This reduction is compensated with a second, symmetrical, transfer line[2].

The surface ionizer version.

The standard surface ion source had its axis radially joined to the *megatarget*, with no other element in between, leaving a tiny section ratio $\frac{ion\ source}{megatarget}$. Further development on the coupling *ion source-target* and on the ion source size should significantly increase the throughput of surface ionized species.

7.2 Yield predictions.

7.2.1 This chapter.

This chapter focuses on the yield estimates and optimization of the high power, two-stage concentric target, *megatarget*, intended to boost the production of most NuPECC reference elements. Results from previous chapters, corresponding to improvements in existing targets, are integrated with other predictions into the discussions of forecasted beams.

Most of the radioactive throughput from high power targets is produced by reactions in powder materials such as UC_x. This being the case, a new feature had to be added to the MC `RIBO` release code in order to compute effusion even when the microscopic geometry is just known in average terms (porosity of powder...). Section 3.6 described how this regime is implemented in `RIBO`. The adopted strategy would ideally be:

At ISOLDE *it is assumed* $UC_{1.4}$

[2]The two symmetric lines acting together do not double the conductance since paths joining the two are possible; they are not fully parallel.

1. As a first step the `RIBO` code is provided with a set of subroutines to emulate the transport of particles inside a powder.

2. The parameters of the host material are inferred by comparison of sets of simulations to experimental data.

3. Once the powder satisfactorily described, the *megatarget* is designed and the conventional transfer lines are adapted to the new geometry.

4. A file is written to describe the target and then used as input to the upgraded MC code.

5. Simulations are carried out on a variety of similar targets, with differential changes between each other. The aim is to study the effect of the design parameters on the extraction efficiency.

6. A package of applications is added for the analysis of the data. Results are stored in arrays that allow computing the release of any isotope from a single simulation, provided that the release parameters (diffusion coefficient, sticking time) and half-life are known.

7.2.2 Scheme of the calculations.

At this point, having developed a module for continuous media, the Monte Carlo simulation code contains all necessary models to simulate the release from most of the candidate targets for the EURISOL facility. The EURISOL TIS preliminary study ought to include the relative gain factors of EURISOL RIB production towards existing beams (ISOLDE yields will be taken as reference). These numbers should give a first hint about the feasibility and scope of success

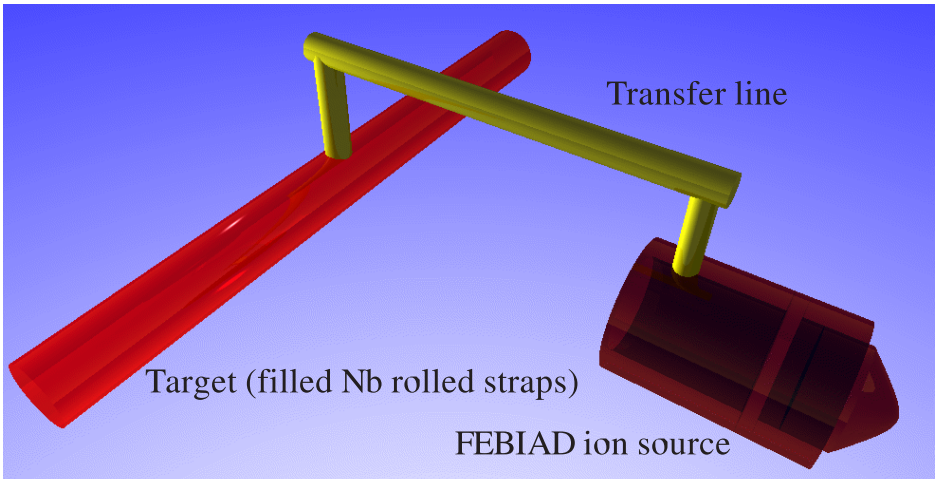

Figure 7.2: Ray tracing 3d-view of the standard UC *ISOLDE* target coupled to the FEBIAD ions source through the MK7 line. 3D-RIBO was used in conjunction with Povray.

of EURISOL and could point out the domains that require a bigger dedication.

Comparison of a given beam involves two stages:

1. Simulations of the existing beam and comparison to experimental data: This will serve as validation stage for fully defined targets or as tune-up stage when some unknown parameters have to be found (e.g. powder parameters and diffusion coefficient).

2. Simulation of the presumed future target: This stage, which includes a first-degree target optimization, should be followed by a dedicated design study.

Each of the stages involves again two steps:

- Calculation of the production ($\frac{generated\ isotopes}{incident\ protons}$).
- Calculation of the release fraction ($\frac{extracted\ isotopes}{generated\ isotopes}$).

The first substage (production) is achieved by combining several codes that use simulated and experimental cross sections, depending on the energy range. This chain of calculations was applied to three typical starting cases:

1. Standard target directly bombarded by a proton beam.

2. Standard target bombarded by secondary radiation (neutrons) generated in a parallel converter.

3. Annular target with a central proton-neutron converter.

The second step casts the extraction efficiency and is mainly carried out by the release MC code. Not all numbers have been simulated, some are educated guesses, interpolated between neighboring results while some others come from experimental evidence.

7.2.3 Production calculations.

Hypothesis and tools.

All calculations were done with the nuclear cascade code MCNPX [113], allowing multi-particle transport and energy deposition (balance systematically checked) for p, n, d, t, ^{3}He. LANL T-2 neutron libraries were used up to 150 MeV while for higher energies theoretical models within MCNPX were employed (ISABEL intra-nuclear cascade model, ORNL evaporation-fission model [113]). ENDF-VI data files [114] were used for U up to 20 MeV.

Simulations that are considered here[3] concern in the first place standard ISOLDE UC_x (3.0 g/cm^3) cylindric targets bombarded by 1.4 GeV protons[4] impinging directly into the target base or into a W (19,3 g/cm^3) p-n converter placed at 2.3 *cm*, as shown in fig.7.3 (page 171). The second set of calculations (shown in fig.7.4) predicts the yields in the annular two-stage-type of targets,

[3]The same methodology has been applied to many other materials such as CaO, Nb, Ta, ThC_4, ThO_2, ThS_2, ZrC_4 and ZrO_2.

[4]The primary beam of protons had a transversal Gaussian distribution of FWHM = 0.518 *cm*.

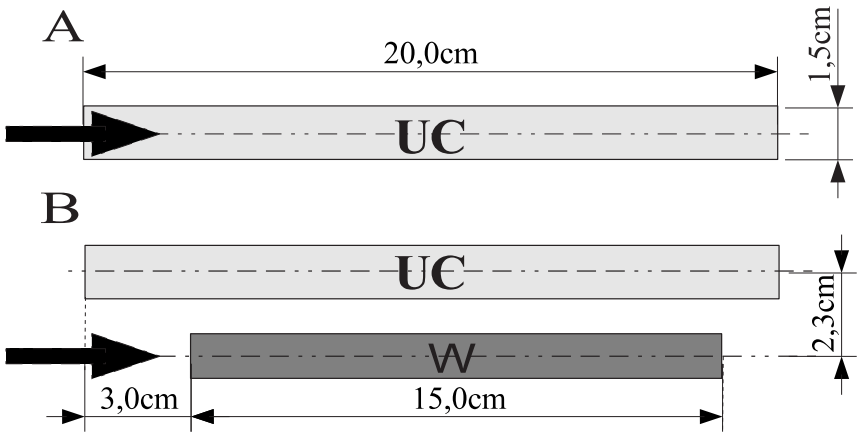

Figure 7.3: Schematic layout of direct and two-stage standard UC_x targets at ISOLDE.

receiving the proton flux in a central Hg converter (13.6 g/cm^3) and in a 50 cm otherwise standard UC_x target irradiated directly by protons. The results obtained for the existing targets are used to validate the codes upon comparison to in-target production rates, which are in turn inferred from experimental data[5]. Most times, simulations prove accurate, but even when discrepancies are found, precise gain factors can be obtained. This is indeed possible because presumed deviations in the codes cross sections tend to cancel out when making the ratios (= gain factors) between the standard and the projected targets. Thus, the most robust way to predict absolute yields consists in multiplying the measured data for the present targets by the gain factor, obtained in turn as the quotient of extraction efficiencies, both simulated. Exceptions to this rule are contemplated; numbers will be crosschecked and compared to its neighbors to obtain performing and coherent results.

[5]Validation is only possible when all parameters of the simulations are known. Otherwise, this phase serves precisely to fit those, e.g., Powder targets.

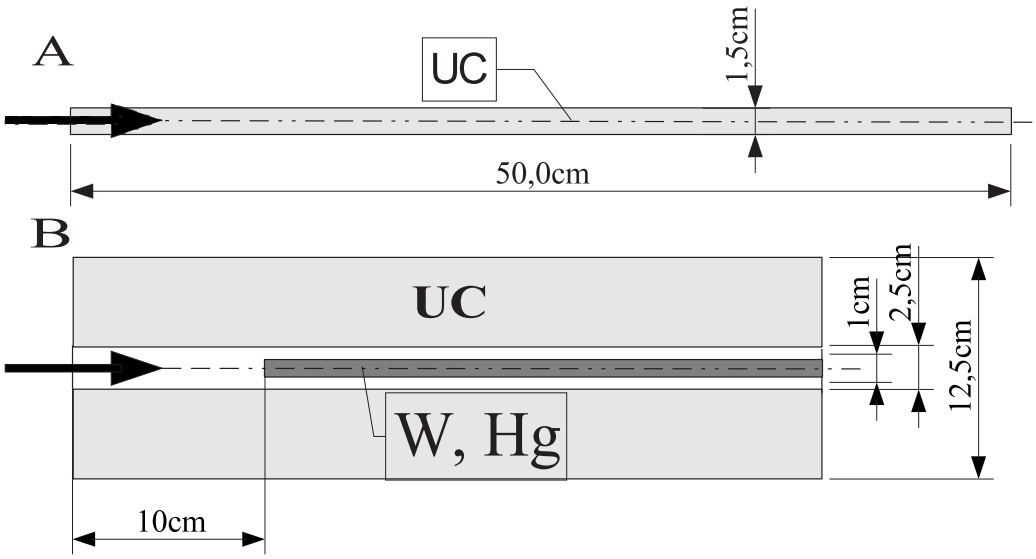

Figure 7.4: Schematic layout of possible direct and two-stage UC_x EURISOL targets.

Energy deposition.

In order to map the energy deposition of all transported particles (except for neutrinos) and the density of fissions, UC_x targets (standard and *megatarget*) and Hg converter were cylindrically meshed in cells of $\Delta r = 1$ *cm*, $\Delta L = 1$ *cm*.

From a posterior analysis on other materials, it could be concluded that for dense materials energy tends to be deposited near the beam impact area; the front face acts as a shield, so that adding material in the opposite extreme has little effect on the energy distribution in the front area. This effect is sharp in the Hg converter (and even more in W) where most reactions take place in the first 13 *cm*, reaching a maximum of about 35 kW/cm^3. For the standard UC_x target, in turn, the heating power is more homogeneous (variations taking place mainly in the longitudinal direction), and even with 50 *cm* not all 1 GeV protons are stopped, which keeps the maximum heating below 7.1 kW/*cm*. The neutron energy

spectra have the maximum at $\sim$ 3 MeV for the 0.5-*cm* radius targets in all materials. This value tends to go down as the target diameter increases.

As for the *megatarget*, simulations were performed for two different inner radii, 1.25 and 1.75 *cm*, with a constant radial thickness of 5 *cm*. Results can be compared from fig.7.5 and fig.7.6 (on pages 182 and 183). Fission distributions look almost identical, except for a small area around the inner diameter, 5 *cm* from the front face, corresponding to the maxima. Due to its closer vicinity to the converter, the small version of the *megatarget* registers a higher peak of fission in that region. The design study should evaluate if it is worthwhile to reduce the peak of energy by enlarging the target, even if that implies a loss of extraction efficiency (but also a bigger volume and, therefore, more production).

Numerically, the total number of fissions was around 0.375 fissions/proton for both versions, just slightly higher for the bigger target. Consequently, bearing in mind the importance of the extraction efficiency, here the smaller *megatarget* will be kept for the remaining calculations. The previous graph 7.5 also suggested that the converter should be pushed some 10 *cm* backwards so that the deepest *isofission* curves would be integrally contained in the target. Simulations were repeated with the shifted converter and, apparently, predictions were fulfilled (fig.7.7, page 184).

7.2.4 Simulations of the release efficiency in UC_x targets.

Scheme of the calculations.

The probability distribution of the release of isotopes from UC_x powder targets can be obtained with `RIBO` if the release parameters (Diffusion, average flight

time and average sticking time for collisions) are known. This justifies the following scheme:

1. Release curves were both simulated and searched for through the experimental database at ISOLDE.

2. Next the release parameters were adjusted by comparing the experimental and the simulated curves.

3. Then, simulations were performed for other target geometries, conserving the release descriptors.

4. Finally, a package of applications was written with the goal of automatizing the manipulation and the extrapolation of results to isotopes other than the one used at the root of this chain of computations.

Getting the release parameters. Validation.

The ISOLDE standard UC_x target is composed of a 20 *cm* long, 2 *cm* inner diameter graphite vane, filled with UC_x+C pills (a list of references on UC_x is included in [96]). The target will be linked to a FEBIAD ion source through a cold line (fig.4.1), mainly transparent to noble gases.
The principles of the definition of the free parameters are extensively exposed in chapter 3. The parameters are:

- The diffusion parameter (η) in an average value for different sizes and temperatures of the powder grain.

- The mean flight path traced by the isotope between two consecutive collisions in the target bulk, *FP*.

- The average sticking time at every collision, t_s.

(The procedure is sketched in fig.7.8.) These parameters were fitted for ^{119}Sn, ^{59}Ni, ^{70}Ga, ^{6}He, ^{23}Ne, ^{40}Ar, ^{90}Kr, ^{203}Fr in UC_x and ^{203}Fr in ThC_x. Simulations were run for three different flight paths FP_1, FP_2 and FP_3[6]. For each isotope, diffusion was analytically plotted for a candidate diffusion coefficient, $\eta_{candidate}$ and then convoluted with the three effusion profiles, all affected with a certain sticking time $t_{s(candidate)}$. A single simulated release curve was thereby obtained for each isotope by quadratically inter/extrapolating $FP_{candidate}$ from the three convoluted curves. The candidate release curve was then plotted together with the experimental one, and the triplet (η, FP, t_s)$_{candidate}$ was modified until the two curves matched. Although fitting was partially assisted by numerical error minimization, visual comparison gave at a fast glance important information on where to explore for the optimal triplet. In any case, so as to avoid pre-established conclusions, the procedure was carried out blindly, not paying attention to the consistency of the data until the end of the procedure. However, in order to save work, the sticking coefficient was set to zero for noble gases, thereafter transforming the three-dimensional problem into a two-dimensional one. Another constraint was that FP should be characteristic of the target and almost isotope independent (neglecting feeble effects as the atom/powder size, atom-surface collision peculiarities...), meaning that a single value should be found for the same matrix (one for UC_x, a different value for ThC_x, one for BeO...). Thus, optimization could not be done individually for each isotope but rather globally over all isotopes extracted from the same target.

Results of the fits can be seen and compared in table A.6 (on page 26) and the corresponding release curves are sketched in figures 7.9, 7.10. The graphs show that noble gases are simulated less accurately than other elements because their

[6]This was done just once for all the isotopes since the geometry was the same for them all.

release curves arise from fitting two parameters instead of three ($t_s = 0$), but, despite that, calculations are acceptably close to experimental results. As for the fitting parameters, in some cases the values have only been bounded because at a certain point the graphs became insensible to further changes and, therefore, precise values could not be defined. In general terms, the $\eta(A)$ dependency found was correct and the sticking times relative order inferred for Sn, Ni, Ga, agree to experimental evidences at ISOLDE.

These values constitute a first outstanding outcome of `RIBO`, but they should be used with caution: although strongly correlated, the flight path keeps a non-obvious relation to the powder porosity; the sticking time depends on the temperature and the diffusion parameter comprehends the diffusion coefficient and grain size; both susceptible to vary in circumstances other than the ones given at ISOLDE.

Simulations for *megatarget*.

The Monte Carlo code with the validated powder target capability was then used to compute the release of Kr from the concentric 40 *cm* long neutron converter target. Kr isotopes, whose birth position and amount is determined in section 7.2.3, would be generated in sheath rings of according statistical weights.

The final goal

Starting from a concentric 40 *cm* bulk of UC[7], slight modifications in the container and in the powder distribution were performed to improve the release speed. An array of channels of variable cross section could have been ideal in terms of pumping efficiency, but drilling and sustaining such channels in the powder would be technically infeasible. Therefore, only basic shaping was considered for the powder and additional modifications were done to the

[7] UC is used instead of UC_x, but the referred mixture is always the ISOLDE uranium carbide, $UC_{1.4}$.

container shape. Although simulations converged quickly, sources of uncertainty (shock wave, cross sections, sintering...) are multiple, implicating that results should be cautiously interpreted. Brief simulations scanned through the trends of the extraction efficiency from the target in terms of the inner distribution of UC_x powder. In attendance of a dedicated design study, a first order optimal configuration was found for two longitudinal cylinders of UC_x separated by an 8 *mm* wide gap. That central space acts as a pumping channel much as the effusion shortcut found in the axis of the rolled targets (chapter 6). Several lengths were tested too. Under about 0.5 s long half-lives it does not pay to have such a long target. Average release times scale linearly to the length of the target. In a similar way, the standard UC_x ISOLDE target is as performing (letting aside the incident beam factor) as the concentric target for short half-lives. Moreover, from a more analytical point of view, it is observed that, the extraction opening being so small, atoms have to follow a long path inside the target so that the original coordinates (radius, azimuth or length) are anecdotal and play a secondary role.

7.3 Results.

7.3.1 Gain factors.

Interpretation of the tables

For fixed primary beam current and ionization efficiencies the enhancement of the isotope beam production is expressed in the third column of the collection of tables displayed in the appendix section A.8, and in [96]. These gain factors (EURISOL *versus* ISOLDE) are obtained as product of the in-target production relative gain and the release efficiency gain/loss factor.

MCNPX [113] and CINDER [115] codes were combined to simulate the in-target isotope production for EURISOL target and primary beam converter

configurations as well as for ISOLDE experiments. The first simulations were then divided by the latter ones, which had been previously compared to the experimental measurements as validation proof. The gain factors obtained in this way are quite robust to minor code cross-section imprecisions since those should mainly cancel out. Cases that have not been simulated are assumed to converge to the most frequent values, apparently rather isotope independent (34 for the *megatarget*, 1.6 for the 50 cm ISOLDE target).

Likewise, the release efficiency gain/loss factors were obtained as the ratio of the simulated release fractions for EURISOL and for the present targets. This was carried out by producing the intrinsic release curves with the diffusion - effusion - sticking - ionization simulation code and then applying the corresponding decay factors. As for the former step, the simulations were primarily compared to existing experimental results or even tuned with them to obtain unknown release parameters. This step is skipped for long-lived isotopes.

7.3.2 Optimal cylindrical targets.

The same technique was applied to standard ($\Phi = 15\ cm$) cylindrical targets of variable length. The production step was uniquely computed with MCNPX and CINDER while extraction was simulated with `RIBO`.

Results can be applied to many isotopes

The release vectors expressing the number of collisions, normalized diffusion path and flight path for every history were then introduced into the analyzing package to compute the release fraction for every isotope and target length. Finally those numbers were scaled to the target length (the relative low density

and the substantial gain of time justified the assumption of proportional production)[8].

Tables in A.6 display the relative potential to produce radioisotopes in 2 *cm* diameter UC_x targets of lengths 5, 10, 20, 50 *cm*.

7.3.3 Precision of the data.

Improvement factors smaller than one.

For some short-lived isotopes the gain factor is lower than 1. This means that the use of a longer target (50 *cm* long for direct protons) has no positive effect because the improvement of the production is over-balanced by the increased losses derived from a slower extraction. This is just the case for the direct production of $^{70-76}$Ni; a target of a length progressively decreasing from 20 to 5 *cm* (moving towards exotic isotopes) will produce gains of about $10 - 40\ \%$. The same should apply for the indirect production but then the potential boost in the primary beam current allowed by the *megatarget* compensates all extraction losses.

A similar but less pronounced behavior is found in the release of Ga and Sn from UC, where preliminary MC simulations show that for the production of neutron rich isotopes through direct protons the optimal targets should have a length of about 10 *cm*.

Sources of error.

Unlike regular slabs, powder particles show a distribution “of thickness” (grain sizes) so that the diffusion curve is not pure; it arises from a combination of

[8]It should be noted that proportionality is lost due to the finite proton beam emittance, small angle scattering and other beam losses.

diffusion curves (of different η_d). It should be pointed out that the degree of porosity (percentage of free volume) is not sufficient to describe the effusing characteristics of a material. Among other effects, it is important to know whether the porosity is open or closed. At high temperatures sintering starts to close pores and trap cavities are formed deep inside the material. The effort of the effusing atoms to escape those wells is much bigger and this renders the mean free path inferred from experimental fits smaller that the one observed in microscopic pictures.

7.4 Conclusions.

- The use of MCNPX in conjunction with CINDER and with appropriate libraries can successfully predict the relative change of in-target isotope production as a function of a change in the geometry of a target. Absolute prediction is more vulnerable to cross section uncertainties, specially for proton-rich nuclei, but comparison to experimental data helps to establish the absolute level. For relative estimates, the uncertainties in the cross sections mainly cancel out and the remaining errors can be corrected by cross checking consistencies with neighboring results.

- The `RIBO` release code can cope with the release from powder-like structures and may serve as tool to infer release parameters: average sticking time (t_s), diffusion parameter (η) and average flight path (FP). The extracted parameters seem compatible to previous knowledge. However, extrapolation of results to other problems should be effectuated with care because the definition of the parameters includes some unknown variables (e.g. closed porosity).

- The concentric two-stage fission target seems to be the option that best sustains a high flux of primary protons in an axial metallic converter that ultimately produces an intense beam of neutron-rich nuclei. The combined use of the production MC codes and the release MC code with the routines for continuous media foresee yield increase factors up to 40. Then, taking into account the higher acceptance for incoming proton intensities and the expected gains in the ionization efficiency[9], the beams extracted from the concentric target could be six orders of magnitude intenser than the present ones.

- The smaller version of two concentric target options is selected and it is suggested to push the converter 10 cm backwards in order to maximize the neutron flux into the target.

[9] Due to the use of ECR ion sources.

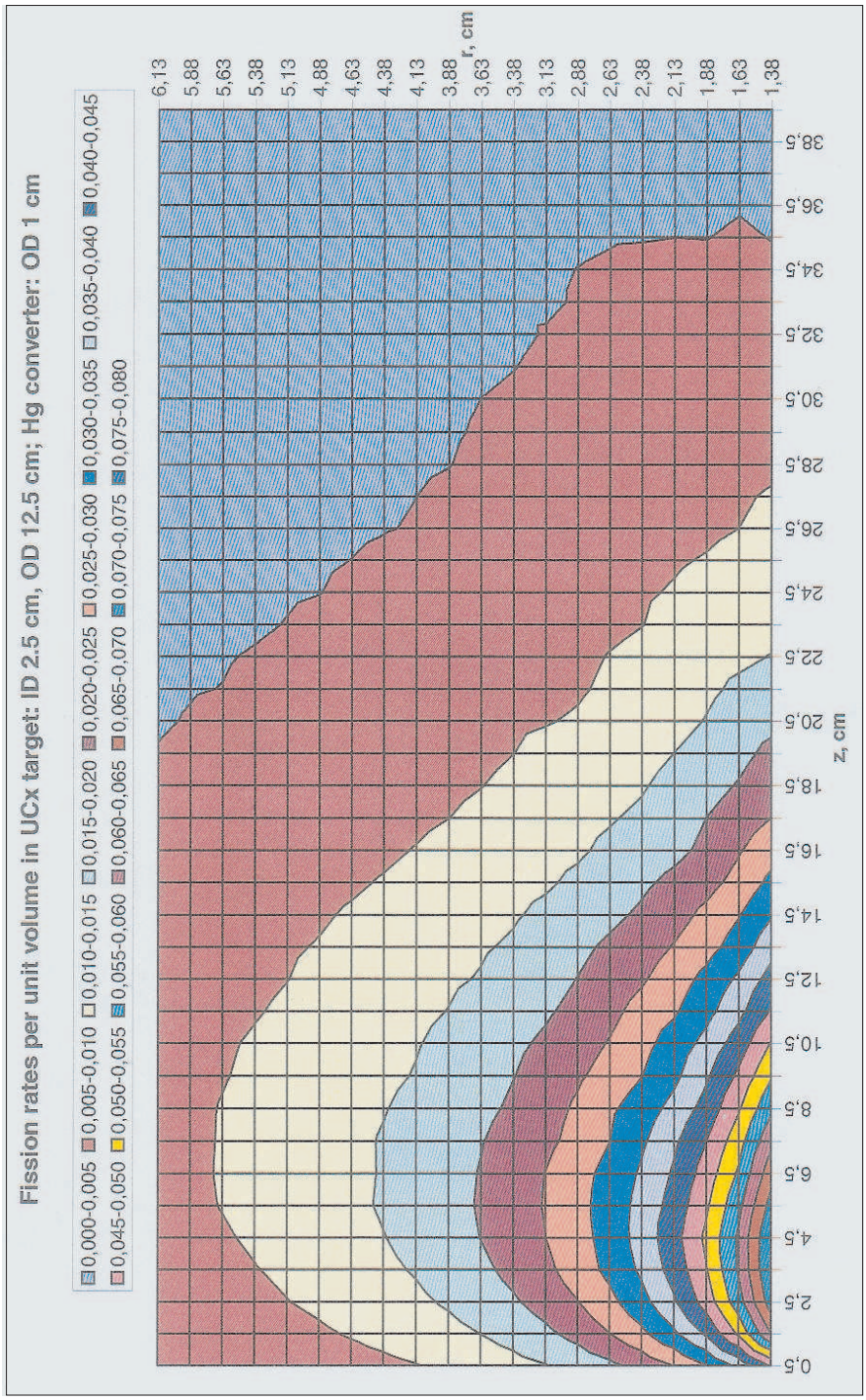

Figure 7.5: Density of fissions in the “smaller” megatarget, irradiated by secondary neutrons generated in a concentric 40 cm long mercury converter aligned with the frontend.

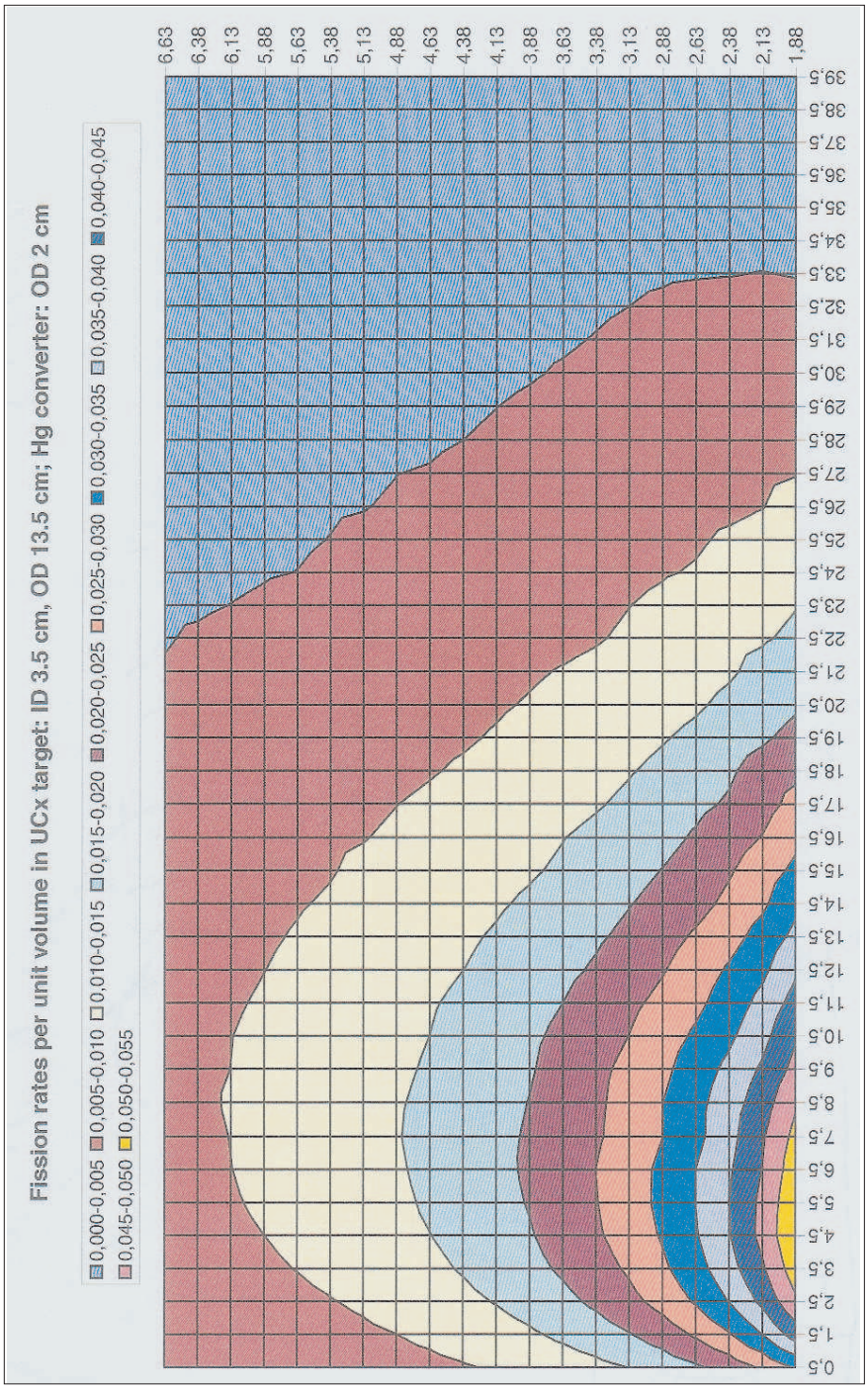

Figure 7.6: Density of fissions in the “bigger” megatarget, irradiated by secondary neutrons generated in a concentric 40 cm long mercury converter aligned with the frontend. Z units are cm.

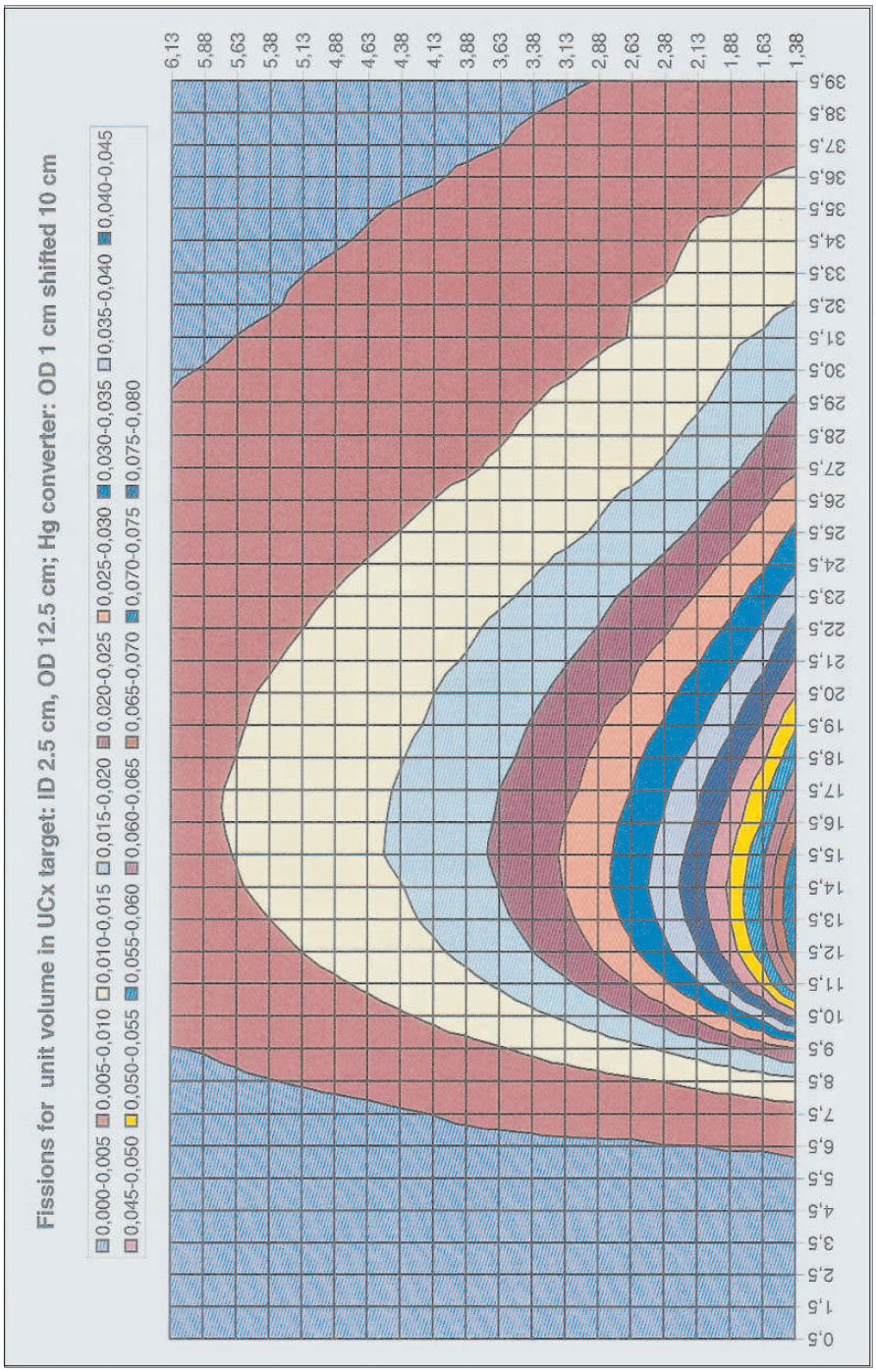

Figure 7.7: Density of fissions in the "smaller" megatarget, irradiated by secondary neutrons generated in a concentric 40 cm long mercury converter shifted 10 cm from the frontend. Z units are cm.

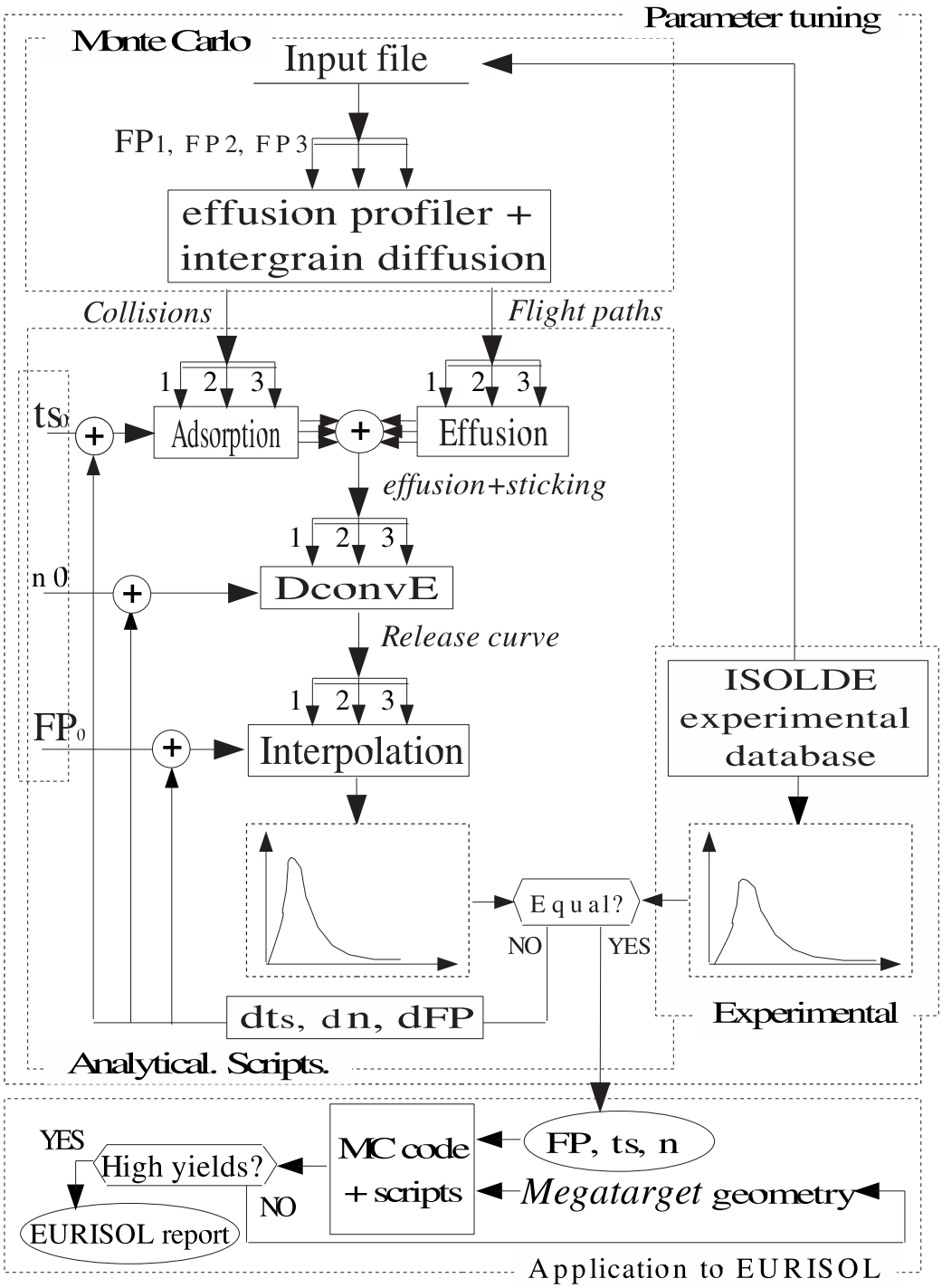

Figure 7.8: Scheme of tasks to fit the release parameters through simulations, analytic calculations and experimental data. Application for the optimization and yield prediction of megatarget.

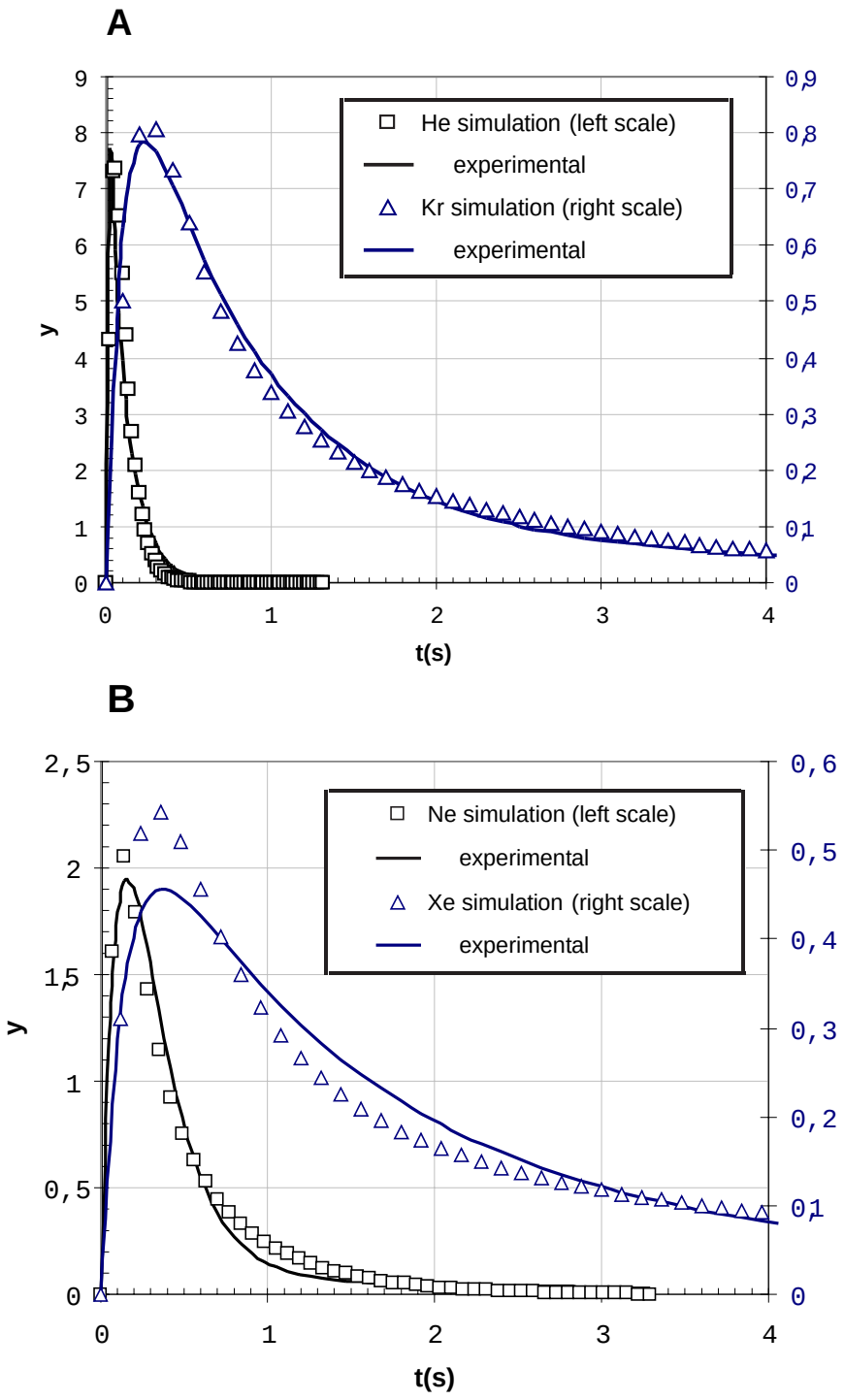

Figure 7.9: Experimental and simulated intrinsic release curves of He, Kr, Ne and Ar from standard ISOLDE UC_x targets (stable isotopes).

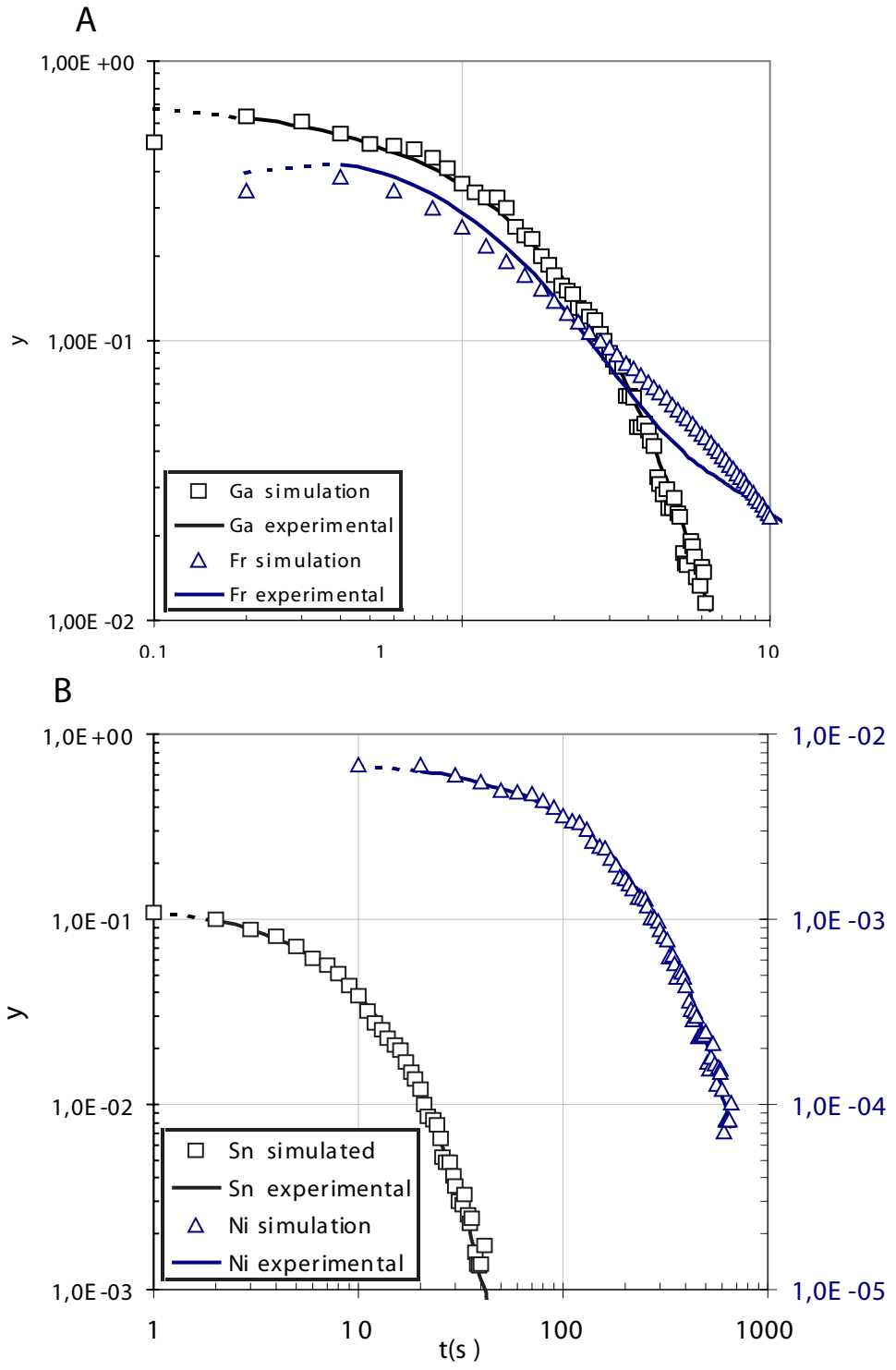

Figure 7.10: Experimental and simulated intrinsic release curves of Ga, Fr, Sn and Ni from standard ISOLDE UC_x targets (stable isotopes).

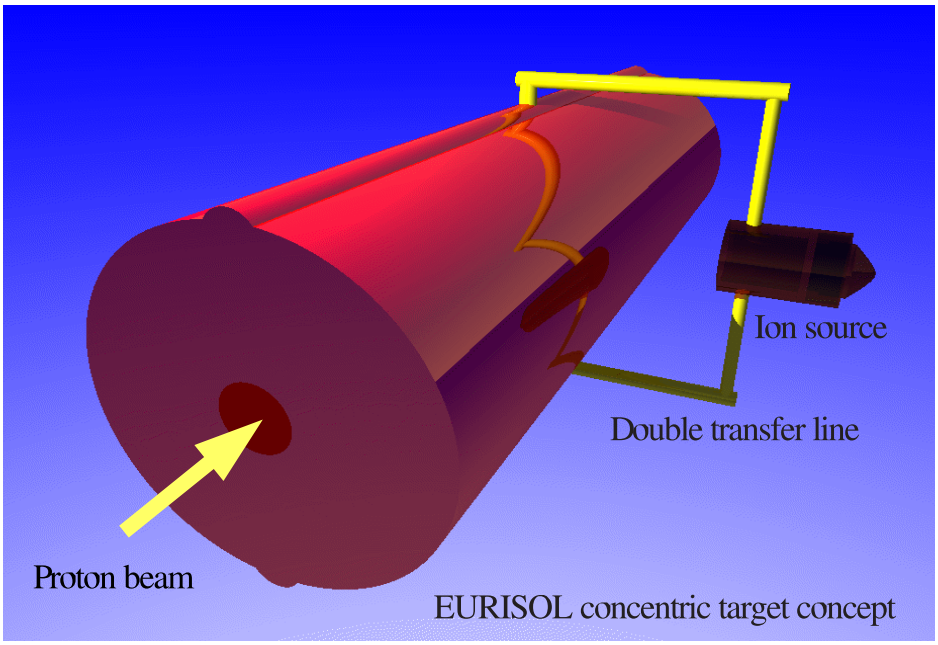

Figure 7.11: Ray tracing 3d-view of the preliminary version of the UC *EURISOL* target, coupled to the ion source through multiple MK7 lines and including effusion enhancement channels.

Chapter 8

Application to other notable research fields.

THE PREVIOUS CHAPTERS HAVE ILLUSTRATED the development and usage of some simulation and analysis tools for the optimization of the main groups of target types, namely parallel foil targets, rolled foil targets and powder targets. In this chapter yet one more type of target is introduced: the one filled with fibers (or felt). The treatment of such elements is analogue to the one described for EURISOL, but in this case the beneficiary is the βbeam neutrino factory. The work is finally completed with some more applications of different nature; desorption based studies will lead to discuss about carbon beams, then Pb beams will be computed, and finally other kinds of applications will be suggested.

8.1 Yield predictions for the βbeam neutrino factory.

The β-beam [116] constitutes a novel concept for a neutrino factory. Neutrinos are non-electrically charged, very light (massless?) particles[1], which have adopted a central role in the confirmation of a number of key theories in fundamental physics. These uncharged leptons exist in three 'flavors', electronic, muonic and tauonic and their rare interactions with matter can actually 'switch them' (make them oscillate) from one flavor to another. In fact, the detection of non-unbalanced amounts of neutrino flavors upon certain interactions shall confirm the hypothesis that attributes a non-nil mass to neutrinos. For that sake, experiments handling intense and pure beams of neutrinos are needed: the neutrino factories.

Neutrinos can be "easily" produced in two out of its three flavors. Traditionally the neutrino factory would be muon flavored; a proton beam would impinge into a target to originate pions and those would decay into muons that, in turn, after bunching, cooling and accelerating would decay into muon-neutrinos. A more novel idea consists in producing electron-neutrinos; starting again with a proton beam, short-lived β-decaying isotopes are created through the nuclear reactions induced by protons or by neutrons (specially if a proton-neutron converter is placed in between). Like the muons, the radioisotopes will then decay in a ring made of long straight sections. Each section will be pointing towards an experimental neutrino detection facility placed at long enough distances for neutrino oscillations to occur. The β-neutrino beam is singly flavored (first

[1] In words of Frederick Reynes [117], who, together with Clyde Cowan observed for the first time this sub-atomic particle in 1957, they are "the most tiny quantity of reality ever imagined by a human being."

family of leptons), well focused, it needs no lossy cooling stage, and has accurately known energy and intensity. The muon-neutrino option produces more energetic and therefore more efficiently detected neutrinos but with a lower flux and with flavor mixing

The following sections will focus on the βbeam production. The methodology that was followed is analogous to that used for the isotope production with powder targets at chapter 7. In a first stage suitable radioisotope production will be estimated and then the release efficiency will be determined. The latter step is composed of the fiber properties tuning phase and the release prediction simulations.

8.1.1 He and Ne beams from oxide fiber targets.

The mother radioisotopes should have proper β-decay half-life and endpoint energy as well as fast release properties. These criteria are fulfilled by light noble gas isotopes with half-lives of the order of 1 s: ^{18}Ne and ^{6}He.

^{6}He could be intensely produced in beryllia fiber targets (10^{13} a/s) via ^{9}Be(n,α)^{6}He reactions (fig.8.1) caused by spallation neutrons generated in a close-by heavy proton-neutron converter [118]. Such targets would combine the fast release of oxide matrices (as compared to metallic Be), the lower tendency of fibers to sinter (with respect to powders) [119] a refractory behavior (more than Li) and relatively high production (bigger than ^{6}Li(n,p)). A further step in the analysis suggests greater target sizes and, consequently, release efficiency calculations become critical.

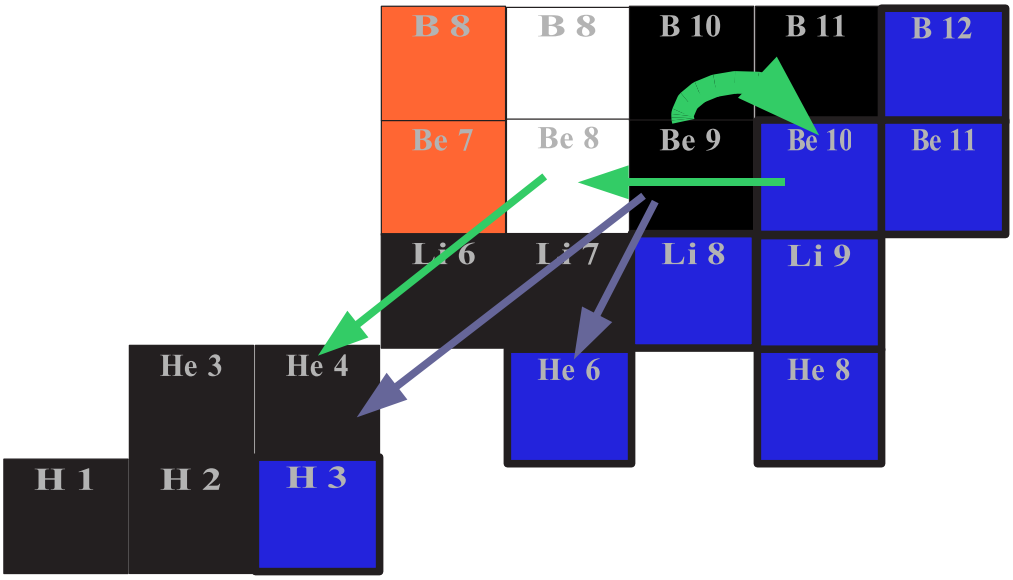

Figure 8.1: Production of ^{6}He in Be.

8.1.2 Prediction of ^{6}He and ^{18}Ne yields.

The following subsections will be dedicated to the calculation of the fraction of ^{6}He and ^{18}Ne that could be extracted from BeO fiber targets. Calculations begin with a section that analyzes the production phase; the following ones are devoted to the release efficiency computations.

The *a priori* unknown parameters for continuous media (target packing density $\sim$FP), diffusion parameter η and average sticking time t_s are fitted from recurrent simulations of the experimental data collected with ISOLDE fiber targets. This is the zeroth stage of the overall work.

8.1.3 Release of ^{6}He and ^{18}Ne from ISOLDE fiber targets.

The initial step to produce simulations capable of reliably forecasting the yield in future targets consists in finding out the particular release parameters of the target material, porosity, diffusion and sticking properties. In order to determine the

yield of ^{6}He and ^{18}Ne, both radioactive, the extraction efficiency has to be calculated. The atoms will diffuse out of the fibers (assumed to be infinite straight cylinders), they will move between those until finding a free volume through which they will effuse (eventually they will be trapped again by the fibers) until they find the way out of the system.

This process therefore depends on the following release parameters: diffusion parameter (η), geometry of the system and, in particular flight path between collisions in the powder (FP) and sticking times (t_s). In the previous list the sticking is assumed to be nil and the geometry of the walls is also known (as an input file). Nonetheless, the flight path between collisions in the fiber and the diffusion parameter are to be fitted from experimental results.

Oxide Fiber materials.

At ISOLDE experiments with different oxide targets are currently performed, e.g., ZrO_2, CeO_2, Al_2O_3 and TiO. The first three targets materials are bought from a single company, the fourth one is produced in-house by applying the standard public procedure provided by that company. Despite following all known steps, the TiO fibers become more brittle. As BeO is toxic, producing it would require a more delicate procedure; glove-box, qualified lab... This justifies putting more effort into developing the technique with TiO before trying with BeO. As a drawback, present calculations have to be based on parameters tuned from the release from other oxide targets, mainly ZrO_2.

TiO is used instead of BeO

Fitting. Considerations.

Experimental results look similar at a first glance but their corresponding fits show a substantial dispersion [52]. In fact, some fits include a fast component

rise time constant (t_r) of about 2 ms while the HV is OFF (before 6 ms)[2]. Therefore the fits of such fast rises are marginally reliable.

ISOLDE targets have a standard target container with fibers that for the calculations will be assumed to fill up the cylinder up to a level of 7 mm from the central plane. A sketch of the target-MK7 ion source input file is shown in fig.6.3. The fit of the triplet FP, D and t_s to the experimental results is reduced to the fitting of FP and D, as t_s is assumed to be 0 for He and for Ne (noble gases). However, for these release curves, the fits are rather insensitive to changes of FP, which implies that they cannot be determined with high precision.[3]

Fitting. Results.

Simulated release of ^{6}He has been successfully fitted to the CaO and ZrO_2 ISOLDE targets. The average flight path between two consecutive collisions in the fibers has been found to be 250 μm, and the corresponding diffusion inverse time constants, η were 3.16 and 2.37 s^{-1}, respectively. As for ^{18}Ne, the TiO target was also analyzed. For that last case, the optimum fitted flight path was somewhat smaller (tighter target), 100-200 μm. The diffusion inverse time constants of ^{18}Ne for CaO, ZrO_2 and TiO are 1.46, 0.711 and 0.0987 s^{-1}. All results and their corresponding release curves are summarized in table A.6 and figure 8.2.

[2]This is done to prevent discharges that could take place with the very many ions that are produced at the beginning in the air surrounding the frontend.

[3]Luckily, vague values of FP should not seriously distort derived calculations as insensitivity to FP is expected to persist.

8.1.4 Release of ^{6}He and ^{18}Ne from ISOLDE *megatarget*.

Input file.

The concentric input file *BfactHe.t* composed of 6 cells enclosed by a total of 11 surfaces has a source of He atoms that follows a Gaussian of $\sigma = 3$ cm. Fig.8.3, sketches the 10 cm BeO shell, contained in a 30 cm long oven with a central hole where the converter is introduced. The transfer line is placed close to the target front end so as to keep the ion source away from the main stream of scattered neutrons. Delay times are measured at 16 cm from the target vertical plane. Further impedances are expected although their particular shape should be conditioned by the ion source peculiarities and that altogether belongs to a design study.

Simulation of the release of ^{6}He.

The input file is simulated for FP = $250\ \mu m$ and $t_s = 0$. Effusion is convoluted with a diffusion profile of $\eta = 2.37\ s^{-1}$. The release curve that is obtained is drawn in fig.8.4.*A* together with its corresponding analytical fit. The analytical parameters that best describe the simulation results are $t_r = \ 155\ ms$, $t_f = \ 155\ ms$, $t_s = \ 650\ ms$, $\alpha = 0.97$. The release fraction for ^{6}He, whose half-life is 0.807 s, can now be computed by using 8.1 (ratio of integrals). The result is 0.574, that is, 57.4 $\%$ of the ^{6}He that is produced in the target crosses the gage before decaying.

$$\varepsilon_r = \frac{\int_0^\infty R\left(\alpha, t_r, t_f, t_s\right) \cdot \exp\left(-\frac{t}{T_{1/2}} \ln 2\right) \cdot dt}{\int_0^\infty R\left(\alpha, t_r, t_f, t_s\right) \cdot dt} \tag{8.1}$$

Simulation of the release of ^{18}Ne.

The input file is again simulated for FP = $250\ \mu m$ and $t_s = 0$. Effusion is now convoluted with a diffusion profile of $\eta = 1.46\ s^{-1}$. The corresponding release curve and its associated analytical fit are show on fig.8.4.*B*. The analytical parameters are found to be $t_r = 225\ ms$, $t_f = 740\ ms$, $t_s = 850\ ms$, $\alpha = 0.9$. These figures will cast a release fraction for ^{18}Ne ($t_{1/2} = 630\ ms$) of 36.5 $\%$, meaning that about one third of the radioactive atoms go through the gage.

Error analysis.

In spite of the fact that the method seems rather accurate, several remarks have been made as to the distorting factors and, specially to the lack of sensitivity to the average flight path (FP). In this scenario, an error propagation study of the results is worthwhile. For that sake, in the first place, simulations were carried out for FP$\pm$30 $\%$ off the nominal value FP = $250\ \mu m$. The derived release efficiencies proved to be very robust (insensible) to such variations; they changed by about 3 $\%$, thus an order of magnitude below the change on FP (30 $\%$).[4]

As for the reduced diffusion parameter, η was again shifted by $\pm$30 $\%$. The newly obtained released fractions were modified only once by some 3 $\%$. The same analysis was repeated for ^{18}Ne and sensitivity to variations in FP and η was just slightly higher than in ^{6}He. Table 8.1 summarizes these remarks.

[4]This should not be too surprising as all this section is motivated by the primary lack of sensitivity of the starting fits to the FP. Fortunately, as it was pointed out from the beginning, the imprecision in FP is rather irrelevant also for the βbeam target.

FP_0	η_-	η_0	η_+
^{6}He	55.28 *(-3.8%)*	57.47	58.70 *(+3.1%)*
^{18}Ne	34.12 *(-6.5%)*	36.48	37.90 *(+4%)*
η_0	FP_-	FP_0	FP_+
^{6}He	55.49 *(-3.4%)*	57.47	58.40 *(+1.7%)*
^{18}Ne	34.60 *(-5%)*	36.48	37.40 *(+2.5%)*

Table 8.1: Release efficiency (and relative variation with respect to the reference values) of ^{6}He and ^{18}Ne from the β-Beam neutrino target for different diffusion coefficients and fiber free flight paths. Subscripts $_-$, $_0$ and $_+$ stand for the -30 %, the reference and the +30 % values of η and FP. The offset values (%) are quoted between brackets.

8.2 Carbon beams.

ISOL beams of carbon are interesting for a multitude of applications, e.g., the ^{9}C β^+ decay to the particle unstable ^{9}B (decaying into two alphas and one proton) allows precise studies of deviations from the mirror symmetry in the $A = 9$ system. On the neutron-rich side, the break-up of the single-neutron-halo nucleus ^{19}C has been studied at in-flight facilities with very controversial results on its binding energy which could finally be solved by measuring the mass directly at ISOLTRAP. Beams of $^{9-16}$C have been produced at ISOLDE mainly in form of CO^+ [119], but the release efficiency deduced from the ratio of measured yields and known cross-sections is low: about 1.3 % in the best case. We need to find where in the target and ion source unit most of these losses occur to eliminate them. The `RIBO` MC simulation code gives the average number of collisions against each surface of the target and ion source. Let us assume an "allowed delay time" of 100 ms for each of the surfaces. Dividing that figure by the number of collisions upon the respective surface we find the "maximum allowed" desorption time per collision. With the Frenkel equation and a roughly known average temperature of the surface we can then estimate from the desorption time the "maximum allowed" desorption enthalpy (using a time

Estimation of the desorption enthalpies of C

constant $\tau_0 = 10^{-13}$ s), as shown in table 8.2. We see that all graphite and tantalum surfaces are critical since CO could chemically react with them, corresponding to an "adsorption enthalpy" of many hundred kJ/mol, i.e. far more than the "allowed" value. Wherever possible these surfaces have to be replaced by chemically inert (i.e. E_d close to 0) ones like, e.g., quartz. This could be done rather easily for the target container and the transfer lines by inserting an appropriate tube. However, the FEBIAD should be replaced by an ECRIS. The latter has neither a hot cathode nor a grid, and the plasma chamber can be made from aluminum, which has a rather inert aluminum oxide surface. This leaves now the collisions within the target material (oxide powder or fibers) as the dominant source of delays. The optimum material has to be found by measuring the desorption enthalpies of CO and CO_2 from oxide surfaces via thermo-chromatography.

Target or ion source part	Material	T $[K]$	Number of collisions	desorption $time[s](max)$	E_d max $[kJ/mol]$
Fiber target	Oxide	1273	$4.3{\cdot}10^{+5}$	$2.3{\cdot}10^{-6}$	-180
Powder target	Oxide	1273	$6.7{\cdot}10^{+7}$	$1.5{\cdot}10^{-8}$	-126
Target tube	Ta, Re, Pt	1273	$1.0{\cdot}10^{+4}$	$1.0{\cdot}10^{-4}$	-219
Vert. transfer lines	Ta	773	400	$2.5{\cdot}10^{-3}$	-154
Horiz. transfer line	Cu, steel	323	800	$1.3{\cdot}10^{-3}$	-62
I. S. before grid	steel	473	140	$7.1{\cdot}10^{-3}$	-98
Cathode	Ta	2273	10	$1.0{\cdot}10^{-1}$	-522
Grid	graphite	2273	24	$4.2{\cdot}10^{-2}$	-506
Plasma chamber	Mo, graphite	1773	80	$1.3{\cdot}10^{-2}$	-377

Table 8.2: Characterization of the surfaces of a MK7-FEBIAD target-ion source with a powder or a fiber oxide target, and simulation of the average number of collisions to these surfaces.

8.3 Pb beams.

The mean square charge radii of $^{183-189}$Pb have recently been determined by measuring the isotope shifts by in-source resonance ionization spectroscopy [120]. There is large interest in extending this study to ^{182}Pb, but the latter isotope is produced less abundantly and has a much shorter half-life: 55 ms. Therefore it is crucial to optimize the product of in-target production rate and release efficiency from the target and ion source unit. Even if this product shows to be rather constant when shortening the target length, it is still of interest to perform such an optimization. With a shorter target, less isobaric contaminations (here ^{182}Tl) and less radon diffusing through the beam-lines are produced, both being the main sources of background for the used alpha detector.

The release of Pb from a standard ISOLDE target was compared to the simulation curve described in chapter 6 adjusted for mass 183 and with free parameters FP, t_s and η, corresponding to the average flight path between two consecutive collisions in the target bulk, the average sticking time and the diffusion parameter. By fitting the simulated curve to match the experimental one, FP, t_s and η were fixed at 15 μm, $10^{-9.5\pm0.5}$s and 0.1 s^{-1}. Then, the simulations carried out in chapter 6 for different target lengths were used as input for *analyze* with the masses and half-lives of $^{181-183}$Pb. Results are summarized in table 8.3. If production of Pb isotopes were strictly proportional to the target mass, then the lengths conducting to the highest yields would approximately be somewhere between 10 to 20 mm for ^{181}Pb and then progressively higher for longer-lived isotopes. However, as observed in chapter 7, in-target production soon saturates with increasing length. This shifts the optimum length to lower values, for instance, if the 5 cm long target produced up to 40 $\%$ of the 20 cm

^{182}Pb shall be produced with a short target

production instead of 25 $\%$ then a 5-7 cm target would be optimum in ^{181}Pb yield.

A	$T_{1/2}[ms]$	$R(5)/R(20)$	$R(10)/R(20)$	$R(20)[\%]$	$R(20)/R(50)$
181	45	3.3	1.9	*4*	2.9
182	55	3.1	1.9	*5.1*	3
183	300	1.9	1.4	*27*	2.3

Table 8.3: Relative release efficiencies R(x)/R(20) for $x < 20$ cm and R(20)/R(x) for $x = 50$ cm, and R(20) for Pb isotopes in a UC_x target with a surface ionizer.

8.4 Other applications.

Among other imaginable applications, these seem quite straightforward.

- Radioactive deposition: The ability to track particles through vacuum systems can be exploited to plot radioactive deposition charts. This is achieved by simply setting sticking coefficients of the concerned surfaces and printing out the final coordinates of atoms after sticking, including time. Then with $\{x, y, z, t_0\}$ and with the decay law the radioactivity at a given point can be evaluated. The `RIBO` code has been upgraded to handle these calculations, as a reply to the needs expressed by MAFF[5] [121], a partner of the TARGISOL [122] project.

- Heat transfer calculations: heat conduction is indeed described through diffusion equations. Moreover, heat radiation describes the interchange of 'particles' (photons) between surfaces at different temperatures. To compute heat radiation the geometric factors between sometimes complicated geometries are needed in conjunction with the surface properties, emissivity and reflectivity, strongly linked to the surface conditions (roughness, finish, etc.). All these ingredients are explicitly or potentially included in the MC code.

- Dosimetry calculations. The code does not compute the interactions of atoms with matter. However, for many dosimetry calculations it is enough to know the viewing angle intercepted between the target and the emitter, which could easily be calculated with the simulation program.

[5] Munich accelerator for fission fragments

8.5 Conclusions.

- The `RIBO` code has been applied to predict the decay losses of ^{6}He and ^{18}Ne from concentric BeO fiber targets. The method implied the estimation of the diffusion time constant in CaO, ZrO_2 and TiO, showing decreasing values for the specified order. The release fractions for this geometry and conditions were 57 $\%$ (^{6}He) and 36 $\%$ (^{18}Ne) and the involved errors were below 3 $\%$ for presumed uncertainties of 30 $\%$ in the inferred parameters (diffusion time constant and average free flight path).

- Simulations casting the number of collisions of C atoms with the elements of an ISOLDE powder target - MK7 FEBIAD, together with thermo-chromatography adsorption enthalpy measurements (now being completed), lay out the way for the optimization of carbon beams.

- In the thick target isotope production assumption, the yield of Pb isotopes as a function of the target length is rather flat, the excess/defect of production being compensated by a lower/higher release fraction. Dedicated production simulations should be performed to verify if shorter targets (most likely in the region 7-12 cm) could be better Pb producers.

- The 3-D structure of the code and the different memory cards (number of collisions, absorption coefficient) and collision models allow the usage and customization of the `RIBO` code for other applications in diverse domains such as dosimetry, heat transfer and radioactive deposition.

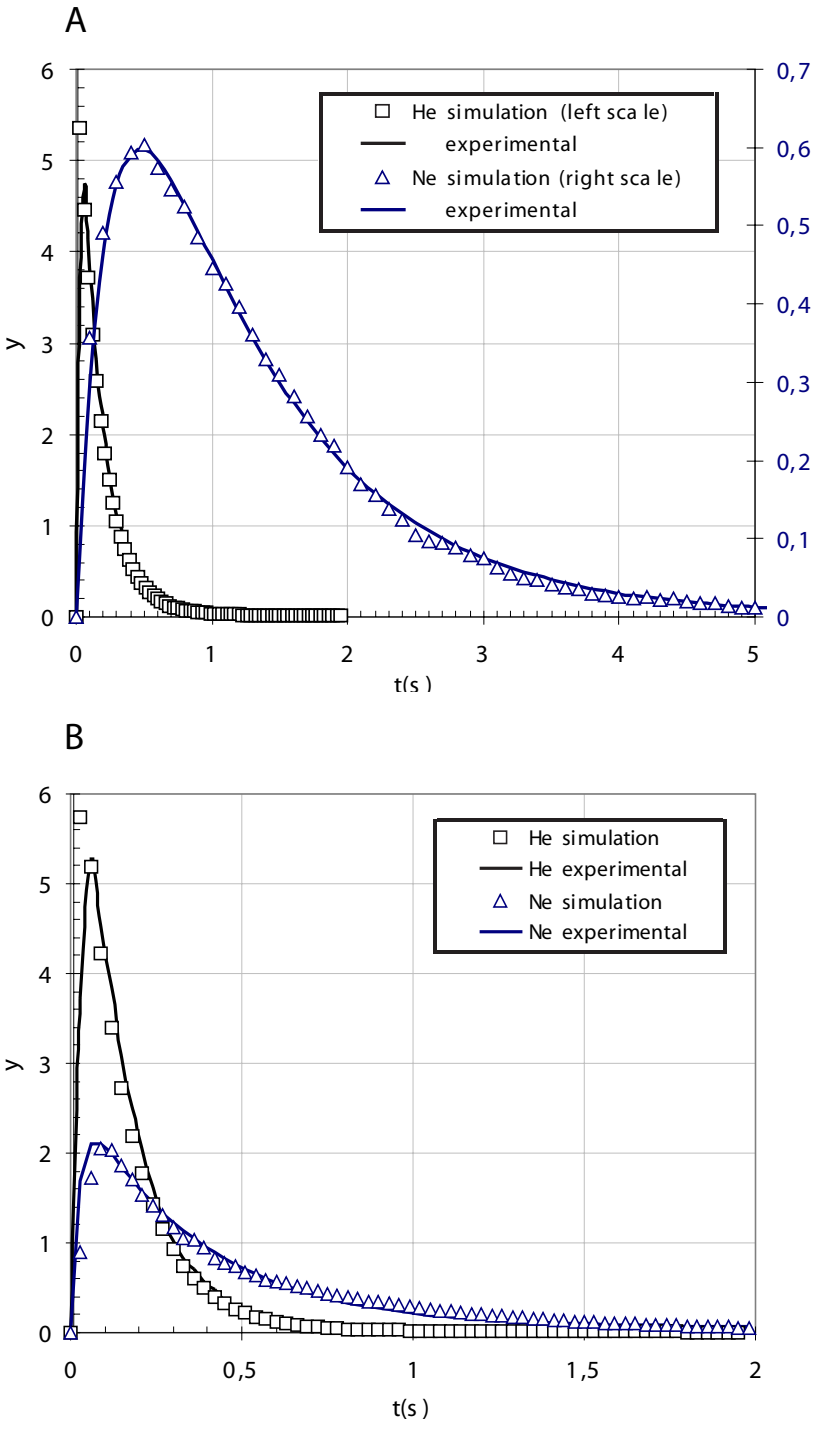

Figure 8.2: Experimental and simulated intrinsic release curves of He, and Ne from standard **A**) ZrO_2 and **B**) CaO targets (stable isotopes).

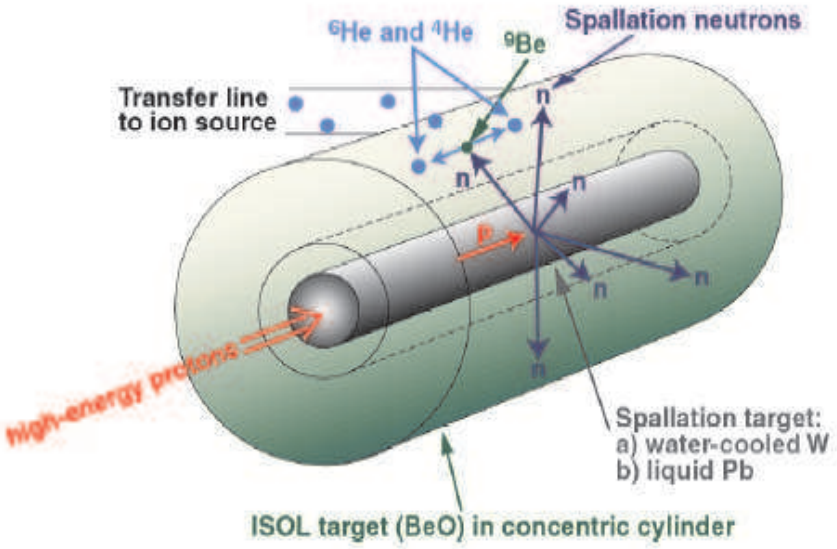

Figure 8.3: Schematic representation of the two stage BeO target.

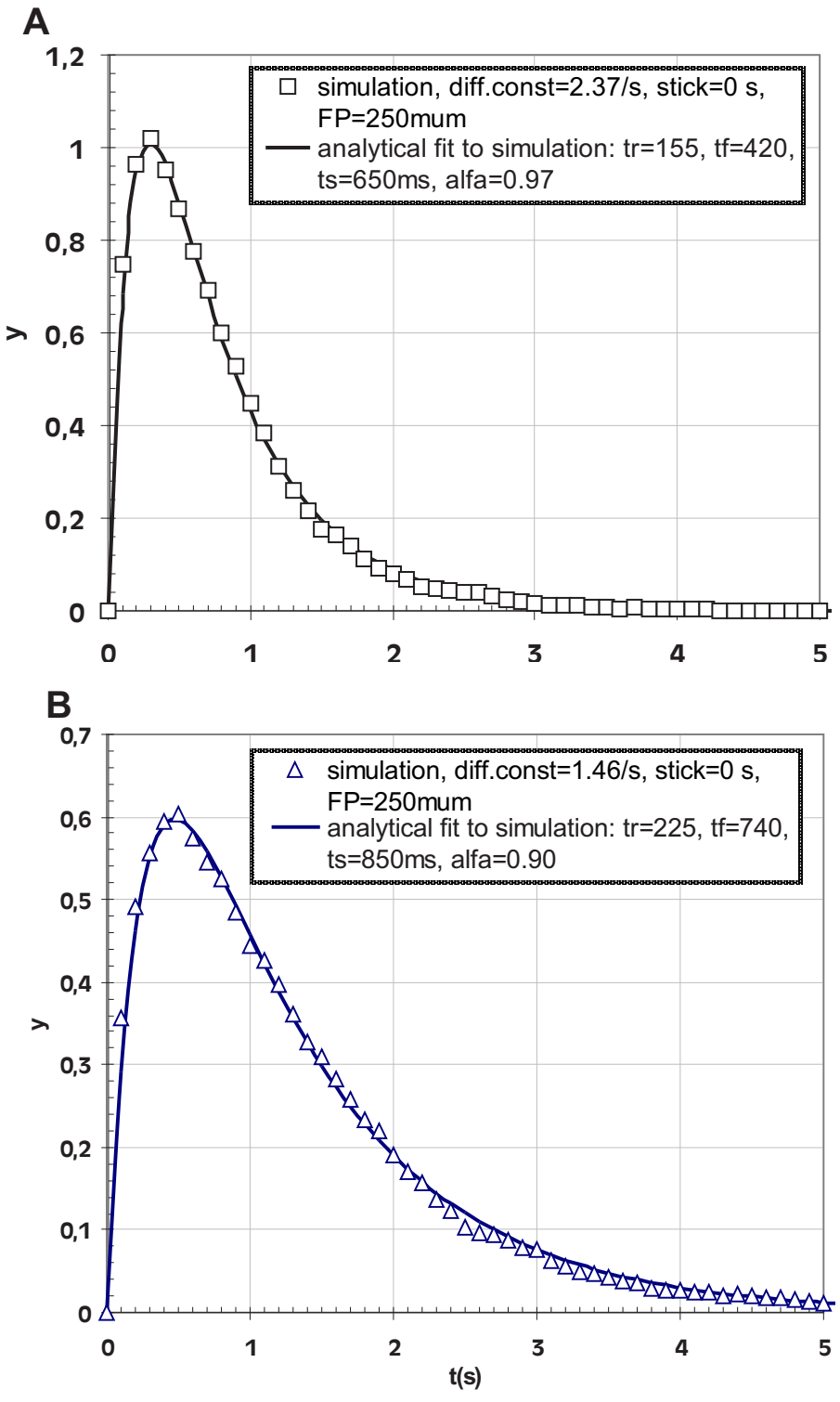

Figure 8.4: Simulated and fitted curves for the release of **A**) ^{6}He and **B**) ^{18}Ne from a 30 cm long 24-4 cm diameter BeO target.

Reference List

[1] The ISOLDE facility. website. http://isolde.web.cern.ch/ISOLDE/.

[2] L. Maunoury, O. Bajeat, R. Lichtenthäler, and A. Villari. Temperature simulations for the SPIRAL ISOL target. *Nucl. Inst. and Meth.* ***B***, 2001. submitted.

[3] R. Lichtenthäler et al. *A simulation of the temperature distribution in the* SPIRAL *target*. Report, GANIL, Caen, August 1997.

[4] G.L. Saksaganskii. *Molecular Flow in Complex Vacuum Systems*. Gordon & Breach Science Publishers, New York, 1988.

[5] C. Kittel. *Introduction to Solid State Physics*. John Wiley & Sons Inc, 7^{th} edition, 1996.

[6] CERN. *Physics Analysis Workstation*. CERN, paw.support@cern.ch. wwwasd.web.cern.ch/wwwasd/paw.

[7] Persistence Of Vision Pty. Ltd. *Persistence Of Vision*. Pty. Ltd, Williamstown, Victoria, Australia, 2004. Software.

[8] M. Webster. *The Merriam Webster Dictionary*. Pocket Books, 1984.

[9] M.E. Glicksman. *Diffusion in solids: field theory, solid-state principles and applications*. NY Wiley, 2000.

[10] J. Crank. *The Mathematics of Diffusion*. Oxford University Press, 1980.

[11] A.E. Fick. *Ann. Phys.*, 94:59, 1855.

[12] A.D. LeClaire. *Prog. Metal. Phys.*, 306, 1949.

[13] G.J. Beyer. *Nucl. Inst. and Meth.*, 146:419, 1977.

[14] M. Fujioka and Y. Arai. Diffusion of radioisotopes from solids in the form of foils, fibers and particles. *Nucl. Inst. and Meth.*, 186:409–412, 1981.

[15] J.R. Beeler. Difusion tensor for slab geometry. Technical Report, Cincinnati, APEX-488, 2001. General Electric Co. Aircraft Nuclear Propulsion Dept.

[16] C. Lau et al. Recent studies to improve release properties from thick ISOL fission targets. Institut de Physique Nucleaire d'Orsay.

[17] B. Mustapha and J.A. Nolen. Optimization of ISOL targets based on monte-carlo simulations of ion release curves. *Nucl. Inst. and Meth.* ***B***, 204:286–292, 2003.

[18] A. Latuszynski. Investigation of the diffusion process at electromagnetic separation of the radioactive isotopes of rare-earth elements. *Nucl. Inst. and Meth.*, 123:489–494, 1975.

[19] R. Kirchner. *Nucl. Inst. and Meth.* ***B***, 80:186, 1992.

[20] Y. Yang. *The Monte Carlo Simulation of Physical Vapor Deposition*. PhD thesis, University of Virginia, 2000.

[21] E. Hecht. *Optics*. Schaum's Outline Series. McGraw-Hill, 1975.

[22] L.B. Loeb. *The Kinetic Theory of Gases*, volume VII. New York, McGraw-Hill, second edition, 1934.

[23] M.N. Kogan. *Rarefied Gas Dynamics*, volume 88-89. Plenum Press, 1969.

[24] Latech. Topography. website. latech.edu/tech/engr.

[25] Inc. J& L Specialty Steel. Fantastic finishes. website.

[26] Inc. Precision Devices. Surface metrology guide. surface profile parameters. website. predev.com/smg.

[27] D. Greenberg et al. A framework for realistic image synthesis. In Turner Whitted, editor, *Annual Conference Series*, pages 477–494. SIGRAPH, August 1997.

[28] B. Cabral, N. Max, and R. Springmeyer. Bidirectional reflectance functions from surface bump maps. computer graphics. In Turner Whitted, editor, *Annual Conference Series*, volume 21. SIGRAPH, 1987.

[29] J.C. Maxwell. *On the Dynamical Theory of Gases*. F.R.S.L.& E, 1866.

[30] J.C. Maxwell. *On Stresses in Rarified Gases arising from Inequalities of Temperature*. Univ. Cambridge, 1878.

[31] Basic illumination, diffuse reflection using lambert's law.

[32] J.H. Lambert. *Photometria sive de mensure de gratibus luminis, colorum umbrae*. Eberhard Klett, 1760.

[33] B.T. Phong. Illumination for computer generated images. *ACM*, 18(6):311–317, 1975.

[34] K. Torrance and E. Sparrow. Theory for off-specular reflection from rough surfaces. *Journal of the Optical Society of America*, 57:1105–1114, 1967.

[35] R.J. Wagner. Shadowing of randomly rough surfaces. *Journal of the Acoustical Society of America*, 41(1):138–147, 1966.

[36] J.F. Blinn. Models of light reflection for computer synthesized pictures. *ACM*, 19(10):542–547, 1977. SIGGRAPH 77.

[37] R.L. Cook and K.E. Torrance. A reflectance model for computer graphics. In *Annual Conference Series*, volume 15, pages 307–316. SIGRAPH, 1981.

[38] P. Poulin and A. Fournier. A model for anisotropic reflection. *Computer Graphics*, 24:273–282., 1990.

[39] A. Siber. *Theory of thermal energy inert atom scattering from surface vibrations*. PhD thesis, Zagreb Institute of Physics, 2000.

[40] N.V. Blinov and D.V. Kul'ginov. Quasi-classical description of the single-phonon scattering of an atom by a surface in the diffraction regime. *Zh. Tekh. Fiz.*, 65:93–105, 1995.

[41] A. Siber. The simplest formulas for the prediction of an outcome of inelastic atom-surface scattering in a semiclassical regime, a short overview. Private Communication, 2001.

[42] B. Baule. *Ann. Phys.*, 145, 1914.

[43] C. Romano and C. López. Capacidad caloríca y temperatura de debye: cálculos y mediciones. report, Laboratorio 5 - Facultad de Ciencias Exactas y Naturales - Universidad de Buenos Aires, 2001.

[44] M.G. Saint-Laurent. Première approche de la diffusion - effusion pour des éléments lourds produits par SPIRAL phase ii. GANIL internal document, 2001.

[45] J.C. Bilheux and G.D. Alton. Simulation of the effusive-flow of reactive gases in tubular transport systems: Radioactive ion beams applications. *Nucl. Inst. and Meth.* ***B***, 2003.

[46] R. Kirchner et al. An ion source with storage capability for bunched beam release and controlled chemical separation. *Nucl. Inst. and Meth.* ***A***, 247:265–280, 1986.

[47] B. Eichler, S. Hbener, and H. Roßsbach. Adsorption flüchtiger metalle auf metallischen oberflächen und möglichkeiten ihrer anwendung in der kernchemie - berechnung der adsorptionsenthalpien der actinoide. *Rep. ZfK-560, Zentralinstitut für Kernforschung*, 1985.

[48] U. Köster. *Yields and spectroscopy of radioactive isotopes at LOHENGRIN and* ISOLDE. PhD thesis, Physik-Department der Technischen Universität München, 2000.

[49] R. Clausius. *The Mechanical Theory of Heat*. MacMillan, London, 1879.

[50] R. Clausius. *Annals of Science*, 14:185–196, 1958.

[51] J. Delafosse and G. Mongodin. Les calcules de la technique du vide. Technical report, Soc. Française des Ingénieurs et Techniciens du Vide, 1961.

[52] J. Lettry et al. Pulse shape of the ISOLDE radioactive ion beams. *Nucl. Inst. and Meth.* ***B***, 126:130–134, 1997.

[53] J.R.J. Bennett. An improved analytical model of diffusion through the RIST target. *Nucl. Inst. and Meth.* ***B***, pages 211–214, 2003.

[54] S. Dushman. *Scientific Foundations of Vacuum Technique*. Mir, Moscow, 1964.

[55] P. Clausing. *Ann. Phys.*, 5(12):961, 1932.

[56] B.P. Porodnov et al. *Problems of Atomic Science and Technology*, volume 2 of *High-Vacuum Physics and Technology Series*. Kharkov Physicotechnical Institute, 1977.

[57] L.N. Rozanov and V.V. Shchenev. *Electric Vacuum and Gas-Discharge Instruments, 1*. Number 4 in Electronic Engineering. 1974.

[58] J.N. Chubb. Monte Carlo studies of free molecular gas flow though various vacuum structures. In *Proc* 4^{th} *Intl Vacuum Congress*, 1968.

[59] Landolt Börnstein. *Diffusion in Solid Metals and Alloys*, volume 26 of *Numerical Data and Functional Relationships in Science and Technology*. Springer-Verlag, 1990.

[60] A. Soukhanov. *Encarta World English Dictionary*. St. Martin's Press, 1999.

[61] S. Johnson. *The American Heritage Dictionary of the English Language*. NEW YORK: BARTLEBY.COM, fourth edition, 2000.

[62] H. Ravn and B.W. Allardyce. *On-Line Mass Separators*, volume 8 of *Treatise on Heavy-Ion Science*, pages 363–439. CERN-EP-87-105; CERN-PS-87-50-SC, 1989.

[63] R. Kirchner. International conference of low energy ion beams. volume 38, page 29. Institute of Physics, Bristol, Inst. Phys. Conf. Ser., 1978.

[64] R. Neugart. *Progress in Atomic Spectroscopy*. Plenum Press, New York and London, 1987.

[65] F. Buchinger et al. *Nucl. Inst. and Meth.* ***B***, 202:253, 1982.

[66] W. Klempt, J. Bonn, and R. Neugart. *Phys. Lett.* ***B***, 82:47, 1979.

[67] A. D. McNaught and A. Wilkinson. *IUPAC compendium of Chemical Terminology, The Gold Book.* Blackwell Science, second edition, 1997.

[68] I. Langmuir and K.H. Kingdon. Thermoionic effects caused by vapours of alkali metals. In *Proc. Roy. Soc. London*, volume 107, pages 61–79, 1925.

[69] SIMION 3D^{TM}. *Ion and Electon Optics Software*. www.sisweb.com/simion.htm.

[70] R. Kirchner and E. Roeckl. Investigation of gaseous discharge ion sources for isotope separation on-line. *Nucl. Inst. and Meth.*, 13, 1976.

[71] W. Lotz. *Z. Phys*, 232:101, 1970.

[72] V.A. Bernshtam, Yu V. Ralchenko, and Y. Maron. Empirical formula for cross section of direct electron-impact ionization of ions. *J. Phys* ***B****: At. Mol. Opt. Phys.*, 33:5025–5032, 2000.

[73] Rice University. Electron-impact ionization cross sections. webpage, 2004. www.ruf.rice.edu/ atmol/data.

[74] Computer Simulation Technology. *The advanced Simulation Tool for Electromagnetic Analysis and Design MAFIA-4*. www.cst.de.

[75] P. Spä dtke. *Kobra3-INP*. Scientific Software development, 2001.

[76] J.D. Jackson. *Classical Electrodynamics*. John Wiley & Sons, New York NY, second edition, 1975.

[77] P. Strehl. Beam instrumentation and diagnostics. GSI-darmstadt, Joint Universities Accelerator School 2000 lecture notes, 2000.

[78] J.R.J. Bennett. Targets for the production of high intensity radioactive ion beams. *Nucl. Inst. and Meth.* ***B***, 126:105–112, 1997.

[79] J.R.J. Bennett. Effusion in RNB targets, a simple conductive approach. *Nucl. Inst. and Meth.* ***B***, 155, 1999.

[80] J.R.J. Bennett. Measurements of intense beams of ^{11}Li from a Tantalum foil target. *Nucl. Inst. and Meth.* ***B***, 155, 1999.

[81] A. Cobis, D.V. Fedorov, and A.S. Jensen. The continuum structure of the borromean halo nucleus ^{11}Li. *Phys. Lett.* ***B***, 424, 1998.

[82] E. Garrido, D.V. Fedorov, and A.S. Jensen. Spin-dependent effective interactions for halo nuclei. *Phys. Rev.* ***C***, 68, 2003.

[83] G.J. Beyer et al. The role of diffusion in ISOL targets for the production of radioactive ion beams. *Nucl. Inst. and Meth.* ***B***, page 225, 2003.

[84] A. Kankainen and M. Santana Leitner et al. Optimization of Kripton yields for rp-process at ISOLDE (CERN). *Nucl. Inst. and Meth.* ***A***, 746:433c–436c, 2004.

[85] R.K. Wallace and S.E. Woosley. Explosive hydrogen burning. *Astrophys. J. Suppl*, 45:389, 1981.

[86] B. Blank et al. *Phys. Rev. Lett.*, 74:4611, 1995.

[87] A. Jokinen et al. Proton instability of ^{73}Rb. *Zeit. Phys.* ***A***, 355:227–230, 1996.

[88] X.J. Xu et al. *Phys. Rev.* ***C***, 55:553, 1997.

[89] CERN. Experiment IS394. ISOLDE experiment, September 2002.

[90] T. Giles et al. The high resolution spectrometer at ISOLDE. *Nucl. Inst. and Meth.* ***B***, suppl.(204):497–501, 2003.

[91] M. Oinonen et al. Beta-decay half-lives of sup ^{70}Kr and sup ^{74}Rb. *Nucl. Phys.* ***A***, 701:613–620, 2002.

[92] M. Oinonen et al. β decay of the proton-rich $t_z = -1/2$ nucleus, ^{71}Kr. *Phys. Rev.* ***C***, 56:745–752, 1997.

[93] A. Joinet. *La production de faisceaux d'ions radioactives chimiquement reactifs par separation en ligne*. PhD thesis, IPN Orsay, 2003.

[94] T. Bjørnstad et al. *Nucl. Inst. and Meth.* ***B***, 26:174, 1987.

[95] K. Perajarvi, U.C Bergmann, V.N. Fedoseyev, A. Joinetand U. Koester, C. Lau, J. Lettry, H. Ravn, M. Santana Leitner, and the ISOLDE collaboration. Studies of release properties of ISOLDE targets. *Nucl. Inst. and Meth.* ***B***, 204:272–277, 2003.

[96] EURISOL TIS group. Targets and ion sources for EURISOL. the EURISOL report. Published by GANIL, December 2003. www.ganil.fr/eurisol.

[97] J.S. Hendricks et al. MCNPX, version 2.5.e. Manual, Los Alamos National Laboratory. New Mexico., 2004. mcnpx.lanl.gov/.

[98] A. Fassò, A. Ferrari, and P.R. Sala. Electron-photon transport in FLUKA: status. In F. Barao, M. Nakagawa, L. Tavora, and P. Vaz, editors, *Proceedings of the MonteCarlo 2000 Conference, Lisbon, October 23–26 2000*, pages 159–164. Springer-Verlag Berlin, October 2001.

[99] A. Fassò, A. Ferrari, J. Ranft, and P.R. Sala. FLUKA: Status and prospective for hadronic applications. In A. Kling, F. Barao, M. Nakagawa, L. Tavora, and P. Vaz, editors, *Proceedings of the MonteCarlo 2000 Conference, Lisbon, October 23–26 2000*, pages 955–960. Springer-Verlag Berlin, October 2001.

[100] EURISOL project. The EURISOL report. Published by GANIL, December 2003. www.ganil.fr/eurisol.

[101] CERN 86-05. ISOLDE *Users Guide*. CERN GE-23 Switzerland.

[102] J.A. Nolen. 3^{rd} Internat. Conf. on Radioactive Nuclear Beams, D.J. Morrissey, Editions Frontieres, Gif-sur-Yvette, 1993.

[103] C. Lau et al. Production of neutron-rich surface ionised nuclides at PARRNe. *Nucl. Inst. and Meth.* ***B***, 204:246, 2003.

[104] B. Roussiere et al. Release properties of UC_x and molten U targets. *Nucl. Inst. and Meth.* ***B***, 194:151–163, 2002.

[105] F. Clapier et al. *Phys. Rev.*, (ST-AB1):013, 1998.

[106] F. Ibrahim et al. Photofission for the production of radioactive beams: experimental data from an on-line measurement. *Eur. Phys. J.* ***A***, 15:357–360, 2002.

[107] R. Díaz, J. Gallego, and M. Santana. Validation of the Monte Carlo code MCNP4b for the coupled transport of electrons and neutrons. Master's thesis, Politechnic Univeristy of Catalonia UCP-ETSEIB, 1999.

[108] L. Maunoury. *Production de faisceaux d'ions radioactifs multichargés pour* SPIRAL. PhD thesis, GANIL, 1998. GANIL T98 01.

[109] SPES collaboration. SPES project study. Technical Report LNL-INFN (REP) 145/99, INFN Legnaro, 1999. www.lnl.infn.it/spes.

[110] G. Auger et al. High intensity beams at GANIL and future opportunities: LINAG. GANIL report, 2001.

[111] IFMIF. Ifmif project (international fusion materials irradiation facility). www.frascati.enea.it/ifmif/.

[112] J.A. Nolen et al. Development of windowless liquid lithium targets for fragmentation and fission of 400-kw uranium beams. *Nucl. Inst. and Meth.* ***B***, 204, 2003.

[113] L.S. Waters. MCNPX^{TM} *USER's MANUAL*. Los Alamos National Laboratory, 1999.

[114] V. McLane. ENDF-201, ENDF/B-VI summary documentation supplement 1, ENDF/HE-VI summary documentation. Brookhaven National Lab., Upton, NY (United States), 1996.

[115] W.B. Wilson, T.R. England, and K.A. Van Riper. Status of CINDER90 codes and data. Knoxville, Tennessee, USA., September 1998. Los Alamos National Laboratory, 4^{th} Workshop on Simulating Accelerator Radiation Environments.

[116] Beta beam site. beta-beam.web.cern.ch/beta-beam/.

[117] F. Reynes and C.L. Cowan. The neutrino. *Nature*, 1956.

[118] H.L. Ravn. The CERN target and horn concept for a neutrino factory based on muon beams. Tsukuba, Japan, 2002. CERN, NuFACT01.

[119] U. Köster et al. Oxide fiber targets at ISOLDE. *Nucl. Inst. and Meth.* ***B***, 204:303–313, 2003.

[120] ISOLDE collaboration. Study of the neutron deficient Pb and Bi isotopes by simultaneous atomic- and nuclear spectroscopy. ISOLDE Experiment IS407.

[121] T.v. Egidy et al. The Munich Accelerator for Fission Fragments (MAFF) at the new reactor FRM ii. *Acta-Physica-Slovaca*, 49(1):107–116, 1999.

[122] U. Köster et al. The TARGISOL project. EU-project HPRI-CT-2001-50033.

[123] N.V. Mokhov. *The* MARS *Code System User's Guide, Version 13(95) Reference Manual*. Fermilab, 1995.

[124] N.V. Mokhov. *Status of MARS Code*. Fermilab, fermilab-conf-03/053 edition, 2002. www-ap.fnal.gov/MARS.

[125] S. Agostinelli et al. Geant4, a simulation toolkit. *Nucl. Inst. and Meth.* ***A***, (506):250–303, 2003. wwwasd.web.cern.ch/wwwasd/geant4/geant4.html.

[126] H.M. Kalos and A.P. Whitlock. *Monte Carlo methods*. New York, Wiley & Sons, 1986.

Appendix A

Ancillary software and Physical models.

A.1 Vacuum theory.

The link between the Kinetic Theory, diffuse reflection and the tables of conductances is usually taken for granted and seldom proved. Due to its key importance for the central subject of the thesis (effusion), the principal premises will be shown below.

The starting point is the law derived by Clausius, that expresses the flux of impacting particles (Φ) onto a surface in terms of their average speed (c) and the density of those (n).

$$\Phi = \frac{c}{4} \cdot n \tag{A.1}$$

And in differential form:

$$d\Phi = \frac{\vec{v}}{4} \cdot dn \tag{A.2}$$

Now, the classical tangential momentum (k_i) transferred by a fraction of atoms dn of mass m and speed v to a differential of surface dS over a time lap dt and the corresponding integrated momentum (K) are:

$$\left.\begin{array}{c} k_i = v \cdot m \\ dK = k_i \cdot d\Phi \cdot dS \cdot dt \end{array}\right\} \Rightarrow K = \frac{1}{4} \cdot dS \cdot dt \cdot \int k_i \cdot dn \tag{A.3}$$

In A.3 the integral can be operated if the Maxwell Boltzmann distribution is assumed for the speeds (v) of the atoms. Moreover, the expression will depend on the average speed (c), which, in turn can be written in terms of the pressure (P) by using a known formula of the kinetic theory of gasses. Thus, these two expressions:

$$dn = \frac{4 \cdot n}{\alpha^3 \cdot \sqrt{\pi}} \cdot v^2 \cdot e^{-\left(\frac{c}{v}\right)^2} \cdot dv \tag{A.4}$$

and

$$P = \frac{\pi}{8} \cdot \rho \cdot \bar{c}^2 \tag{A.5}$$

enable to write the total transfer of tangential kinetic moment as:

$$K_{MB} = \frac{3\,\pi}{32} \cdot \rho \cdot \bar{v} \cdot v \cdot dS \cdot dt \tag{A.6}$$

where

$$\alpha = \frac{c \cdot \sqrt{\pi}}{2} \tag{A.7}$$

and the mass density density (ρ) is:

$$n \cdot m = \rho \tag{A.8}$$

This can be written in terms of the cross section of the pipe (O)

$$K_{gas} = \frac{3}{8} \cdot \sqrt{\frac{\pi}{2}} \cdot \rho \cdot \sqrt{\frac{P}{\rho}} \cdot v \cdot O \cdot dl \cdot dt \tag{A.9}$$

Now the counter-force is, trivially,

$$K_P = -S \cdot \left(\frac{dP}{dl} \right) \cdot dl \cdot dt \tag{A.10}$$

The flow of atoms through the pipe is:

$$Q_t = P \cdot v \cdot {}^{O}\!/_{\rho} \tag{A.11}$$

Then, combining A.9, A.10 and A.11:

$$Q_t = -\frac{S^2}{O} \cdot \left(\frac{8}{3} \sqrt{\frac{2}{\pi}} \right) \cdot \sqrt{\frac{P}{\rho}} \cdot \frac{dP}{dl} \tag{A.12}$$

Integrating the equation the coefficient of ΔP is identified as the conductance of the system.

$$Q = \frac{\Delta P}{Z} = C \cdot \Delta P \tag{A.13}$$

A.2 Diffusion and analysis software.

The off-line analysis of diffusion, and effusion data (including sticking) requires a number of tools that can grind the release curve for any change of the set of release parameters (diffusion time connstant, momenta of the atoms, average sticking time, porosity of the powder. . .). In particular, quite often diffusion curves are exclusively generated analytically from the existing formulas and the results need then to be convoluted with the time histograms of effusion. These tasks, *a priori* elementary, should be conducted with care, specially in sensitive regions like that of the release peaks. Prospective users may be interested in the Visual Basic scripts given below, which include diffusion generation, diffusion coefficient fitters, fine convoluters that generate a first order spline prior to convolute continuous functions (instead of discrete points). . .

Some of the used functions are:

CONVOLUTE performs a simple discrete convolution of two distributions of points of the same time grid.

```
FUNCTION CONVOLUTE(d1 As Range, d2 As Range, initRow As Range)
  Dim i, j, k, length As Integer
  Dim a As Double
  k = initRow.Row - d1(1).Row + 1
  i = 1                                                          1
  a = 0
  IF (k = 1) THEN
     ELSE
     DO
        j = 1                                                    2
     DO
     IF (i + j = k) THEN
        a = a + d1(i) * d2(j)
     END
        j = j + 1                                                3
     LOOP UNTIL j = k
```

```
            i = i + 1
        LOOP UNTIL i = k
    END IF
    CONVOLUTE = a
END FUNCTION
```

IDiff computes the diffusion release fraction from a foil, fiber or powder of diffusion parameter *gamma* after a time *T*.

```
FUNCTION IDiff(T As Double, gamma As Double, target As Integer)
  Dim Pi, P, beta, j0n, N, Nmax, i As Double
  Pi = 3.1415927
  Pi2 = Pi * Pi
  Nmax = 2000
  P = 0
  i = 1
  IF (target = 1) THEN
      N = 0
      DO
          i = 2 * N + 1
          P = P + Exp(-(i * i * T * gamma)) / (i * i)
          N = N + 1
      LOOP UNTIL N = Nmax
      P = (8 / Pi2) * P
  END IF
  IF (target = 2) THEN
      N = 1
      DO
          beta = (N - 0.25) * Pi
          j0n = beta + ((1 / 8) * (beta^(-1))) - ((31 / 384)
      * (beta^(-3))) + ((3779 / 15360) * (beta^(-5)))
      - (0.6598931 * (beta^ (-7)))
          P = P + Exp(-(((j0n / Pi)^2) * 4 * T * gamma))
      / (j0n^2)
          N = N + 1
      LOOP UNTIL N = Nmax
      P = 4 * P
  END IF
  IF (target = 3) THEN
      N = 1
      DO
          P = P + Exp(-(N * N * 4 * T * gamma)) / (N * N)
          N = N + 1
      LOOP UNTIL N = Nmax
      P = (6 / Pi2) * P
  END IF
  IDiff = 1 - P
END FUNCTION
```

DconvE convolutes Diffusion and effusion. It generates the Diffusion profile, does a linear spline for effusion and diffusion and then convolutes the two functions.

```
FUNCTION DconvE(T1 As Double, e As Range, iRow As Range, gamma As Double,
target As Integer)
   Dim i, ni, j, k, length, N, Nmax As Integer
   Dim P, x, C, m, Pi2, Pi, ani, bni, tn, td, mmax, beta, j0n As Double
   Dim a(10000) As Double                                                  12
   Dim b(10000) As Double
   Pi2 = 9.869604
   Pi = 3.149265
   mmax = 50
   'Pi2 = 9                                                                13
   N = 2
   a(N) = e(N) / T1
   b(N) = 0
   Nmax = e.Rows.Count
   N = N + 1                                                               14
   DO
       a(N) = (e(N) - e(N - 1)) / (2 * T1)
       b(N) = e(N) - a(N) * ((2 * N - 3) * T1)
       N = N + 1
   LOOP UNTIL N > Nmax + 0.1                                               15
   N = iRow.Row - e(1).Row + 1
   tn = (2 * N - 2) * T1
   ni = 1
   P = 0
   IF (target = 1) THEN                                                    16
     DO
        td = tn - (2 * ni - 2) * T1
        ani = -a(ni + 1)
        bni = b(ni + 1) + a(ni + 1) * tn
        m = 0                                                              17
        DO
             i = 2 * m + 1
             C = -(i * i * gamma)
             P = P - (gamma / C) * Exp(C * (td - T1)) * (ani * ((td - T1)
      - (1 / C)) + bni)                                                    18
```

```
            P = P + (gamma / C) * Exp(C * (td)) * (ani * ((td) - (1 / C))
        + bni)
            m = m + 1 + 0
         LOOP UNTIL m > mmax
         ani = -a(ni + 2)                                                    19
         bni = b(ni + 2) + a(ni + 2) * tn
         m = 0
         DO
            i = 2 * m + 1
            C = -(i * i * gamma)                                             20
            P = P - (gamma / C) * Exp(C * (td - 2 * T1)) * (ani * ((td - 2
        * T1) - (1 / C)) + bni)
            P = P + (gamma / C) * Exp(C * (td - T1)) * (ani * ((td - T1) -
        (1 / C)) + bni)
            m = m + 1                                                        21
         LOOP UNTIL m > mmax
         ni = ni + 1
      LOOP UNTIL ni > N - 0.9
      P = (8 / Pi2) * P
      IF (N + 0.1 $<$ 2) THEN                                                22
         DconvE = 0
      ELSE
         DconvE = P
      END IF
   END IF                                                                    23
   IF (target = 2) THEN
      DO
         td = tn - (2 * ni - 2) * T1
         ani = -a(ni + 1)
         bni = b(ni + 1) + a(ni + 1) * tn                                    24
         m = 1
         DO
            beta = (m - 0.25) * Pi
            j0n = beta + ((1 / 8) * (beta^(-1))) - ((31 / 384) *
           (beta^(-3))) + ((3779 / 15360) * (beta^(-5)))                     25
           - (0.6598931 * (beta^(-7)))
            C = -((j0n / Pi)^2) * 4 * gamma
            P = P - (1 / (j0n^2)) * Exp(C * (td - T1)) * (ani *
           ((td - T1) - (1 / C)) + bni)
            P = P + (1 / (j0n^2)) * Exp(C * (td)) * (ani * ((td)             26
```

```
        - (1 / C)) + bni)
          m = m + 1 + 0
      LOOP UNTIL m > mmax
      ani = -a(ni + 2)
      bni = b(ni + 2) + a(ni + 2) * tn                                    27
      m = 1
      DO
          beta = (m - 0.25) * Pi
          j0n = beta + ((1 / 8) * (beta^(-1))) - ((31 / 384) *
        (beta^(-3))) + ((3779 / 15360) * (beta^(-5)))                     28
        - (0.6598931 * (beta^(-7)))
          C = -((j0n / Pi)^2) * 4 * gamma
          P = P - (1 / (j0n^2)) * Exp(C * (td - 2 * T1)) *
        (ani * ((td - 2 * T1) - (1 / C)) + bni)
          P = P + (1 / (j0n^2)) * Exp(C * (td - T1)) * (ani             29
        * ((td - T1) - (1 / C)) + bni)
          m = m + 1
      LOOP UNTIL m > mmax
      ni = ni + 1
  LOOP UNTIL ni > N - 0.9                                                 30
  P = -4 * P
  IF (N + 0.1 < 2) THEN
      DconvE = 0
  ELSE
      DconvE = P                                                          31
  END IF
END IF
IF (target = 3) THEN
  DO
      td = tn - (2 * ni - 2) * T1                                         32
      ani = -a(ni + 1)
      bni = b(ni + 1) + a(ni + 1) * tn
      m = 1
      DO
          i = 2 * m                                                       33
          C = -(i * i * gamma)
          P = P - (gamma / C) * Exp(C * (td - T1)) * (ani * ((td - T1)
        - (1 / C)) + bni)
          P = P + (gamma / C) * Exp(C * (td)) * (ani * ((td) - (1 / C))
        + bni)                                                            34
```

```
            m = m + 1 + 0
        LOOP UNTIL} m > mmax
        ani = -a(ni + 2)
        bni = b(ni + 2) + a(ni + 2) * tn
        m = 1
        DO
            i = 2 * m
            C = -(i * i * gamma)
            P = P - (gamma / C) * Exp(C * (td - 2 * T1))
          * (ani * ((td - 2 * T1) - (1 / C)) + bni)
            P = P + (gamma / C) * Exp(C * (td - T1))
          * (ani * ((td - T1) - (1 / C)) + bni)
            m = m + 1
        LOOP UNTIL m > mmax
        ni = ni + 1
    LOOP UNTIL ni > N - 0.9
    P = 4 * (6 / Pi2) * P
    IF (N + 0.1 < 2) THEN
        DconvE = 0
    ELSE
        DconvE = P
    END IF
  END IF
END FUNCTION
```

FRelease computes the extraction efficiency for a given half-life and a release curve. It takes into account the tail, for which it makes an decaying exponential fit.

```
FUNCTION FRelease(T As Range, DE As Range, tao As Double)
  Dim N, Nmax As Integer
  Dim C, Irel, tot, tail, Itail As Double
  N = 1
  Nmax = DE.Rows.Count
  C = (Log(2) / Log(Exp(1))) / tao
  Irel = 0
  tot = 0
  DO
      Irel = Irel + DE(N) * Exp(-C * T(N))
```

```
        tot = tot + DE(N)
        N = N + 1
    LOOP UNTIL N > Nmax + 0.1
    N = 1
    Irel = Irel * T(1)
    tail = 1 - tot * T(1)
    Itail = tail * (DE(Nmax) / (DE(Nmax) + (C * tail))) * Exp(-C * T(Nmax))
    'FRelease = (Irel + Itail) / (tot + tail)
    FRelease = Irel + Itail
END FUNCTION
```

41

42

SquareFit fits tree pairs (x_i,y_i) i=1:3 to a second degree equation $y = a \cdot x^2 + b \cdot x + c$, then it gives the y prediction for a given x. s

```
FUNCTION SquareFit(x1 As Double, x2 As Double, x3 As Double, y1 As Double,
y2 As Double, y3 As Double, x As Double)
    Dim a, b, C, d, x12, x22, x32 As Double
    x12 = x1 * x1
    x22 = x2 * x2
    x32 = x3 * x3
    a = -(x1 * (y2 - y3) - x2 * (y1 - y3) + x3 * (y1 - y2))
    b = (x12 * (y2 - y3) - x22 * (y1 - y3) + x32 * (y1 - y2))
    C = (x12 * (x2 * y3 - x3 * y2) - x22 * (x1 * y3 - x3 * y1)
+ x32 * (x1 * y2 - x2 * y1))
    d = (x1 - x2) * (x1 - x3) * (x2 - x3)
    SquareFit = (a * x * x + b * x + C) / d
END FUNCTION
```

43

44

Besides these functions, designed to run as a VB macro in a worksheet, a set of FORTRAN applications were developed to compute the release of various isotopes from a single run. The following programs form part of this package: **start analyze histogram FractR tableR table2**. They require the diffusion applications: **Diffusion difftime**.

A.3 Collisions.

When an atom reaches a surface the code checks whether it is a wall or just an 'etherial' frontier between two communicating cells. In the second case the hosting cell number would be updated to that of the new cell and the simulation would carry on with the same 7-coordinates (3 for the position 3 for the speed and 1 for time). Otherwise, the code will simulate a collision with the wall:

```
SUBROUTINE bounce(nsur,SUR,surn,x,y,z,ux,uy,uz,COL1,COL2,COL3,COL4,A,type)
```

This subroutine will start by computing the inner normal unity vector (gradx,grady,gradz) of the surface (*surn*) at the impact point (x,y,z); this will serve as a reference vector to calculate the direction of the reflected atom. First the gradient will be computed to the equation of the surface, then changed of sign and finally normalized.

```
SUBROUTINE grad(x2,y2,z2,xy,xz,yz,x1,y1,z1,x,y,z,gradx,grady,gradz,surn)
  real*8 x,y,z,gradx,grady,gradz,modgrad
  real*8 x2,y2,z2,xy,xz,yz,x1,y1,z1
  integer*4 surn
  gradx = 2*x*x2 + y*xy + z*xz + x1                                    45
  grady = 2*y*y2 + x*xy + z*yz + y1
  gradz = 2*z*z2 + x*xz + y*yz + z1
  CALL signGrad(gradx,grady,gradz,surn)
  CALL renorm(gradx,grady,gradz)
END                                                                    46
```

A.3.1 Elastic.

If elastic collisions have been activated at runtime ('S' option, see B.4) then the code will apply the Snell law of reflection (incident and reflected azimuthal angles are equal, polar angle changes in π rad) of reflection on the velocity vector (ux,uy,uz) taking the inner unitary vector as central bisecting angle.

```
      SUBROUTINE snell(ux,uy,uz,gradx,grady,gradz)
        real*8 ux,uy,uz,gradx,grady,gradz,k
        k = (gradx*ux+grady*uy+gradz*uz)
        ux = ux - 2 * k * gradx
        uy = uy - 2 * k * grady                                    47
        uz = uz - 2 * k * gradz
      END
```

As for the energy, it is not modified.

A.3.2 Inelastic.

If collisions are forced to be inelastic at runtime ('B' option, see B.4) then the code will compute the cosine law around the inner versor (the subprogram *surfaceBase* constructs a local orthogonal reference system with one axis parallel to the inner unitary vector):

```
      SUBROUTINE cosineLaw(Swx,Swy,Swz,ux,uy,uz)
        real*8 zero,alpha,beta
        real*8 Sux,Suy,Suz,Svx,Svy,Svz,Swx,Swy,Swz,ux,uy,uz
        external rand
        zero=0.0                                                   48
C       alpha = ACOS(1-(2*rand(zero)))/2.0
        alpha = asin(rand(zero))
        beta = 6.2831854 * rand(zero)
        CALL surfaceBase(Sux,Suy,Suz,Svx,Svy,Svz,Swx,Swy,Swz)
        a = SIN(alpha) * COS(beta)                                 49
        b = SIN(alpha) * SIN(beta)
        c = COS(alpha)
        ux = (a * Sux) + (b * Svx) + (c * Swx)
        uy = (a * Suy) + (b * Svy) + (c * Swy)
        uz = (a * Suz) + (b * Svz) + (c * Swz)                     50
        CALL renorm(ux,uy,uz)
      END
```

```
      SUBROUTINE cosineLaw(Swx,Swy,Swz,ux,uy,uz)
        real*8 zero,alpha,beta
```

reference system oriented towards the gradient

```
      real*8 Sux,Suy,Suz,Svx,Svy,Svz,Swx,Swy,Swz,ux,uy,uz
      external rand
      zero=0.0                                                          51
C     alpha = ACOS(1-(2*rand(zero)))/2.0
      alpha = asin(rand(zero))
      beta = 6.2831854 * rand(zero)
      CALL surfaceBase(Sux,Suy,Suz,Svx,Svy,Svz,Swx,Swy,Swz)
      a = SIN(alpha) * COS(beta)                                        52
      b = SIN(alpha) * SIN(beta)
      c = COS(alpha)
      ux = (a * Sux) + (b * Svx) + (c * Swx)
      uy = (a * Suy) + (b * Svy) + (c * Swy)
      uz = (a * Suz) + (b * Svz) + (c * Swz)                            53
      CALL renorm(ux,uy,uz)
      END
```

In addition, inelastic collisions imply a transfer of energy between the surface and the projectile. Normally the thermalisation is complete (option 'Y' at runtime, consult the manual at B.4, page 45 of the annex section). The Maxwell-Boltzmann distribution is then used to sample/fix the energy of the outgoing atom.

```
      SUBROUTINE Boltzmann(ux,uy,uz,T,A,mode)
      real*8 e,vMB,vmp,T,c,scale,zero,P1,P2,Pmax
      real*8 ux,uy,uz,A
      character*80 mode
      external rand                                                     54
      zero=0.0
      vmp=sqrt(16629*T/A)
      IF (mode.eq.'N') THEN
         e=2.718281828
         scale=10*vmp                                                   55
         Pmax=(vmp*vmp)/e
         P1=1.0
         P2=0.0
\marginlabel{Rejection method\\}
         DO WHILE (P1.gt.P2)                                            56
            P1=Pmax*rand(zero)
```

```
            vMB=scale*rand(zero)
            P2=(vMB*vMB)*exp(-((vMB/vmp)**2.0))
        END DO
    ELSE
        vMB=1.128379*vmp
    END IF
    CALL VECprodNUM(ux,uy,uz,vMB)
END
```

A.3.3 Semi classical model.

This is the implementation of the model described in section 3.2.4.[58]

```
    SUBROUTINE Diffract(gradx,grady,gradz,ux,uy,uz,sigma,alattice,
Td,T,A,m,E,deltaE,COL2,COL3,mode)
    real*8 gradx,grady,gradz,ux,uy,uz,m,alattice,Td,T,A
    real*8 g,mu,sigma,sigmaE,E,deltaE,deltavSu,deltavSv,deltaEv
    real*8 Sux,Suy,Suz,Svx,Svy,Svz,Swx,Swy,Swz
    real*8 vSu,vSv,vSw,v
    real*8 C,h,k
    real*8 COL2,COL3
    character*12 mode
    *******
    Swx=gradx
    Swy=grady
    Swz=gradz
    CALL surfaceBase(Sux,Suy,Suz,Svx,Svy,Svz,Swx,Swy,Swz)
    vSu=ux*Sux+uy*Suy+uz*Suz
    vSv=ux*Svx+uy*Svy+uz*Svz
    *******
    sigmaE=sigma
C   alattice is the lattice characteristic distance in A
    alattice=3.3013
C   C=(1.6*alattice*k*Td)/(1.41*h)
    C=2.35744*alattice*Td
    sigma=sigmaE/(m*C)
    mu=0
```

[58] The **Gaussian** function samples a number **g** from a gaussian distribution whose mean value and variance are *mu* and *sigma*.

```
      CALL gaussian(g,mu,sigma)                                    63
      deltavSu=g
      CALL gaussian(g,mu,sigma)
      deltavSv=g
      vSu=vSu+deltavSu
      vSv=vSv+deltavSv                                             64
      *******
      v=SQRT((2/m)*(E-deltaE))
      vSw=SQRT((v*v)-(vSu*vSu)-(vSv*vSv))
      IF (vSw.ge.0) THEN
         COL3 = COL3 + 1                                           65
         ux=(vSu*Sux)+(vSv*Svx)+(vSw*Swx)
         uy=(vSu*Suy)+(vSv*Svy)+(vSw*Swy)
         uz=(vSu*Suz)+(vSv*Svz)+(vSw*Swz)
      ELSE
         COL2 = COL2 + 1                                           66
         CALL cosineLaw(gradx,grady,gradz,ux,uy,uz)
         CALL Boltzmann(ux,uy,uz,T,A,mode)
      END IF
   END
```

Relevant data are expressed at A.2 on page 24 of this annex.

A.3.4 Phong.

The 'latent' option for Phong collisions has been implemented as follows:

```
\marginlabel{\textbf{n} is correlated with\\ the roughness\\}

   C SUBROUTINE Poth(ux,uy,uz,gradx,grady,gradz,rc)
   C     real*8 ux,uy,uz
   C     real*8 Sux,Suy,Suz,Svx,Svy,Svz,Swx,Swy,Swz,gradx,grady,gradz  67
   C     real*8 rc,alpha,beta,cosphi,n,zero
   C     external rand
   C
   C     zero=0.0
   C     n=2.7181**(rc*5.887)                                         68
   CCC     Compute the cos(phi)=R*grad
   C     cosphi= gradx*ux+grady*uy+gradz*uz
   CCC     Sample alpha from cos(alpha) between 0 and 90-phi
```

```
C     alpha = asin(rand(zero)*cosphi)
CCC     Sample the distribution cos(alpha)**n By REJECTION from cos(alpha)   69
C     DO WHILE (rand(zero).ge.(cos(alpha))**(n-1.0))
C        alpha = asin(rand(zero)*cosphi)
C     END DO
CCC     Now sample the azimuthal angle.
C     beta=rand(zero)*2*3.14159265                                            70
C     Swx=gradx
C     Swy=grady
C     Swz=gradz
C     CALL surfaceBase(Sux,Suy,Suz,Svx,Svy,Svz,Swx,Swy,Swz)
C     a = SIN(alpha) * COS(beta)                                              71
C     b = SIN(alpha) * SIN(beta)
C     c = COS(alpha)
C     ux = a * Sux + b * Svx + c * Swx
C     uy = a * Suy + b * Svy + c * Swy
C     uz = a * Suz + b * Svz + c * Swz                                        72
C     CALL renorm(ux,uy,uz)
C END
```

A.4 Electron beam impact plasma ionization cross sections. plION.

A summarized enumeration of the species available for the database of electron beam ionization cross sections, *plion.dat* is:

Atoms: H, He, Ne, Ar, Kr, Xe.

Small Molecules: H_2, N_2*, N_2+, O_2*, NH_3, H_2O, D_2O, H_3O^+, CO, NO, CO_2. *The ones used in FEBIAD sources*

Atmospheric molecules: H_2S, N_2O, NO_2, O_3, CS, COS, S_2, SO_2, CS_2.

Hydrocarbons: CH, CH_2, CH_3, CH_4, C_2H_2, C_2H_4, C_2H_6, C_3H_8, C_6H_6.

Oxigenates: CHO, CH_2O, C_2H_3O.

Silicon compounds: SiH, SiH_2, SiH_3, SiH_4, Si_2H_6, $Si(CH_3)_4$.

Ge Hydrides: GeH, GeH_2, GeH_3, GeH_4, Ge_2H_6.

SiF_x: SiF, SiF_2, SiF_3.

SF_x: SF, SF_2, SF_3, SF_4, SF_5, SF_6.

Fluorocarbons: CF, CF_2, CF_3, C_2F_6, C_3F_8.

Boron compounds: BCl, BCl_2, BCl_3, BF, BF_2, BF_3.

Other compounds: CH_3Br, CH_3Cl, CH_3F, CH_3I, CH_3OH, C_2H_5OH, C_3H_7OH, SF_6.

plION is a subfunction of the main program, though it can be used separately for the calculation of plasma ionization cross sections at a given ion and electron energy.

A.5 Surface ionization. *surfION*.

The program SURFION is used internally by the MC `RIBO` code, though it can be executed separately for the calculation of the probability of surface ionization of an atom or compound upon impact to a given substrate. The databases consulted by SURFION are:

A.5.1 workf.dat

```
Work functions for several atoms. first column=sumZ. second Wf(eV) third type:
0:element;1:Boride;2:Carbide;3:Oxide;4:CeCompounds,...
6     4.5    0
22    3.9    0
40    4.12   0
```

41 4.19 0
42 7.15 0
72 3.6 0
73 4.25 0
74 4.54 0
75 4.96 0
77 5.27 0
78 5.32 0
90 3.38 0
32 3.9 1
87 2.7 1
28 3.35 2
46 2.18 2
78 3.5 2
79 3.14 2
80 3.6 2
102 3.5 2
50 4.7 3
56 3.96 3
74 2.3 3
186 4.65 3
90 4.96 3
106 2.6 3
443 2.69 4
0

A.5.2 sion.dat

This is the database. Add elements but end by 0 and add comments only in this line.

Z Wi[eV] Ae[eV g0 g+ g-
1 13.6 0.75 2 1 1
2 24.59 0 1 1 2
3 5.39 0.62 2 1 1
4 9.32 0 1 2 0
5 8.3 0.28 2 1 1
6 11.26 1.26 1 2 4
7 14.53 0 4 1 0
8 13.62 1.46 5 4 4
9 17.42 3.4 4 5 1

10	21.56	0	1	4	0
11	5.14	0.55	2	1	1
12	7.65	0	1	2	0
13	5.99	0.43	2	1	1
14	8.15	1.39	1	2	4
15	10.49	0.75	4	1	5
16	10.36	2.08	5	4	4
17	12.97	3.61	4	5	1
18	15.76	0	1	4	0
19	4.34	0.5	2	1	1
20	6.11	0.02	1	2	0
21	6.56	0.19	4	3	5
22	6.83	0.08	5	4	4
23	6.75	0.53	4	1	1
24	6.77	0.68	7	6	6
25	7.43	0	6	7	0
26	7.9	0.15	9	10	10
27	7.88	0.66	10	9	9
28	7.64	1.16	9	11	6
29	7.73	1.24	2	1	1
30	9.39	0	1	2	0
31	6	0.41	2	1	1
32	7.9	1.23	1	2	4
33	9.82	0.81	4	1	5
34	9.75	2.02	5	4	4
35	11.81	3.36	4	5	1
36	14	0	1	4	0
37	4.18	0.49	2	1	1
38	5.69	0.05	1	2	0
39	6.22	0.31	4	1	5
40	6.63	0.43	5	4	4
41	6.76	0.89	2	1	1
42	7.09	0.75	7	6	6
43	7.28	0.55	6	7	9
44	7.36	1.05	11	10	10
45	7.46	1.14	10	9	10
46	8.34	0.56	1	6	6
47	7.58	1.3	2	1	1
48	8.99	0	1	2	0
49	5.79	0.4	2	1	1

50 7.34 1.11 1 2 4
51 8.36 1.05 4 1 5
52 8.61 1.05 4 1 5
53 10.45 3.06 4 5 1
54 12.13 0 1 4 0
55 3.89 0.47 2 1 1
56 5.21 0.14 1 2 0
57 5.58 0.47 4 5 5
58 5.54 0.26 9 8 0
59 5.47 0.11 10 9 0
60 5.53 0.1 9 8 0
61 5.58 0 6 5 0
62 5.64 0.6 1 2 0
63 5.67 0 8 9 0
64 6.15 0.34 5 5 0
65 5.86 0.5 16 17 0
66 5.94 0.16 14 18 0
67 6.02 0 16 17 0
68 6.11 0 13 14 0
69 6.18 0.03 8 9 0
70 6.25 0.01 1 2 2
71 5.43 0.26 4 1 0
72 6.83 0 5 4 0
73 7.55 0.32 4 3 1
74 7.86 0.82 1 2 6
75 7.83 0.15 6 7 9
76 8.44 1.08 9 10 0
77 8.97 1.56 10 11 9
78 8.96 2.13 7 6 6
79 9.23 2.31 2 1 1
80 6.11 0.38 2 1 1
81 6.11 0.38 2 1 1
82 7.42 0.36 1 2 4
83 7.29 0.94 4 1 5
84 8.42 1.9 5 0 4
85 0 2.8 4 0 1
86 10.75 0 1 0 0
87 4.07 0.5 2 1 0
88 5.28 0.15 1 2 0
89 5.17 0.35 4 1 0

90 6.31 0.37 5 4 0
91 5.89 0.3 12 9 0
92 6.19 0.3 13 10 0
93 6.27 0.3 12 13 0
94 6.03 0 1 2 0
95 5.97 0 8 9 0
96 5.99 0.3 5 8 0
97 6.2 0 16 17 0
98 6.28 0 17 18 0
99 6.37 0 16 17 0
100 6.5 0 13 0 0
101 6.58 1 8 0 0
102 6.65 0 1 2 0
0

A.6 Yield dependence on target length.

Several lengths (50, 100, 200 and 500 mm) have been scanned in order to find an optimal configuration for the 15 mm diameter standard (200 mm long) ISOLDE UC target. The generation of isotopes has been assumed to scale proportionally to the length. This assumption is slightly optimistic for the longest target, but it is quite appropriate for the thin versions. The effusion profiles for Ni, Ga, Sn, Fr with a surface ionizer and of Kr and Ar with MK7-FEBIAD ionizers were computed and the corresponding release fractions for their isotopes were evaluated by use of *analyze* (which convolutes effusion and diffusion and applies the decay factor). Next, the release fractions were normalized to the generation. Finally, the results were divided by the values obtained for the standard target. The obtained numbers express the yield potential for each isotope with respect to the standard target. The following tables include these figures of merit for the 5, 10 and 50 cm and also for the *megatarget* (in that case generation simulated). A column shows the release fractions for the reference target.

A	$T_{1/2}$	R(5)/R(20)	R(10)/R(20)	R(20)[%]	R(20)/R(50)
67	21	2.7	1.8	*16.8*	2.7
68	29	2.5	1.7	*22.1*	2.6
69	11.2	3.2	1.9	*9.3*	2.8
69	3.5	4.0	2.1	*2.6*	2.8
70	6	3.7	2.0	*4.9*	2.8
71	2.56	4.0	2.1	*1.8*	2.7
74	0.9	4.4	2.2	*0.43*	2.9
76	0.24	5.4	2.5	*0.06*	3.29

Table A.1: Relative release efficiencies R(x)/R(20) for $x < 20$ cm and R(20)/R(x) for $x = 50$ cm, and R(20) for Ni isotopes in a UC_x target with a surface ionizer.

A.7 Release Parameters.

The sets of (FP,η,t_s) parameters chosen to describe the release from several isotope-matrix combinations are given in table A.6. For precise extrapolations, these results should be interpreted with certain reserves; otherwise they provide a good starting estimate for many applications. Fig 8.2 proves the accuracy of some of the fits.

A.8 EURISOL Beams.

The results of the simulations for the target conditions described in ch. 7 are presented in tables A.7, A.8, A.9 and A.10. The third column of each table, called *release* expresses the ratio between the extraction efficiency in simulated for the *megatarget* and that of the ISOLDE 20 cm long target at standard conditions. This factor (smaller than one) is multiplied by the relative gain in total production (a consequence of having more target material in *megatarget*) and it is stored in the fourth column. The last column results from multiplying the relative efficiencies (of columns three and four) by the present beam intensity

H ...																	**He** ...
Li 344	**Be** 1440											**B** ...	**C** 2230	**N** ...	**O** ...	**F** ...	**Ne** 75
Na 158	**Mg** 400											**Al** 428	**Si** 645	**P** ...	**S** ...	**Cl** ...	**Ar** 92
K 91	**Ca** 230	**Sc** 360	**Ti** 420	**V** 380	**Cr** 360	**Mn** 410	**Fe** 470	**Co** 445	**Ni** 450	**Cu** 343	**Zn** 327	**Ga** 320	**Ge** 374	**As** 282	**Se** 90	**Br** ...	**Kr** 72
Rb 56	**Sr** 147	**Y** 280	**Zr** 291	**Nb** 275	**Mo** 450	**Tc** ...	**Ru** 600	**Rh** 480	**Pd** 274	**Ag** 225	**Cd** 209	**In** 108	**Sn** 200	**Sb** 211	**Te** 153	**I** ...	**Xe** 64
Cs 38	**Ba** 110	**La** 142	**Hf** 252	**Ta** 240	**W** 400	**Re** 430	**Os** 500	**Ir** 420	**Pt** 240	**Au** 165	**Hg** 71.9	**Tl** 78.5	**Pb** 105	**Bi** 119	**Po** ...	**At** ...	**Rn** 64
Fr ...	**Ra** ...	**Ac** ...															
			Ce ...	**Pr** ...	**Nd** ...	**Pm** ...	**Sm** ...	**Eu** ...	**Gd** 200	**Tb** ...	**Dy** 210	**Ho** ...	**Er** ...	**Tm** ...	**Yb** 120	**Lu** 210	
			Th 163	**Pa** ...	**U** 207	**Np** ...	**Pu** ...	**Am** ...	**Cm** ...	**Bk** ...	**Cf** ...	**Es** ...	**Fm** ...	**Md** ...	**No** ...	**Lr** ...	

Table A.2: Low limit Debye temperatures $[K]$ [5].

A	$T_{1/2}$	R(5)/R(20)	R(10)/R(20)	R(20)[%]	R(20)/R(50)
61	0.15	3.2	1.92	*9.8*	2.8
62	0.116	3.41	1.96	*7.5*	2.8
63	32.4	1.03	1.02	*96.6*	1.1
64	157.6	1.01	1	*99.3*	1
75	126	1.01	1	*99.1*	1
76	32.6	1.03	1.02	*96.6*	1.1
77	13.2	1.06	1.04	*91.9*	1.2
78	5.09	1.16	1.11	*81.3*	1.4
79	2.847	1.28	1.18	*70.7*	1.7
80	1.697	1.45	1.27	*58.7*	1.9
81	1.217	1.6	1.35	*50.3*	2.1
82	0.599	2.04	1.55	*32.5*	2.5
83	0.31	2.58	1.75	*19.2*	2.7
84	0.085	3.53	2	*5.1*	2.8
85	0.05	3.88	2.04	*2.7*	2.7
86	0.03	4	2.05	*1.4*	3.0

Table A.3: Relative release efficiencies R(x)/R(20) for $x < 20$ cm and R(20)/R(x) for $x > 50$ cm, and R(20) for Ga isotopes in a UC_x target with a surface ionizer.

A	$T_{1/2}$	R(5)/R(20)	R(10)/R(20)	R(20)[%]	R(20)/R(50)
106	115	1.04	1.03	*94.9*	1.11
107	174	1.03	1.02	*96.6*	1.08
125	571.2	1.01	1.01	*98.9*	1.02
127	247.8	1.02	1.02	*97.6*	1.05
128	6.5	1.59	1.35	*50.7*	2.1
129	133.8	1.03	1.02	*95.6*	1.1
130	223.2	1.02	1.01	*97.3*	1.06
131	56	1.08	1.06	*90*	1.22
132	39.7	1.11	1.08	*86.5*	1.3
133	1.45	2.68	1.77	*17.7*	2.74
134	1.12	2.91	1.84	*14.0*	2.79
135	0.53	3.51	1.98	*6.7*	2.82
136	0.25	3.93	2.06	*2.8*	2.73
137	0.19	4.03	2.08	*2.0*	2.68
138	0.1 ?	4.17	2.12	*0.8*	2.68

Table A.4: Relative release efficiencies R(x)/R(20) for $x < 20$ cm and R(20)/R(x) for $x = 50$ cm, and R(20) for Sn isotopes in a UC_x target with a surface ionizer.

A	$T_{1/2}$	R(5)/R(20)	R(10)/R(20)	R(20)[%]	R(20)/R(50)
202	0.34	1.97	1.5	*12.9*	2.5
203	0.55	1.67	1.36	*19.6*	2.2
205	3.85	1.23	1.11	*53.5*	1.31
206	15.9	1.15	1.08	*74.5*	1.16
207	14.8	1.16	1.09	*73.5*	1.16
209	50	1.08	1.05	*87.8*	1.17
211	186	1.03	1.02	*95.9*	1.05
213	34.6	1.1	1.06	*84.1*	1.13
220	27.4	1.12	1.07	*81.4*	1.14
223	1308	1	1	*99.4*	1.01
224	198	1.03	1.02	*96.1*	1.05
225	240	1.02	1.01	*96.7*	1.04
226	48	1.08	1.05	*87.3*	1.11
227	148.2	1.03	1.02	*95.0*	1.06
228	39	1.09	1.06	*85.3*	1.12
230	19.1	1.14	1.08	*76.9*	1.15
232	5	1.22	1.11	*57.3*	1.27

Table A.5: Relative release efficiencies R(x)/R(20) for $x < 20$ cm and R(20)/R(x) for $x = 50$ cm, and R(20) for Fr isotopes in a UC_x target with a surface ionizer.

Matrix	Isotope	$\eta[s^{-1}]$	-log($t_s[s]$)	FP[μm]
UC_{ISOLDE}	^{6}He	4.34	∞	15
	^{23}Ne	0.48	∞	15
	^{40}Ar	0.336	∞	15
	^{90}Kr	0.114	∞	$\geq$15
	^{203}Fr	$\leq$0.022	$\geq$9	15
	^{70}Ga	3.55	6.82	15
	^{119}Sn	1.03	6.0	15
	^{59}Ni	$\geq$0.118	4.63	15
	^{184}Pb	0.1	9.5	15
ThC_{ISOLDE}	^{203}Fr	0.79	6.05	15
ZrO_2	^{6}He	2.37	∞	250
T = 2200 K	^{18}Ne	1.46	∞	250
CaO	^{6}He	3.16	∞	250
T = 1543 K	^{18}Ne	0.71	∞	250

Table A.6: Diffusion time constant, average sticking time and average free flight of several isotopes in various powder and fiber matrices at ISOLDE running temperatures.

Ion	Half-life	Release eff.	Target gain	Expected beam
^{67}Ni	21 s	$2.9{\cdot}10^{-2}$	1.0	$1.5{\cdot}10^{6}$
^{68}Ni	29 s	$3.3{\cdot}10^{-2}$	1.1	$3.0{\cdot}10^{6}$
^{69g}Ni	11.2 s	$2.3{\cdot}10^{-2}$	0.8	$1.1{\cdot}10^{6}$
^{70}Ni	6.0 s	$1.5{\cdot}10^{-2}$	0.6	$5.0{\cdot}10^{5}$
^{71}Ni	2.56 s	$1.8{\cdot}10^{-2}$	0.5	$1.3{\cdot}10^{5}$
^{74}Ni	0.9 s	$1.5{\cdot}10^{-2}$	0.4	$1.4{\cdot}10^{4}$
^{76}Ni	0.24 s	$1.3{\cdot}10^{-2}$	0.4	$1.7{\cdot}10^{2}$

Table A.7: Release efficiency gains, target gain (release $\times$ production) and forecast intensities for a 4 mA beam in a UC megatarget+RILIS, assuming an improvement factor of the ionization efficiency of 8.3.

and by the improvement factors expected for the ionization efficiency and for the primary beam intensity.

Ion	Half-life	Release eff.	Target gain	Expected beam
^{70}Ga	21.14 m	1.0	34	$1.5{\cdot}10^{9}$
^{73}Ga	4.86 h	1.0	34	$5.5{\cdot}10^{9}$
^{74}Ga	8.12 m	1.0	31.4	$5.5{\cdot}10^{9}$
^{75}Ga	126 s	$7.7{\cdot}10^{-1}$	26.3	$7.4{\cdot}10^{9}$
^{76}Ga	32.6 s	$4.7{\cdot}10^{-1}$	15.9	$3.8{\cdot}10^{9}$
^{77}Ga	13.2 s	$2.7{\cdot}10^{-1}$	9.0	$2.3{\cdot}10^{9}$
^{78}Ga	5.09 s	$1.3{\cdot}10^{-1}$	4.3	$8.1{\cdot}10^{8}$
^{79}Ga	2.847 s	$8.1{\cdot}10^{-2}$	3.4	$7.6{\cdot}10^{8}$
^{80}Ga	1.697 s	$5.6{\cdot}10^{-2}$	1.5	$1.6{\cdot}10^{8}$
^{81}Ga	1.217 s	$4.5{\cdot}10^{-2}$	1.5	$9.8{\cdot}10^{7}$
^{82}Ga	0.599 s	$2.9{\cdot}10^{-2}$	1.0	$1.2{\cdot}10^{7}$
^{83}Ga	0.31 s	$1.9{\cdot}10^{-2}$	0.6	$2.2{\cdot}10^{6}$
^{84}Ga	85 ms	$6.9{\cdot}10^{-3}$	0.2	$4.6{\cdot}10^{3}$
^{85}Ga	? 50 ms	$3.6{\cdot}10^{-3}$	0.1	$2.9{\cdot}10^{2}$

Table A.8: Release efficiency gains, target gain (release $\times$ production) and forecast intensities (slightly underestimated) for a 4 mA beam in a UC megatarget+RILIS, assuming an improvement factor of the ionization efficiency of 2.5.

Ion	Half-life	Release eff.	Target gain	Expected beam
^{87}Kr	76.3 m	1.0	35.7	$1.1{\cdot}10^{12}$
^{88}Kr	2.84 h	1.0	39.5	$2.6{\cdot}10^{12}$
^{89}Kr	3.15 m	$9.5{\cdot}10^{-1}$	38.1	$4.3{\cdot}10^{12}$
^{90}Kr	32.32 s	$8.1{\cdot}10^{-1}$	28.5	$4.7{\cdot}10^{12}$
^{91}Kr	8.57 s	$5.7{\cdot}10^{-1}$	18.2	$2.7{\cdot}10^{12}$
^{92}Kr	1.84 s	$2.3{\cdot}10^{-1}$	7.8	$7.4{\cdot}10^{12}$
^{93}Kr	1.286 s	$1.6{\cdot}10^{-1}$	5.9	$2.0{\cdot}10^{11}$
^{94}Kr	212 ms	$3.2{\cdot}10^{-2}$	1.8	$5.7{\cdot}10^{9}$
^{95}Kr	114 ms	$1.7{\cdot}10^{-2}$	1.1	$3.3{\cdot}10^{8}$

Table A.9: Release efficiency gains, target gain (release $\times$ production) and forecast intensities for a 4 mA beam in a UC megatarget+MK7, assuming an improvement factor of the ionization efficiency around 21.

Ion	Half-life	Release eff.	Target gain	Expected beam
^{109}Sn	18.0 m	1.0	34.0	$3.1{\cdot}10^{8}$
^{110}Sn	4.11 h	1.0	34.0	$3.2{\cdot}10^{8}$
^{111}Sn	35.3 m	1.0	34.0	$5.6{\cdot}10^{9}$
^{113}Sn	21.4 m	1.0	34.0	$2.5{\cdot}10^{10}$
^{117}Sn	13.60 d	1.0	34.0	$4.6{\cdot}10^{11}$
^{119}Sn	293.1 d	1.0	34.0	$6.0{\cdot}10^{11}$
^{123}Sn	40.06 m	1.0	34.0	$1.1{\cdot}10^{12}$
^{125}Sn	9.52 m	$7.7{\cdot}10^{-1}$	26.3	$1.2{\cdot}10^{12}$
^{127}Sn	4.13 m	$6.0{\cdot}10^{-1}$	20.4	$8.8{\cdot}10^{11}$
^{128}Sn	6.5 s	$6.0{\cdot}10^{-2}$	1.9	$5.7{\cdot}10^{10}$
^{129}Sn	2.23 m	$4.5{\cdot}10^{-1}$	11.9	$5.2{\cdot}10^{11}$
^{130}Sn	3.72 m	$5.7{\cdot}10^{-1}$	15.2	$1.2{\cdot}10^{12}$
^{131}Sn	56.0 s	$2.6{\cdot}10^{-1}$	8.2	$1.6{\cdot}10^{12}$
^{132}Sn	39.7 s	$2.0{\cdot}10^{-1}$	6.9	$9.3{\cdot}10^{11}$
^{133}Sn	1.45 s	$2.5{\cdot}10^{-2}$	0.9	$5.6{\cdot}10^{10}$
^{134}Sn	1.12 s	$2.2{\cdot}10^{-2}$	0.8	$5.9{\cdot}10^{9}$
^{135}Sn	530 ms	$1.5{\cdot}10^{-2}$	0.5	$3.6{\cdot}10^{7}$
^{136}Sn	250 ms	$9.8{\cdot}10^{-3}$	0.3	$6.8{\cdot}10^{5}$
^{137}Sn	190 ms	$8.2{\cdot}10^{-3}$	0.3	$1.9{\cdot}10^{4}$
^{138}Sn	100 ms ?	$4.2{\cdot}10^{-3}$	0.1	$1.9{\cdot}10^{2}$

Table A.10: Release efficiency gains, target gain (release $\times$ production) and forecast intensities for a 4 mA beam in a UC megatarget+RILIS, assuming an improvement factor of the ionization of 5.0.

Appendix B

Monte Carlo code. RIBO user manual.

B.1 RIBO, an MC code for isotope release optimization. Overview.

The Radioactive Ion Beam Optimiser, RIBO, is a scientific Monte Carlo simulation program focused on the optimization of radioactive ion beam production. It tracks the paths of atoms through ISOL targets, from generation (not included, this step should be calculated with codes like MCNPX [97], MARS [123, 124], FLUKA [98, 99]...) to ionization and extraction. It includes the following models:

Features of RIBO

- Diffusion from slabs, fibers or powder.
- Effusion in the molecular flow and the intermediate regime. Cosine law.
- Effusion through porous media.
- Absorption (condensation) to the walls.
- Adsorption-desorption on the walls (temporary retention).

- Specular effusion.
- Effusion through crystal systems (vibrations)[1].
- Roughness effects (latent option).
- Surface ionization.
- Plasma ionization.
- Ion recombination.
- Ion transport in electric and magnetic fields. Emittance plots.

Other models are in consideration and could be implemented as a result of the common effort of a community of prospective users. Developments should be centralized through a web-page.

There exists a number of applications to assist to write the input file and to analyze the output data[2]. Moreover, external programs could be coupled to expand the options of the present distribution.

B.2 Setup.

B.2.1 Description of files.

The RIBO code is distributed and backed by a number of FORTRAN files, data libraries and text files. The present distribution spans over the following files:

1. RIBO.sh, Diffuse.sh, 3D-RIBO.sh, RATE.sh

[1] It needs further development.
[2] A set of PAW-based applications is under developement

2. init.s, main.s, powder.s, surfion.s, plion.s, povray.s EMfield.s convgeom.s, emittance.s, translate.s, rotate.s, diffuse.f

3. `RIBO`, convgeom

4. plion.dat, workf.dat, sion.dat

5. test.inp, test.out, batch

6. manual.dvi, manual.pdf

In order to run the plasma and surface ionization utilities independently, these additional files are needed:

1. initsurfION.f surfION.e

2. initplION.f plION.e

Moreover, for the graphical options (*Diffuse*, *3d-RIBO* and *Trace*) the two freely available programs are required:

1. Physics Analysis Workstation [6].

2. Persistence of Vision, Povray [7].

B.2.2 Installation.

Place all the pre-compiled files (*.s) and the databases in a single directory. Then give execution rights to the installation routine, named *install*.

```
> chmod +x install
```

Execute install to proceed with the installation:

```
> ./install
```

Then you should enable execution permission on the executable file that has been created:

```
$>$ chmod +x RIBO
```

Finally you should edit your bash profile to include the path of the executable file or you can run it from the installed directory simply typing:

```
>./RIBO
```

Depending on the shell and configuration, typing 'bash' or 'sh' before 'RIBO' may also work.

Once installed, in order to use the program, an input file has to be created. The following instructions explain how to do this. Alternatively, you can test the installation with the test.inp file. Just remember to give the appropriate file path at runtime. Results will be stored in an output file whose name will be of your choice. Before doing a first test, it should be reminded that naming an output file with an existing file name will overwrite the existing one.

B.3 Input file.

The input file contains the information of the geometric arrangement of the target, the starting properties and nature of atoms and the end conditions. Choices about the physical models to be employed and determination of the output modes are decided interactively at run time.

The input file is organized in four (or five) cards[3] each of them grouping different sets of information. Every card is initiated by a key word which must not be

[3]This term of the computing jargon, comes from the days when punch cards where inserted in early computers to transmit a set of data.

changed (it is case sensitive) followed by a line that explains the inputs to come. The explaining line can be edited but not deleted. The next lines contain the core information of the card, like the coefficients of the equations of the surfaces or the logic of the cells. Extra line spacing within a card or between cards is authorized since the program skips blanc spaces. Concerning the columns of text, there are no constraints on the horizontal spacing of elements within a line. However, an even arrangement of elements in columns helps to clarify the input file and to find possible mistakes.

The first two cards give the entire geometry of the system (walls and volumes) through which particles will effuse. This means that outer elements where atoms cannot reach shall not be described (e.g. if particles effuse through a tube only the inner bore is given as input; the outer surface defining the core is omitted). First comes the card **Surfaces**, corresponding to the walls of the system. Second, the card **Cells** describes the elementary cells that are enclosed by the given surfaces.

Third, the **Source** card, which contains all information about the initial state of the atoms (position, speed, mass) and fourth the card **Tally**, which gathers the end conditions of the simulation.

Usually, time and velocity histograms are processed from the raw output data. However, in some cases it may be useful to get directly a histogram of the release times. This can be solicited by a fifth card called *Histogram*.

B.3.1 *Surfaces* card.

This card contains all the information of the walls (surfaces) that bound the effusion paths of atoms. In some Monte Carlo codes [98, 99] these are known as *bodies*.

The program works internally with the equations of quadrics[4], which are introduced in the *Surfaces* card. The first lines look like this:

Surfaces
n RC T X2 Y2 Z2 XY XZ YZ X Y Z C
third line
fourth line
...

The third, fourth, fifth ..., (n+2)th line have the information of the surfaces 1, 2, 3 ..., n. In each of these lines the first entry corresponds to the surface number, 1, 2, 3 ... Numbering should be done in consecutive jumps of 1 unity starting with 1. The second entry contains simultaneously two parameters of the surface nature, the roughness index (RC) - only relevant if Phong [33] reflections are active (see chapter 3.2.3) - is stored in the integer part and the absorption probability in the decimal part[5]; the temperature (T) - in Kelvin - of the surfaces is shown in the third entry, and the nine remaining numbers fully define any surface of second degree (quadric). The family of *quadrics* comprises planes, cylinders, cones, spheres, hyperboloids... With this base of surfaces almost any arbitrary shape can be approached with a moderate consumption of memory and computation time. Smooth bends of tubes could have been modeled in a single surface: a toroid. However, these belong to fourth degree surfaces (quartics), for which 33 parameters are needed. This is too costly and rather unmanageable, which means that such surfaces must be implemented in pieces.

Toroids have to be approached by several cylinders

A plane with an equation x = 1 could be implemented as (geometric entries):

0 0 0 0 0 0 1 0 0 1

The last number corresponds to the independent term (C). Naturally, any proportional equation would be equivalent, e.g:

[4] $c_{x^2} \cdot x^2 + c_{y^2} \cdot y^2 + c_{z^2} \cdot z^2 + c_{xy} \cdot x \cdot y + c_{xz} \cdot x \cdot z + c_{yz} \cdot y \cdot z + c_x \cdot x + c_y \cdot y + c_z \cdot z = C$

[5] e.g. 200.05 would mean that the surface is not diffusive (RC=200 $\sim$ Aluminum) and that its absorption coefficient is 0.05 (5 $\%$ of the impacting atoms condense to the surface).

0 0 0 0 0 0 -25 0 0 -25

A sphere centered at the origin of radius R would be $x^2 + y^2 + z^2 = R^2 = C$, thus:

1 1 1 0 0 0 0 0 0 R^2

If the sphere is centered at x_0, y_0, z_0 then, the equation transforms to $(x - x_0)^2 + (y - y_0)^2 + (z - z_0)^2 = 3^2$, hence:

1 1 1 0 0 0 -2x_0 -2y_0 -2z_0 ($R^2 - {x_0}^2 - {y_0}^2 - {z_0}^2$)

Similarly, ellipsoids and cylinders can be implemented. Moreover, arbitrarily oriented figures may be obtained by applying the rotation equations over the coordinates. For instance, an ellipsoid with an axis **a** in the x, y plane forming an angle α with respect to the x coordinate can be introduced by applying a rotation α_z; $\hat{x}$ is replaced by $cos(\alpha) \cdot x + sin(\alpha) \cdot y$ and $\hat{y}$ by $sin(\alpha) \cdot x - cos(\alpha) \cdot y$. Therefore: $a^2 cos(\alpha) \cdot x + sin(\alpha) \cdot y^2 + b^2 sin(\alpha) \cdot x - cos(\alpha) \cdot y^2 + c \cdot z^2 = 1$

It should be remarked that the number of surfaces accepted by `RIBO` is unlimited, but, naturally, if simplifications conduct to less elements, then the CPU power requirements will be lower and results will be obtained faster.

Unlimited number of objects

At this point some prospective users might be thinking that the level of complication involved in writing the input file is fairly high. Responding to the demands of the first groups that have been exposed to these explanations, a routine called **convgeom** has been written to assist in the generation of the *Surfaces* card.

When executing **convgeom**, the user is asked to choose a surface type, it can be a plane (P), a sphere (S), a Cylinder (C), an ellipsoid (SQ), a cone (K) or a general quadric equation (GQ). Depending on this first choice, `RIBO` then asks to specify the radius, or the position of the plane, or the orientation of the plane/cylinder, or

the radii of the ellipsoid. Then, the user can decide to rotate the surface by specifying the two Euler angles (or equivalently the two angles of the new $\hat{x}$ axis) and to make a translation. Finally the temperature of the surface is introduced and then the user can continue to define the second surface, and so on. The program writes into the input file the Surfaces card, including the headers. For example:

```
> convgeom
 what is the input file name?
INPUT
 surface number 1
 P:plane,S:Sphere,C:Cylinder,K:cone,SQ:ellipse,GQ:gen
P
 YZ (PX), XZ (PY), XY (PZ), AX+BY+CZ=D (P)
PX
 position?
1
 eq:   0.  0.  0.  0.  0.  0.  1.  0.  0.  1.
 rotation? give polar angles of new x vector
 (polar,azimuthal)=(90,0) ==> no rotation
90 45
 rotation   90.  45.
 (alpha,beta)=   0.  0.  0.  0.  0.  0.  0.707107  0.707107  0.  1.
 translation?give x0,y0,z0
1 1 0
  (x0,y0,z0)=   1.  1.  0.
 X(x0,y0,z0)=   0.  0.  0.  0.  0.  0.  0.707107  0.707107  0.  2.414214
 what is the temperature of the surface[K]?
2000
 add surface? (Y/N)
Y

 surface number 2
 P:plane,S:Sphere,C:Cylinder,K:cone,SQ:ellipse,GQ:gen\
C
 Radius=?
2
 CX, CY, CZ?
```

```
CX
 eq:   0.  1.  1.  0.  0.  0.  0.  0.  0.  4.
 rotation? give polar angles of new x vector
 (polar,azimuthal)=(90,0) ==> no rotation
90 30
 rotation   90.  30.
 X(alpha,beta)=   0.250000  0.750000  1. -0.866025  0.  0.  0.  0.  0.  4.
 translation?give x0,y0,z0
0 0 0
 X0  0.250000  0.750000  1. -0.866025  0.  0.  0.  0.  0.  4.
 (x0,y0,z0)=   0.  0.  0.
 X(x0,y0,z0)=   0.250000  0.750000  1. -0.866025  0.  0.  0.  0.  0.  4.
 what is the temperature of the surface[K]?
1500
 add surface? (Y/N)
N
```

The generated input file would look like:

```
Surfaces
n  RC  T  x2  y2  z2  xy  xz  yz ...
1 0.5 2000. 0. 0. 0. 0. 0. 0. 0.707106766 0.707106797 0. 1.
2 0.5 1500. 0.250000013 0.749999987 1. -0.866025418 0. 0. 0. 0. 0. 4.
```

It would now remain to define the cells.

B.3.2 *Cells* card.

This card includes the logic expressions that assemble the previously defined surfaces into the delimiting elements that enclose *cells* (these are referred to as **regions** in e.g. FLUKA [98] or GEANT4 [125]). Surfaces may extend infinitely, and therefore bounds are required to define real elements, thus the mechanism of cells. It should be stressed that cells are **finite** subspaces. This card has the following structure:

```
Cells
n  S1  S2  S3...
```

third line

fourth line

...

The third, fourth, fifth... (n+2)th lines correspond to the definition of the cells, 1,2,3 ... n, whose first element is precisely the cell number. The following columns define the cell volume in terms of the bounding surfaces. The MC code understands the cells as an intersection of the subspaces divided by a collection of surfaces; the boolean union operation is not defined; regions that require such an operator have to be split into several cells.

Boolean logics based on intersections

As an example of a simple cell, cell 1 comprises the volume over the plane 1, under the plane 2 and inside the sphere 3 then. The corresponding third line in the cells card is:

1 1 -2 -3

The recommended methodology consists in sketching the geometry and numbering the surfaces and cells onto this drawing. In some cases the concept *under* or *over* is not clear - like with oblique planes - then the guiding concept is the normal (unitary) vector at the surface; if the cell is to the side of the normal of the surface then the sign is positive, otherwise it is negative. This may again seem to lead to dubious cases. It should then be reminded that the gradient of the surface at a given point unambiguously defines the normal vector.

Sign defined by the gradient

Remarks:

- The MC code does NOT impose any restriction to the maximum number of cells of a given problem nor on the number of limiting surfaces of a given cell.
- The cells definitions have to be completed with zeros up to the maximum cell degree.

- The zeros in the cells definitions have to be put at the end.

- Cells are 'convex' elements; They are exclusively defined with the boolean intersection operator, and not with the union one.

The effort done with **convgeom** is directed to achieve the importation of geometry files whose format is compliant to other MC codes (e.g. MCNPX [97]). This shall enable to write the input files under those formats and to benefit from the plotting options offered by them.

B.3.3 *Source* card.

The *Source* card has up to 1+14 entries that describe the source atoms, their starting position and the velocity distribution. The first entry is a character that encodes the geometric distribution shape of the generated atoms. The following vector of 14 numbers gives details of the source: mass number (A) ($S(1)$), temperature ($S(2)$), semi-angle -α- of aperture of the luminous cone ($S(3)$) with respect to the central direction of emission ($S(4)$, $S(5)$, $S(6)$), the birth coordinates centroid ($S(7)$, $S(8)$, $S(9)$), and details regarding the shape of the distribution. Coordinates from S(7) to S(14) are explained below:

Maximum 15 entries for the source

1. **P**oint source. Only three geometric parameters are needed: x_0, y_0, z_0.

2. **S**pherical source. Like the point source with a radius: x_0, y_0, z_0, R.

3. **B**ox source. Particles are sampled within a parallelepiped centered at x_0, y_0, z_0, with sides of *full* lengths L_x, L_y, L_z and oriented in space with the angles θ, φ.

4. **T**arget generation. The starting position is sampled inside a cylinder centered at x_0, y_0, z_0, of radius R, *full* length L_x, Gaussian radial dispersion $sigma$, and angles $\hat{n}$: θ, φ.

   Some remarks have to be made at this stage:

- A **C**ylinder category has not been included because random cylindrical birth distributions are a special case of **T**arget with $sigma = 0$.
- All angles -aperture cone and axis orientation- should be given in degrees.
- The atom temperature (in Kelvin) expresses the energy (velocity) of the atoms. If it is unknown then a good value is that of the wall temperatures since thermalization should fully have taken place after a few hundred collisions.
- The central angle of emission is indeed a velocity (unitary) directing vector. However, normalization is **not** required, it is done internally, e.g., 2 1 1 (not normalized) can be given instead of 0.8165 0.4082 0.4082 (normalized but not fully precise).
- For isotropic generation $\alpha = 180\,^\circ$, for focused beams $\alpha = 0$. In no case it can be omitted.
- Dimensions are expected, like elsewhere, in cm.
- The default axis for the cylinder and target is $\hat{x}$. If the cylinder has its axis in $\hat{y}$ then, (θ, φ) = (90 °,0), if it is in $\hat{z}$, then (θ, φ) = (0,90 °). Note that these rotations only affect the geometry of generation and not the velocity vectors. This means, in particular, that angles like (-90 °,0) or (0,-90 °) would also be valid for the two examples just shown. In these trivial examples this does

not matter, but, for more complicated cases the parity property avoids errors of 'sign'.

- In total, for the point source 1+6+3 data are needed, 1+6+4 for spheres and 1+6+8 for the rest.

A simulation for a given source gives way to various sets of events (collisions, flight paths...). If these events are sorted into histograms, the resulting distributions can be added and subtracted to those of other simulations. This permits to reproduce almost any source by performing additions and subtractions from the elementary sources. Thus, e.g. the flight path of atoms born in a cylindric ring can be obtained by subtracting the pondered flight path distribution of a small cylindric source to that of a bigger one. Normalization has to take into account the volume of the respective sources and the number of histories[6]. As a first step, all histograms could be normalized to unity and then they could be weighted proportionally to the spatial volume of the sources. Analogue procedures are possible for complicated velocity spectra.

Another possibility to work with more elaborate sources is to force generation inside a given cell. This option is offered at runtime:

```
source limited to a cell? give cell number.
 0: no constraint | <0: just generate geometry plot
```

A basic delimiting source is needed every time. The primary container source, chosen between *Point, Sphere, Target* and *Box* should include the entire source cell. If the introduced cell number is '0' then the method remains inactive. If it is negative, then `RIBO` will not do any simulation, it will just generate a plot of the

[6]In Monte Carlo jargon, each individual repetition is called *history*, and the whole group of histories is called *simulation*, whose *size* will be the number of histories.

geometry (see B.6). Otherwise particles will be sampled exclusively inside the selected cell. This method can be universally used, e.g., an infinite sphere containing a dodecahedron, but in order to perform efficient simulations the volume of the primary source ought to match the cell dimensions as closely as possible (this is similar to the concept of **the rejection sampling technique** [126]). For instance, sampling the birth of atoms homogeneously inside the volume of a $\frac{1}{4}$-sector of a cylinder - cell **2** in the example below - can be carried out first by defining a source cylinder C of the same radius and then by using the cell delimiter command. The efficiency of the method corresponds to the fraction of the cylinder sector (here it is 25 $\%$).

Surfaces

n	RC	T	X2	Y2	Z2	XY	XZ	YZ	X	Y	Z	C
1	0.5	298	0	0	0	0	0	0	1	0	0	0
2	0.5	298	0	0	0	0	0	0	1	0	0	10
3	0.5	298	0	1	1	0	0	0	0	0	0	1
4	0.5	298	0	0	0	0	0	0	0	1	0	0
5	0.5	298	0	0	0	0	0	0	0	0	1	0

Cells

n	S1	S2 ...
1	1	-2 -3 4 5
2	1	-2 -3 4 -5
3	1	-2 -3 -4 5
4	1	-2 -3 -4 -5

Source

Type	M	T	Alpha	nx	ny	nz	x	y	z	L	s	th	phi
C	40	298	180	1	0	0	5	0	0	10	0	0	0

Tally

S	Nmax	Tmax	Tpmax
2	1000	110	101

. . . At runtime . . .

```
source limited to a cell? give number. 0 for no limit
```

The cell-delimited source command is more powerful than the composition (additions or subtractions) of simulations and can simulate more complicated distributions; e.g., a ring can be simulated by both ways but a cylinder sector is only produced by the cell restrictor, as just shown.

The instructions given up to this point already offer a a fairly high control of the geometry distribution of the starting atoms and also give the possibility to choose the initial speed, the direction and the semi-aperture angle of an isotropic emission cone. However, the user may want to define fancier distributions: correlation of velocity and position coordinates, speed distributions, position dependent weights...the possibilities are infinite. Responding to these potential needs, a new source mode called *File* should allow users to use the 7-vector {time, position(3), speed(3)} as input coordinates for `RIBO`, which will read them from a file. This function can work cooperatively with the output mode 11 (Convolution), which gives these coordinates at a certain surface of the system.

Moreover, a file named *source.f* detached from the main program will be available in a near future so that users can edit the source code of the source, to adapt it to particular cases.

B.3.4 The *Tally* (end) card.

The end conditions are preceded by a line with the word *Tally*. There are four inputs, the first and last are relative to the individual histories and the two intermediate fix the end conditions for the global simulation. An end Tally looks like this:

```
Tally
S    Nmax    Tmax   Tpmax
3     6000    750    10
```

The text and the case of the first line are unmodifiable, the second line is indicative and should not be omitted although it can be edited at the user taste. The first number in the last line indicates the surface used as detector for the atoms. When atoms reach this surface, the history is completed and a new atom is simulated. The fourth number alternatively terminates the current history if the individual flight time reaches a certain threshold[7]. Setting a low threshold can be useful to have a fast scan of a rapid release peak, sparing the long simulations of the tails of the release distributions. For release fitting purposes, however, the threshold should be high, in order to avoid annoying normalization issues. The second number displays the number of histories (size of the simulation) and the third one the maximum elapsed time. The simulation is finished as soon as any of these two events takes place: maximum time OR maximum number of atoms (histories).

B.3.5 *Histogram* card.

This card is optional, it is used to automatically produce a histogram of the release times thus avoiding more tedious analysis of data. This card comes after *source* and starts by the key word *Histogram*, unmodifiable. The next line is explanatory (though not deletable), it tells that the following line will define the time grid of the histogram. That grid, described in the third line, is built up by the starting points of the corresponding intervals (measured in seconds). These need not be constant, but it should be pointed out that if irregular bins are used, then the values of the histogram would have to be normalized accordingly (RIBO does not correct for the size of the interval). Moreover, there is no limit to the number of intervals.

[7] Unlike the other threshold times, this one is not CPU time, but physical flight time.

```
Histogram
I1      I2      I3      I4
0.001  0.002  0.003  0.005
W
1       1       1       1
```

The fifth line should contain the character 'W' and may not be modified or omitted. The last line has as many numbers as defined intervals. This line shall specify the weight of the intervals, not only for specific normalization purposes but also for a variance reduction method of the Russian roulette type, partly implemented in the last version. For the time being the numbers are needed for a correct compilation of the input file, but their value has no effect on the resulting histogram.

B.4 Executing RIBO. Runtime options.

At run time the user interacts with the program in order to define the input and output file names, the type of output, the models to be used and the options that shape out the results of the simulations.

In the first place the user introduces the file name of the **input file** and of the *output file*[8]. The input file name needs no particular extension, usually *.t is used, getting at the fact that the file describes a *t*arget, but *.inp or any other choices are also accepted:

```
  Name of the input file?
/user/simulations/InputFiles/rectangle.t}
```

The name of the **output file** again needs no particular extension, *.out is quite intuitive (*.o should be avoided as it may lead to confusion between the output files and the object (assembled) files).

[8]Under some circumstances it may be necessary to specify the full path.

```
 Name of the output file?
(Beware it will overwrite the existing file)
/user/simulations/OutputFiles/rectangle.out
```

The code then asks whether a histogram card is present in the input file (see B.3.5), answering ‘Y‘ and not having written the Histogram card in the input file will be the fastest way to stop the program.

```
histogram mode(Y,N)?
```

If the user wishes to intersect the domain covered by *Source* (see B.3.3) with the volume restricted by a given cell, it is then asked to specify the cell identifier. Otherwise, the value ‘0‘ will impose no restriction.

```
source limited to a cell? give number. 0 for no limit
```

The following module activates the ionization mode. Depending on the choice additional parameters will be demanded.[9]

```
what type of ionization?
No Ioniz.=1, Plasma=2, Surf.=3, Absorption=4
```

As a function of the previous choice four options are then possible:

1. If RIBO is run without ionization, then no more data will be required at this point and the program will continue to collect the runtime parameters.

2. If ionization is activated, then the code will ask into how many cells the ion source expands.

Configuring the ion source

[9] A fourth option including laser ionization could be available in the future. The fifth option is not really an ionization mechanism, it is used to map the distribution of radioactive atoms stuck in the walls as a consequence of prolonged sticking.

```
 how many ionizing cells? max is ncell
 .
 .
 how many ionizing surfaces in cell 3?
1
Ionizer surface number 1 in ion cell 1?
9
```

- If *Plasma* ionization has been chosen, then the RIBO code will start by asking which are the indexes of all the ionizing cells, then it will demand the the flux of electrons and the program **plION** will take charge of the calculation of the electron impact direct ionization cross section subsequently asking for the energy of the electron beam, the species to be ionized and the sought ion state[10].

- If *Surface* ionization is chosen, then the program will ask for the cell index of the first ion cell and for its corresponding surface ionizers, then it will do the same for the second ion cell and so on. Next a program called **surfION** will be launched and it will ask which is the number of the surface that corresponds to the ionizer , and then it will demand the atomic numbers of the projectile and of the substrate, or, in their default, the work function, their mass number and the type of compound (Boride, Carbide, Element...).

3. If absorption has been activated, then, after each collision to the walls, the code will check if the particle condenses in the surface. In order to do so, a uniform random number is compared to the absorption probability on the surface, which should have previously been introduced in the input file,

Activating absorption in the walls

[10]The database (plion.dat) should be consulted to see if the wished ion is tabulated.

in the decimal part of the second input of each surface (the integer part corresponds to the roughness parameter) as explained in B.3.1.

From the fan of phenomena implemented in RIBO, after having decided about ionization, the user is asked to specify which of the remaining steps will be included in the simulation.

```
SELECT MODE:
 1: Diffusion
 2: Effusion
 3: Diffusion+Effusion
recommended 2
```

1: Diffusion If the user only wants to simulate Diffusion (this can't be so if Ionization is activated), then an ulterior option asks whether it will be in-grain or inter grain diffusion or both.

```
Diffusion/Powder.effusion/Both $[D/P/B]$?
```

In any case, one can obtain average parameters only or delay distributions[11].

```
CHOOSE THE OUTPUT MODE:(recommended 13)
 1: Only average figures
 2: Diffusion delay distribution
```

2: Effusion The recommended and standard option is '2' because diffusion can be simulated separately with **diffprof**. If only effusion is chosen (in addition or not to ionization), then the alternatives thereby available are:

- `1: Only average figures` For the measurement of conductances.
- `3: Effusion delay distribution` This is useful when interaction with walls is irrelevant (no sticking).

[11] Required if time histograms are to be plotted.

- 5: Number of collisions Useful to study desorption enthalpies.
- 6: Velocity direction spectra If this option is chosen, then an ulterior choice is given:

  3-v Components or Projection over vector(C/P)? In the second case the three components of the projector have to be introduced.
- 7: Particle tracking options This point is explained at B.5.
- 10: Time(eff) and angular distribution Like option 7 with an additional vector of effusion times.
- 11: Convolution (t,x,y,z,ux,uy,uz) This option casts a sextuple of results. It permits to study the correlations between speed and position, speed and time, radius and time... Moreover, the raw simulated data (or the correlation laws obtained from it) could serve as input conditions for another calculation that would describe a continuing piece of the system. The results could then be processed using the associations of conductances (section 3.4). This technique breaks up CPU-over demanding systems, but its accuracy decays when the reflection from downstream parts towards the source becomes relevant[12].
- IF THERE IS POWDER... These options regard structures with powder or fiber.
- 12: Delay in the effusion out of the powder
- 13: Powder / Effusion / Ncollisions This option produces a triplet of results, with dwell times in powders, effusion times and number of collisions.
- 14: Powder + Effusion / Ncollisions Like the previous choice, but with the first two numbers confused in one.

[12]The methodology is optimal for systems with accused throttles.

3: Diffusion+Effusion This option combines the first two. The advantage is that the final release times (diffusion+effusion) are obtained without need of convoluting an analytical diffusion formula with a fitted histogram of effusion. The drawback is that diffusion is sampled, and therefore it includes a stochastic, artificial error.

4: Conductance calculator (Clausing Coefficient) This option estimates the conductance between two sections in terms of the Clausing coefficient. For technical reasons, the surfaces cannot coincide with the *endsurface* defined in the *Tally* card.

```
1: Only average figures
Introduce the beginning and ending surfaces
```

Extracting conductances for analytic vacuum calculations

The next alternative concerns the physic model to be used for the reflection of atoms from the walls. Specular reflection may be used to represent reflections of light in systems of mirrors, Lambertian reflections follow the cosine model and thermalize the energy of the projectile to that of the surface, and exact reflections include information of the crystal lattice and of its vibrations.

Reflection models

```
 What kind of treatment of the collisions?
S=specular(very low E),B=Knudsen-Lambert,D="exact"
 recommended B
```

During runtime the user can decide between having the energy of the reflected particles sampled from the Maxwell-Boltzmann distribution or fixing its energy to the average of the distribution. The second option saves CPU time while preserving precise results if the number of collisions is high enough (central theorem of the limit for normal distributions), but it may give way to notorious statistical errors in situations where few collisions take place.

```
Average energy(Y,N)?(for high number of collisions
recommended Y
```

Including temporary sticking

It has been shown that the number of collisions suffered by each particle in its path to the exit of the system (or before ionization) can be included among other output numbers. Nonetheless, in some circumstances it may be interesting to include sticking in the release times.

```
Sticking time$[s]$? (e.g. 5E-9; 0 for noble gases)
 recommended 0, and you add it later
```

Selecting target filling

The following step decides if the module for continuous media shall be used. If there is no continuous porous material (only slabs or empty system, etc.) then the option 'S' shall be used. The choice between powder and fiber is only relevant when diffusion is included in the calculation.

```
target filling: Slabs Fibers or Powder [S/F/P]?
```

If 'F' or 'P' are chosen then the program will need to know the average flight path of atoms in the Fiber or Powder. It will also ask for the probe spheres that should be used as macro steps for faster calculation.

residual pressure

The pressure inside the system is introduced in order to enable collisions between gas atoms.

```
STARTING MODULE FOR INTERACTIONS BETWEEN ATOMS
residual pressure?[Torr](0 for molecular flow)}
```

If no more input is given, the program will estimate the mean free path between atom collisions from statistical considerations. Alternatively, if the mean free path is known, it should be provided.

```
OR ENTER MEAN FREE PATH[cm] (0 if you ignore it)
```

In case of ionic transport, the emittance is computed with the program *emittance.f*. The central axis has to be modified to match the particularities of each case. The output is written in emit.map.

```
**************************************************************************
***     EEEEE  M    M  II  TTTTT  TTTTT   AAA   N    N   CCCC  EEEEE     ***
***     E      MM  MM  II    T      T     A   A  NN   N  C      E         ***
***     EEEE   M M M  II    T      T     AAAAA  N N  N  C      EEEE      ***
***     E      M    M  II    T      T     A   A  N  NN  C      E         ***
***     EEEEE  M    M  II    T      T     A   A  N   N   CCCC  EEEEE     ***
**************************************************************************
*
      SUBROUTINE emittance(epsilon,x,y,z,ux,uy,uz)
       real*8 epsilon(2),x,y,z,ux,uy,uz,U(3),R(2),Pi
       Pi=3.14159257
*    Modify this according to the exit axis and position
       U(1)=ux
       U(2)=uz
       U(3)=uy
       R(1)=x-0.0
       R(2)=z-1.0
*    Safeguard condition
       IF (U(3).eq.0.0) THEN
         write(6,*)'Warning: extraction axis perpendicular to velocity'
         U(3)=1E-12
       END IF
*
       write(4,'(1X,F8.4,F9.5,F8.4,F9.5)')R(1),U(1)/U(3),R(2),U(2)/U(3)
       epsilon(1)=epsilon(1)+10*R(1)*1000*atan(U(1)/U(3))/Pi
       epsilon(2)=epsilon(2)+10*R(2)*1000*atan(U(2)/U(3))/Pi
      END
```

At this point the program has all necessary elements to pursue simulations, eventually including in-grain diffusion in slabs, particles or fibers, inter-grain diffusion through powders or fibers, effusion in molecular or intermediately pressurized systems, with mirror like walls, diffusive walls or crystals, and ionization in plasma chambers or surface ionizers. After preprocessing some messages will appear in the screen and simulations will start. The connectivity

matrix will be stored in a file called CCONM and the results will be stored in the output file.

B.5 Debugging running errors.

Running a Monte Carlo code is similar to programming: every little thing that is overlooked contains a potential bug and it will most likely induce an error at some point. The time required to detect and to fix the bug will exceed the amount of work needed to avoid such flaws from the beginning. This general recommendation concerns specially the implementation of the geometry. It is strongly advised to take some time to do a sketch of the system as it will be modeled, drawing and labeling each surface and marking the cells. Eventually this step may already help to rise some questions about the optimality of the target and often new configurations are immediately suggested. Moreover, the sketch helps to attain a logic numbering of surfaces and of cells, this will in turn aid to write the input file and also to introduce future modifications. Once the input file completed, it should be reread, cross checking with the sketch, counting the number of cells and surfaces, verifying that no space is undefined or multiply defined. If the file has been correctly tabulated, a fast glance will spot typing errors from the irregularities in the columns of data.

As what concerns the systematics, another advice is to make several stages before reaching the full complexity of the problem. This enables to progressively correct mistakes; for instance, first one can implement the system of tubes with a simple source (point source), then, after debugging, insert the target material (foils or powder…), and, only after proper running, implement a more complex

source, etc. If this were done in one go, it would be harder to disentangle the individual causes of the overall errors.

If a major error has been produced the program will terminate, complaining about some input/output error. If this happened it could be due to any of these causes:

- Some of the lines needed have been forgotten (like the card names or the explanatory lines).
- A coefficient in the cells definition has been omitted, typically some zero, or the roughness coefficient, or the independent term.
- All cells do not have the same number of elements; some cell has not been completed with zeros.
- The source type is not compatible with the number of source parameters (missing orientation angles or particle mass, or temperature . . .).
- An additional line has been written somewhere (line breaking is not authorized).

Once the input file is 'digested' by the program, it is preprocessed and a message summarizes the geometry, telling the number of surfaces, the number of cells and the maximum number of surfaces that contour a cell.

```
reading geometry...
7 surfaces 2 cells 6 surf.per cell}
DONE
```

The MC code then assembles the geometry, thereby networking the cells that have a common interface, and then it saves the result into an array. By doing so, each time that `RIBO` verifies whether a particle migrates from the current cell to any neighboring region (this happens after every collision), the amount of checks

needed is reduced to the number of connecting cells, listed in the connectivity matrix (computed only one, at the beginning). That matrix, printed separately in the file **CCONM** condenses a lot of information of the geometry of the system and therefore it aids to cross-check the *Cells* and the *Surfaces* cards of the input file. The file contains a column with several groups of integer numbers; every group starts by the cell number and it is followed by those cells that have a common interface with that given cell[18]. The CCONM matrix of the followed example has only two groups (there are only two cells):

```
1
2
2
1
```

The first group says that cell number 1 (first line) is connected to cell number 2 (second line), the second group says that cell number 2 (third line) is connected to cell number 1 (fourth line). This case is quite trivial but it helps to underline two properties:

- The connectivity matrix is symmetric.
- All groups should at least have two elements so that no cell is isolated from the rest[19]. Every row of the connectivity matrix must have at least two numbers different from zero.

If the source of particles were entirely located outside the system or if the cell source contained some errors, then a message on the screen would clearly warn the user:

```
Error in source card, source out of cell domain?
```

[18] This does by far not mean that these cells are actually touching.
[19] If that were the case an error message would show on screen and in the CCONM file.

This may happen due to an incorrect implementation of the source or to some flaw in the definition of the geometry of the system.
In some cases the errors of geometry are detected by a routine of `RIBO` that casts a message on the screen like:

```
GEOMETRY ERROR!
check cell 2 or surface 4
```

However, many errors are not traced by the code; a vast geometry case compiler is still a pending task for future upgrades of the program.
For the time being one more tool is available for debugging purposes. At runtime, option 7 gives the opportunity to track a particle from birth to termination. This tracking can be made effective in three subsequent choices:

```
Choose one option
 1:coordinates x,y,z
 2:cell history
 3:surface history
```

Normally this is enough to detect persistent geometry mistakes.
In addition to all this, the user can change the end surface and choose closer surfaces (e.g. instead of having the gage at the end of a complex tubular system, it can be first put at the end of the beginning section and then pushed forward to next section, etc.) to ease the detection of the errors of geometry.

B.6 Making 3D model views.

Making a 3D view of the target geometry is one of the fastest options to find out bugs in the geometry and to become aware of the target proportions. This is now possible through *3D-RIBO* and *Povray*. The first program executes `RIBO` and

halts it when the Povray compliant geometry file (*.pov) is created. Next *Povray* is called and the image file (*.tga) is created.

```
> 3D–view input.t 1
```

The flat *1* specifies that the image file will be a thumbnail. *2* or *3* would produce images with higher resolution.

The intermediate *.pov file is a text document with the combinatorial geometry in povray format. This file can be edited to include fancy features, e.g. roughness and special optical effects. Then, 3-D can be run by specifying the proper file extension.

```
> 3D–view input.pov 1
```

B.7 Express Execution with a batch file.

One of the most useful tools is the execution through a batch file. This file permits to execute the program routinely without having to reintroduce the interactive options.

When RIBO is executed all runtime options are automatically recorded in a file whose default name is 'batch'. If the user then wishes to re-simulate the system, it will be enough to type the *.exe file with '<batch' at the end, which means that all interactive data will be taken from the batch file.

The potential of this methodology is vast; a user could edit the batch file, change some input parameters (probably also the output file name) and save it as batch1, then repeat for different parameters for batch2... Finally, a script like:

```
{
code < batch1
code < batch2
```

⋮

}

or even a script with a loop, could produce an enormous amount of data.

B.8 Output file.

The output file contains information about the run, average numbers and variables linked with every history. Its shape depends on the requests made by the user during execution, but in general terms these elements can be outmarked:

- Heading. It includes authoring information and specifies the input file name and path.
- Individual scores. This section may contain the global and fractioned release time and total number of collisions for every simulated atom. This usually constitutes the core goal of the simulations since it permits to reconstruct the intrinsic release functions.
- Preconfigured histogram. This histogram (unnormalized to bin size) appears if the card Histogram is included in the input file.
- Average figures of the release speed. This group of data includes the average release time, the relative time consumption in the diffusion and effusion phases, the amount of in-grain versus inter-grain diffusion time... In presence of ionic fluxes, this output is divided in two groups, for ions and for neutral atoms. This allows assessing the impact of ionization in the effusion path and extraction efficiency.
- Average effusion time in each cell. It permits to see which elements are slowing down effusion.

- Average number of collisions to each surface. This array provides clues on the potential chemical selectivity of each surface, or on its surface ionization power.
- Statistics of the free flight: average distance between two consecutive collisions, average flight path from birth to ionization or up to extraction...
- Statistics of the effusion in a powder or fiber (if present): average free flight path, number of collisions...
- Report of the effect of the residual gas: average free path between two collisions with a gas atom and average number of collisions per history.
- Summary of the ionization scores: ionization probability, estimate of the ionization efficiency and error margin.
- Module integrating computation times.
- Authoring.

In the following section an example illustrates a complete output file presenting almost all modules.

B.9 Examples.

B.9.1 First example. Geometry issues.

The first example consists on bulb full felt with He at 300 K and connected to a pipe of 1 cm diameter with a bend of 90 °. Dimensions are shown in fig.B.1. It is indeed a simple geometry, but attention has to be paid to define the correct subspaces unambiguously. For that sake auxiliary planes are needed. In fig.B.2.

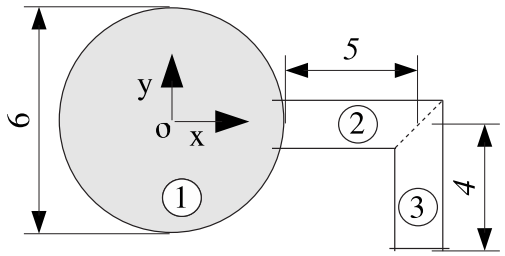

Figure B.1: A simple example consisting on a bulb full of He at 300 K connected to a pipe of 1 cm diameter with a bend of 90 °.

surface 2 is an auxiliary plane that will help to define the second cell, if it was not used, the program could not logically decide between the real cell and the dotted one. In fact, it would allow transmission of particles both to the right and to the left. The same is valid for the crossing of pipes at the surface 4. The *Surfaces*

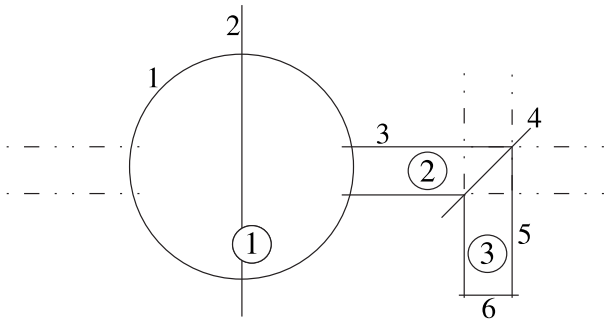

Figure B.2: Surfaces and cells for the first example. Auxiliary surfaces are needed to define the correct subspaces.

card would be something like this:

Surfaces

n	rc	T	x2	y2	z2	xy	xz	yz	x	y	z	C
1	0.5	300	1	1	1	0	0	0	0	0	0	9
2	0.5	300	0	0	0	0	0	0	1	0	0	0
3	0.5	300	0	1	1	0	0	0	0	0	0	0.25
4	0.5	300	0	0	0	0	0	0	1	-1	0	8
5	0.5	300	1	0	1	0	0	0	-16	0	0	-63.75
6	0.5	300	0	0	0	0	0	0	0	1	0	-4

And the *Cells* card would read as:

Cells

n	S1	S2	S3	S4
1	-1	0	0	0
2	1	2	-3	4
3	-4	-5	6	0

The *Source* card, for a homogeneous distribution in the sphere should be:

Source

Type	M	T	Alpha	nx	ny	nz	x	y	z	L	s	th	phi
S	4	300	180	1	0	0	0	0	0				

B.9.2 Second example. Bigger files.

A more realistic example for the field of radioactive ion beams is that of a target made of thin foils. Fig.B.3 sketches a target with a SPIRAL Christmas-tree-like shape [2, 3], intended to dissipate the energy of the beam in steps. Surfaces 1, 2 and 3 are planes and 4 and 5 cylinders; they delimit the target container and the transfer line (cells 1 and 2, respectively). The sixth surface is a cone and the remaining surfaces 1 ÷ n are planes; these surfaces enclose the target slabs (of thickness d) and the spacing between them (δ between two consecutive front faces). The *Surfaces* card would look something like this (the symbols L1,

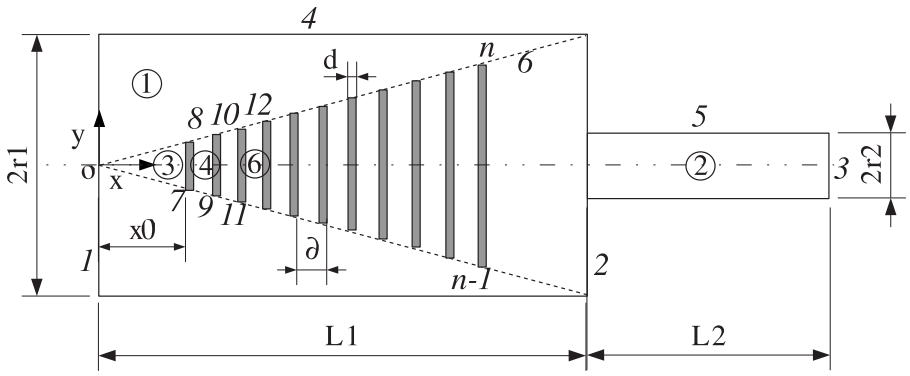

Figure B.3: Sketch of a GANIL-SPIRAL type target [2, 3].

L2. . . should have to be replaced by numeric values):

Surfaces

n	rc	T	x2	y2	z2	xy	xz	yz	x	y	z	C	
1	0.5	300	0	0	0	0	0	0	1	0	0	0	plane
2	0.5	300	0	0	0	0	0	0	1	0	0	L1	plane
3	0.5	300	0	0	0	0	0	0	1	0	0	L2	plane
4	0.5	300	0	1	1	0	0	0	0	0	0	$r1^2$	big cylinder
5	0.5	300	0	1	1	0	0	0	0	0	0	$r2^2$	small cylinder
6	0.5	300	-(r1/L1)^2	1	1	0	0	0	0	0	0	0	containing cone
7	0.5	300	0	0	0	0	0	0	1	0	0	x0	first foil front
8	0.5	300	0	0	0	0	0	0	1	0	0	x0+d	first foil back
9	0.5	300	0	0	0	0	0	0	1	0	0	x0+δ	second foil front
10	0.5	300	0	0	0	0	0	0	1	0	0	x0+d+δ	second foil back

⋮

The *Cells* card would look more or less like this (if the number of elements is big, the best method is to use a spreadsheet to generate surfaces and cells):

Cells

n	S1	S2	S3	S4	
1	1	-2	-4	6	container outside target zone
2	2	-3	-5	0	Transfer line and/or ionizer
3	-6	1	-7	0	cone peak
4	-6	7	-8	0	space between foils 1 and 2
5	-6	8	-9	0	space between foils 2 and 3

⋮

B.9.3 Overall example.

In the standard distribution of files an example input file called *test.inp* and a possible output file called *test.out* are provided. In this section all steps will be thoroughly described: input file, runtime options and interpretation of the output file. Thus, the user shall be able to test the system and to get acquainted to most functions of `RIBO`. Once results are recovered, experiencing with the input file and runtime options is encouraged so as to gain a total control of the program prior to real-case usage. The test example describes a fairly simple geometry (fig.B.4), composed by three cells and 9 surfaces. The first cell is a revolution

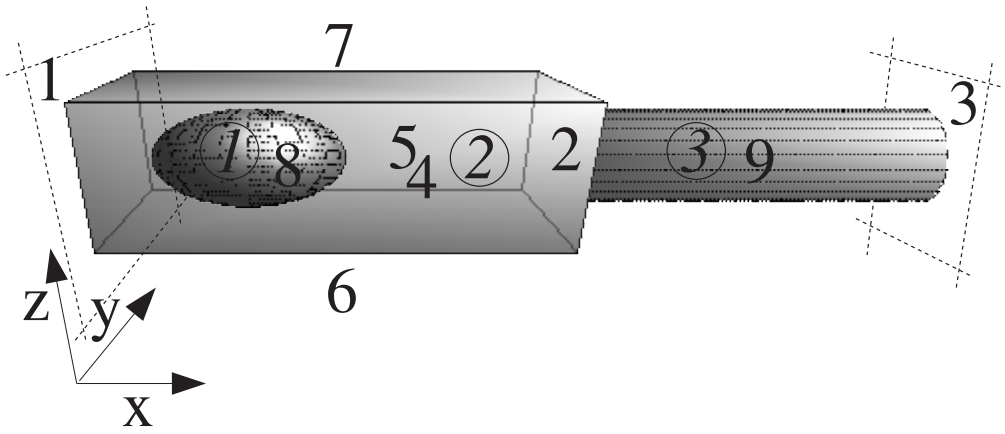

Figure B.4: The target and ion source of example 3.

ellipsoid of axis 1 and 0.25 cm (Rx, and Ry, Rz) long, composed of a powder (particles of 5 μm) where Li atoms (Z=3) are isotropically generated at 298 K, diffusing with $D = 10^{-7} \cdot cm^2 \cdot s^{-1}$ and encountering powder particles every 50 μm. The second cell contains the first one, it is a parallelepiped of 1 cm square side with a length of 5 cm (all walls are at ambient temperature). A 1 cm diameter, 5 cm long pipe (the third surface) is plugged at one end, its cylindric wall is made of W (surface ionizer, Z = 74) at 2000 K and the extreme represents the output surface (end surface). The whole system is under a residual gas pressure of 10^{-4} Torr. This problem involves cell-conditioned generation, in-grain diffusion, inter-grain diffusion (effusion through powder), effusion, atom to atom collisions and surface ionization.

Input file

The details of the problem are found in the input file:

Surfaces

n	RC	T	X2	Y2	Z2	XY	XZ	YZ	X	Y	Z	C
1	0.5	298	0	0	0	0	0	0	1	0	0	-1.5
2	0.5	298	0	0	0	0	0	0	1	0	0	5

```
3   0.5   298   0   0   0   0   0   0   1   0   0   10
4   0.5   298   0   0   0   0   0   0   0   1   0   -1
5   0.5   298   0   0   0   0   0   0   0   1   0   1
6   0.5   298   0   0   0   0   0   0   0   0   1   -1
7   0.5   298   0   0   0   0   0   0   0   0   1   1
8   0.5   298   0.25  1   1   0   0   0   0   0   0   0.25
9   0.6   2000  0   1   1   0   0   0   0   0   0   0.249
Cells
n   S1   S2 ..
1   -8   0   0   0   0   0   0
2   8   1   -2   4   -5   6   -7
3   2   -3   -9   0   0   0   0
Source
Type  M   T   Alpha  nx   ny   nz   x   y   z   R
S   7   298   170   -1   0   0   0   0   0   0.99
Tally
S   Nmax   Tmax   Tpmax
3   300   750   10
Histogram
Intervals
0E-3   2E-3   4E-3   6E-3   8E-3   10E-3   12 E-3   14E-3   16E-3   18E-3   20E-3
W
1   1   1   1   1   1   1   1   1   1   1
```

The primary source that is used here is a sphere, the radius of which equals the maximum radius of the ellipsoid. The cell-limited option will be chosen at runtime.

Runtime options

The sequence of interactions with the program at runtime is screen printed below. Some comments are interpolated:

The ion source may span over multiple cells

```
Name of the input file?
/user/simulations/infiles/test.inp
ifile=
/user/simulations/infiles/test.inp
Name of the output file?(check it does no exist!)
```

```
/user/simulations/outfiles/test.out
 READING INPUT FILE
 ...
 histogram mode(Y,N)?
Y
 reading geometry...
 9 surfaces 3 cells 7 sur.per.cell
  DONE
 source limited to a cell? give cell number.
  0: no constraint | <0: just generate geometry plot
1
 Postprocessing geometry...
  DONE
 what type of ionization?
   No Ioniz.=1, Plasma=2, Surface=3, Absorption=4
3
 how many ionising cells? max is 3
1
 cell number of ion cell number 1
3
 how many ionising surfaces in cell 3?
1
 Ionizer surface number 1 in ion cell 1
9
```

Having selected surface ionization the program SURFION is triggered

```
   Nmax1, Nmax2= 102 27
  atom:
  element (Z)? (0 if you want to define parameters)

 3
  substrate:
  element (Z)? (0 if you want to define parameters)

 74
  0:element;1:Boride;2:Carbide;3:Oxide;4:CeCompound
 s
 0
```

```
 gplus,gzero,gminus,Wf,Wi,Ae  1.  2.  1.  4.54
5.39  0.62
 T?[K]
2000
 positive surface ionization
 alphaS=  0.00360563289
 negative surface ionization
 alphaS=  6.61641972E-11
 betaS=  0.003592679
```

The program chooses positive surface ionization. betaS is the individual probability of ionization after each collision with the ionizer.

```
SELECT MODE:
    1: Diffusion
    2: Effusion
    3: Diffusion+Effusion
     recommended 2
    4: Conductance calculator (Clausing Coefficient).
3
CHOOSE THE OUTPUT MODE:(recommended 13)
    1: Only average figures
    2: Diffusion delay distribution
    3: Effusion delay distribution
    4: Diffusion+Effusion
    5: Number of collisions
    6: Velocity direction spectra
    7: Particle tracking options
    8: Diffusion &(Effusion-Sticking) & N collisions
    9: Diffusion &(Effusion-Sticking)v & Sticking
   15: Diffusion,Effpowder,Effusion,collpow,coll

15
  What kind of treatment of the collisions?
  S=specular(very low E),B=Knudsen-Lambert,D="exact"
   recommended B
B
  Average energy(Y,N)?(for high number of collisions)
   recommended Y
```

```
Y
  Sticking time[s]? (e.g. 5E-9; 0 for noble gases)
   recommended 0, and you add it later
0
  target filling:
  Slabs Fibers or Powder [S/F/P]?
P
  Thickness/diameter[micrometer]? (e.g. 25)
5
  Diffusion coefficient[cm2/s] (e.g. 9E-9)?
1E-7
  Generating diffusion release function...
  v=  949.3955
  mean free path in powder/fiber[um]?
   e.g. UC powder 15, ZrO2 fiber 250
50
  sphere probe radius[um](step path)? e.g. 800

   recommended: 6 x mean free path
250
  sampling a limiting residence time in powder...

   2.05884266
  DONE, tmax powder=  1.61319953E-05
  Characterization of macrocollisions in powder:

   Generating time and angle probability functions

   ... this may take some minutes ...
```

The program prints a matrix with the number of counts (over 10000) in every pixel of angle and time, corresponding to the release of atoms from a macro-sphere of powder

```
0.  30. 248. 245. 139. 101.  59.  31.  26.   9.  4. 12.  1.  3.  3.  0. 0. 1. 1. 0
0. 118. 705. 647. 404. 243. 169.  86.  66.  34  24. 12.  6. 10.  2.  2. 0. 1. 1. 0
0. 173.1142.1081. 685. 448. 249. 161.  97.  50  33. 16. 11.  4.  3.  2. 3. 1. 2. 1
0. 237.1590.1409. 879. 589. 342. 171. 110.  69. 51. 19. 11.  6.  6.  2. 0. 2. 0. 2
0. 284.1838.1697.1068. 638. 411. 219. 169.  93. 58. 42. 13. 14.  5.  5. 1. 1. 0. 0
0. 298.2117.2033.1322. 795. 503. 274. 193. 115  70. 34. 19. 18.  9.  5. 1. 5. 4. 2
0. 356.2276.2152.1445. 810. 493. 313. 177. 104  75. 39. 16. 10. 12.  4. 2. 3. 0. 1
```

```
0. 352.2332.2278.1419. 872. 557. 342. 188. 107  63. 35. 21. 21. 14.  6. 6. 3. 2. 0
0. 358.2452.2210.1476. 847. 533. 328. 203. 122. 76. 54. 26. 18. 16. 10. 7. 5. 1. 2
0. 318.2318.2181.1395. 853. 490. 302. 164. 115  72. 33. 17. 24. 12.  4. 3. 2. 1. 1
0. 301.2249.2049.1325. 794. 474. 292. 189.  87  69. 47. 19. 14. 10.  4. 2. 2. 3. 1
0. 253.2023.1844.1212. 763. 434. 258. 183. 103  55. 39. 28. 14.  8.  4. 2. 2. 1. 2
0. 223.1695.1756.1067. 611. 414. 223. 152.  79  47. 26. 18. 17.  5.  2. 3. 1. 0. 0
0. 174.1499.1419. 938. 596. 295. 182. 128.  72  33. 24. 21.  4.  9.  2. 2. 1. 3. 2
0. 147.1170.1146. 747. 497. 241. 153. 104.  56. 44. 15. 16.  9.  3.  2. 0. 1. 0. 2
0. 121. 944. 922. 584. 370. 216. 127.  82.  47. 30. 16. 11.  7.  4.  4. 4. 0. 0. 1
0.  78. 619. 594. 413. 252. 161.  93.  54.  39. 12. 15.  9.  3.  4.  0. 1. 0. 1. 1
0.  41. 321. 326. 226. 107.  79.  48.  31.  19. 10.  7.  7.  2.  0.  0. 0. 0. 0. 0
0.   9.  74.  76.  39.  19.  15.  12.   6.   2.  0.  2.  0.  0.  0.  0. 0. 0. 0. 0
0.   0.   0.   0.   0.   0.   0.   0.   0.   0.  0.  0.  0.  0.  0.  0. 0. 0. 0. 0
```

```
 DONE
 END OF INITIALIZATION. SIMULATION STARTS!!
 en Init powder tmax=  7.81743336
 STARTING MODULE FOR INTERACTIONS BETWEEN ATOMS
 residual pressure?(Torr)(0 for molecular flow)
1E-4
 OR ENTER MEAN FREE PATH[cm] (0 if you ignore it)
0
 Free mean path between collisions with gas[cm],l,T,d,P:
  49.639892  298.  44.  0.0001
 DONE.
 DONE
 RUNNING...
```

Output file interpretation

The resulting output file displays the following information (comments are interpolated).

```
...
*************************************************** ***
results after processing input file:
/user/simulations/infiles/test.inp
-------------------------------------------------- --
preprocessing CPU time[s]=   1637.
-------------------------------------------------- --
  Tdiff    Tpowder Teffusion Collpowder Collwalls
  0.01700  0.00156  0.02295 29588.1577  1504.0000
  0.05300  0.00111  0.00923 21083.2814   520.0000
  0.04900  0.00065  0.02550 12415.0474  1535.0000
  0.06100  0.00074  0.01094 14003.1784   696.0000
```

Here there are as many lines as thrown atoms

⋮

0.03300 0.00206 0.03519 39087.4725 1926.0000

- -

HISTOGRAM

0	17.
0.002	29.
0.004	21.
0.006	24.
0.008	17.
0.01	18.
0.012	12.
0.014	12.
0.016	14.
0.018	16.
0.02	120.

This means that 120 out of 300 atoms take longer than 20 ms to get ionized.

- -

Average intrinsic delay time[s]= 0.00352790219

Slowest particle took 0.229640706[s]

Estimated decay time(tao)[s]= 0.00081014995

0.[%] of the particles not released

from the bulk before 10.[s].

Average particle time consumption:

62.722875[%Diffusion] 37.277125[%Effu sion]

- - - - - - - - - - - - - - - - - -

AVERAGE DELAY in POWDER: 0.00227700276[s]

DIFFUSION DISTRIBUTED AS:

—- 97.1396846% grain diffusion

—- 2.86031541% intergrain diffusion

- - - - - - - - - - - - - - - - - -

- average effusion time in each cell [%] -

cell	¡time fraction¿
1	0.
2	94.5079864
3	5.49201359

- - - - - - - - - - - - - - - - - -

average number of collisions in each surface

surface	¡collisions¿
1	4.59525808

2	3.59211078
3	0.
4	14.5283256
5	14.5346202
6	14.6472933
7	14.560428
8	0.
9	16.0526647

- -

FREE EFFUSION:

Average free path$[m]$= 1.30483272

Distance between collisions:

average= 1.58107849$[cm]$

highest maximum= 6.98473383$[cm]$

Average number of collisions= 82.5280168

100.%b1 0.%b2 0.%D 0.%S

b1: Stuck particles. Emitted thermally

b2: Surface stuck particles. Thermally emitted

D: Inelastic scattering. Debye surface phonons

S: Almost elastic scattering. Specular reflecti on

- -

EFFUSION IN POWDER:

Average path$[m]$= 0.0617565531

4.51902809$[\%]$ of total path

Average collisions in the powder= 1235.14232

93.7368237$[\%]$ of total

Distance between collisions in powder:

average free mean path 49.9995442$[um]$

RESIDUAL GAS:

Mean free path$[m]$: 49.639892

Average n of collisions with residual atoms:

2.52664708

SURFACE IONIZATION

surface collision ionization probability: 0.0035 92679

ionization efficiency= 6.29458666%

relative error= 14%

Number of histories$[N]$= 300. CPU time$[s]$= 109.

CPU time/history= 0.363333333$[s/history]$

CPU time/collision= 0.000277180187$[s/collision]$

==========

Connectivity matrix.

In this case the matrix of candidate links between cells is very simple:

1
2
2
1
3
3
2

This means that the first cell is only connected to the second (it is indeed so because it is embedded in the latter one), that the second source is connected not only to the first but also to the third one and that the third cell is only linked to the cell number two.

Data analysis.

The results stored in the output file can be analyzed in various manners depending on the specific needs of the problem. Usually the individual parts are imported into a worksheet in order to plot histograms with the possibility to observe the influence of several parameters on the delay time. Whence, a first column of results may contain the diffusion time, and this may be modified proportionally as a function of η. In the same way, the effusion time vector may be adjusted to a particular speed of atoms (proportional to $T^{0.5} \cdot M^{-0.5}$) and the sticking time vector will be obtained by multiplying the array that stores the number of collisions by the individual sticking times.

The array of results shall be divided in equally sized groups in order to compute separate calculations, merge them and compare them. This procedure provides information about the variance of the results.

B.10 Diffuse. A diffusion emulator

DIFFUSE is a bash shell script that manages the core FORTRAN program DIFFUSE.F. It computes diffusion profiles analytically (through the infinite series provided by Fujioka [14] and the second law of Fick [11]) and, for one-dimensional geometries under variable and/or non-homogeneous conditions, numerically (first law of Fick). Additionally, it may compute the diffusion coefficient provided that a release fraction is known at any given time. More details can be found in 2.5.1.

Running DIFFUSE is trivial because it is fully interactive. Fig.B.10 shows the first and second menu choices. In fig.B.5(a) options **1,3,5** permit to plot the drop of total concentration in the slab as a function of time. **5** additionally shows the space dependency (2-D graph). In any of the cases, it is necessary to install PAW [6] to have the functions plotted. Otherwise, the user can take the output data, written in the file *profile.dat* and use his favorite data analyzing program. **2** and **4** invert the diffusion function to extract the Diffusion coefficient from a fixed diffusion release situation.

Based on the chosen option, DIFFUSE poses the following questions:

Insert the number of space nodes

A good compromise between precision and speed of computation would be between 10 and 1000.

Insert the diffusion coefficient [cm2/s]

The units are specified, $[\frac{cm^2}{s}]$

Fractional concentration

Insert the remaining concentration.

e.g. 0.5 would mean that 50 % has diffused out.

Insert the lapse length [s].

It refers to the final time, or the time at which the fractional concentration is measured.

Time definition.

Insert the printing time grid (number intervals).

The time steps for the diffusion calculations are adjusted internally to keep the system stable, but the time steps are often much too small to have them all printed. Thus, the user specifies what should be the time binning.

For the present status of the program, the user needs to introduced the wished time dependencies directly in the corresponding subroutines.

```
      SUBROUTINE timeN(N,i,m,t,dt,a)
        real*8 N(m,2),t,dt,tao,pulse,a,x
        integer*4 i,m
* decay law
        tao=0.097                                                    20
*        tao=27.0
*        N(i,1)=N(i,1)*exp(-log(2.0)*dt/tao)
* pulsing source
        x=(a/m)*i
        pulse=0.5                                                    21
        IF (mod(t,pulse).lt.1.0001*dt.and.t.gt.pulse) THEN
          N(i,1)=N(i,1)+functC(x,a)*1
        END IF
      END
```

For time dependencies, or

```
      FUNCTION functC(x,a)
        real*8 x,a
        x=a-x
        functC=1*exp(-x*10.0/a)*(1-exp(-x*1.0/a))
        x=a-x                                                        22
        functC=1*sin(x*3.1415927/a)**2
```

```
      functC=1
    END
```

For space variations of the concentration or, finally:

```
      FUNCTION D(i,m,a,t,Dc)
        real*8 x,a,t,Dc,r
        integer*4 i,m
        x=da*(i-0.5)
*       D=Dc*sin(x*3.1415927/a)*exp(-t/100)                    23
        D=Dc
*       r=0.999
*       D=((1+r)-(2*r)*(x/a))*Dc
        IF (t.le.1) THEN
*         D=7.7778*Dc                                          24
        END IF
      END
```

For space and time variations in D.

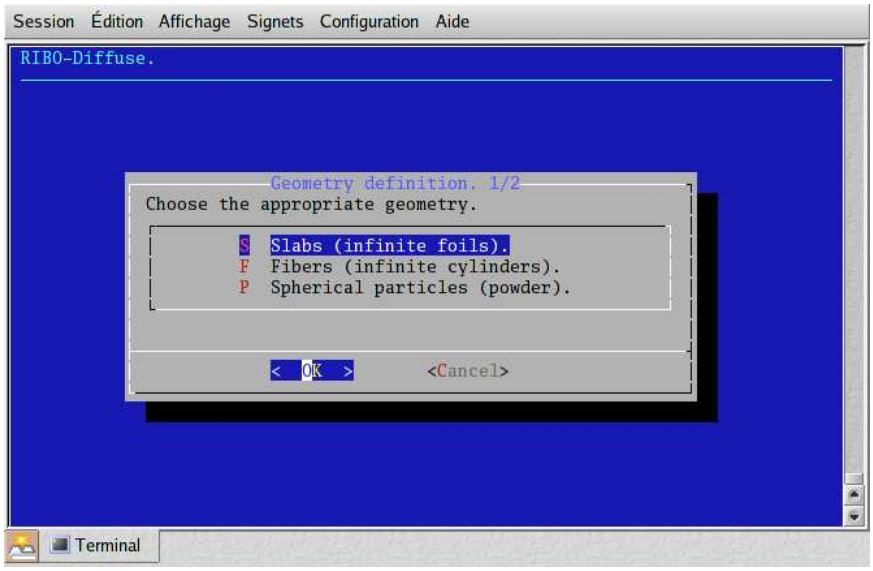

(a) First choice of DIFFUSE.

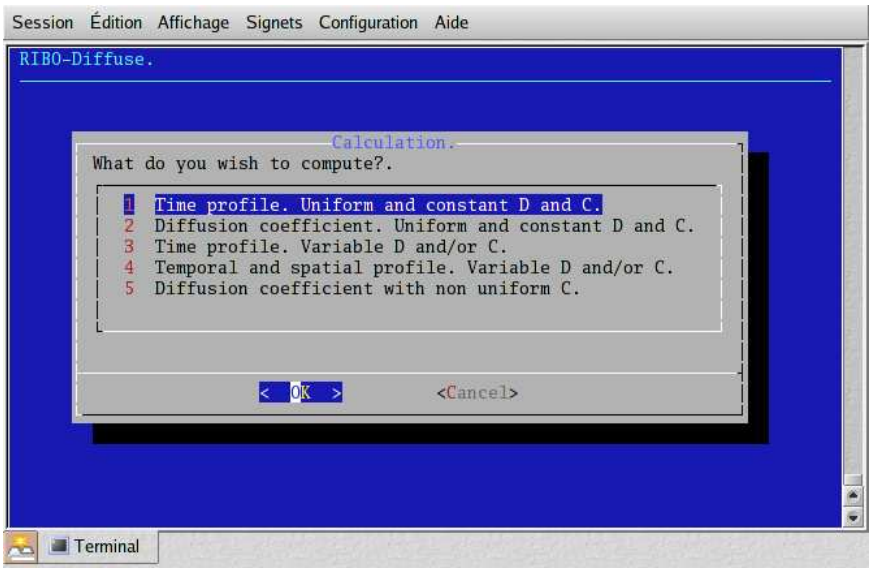

(b) Options for 1-D calculations.

Figure B.5: Screen captures of the interactive DIFFUSE program.